TU Delft

Delft University of Technology

Sustainability of engineered fractured systems

An experimental study on hydro-mechanical properties

Kluge, C.

DOI
10.4233/uuid:4f688b2f-1f2c-4e14-a1be-cc867bb0cd25

Publication date
2021

Document Version
Final published version

Citation (APA)
Kluge, C. (2021). *Sustainability of engineered fractured systems: An experimental study on hydro-mechanical properties*. [Dissertation (TU Delft), Delft University of Technology]. https://doi.org/10.4233/uuid:4f688b2f-1f2c-4e14-a1be-cc867bb0cd25

Important note
To cite this publication, please use the final published version (if applicable).
Please check the document version above.

Copyright
Other than for strictly personal use, it is not permitted to download, forward or distribute the text or part of it, without the consent of the author(s) and/or copyright holder(s), unless the work is under an open content license such as Creative Commons.

Takedown policy
Please contact us and provide details if you believe this document breaches copyrights.
We will remove access to the work immediately and investigate your claim.

This work is downloaded from Delft University of Technology.
For technical reasons the number of authors shown on this cover page is limited to a maximum of 10.

Sustainability of engineered fractured systems

An experimental study on hydro-mechanical properties

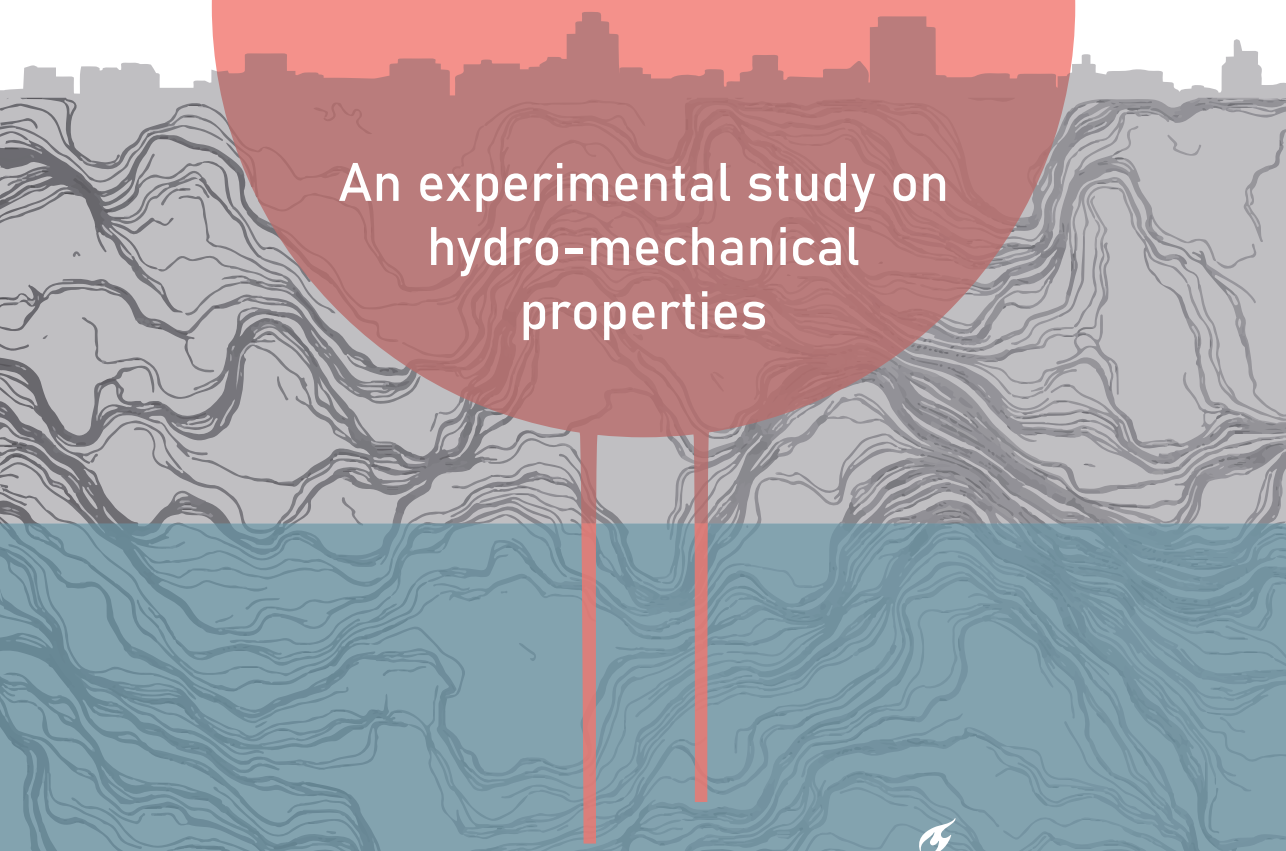

Christian Kluge

TU Delft Delft University of Technology

Sustainability of engineered fractured systems

AN EXPERIMENTAL STUDY ON HYDRO-MECHANICAL PROPERTIES

Proefschrift

ter verkrijging van de graad van doctor
aan de Technische Universiteit Delft,
op gezag van de Rector Magnificus Prof. dr. ir T.H.J.J. van der Hagen,
voorzitter van het College voor Promoties,
in het openbaar te verdedigen op donderdag 1 april 2021 om 15:00 uur.

door

Christian KLUGE

Ingenieur Technische Aardwetenschappen,
Technische Universiteit Delft, Nederland,
geboren te Lutherstadt Wittenberg, Duitsland.

Dit proefschrift is goedgekeurd door de

promotor: Prof. dr. D. Bruhn
copromotor: Dr. A. Barnhoorn

Samenstelling promotiecommissie:

Rector Magnificus,	voorzitter
Prof. dr. D. F. Bruhn,	promoter
Dr. A. Barnhoorn,	promoter
Onafhankelijke leden:	
Prof. dr. W. R. Rossen	Technische Universiteit Delft
Prof. dr. ir. P. L. J. Zitha	Technische Universiteit Delft
Prof. dr. T. Backers	Ruhr-Universität Bochum
Dr. M. Brehme,	Technische Universiteit Delft
Overige leden:	
Dr.-Ing. M. G. Blöcher	GFZ German Research Centre for Geosciences

Keywords: Fractures, sustainability, permeability, laboratory, geothermal

Printed by: Gildeprint

Front & Back: Illustration of fluid flow in fractures in the subsurface.

Copyright © 2021 by C. Kluge

ISBN 978-94-6366-392-2

An electronic version of this dissertation is available at
http://repository.tudelft.nl/.

Time can only be defined by a change of a condition A into a condition B.
If condition A and condition B are similar, no time has passed.
Not making any progress in your project does not waste time.

C. Kluge

CONTENTS

Summary xi

Samenvatting xiii

1 Introduction 1
- 1.1 Rationale . . . 2
- 1.2 Scope of the thesis . . . 4
- 1.3 Thesis outline . . . 4
- References . . . 5

2 On the validity of the cubic law 13
- 2.1 Introduction . . . 14
- 2.2 Methods . . . 14
  - 2.2.1 Fracture topography generation . . . 15
  - 2.2.2 Fluid flow simulations . . . 16
  - 2.2.3 Model verification . . . 17
- 2.3 Results . . . 18
  - 2.3.1 Aperture distribution . . . 19
  - 2.3.2 Variations in fracture displacement . . . 19
  - 2.3.3 Variations in fracture roughness . . . 21
  - 2.3.4 Correction factors for the cubic law . . . 22
- 2.4 Discussion . . . 22
- 2.5 Conclusions . . . 24
- References . . . 24

3 Hydro-mechanical properties of microfaults 27
- 3.1 Introduction . . . 28
- 3.2 Materials & methods . . . 30
  - 3.2.1 Testing equipment . . . 30
  - 3.2.2 Sample material . . . 30
  - 3.2.3 Sample geometry & experimental setup . . . 32
- 3.3 Experimental procedures . . . 33
- 3.4 Experimental results . . . 37
  - 3.4.1 Fracture generation . . . 38
  - 3.4.2 Permeability & dilation evolution during failure . . . 39
  - 3.4.3 Permeability evolution during pore pressure cycling . . . 41
  - 3.4.4 Fracture geometry from x-ray μ-CT scan analysis . . . 44
- 3.5 Discussion . . . 45
  - 3.5.1 Microfault generation . . . 45
  - 3.5.2 Permeability & dilation during fracturing & shearing . . . 48

3.5.3 Sustainability of permeability . . . 49
3.6 Conclusions . . . 52
References . . . 53

4 Enhancement potential & sustainability of microfaults 59
4.1 Introduction . . . 60
4.2 Materials & methods . . . 61
4.2.1 Testing equipment . . . 61
4.2.2 Sample material . . . 62
4.2.3 Sample geometry & experimental setup . . . 63
4.2.4 Experimental procedure . . . 63
4.3 Experimental results . . . 66
4.3.1 Fracture generation . . . 67
4.3.2 Permeability & fracture dilation during faulting . . . 68
4.3.3 Permeability evolution during pore pressure cycling . . . 69
4.4 Microstructural analysis of fault geometry . . . 70
4.4.1 Fault geometry in Odenwald granite . . . 70
4.4.2 Fault geometry in Flechtingen sandstone . . . 73
4.4.3 Image analysis & shear zone width . . . 74
4.4.4 Variations in shear zone width . . . 77
4.5 Discussion . . . 80
4.5.1 Microfault propagation & microfault architecture . . . 80
4.5.2 Impact of fault architecture on hydraulic properties . . . 82
4.5.3 Sustainability of fault permeability . . . 84
4.6 Conclusions . . . 86
References . . . 90

5 The stress-memory effect of fractures 97
5.1 Introduction . . . 98
5.2 Materials & methods . . . 100
5.2.1 Testing equipment . . . 100
5.2.2 Sample material . . . 100
5.2.3 Experimental procedure . . . 101
5.3 Experimental results . . . 106
5.3.1 Sample volume & permeability of the intact rock . . . 106
5.3.2 Tensile fracture generation . . . 107
5.3.3 Fracture permeability & aperture during CCL . . . 108
5.3.4 Fracture stiffness evolution during CCL . . . 110
5.3.5 Permeability & aperture during PCL . . . 110
5.3.6 Fracture stiffness evolution during PCL . . . 111
5.3.7 Fracture roughness exponent before & after testing . . . 113
5.4 Discussion . . . 117
5.4.1 Fracture stiffness & the stress memory effect . . . 117
5.4.2 Relationship of mechanical & hydraulic properties . . . 120
5.4.3 Limitations of the experimental data . . . 122
5.4.4 Sustainability of permeability & implications . . . 124

5.5 Conclusions 125
References 126

6 Discussion & Conclusion **133**
6.1 Integrated Discussion 133
6.2 Conclusions 138
References 139

Acknowledgements **143**

Curriculum Vitæ **145**

List of Publications **147**

SUMMARY

The Earth's subsurface exhibits a high potential for generating and storing energy. Utilizing the subsurface heat by circulating fluids through rocks is known as geothermal energy production. Storing hydrogen gas, synthetic methane gas or heat in the subsurface provides energy at times when renewable sources are ineffective. Such engineered subsurface reservoirs highly depend on the capacity of rock to conduct and store fluids. Faults and fractures create the largest contrasts in flow in these reservoirs. Understanding their hydro-mechanical behaviour is crucial to the success of such projects. Unfortunately, fractured rocks are one of the most heterogeneous media and scientists have studied fractured rocks over decades. Still, each project dealing with fractured rocks has proven to be unique with specific challenges depending on a variety of factors. Laboratory rock testing is a crucial element to derive and understand the physical processes in fractures.

In this thesis, the dependence of fracture permeability on a variety of parameters is studied. The aim is to develop a better systematic understanding of the hydro-mechanical processes controlling the potential of fractures to conduct fluids at a variety of conditions. A specific concern is to determine the sustainability of fracture permeability. This is crucial for the long-term success of any subsurface engineering project. Therefore, several parameters that are assumed to control fracture permeability are considered in laboratory experiments. These include the rock type (clastic vs. crystalline), the fracture type (shear vs. tensile), the fracture geometry (aperture and roughness) and effective stress changes (pore and external stress). Potential geothermal rocks from Europe are considered here in order to directly relate our findings to potential geothermal exploration projects.

The complexity of fracture systems is often simplified with approximations. The cubic law is a famous and frequently used simplifications that describes the flow of fluid through a fracture by assuming two parallel plates separated by a fixed distance. In this thesis, the dependency of the flow through a fracture on the roughness and shear displacement, that causes heterogeneous aperture distribution, was studied in numerical 3D fluid flow simulations (chapter 2). From this study it was found that the cubic law better approximates fracture flow for larger apertures, but fails for smaller apertures. This is due to the disturbance and channelization of flow caused by local aperture changes. It already shows the complexity of flow in fractures. Another simplification is often made when performing laboratory fluid flow experiments in fractured rocks: Shear fractures are approximated by tensile fractures that are manually displaced to a given offset. This neglects any structural features commonly observed during shear fracturing in nature. Therefore, the re-designed "Punch-Through Shear" test was used to be able to monitor the permeability evolution for a realistic shear fracture configuration (chapter 3). This novel testing set-up revealed a potential permeability increase through microfaulting of up to three orders of magnitude at an effective stress of 20 MPa in a granitic rock. Effective pressure cycling of ± 5 and ± 10

MPa was applied to study the sustainability of the generated enhancement. Permeability and dilation is shown to be reversible, which is in contrast to existing studies. It is assumed that the pressure conditions during fracture generation lead to less plastic energy within the microfaulted system compared to displaced tensile fractures. Additionally, it was investigated how the microstructure of a microfault relates to the permeability enhancement in clastic and crystalline rocks (chapter 4). It became obvious, that compared to granite, permeability is not necessarily enhanced in low-porosity sandstone. Microstructural analysis revealed a narrower fault width and less pronounced fault morphology, as well as an absence of a damage zone in sandstone in contrast to granite. Due to the small scale of the laboratory experiments it was attempted to up-scale the fault width distribution by applying a scale-independent roughness exponent. A relation similar to rough fracture surfaces was found for both rocks. Lastly, the fracture closure potential during cyclic loading was investigated (chapter 5). A series of experiments with displaced tensile fractures was performed with different cyclic loading scenarios: constant cyclic loading and progressive cyclic loading. From the experiments a stress-memory effect of fracture stiffness similar to the "Kaiser Effect" in intact rocks was found. It is characterized by a change from a non-linear stiffness trend at previously reached stress levels, to a linear trend at stresses that exceed any previously reached stress level. Combined with continuous permeability measurements, it is suggested that fracture permeability and the contact-area ratio are dependent on the stress-history of rock.

In conclusion, by the simplification of the fracture geometry in laboratory testing, important physical processes are neglected which can lead to totally different outcomes. The most important results that contradict some crucial assumptions are: (I) The cubic law systematically overestimates the permeability in fractures especially at low apertures in rough fractures; (II) shearing does not always lead to a permeability enhancement, but it depends on the rock type and deformation mode during fracture generation; (III) permeability is not necessarily reduced during effective pressure changes, but it depends on the conditions during fracture generation and the resulting energy content. Therefore, we can extend (unfortunately) the range of possible results from laboratory experiments with fractured rocks. This may aid in understanding certain observations from field projects that could not be explained by common assumptions. In addition, some generic observations were made: (IV) The width distribution of small faults follows a self-affine scaling relationship, similar to that of rough fracture surfaces; (V) cyclic loading revealed a stress-memory effect of fracture stiffness, similar to the "Kaiser Effect"; (VI) Fracture permeability and contact-area ratio dependent on the stress-history of rock and are directly related to fracture stiffness. For the motivating question, *what properties control the sustainability of fracture permeability*, it was found that any initial loading of a previously unloaded fracture potentially leads to a permanent permeability reduction. Two factors, however, can lead to a sustainable permeability. Firstly, shear fractures generated under in-situ pressure conditions contain less plastic energy and have a reduced fracture closure potential. Secondly, cyclical loading of a displaced tensile fractures within a certain stress range leads to a reversible fracture closure and stiffness behaviour. Any initial reduction of pore pressure or increase in tectonic stress in a newly generated fracture leads to the largest and most permanent permeability reduction. Natural shear fractures, however, are potentially less vulnerable to effective pressure changes.

SAMENVATTING

De ondergrond van de aarde bezit een hoog potentieel voor het opslaan en opwekken van energie. Het gebruiken van de warmte in de ondergrond door vloeistoffen te laten circuleren door gesteente is bekend als geothermie. Het opslaan van waterstof, synthetisch methaan of warmte in de ondergrond kan zorgen voor energievoorziening op momenten dat dat duurzame bronnen niet voldoende energie kunnen leveren. De bruikbaarheid van ondergrondse reservoirs hangt volledig af van de capaciteit van het gesteente om vloeistoffen te kunnen doorlaten of opslaan. Faults (breuken) en fractures (scheuren) kunnen grote contrasten veroorzaken in stroming in deze reservoirs. Het begrijpen van hun hydromechanische gedrag is cruciaal voor het succes van deze projecten. Helaas zijn fractured reservoirs zeer heterogeen. Wetenschappers hebben hier uitgebreid onderzoek naar gedaan, maar nog steeds is elk project met fractured gesteente uniek met specifieke uitdagingen en een grote verscheidenheid aan verschillende factoren. Het testen van gesteente in laboratoria is een cruciaal element voor het begrijpen voor de fysische processen in fractures.

In deze thesis is de afhankelijkheid van fracture permeabiliteit op verschillende parameters onderzocht. Het doel is om een beter systematisch begrip te ontwikkelen van de hydromechanische processen die de potentie van fractures om vloeistoffen te doorlaten beïnvloeden in verschillende condities. Een specifiek onderzoek is om de duurzaamheid van fracture permeabiliteit te bepalen. Dit is cruciaal voor het lange termijn succes van elk ondergronds technisch project. Om deze reden zijn verschillende parameters, die verwacht zijn om invloed te hebben op fracture permeabiliteit, onderzocht in experimenten. Deze omvatten gesteente type (klastisch vs kristallijn), fracture type (shear vs. tensile), fracture geometrie (opening en ruwheid) en effectieve spanningsveranderingen (porie en externe spanning). Potentieel geothermisch gesteente is hier overwogen zodat de resultaten direct gerelateerd kunnen worden aan potentiele geothermische reservoirs.

Wetenschappers proberen vaak de complexiteit van fractured systemen te versimpelen met benaderingen. De cubic law is een van de meest bekende en meest gebruikte versimpelingen die de vloeistofstroming door fractures beschrijft door aan te nemen dat de fracture bestaat uit twee parallelle platen met een vaste afstand tot elkaar. In deze thesis, is de afhankelijkheid van de stroming door een fracture tot de ruwheid en shear verplaatsing, die heterogene opening verplaatsing veroorzaakt, onderzocht in numerieke 3D vloeistof stroming simulaties (hoofdstuk 2). We hebben gevonden dat de cubic law goed fracture stroming bij grote fracture-openingen kan benaderen, maar faalt bij kleinere fracture-openingen. Dit kan komen door de verstoring en kanalisatie van stroming veroorzaakt door kleine opening veranderingen. Een andere simplificatie wordt vaak gemaakt bij het uitvoeren van vloeistof stroming experimenten in fractured gesteente: Shear fractures worden benaderd door tensile fractures die handmatig zijn verplaatst. Dit verwaarloost structurele kenmerken die vaak voorkomen tijdens shear fracturing. Daarom hebben wij de “Punch-Through Shear”

test opnieuw ontworpen om het mogelijk te maken om de permeabiliteit ontwikkelingen voor realistische shear fracture configuraties te monitoren (hoofdstuk 3). Deze nieuwe test opzet onthulde een mogelijke toename in permeabiliteit door microbreukvorming van tot 3 ordes van grootte bij een effectieve spanning van 20 MPa in een graniet gesteente. Cyclische effectieve spanningen van ± 5 en ± 10 MPa zijn toegepast om de duurzaamheid van de toename in permeabiliteit te onderzoeken. Permeabiliteit en toename in opening bleken omkeerbaar te zijn, wat tegenstrijdig is met bestaande studies. We nemen aan dat de druk condities tijdens het vormen van de fractures leiden tot minder plastische energie in het microgebroken systeem vergeleken met de verplaatste tensile fractures. Daarnaast is er onderzocht hoe de microstructuur van een microbreuk zich relateerd tot de permeabiliteit verbetering in klastisch en kristallijn gesteente (hoofdstuk 4). Het wordt duidelijke dat, vergeleken tot graniet, de permeabiliteit niet noodzakelijk is verbeterd in zandsteen met een lage porositeit. Uit mirostructurele analyses blijkt een kleinere fault-breedte en de absentie van een schade zone in zandsteen, in tegenstelling tot graniet. Door de kleine schaal van onze laboratorium experimenten hebben we geprobeerd om de fault-breedte verdeling op te schalen door een schaal onhafhankelijk ruwheidscompenent toe te passen. We vonden soortgelijke relaties als beschreven voor ruwe fracture oppervlakten voor beide gesteentes. Als laatste, hebben we het fracture sluitingspotentieel tijdens cyclisch belasten onderzocht (hoofdstuk 5). Een serie van experimenten met verplaatste tensile fractures zijn uitgevoerd met verschillende cyclische belasting scenario's: constante cyclische beplating en progressieve cyclische belasting. We vonden uit onze experimenten een spanning herinnering effect van fracture stijfheid gelijk aan het "Kaiser Effect" in intact gesteente. Dit wordt gekarakteriseerd bij een non-lineaire stijfheidstrend en eerder bereikte stress levels, en een lineaire trend bij spanningen die eerder bereikte spanningslevels overtreden. Gecombineerd met doorlopende permeabiliteitsmetingen, suggereren wij dat fracture permeabiliteit en de contactoppervlakte ratio afhangen van de spanningshistorie van het gesteente.

Ter conclusie, bij de simplificatie van de fracture geometrie in laboratorium testen zijn belangrijke fysische processen verwaarloosd, wat kan leiden tot compleet verschillende uitkomsten. De meest belangrijke resultaten die in tegenstrijd zijn met cruciale aannames zijn: (I) De cubic law overschat systematisch de permeabiliteit in fractures, in het bijzonder bij lage fracture-openingen in ruwe fractures; (II) shearing lijdt niet altijd tot een permeabiliteitstoename, maar het hangt af van het gesteente type en de deformatie modus tijdens het genereren van de fractures; (III) permeabiliteit is niet per se verminderd tijdens effectieve drukverschillen, maar het hangt af aan de condities tijdens het genereren van de fracture en het resulterende energie gehalte. Om deze reden kunnen wij (helaas) het bereik van mogelijke resultaten van laboratorium experimenten met fractured gesteente uitbreiden. Dit kan bijdragen in het begrijpen van bepaalde observaties van veld projecten die nog niet uitgelegd konden worden bij vaak voorkomende aannames. Daarnaast vonden we de volgende generieke observaties: (IV) De breedte distributie van kleine faults volgen een zelf-affine schaling relatie, gelijk aan die van ruwe fracturen oppervlakten; (V) cyclisch belasten onthulde een spanning-herinnering effect van fracture stijfheid, gelijk aan het "Kaiser Effect"; (VI) Fracture permeabiliteit en contact-oppervlakte ratio's zijn afhankelijk aan spanningshistorie van gesteente en zijn direct gerelateerd aan fracture stijfheid. Voor onze motiverende vraag, welke eigenschappen controleren de duurzaamheid van fracture permeabiliteit, kunnen we het volgende zeggen: Elke initiële belasting van een eerder onbelaste fracture kan

potentieel leiden tot een permanente permeabiliteitsreductie. Twee factoren kunnen echter leiden tot een duurzame permeabiliteit. Ten eerste, shear fractures gegenereerd onder in-situ druk condities bevatten minder plastische energie en hebben een gereduceerde fracture sluitingspotentie. Ten tweede, cyclische belasting van verplaatste tensile fractures binnen een bepaald druk bereik leiden tot omkeerbaar fracture sluitings- en stijfheidsgedrag. Elke initiële reductie van porie druk of toename in tektonische spanning in een nieuw gegenereerde fracture leidt tot de grootste en meest permanente permeabiliteitsvermindering. Natuurlijke shear fractures zijn echter mogelijk minder kwetsbaar voor effectieve drukveranderingen.

1

INTRODUCTION

1

1.1. RATIONALE

Faults and fractures control the stability of the subsurface and the ability of rock to conduct fluids. They are crucial for the majority of subsurface engineering, such as subsurface energy storage (Bauer et al., 2017), geothermal energy (Rybach, 2003, 2014), nuclear waste repositories (Follin and Stigsson, 2013, Mattila and Tammisto, 2012) and many others. Fractures are discontinuities, which greatly affect the variety of physical properties of the rock mass containing them (Faulkner et al., 2010). Characterising and understanding fractures has been a task for scientists over decades. Despite the enormous scientific work that has been done, fractures often prove to be a critical and surprisingly poorly understood geological feature (Ghassemi, 2012). In the past, different approaches have been applied to define physical properties of fractures and to understand physical relationships controlling them. Classically, fractures are studied in outcrops (e.g. Evans et al., 1997, Fisher and Knipe, 2001, Fossen et al., 2007, Vermilye and Scholz, 1999). The orientation, size and geometry can easily be obtained in the field and provide complex fracture networks that can be used as input data (Bisdom et al., 2014, 2016b, Candela et al., 2009, 2012). Although modern technology enables the digital collection and processing of fracture data from the field, the physical properties can hardly be inferred from such studies. Therefore, laboratory rock testing has become the most popular method to characterise fractures (e.g. Bandis et al., 1983, Chambon et al., 2006, Chen et al., 2014, 2000, Cook, 1992, Cox and Scholz, 1988, Faulkner and Armitage, 2013, Mitchell and Faulkner, 2008, Moore and Lockner, 1995, Teufel, 1987, Walsh, 1981, Watanabe et al., 2009, Wibberley et al., 2000, Ye and Ghassemi, 2018, Zang et al., 2000). Samples taken from outcrops or boreholes are installed into compression apparatus to simulate stresses in the subsurface. Depending on the boundary conditions of the experiments and the geometry and type of sample, different rock and fracture properties can be derived. Although enormous data sets have been produced in the past, the transferability of the physical processes from laboratory scale (μm to cm) to the field scale (cm to km) remains the biggest challenge for geologists today. Field experiments are time-consuming and expensive and can only produce a limited set of data. This is because the deep subsurface is hardly accessible and because of the low spatial resolution from borehole measurements. Underground laboratories provide a unique opportunity to study in-situ processes on a field scale (m) (Cosma et al., 2001, Haimson et al., 1993, Kwiatek et al., 2018, López-Comino et al., 2017, Nussbaum et al., 2011). However, they are limited in terms of stress magnitudes resulting from their relatively shallow depths. Modern high-performance computers allow for complex numerical simulations of the subsurface at any scale (e.g. Cacace and Jacquey, 2017, Cacace et al., 2013, Hofmann et al., 2014, Jacquey et al., 2016, 2018). Over the past two decades, they have become the most popular technology to simulate the stability and fluid flow characteristics. They require a real data set underlying the numerical code and a proper physical implementation. Without such data sets, these simulations are useless when the outcome only depends on the users's concept of the anticipated outcome. The interplay of scales and the resulting uncertainty about physical processes will therefore remain a crucial task for the future. Only interrelated studies have the potential to get closer to a satisfactory solution.

Not only is the characterisation of subsurface fractures critical, but scientists still debate about the types of fractures forming under the wide variety of conditions (Ghassemi, 2012,

McClure and Horne, 2014, Zimmermann et al., 2010). Natural fractures and faults form over geological time spans and are related to tectonic stresses, burial and exhumation, or temperature changes. They can exist as a complex fracture network in a geological unit (Bisdom et al., 2016a,b), or as distinct fault zones (Ben-Zion and Sammis, 2003, Caine et al., 1996, Evans et al., 1997, Faulkner et al., 2010, Peacock and Sanderson, 1991). On the one hand, they provide a chance for utilization by circulating water through them to generate geothermal energy (Bödvarsson and Tsang, 1982, Murphy et al., 1981). On the other hand, they bear a certain risk that water injection will lead to induced seismicity (e.g. Deichmann and Giardini, 2009, Ellsworth et al., 2019, Fryer et al., 2019). Furthermore, they first need to be identified in the subsurface by exploration campaigns. Once located at greater depth, drilling into fractured rock is a technical challenge (Emmermann and Lauterjung, 1997). An alternative is to generate fractures artificially by injecting fluid at high pressure into formerly intact rocks (Economides and Nolte., 1989, Yew, 1997). Although alternative and innovative strategies, such as "Radial Jet Drilling" (Nair et al., 2017, Peters et al., 2015, 2018, Salimzadeh et al., 2019), or chemical and thermal stimulation (Blöcher et al., 2016, Breede et al., 2013, Portier et al., 2007, 2009) technologies, are being used, hydraulic stimulation remains the most promising, but also most publicly-debated technology. Importantly, artificial fractures are different to natural fractures in terms of their geometry and stability.

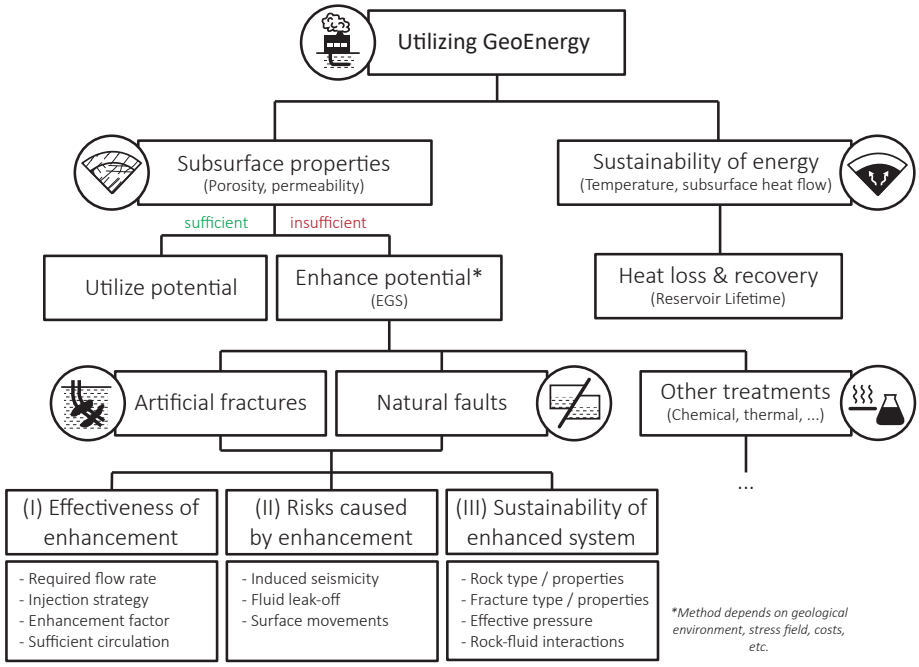

Figure 1.1: Simplified flow chart about how to utilize geothermal energy by enhancing a reservoir using fractures and the associated risks.

1

1.2. SCOPE OF THE THESIS

All fracture types have in common that they should enhance the productivity of a reservoir for energy a sufficient production, i.e. increase the volume rate of fluid flowing through the subsurface. Utilizing geothermal energy is an important component of the future energy mix and the "Energiewende" (Agemar et al., 2014, Chamorro et al., 2014, Dombi et al., 2014, Limberger et al., 2014). Extracting heat from the subsurface is an environmentally friendly technology and heat is available in almost endless amounts in the subsurface. Despite decades of development, geothermal site installation has proven to be very difficult due to the variety of critical parameters. The strategy of how to utilize geothermal energy is outlined in figure 1.1. Largely simplified, the success of a geothermal project depends therefore on the subsurface properties and the sustainability of the energy source itself. The latter depends on the underground heat flow and temperature and therefore controls the economic feasibility and lifetime of a reservoir (Ekneligoda and Min, 2014, Franco and Vaccaro, 2014, Scheck-Wenderoth et al., 2014). Subsurface properties can either be sufficient or insufficient and consequently often require stimulation ("Enhanced Geothermal Systems") (Breede et al., 2013).

As mentioned before, artificial of natural fractures can be used to enhance fluid flow in the subsurface. Numerous European geothermal projects have targeted natural fractures or aimed at generating new fractures (e.g. Blöcher et al., 2016, Cuenot et al., 2006, Genter et al., 2009, Häring et al., 2008, Hofmann et al., 2019, Park et al., 2017, Schindler et al., 2008, Tenzer et al., 2010, Tischner et al., 2007, 2013, Zimmermann et al., 2011). Potential risks to the success of such projects are the effectiveness of the enhancement, side effects caused by the enhancement and the sustainability of the enhanced system are the most crucial parameters (figure 1.1). Although the initial effectiveness could often be demonstrated, less attention were given to the longevity of the enhancement (sustainability) (Portier et al., 2007). Ideally, fractures need to stay open for a long time span to guarantee sufficient flow over the lifetime of a reservoir. The opposite is often documented. After some time, the productivity decreases and at some point economically-critical flow rates might not be achieved anymore. Several reasons are assumed, such as chemical rock-fluid interactions, fines migration, wellbore skin, two-phase flow and most importantly the sustainability of fractures themselves (Blöcher et al., 2016). The sustainability depends on several physical fracture properties, such as rock and fracture type and properties, the impact of effective pressure changes and rock fluid interactions. Stress changes by production and injection scenarios, for example, lead to a mechanical opening and closing of fractures (Bandis et al., 1983). This thesis aims to understand and interrelate hydraulic-mechanical properties of fractures and how they control the sustainability of an enhanced system. The main component of this work is laboratory testing and aims for the identification of critical parameters that control the permeability of fractured rock.

1.3. THESIS OUTLINE

In this work, laboratory testing supplemented by numerical simulations was used to provide answers to the question: *what are the crucial physical properties controlling the sustain-*

ability of fracture permeability? Generally, the strength and permeability of a fracture are controlled by the host rock and fracture properties. Important host rocks properties are the mineral composition, porosity and bonding strength. These are also assumed to control the fracture type and partly the fracture properties (asperity strength). The fracture properties depend on the fracture type (shear or tensile) and the fracture geometry (roughness and aperture) and are altered by applied stresses (pore pressure and external stress). These assumptions provided the outline for this thesis, with a focus on the interplay of the aforementioned dependencies.

After outlining the context and scope of this thesis in this first chapter, the often-applied cubic law will be reviewed in 3D numerical fluid flow simulations in the second chapter (chapter 2). The cubic law is commonly used to simplify the flow in fractures with the approximation of two parallel plates. Here, the validity of this assumption will be tested depending on the roughness and displacement magnitudes of a displaced tensile fracture. Based on the findings that the flow in fractures cannot be simplified by parallel plates, the complexity of shear zones is addressed in the following chapters (chapter 3 and 4). In chapter 3, an innovative experimental testing set-up, the "Punch-Through Shear" test, is used to generate a microfault. The enhancement potential by faulting in granites will be analyzed and the dependence on effective pressure changes will be tested. Chapter 4 addresses how the enhancement potential of permeability by faulting differs between clastic and crystalline rocks. Further, the sustainability of such microfaults during effective pressure changes depending on rock type and conditions during their generation is discussed. The issue of upscaling is addressed by characterizing the fault width distribution by a scale-independent roughness coefficient. Lastly, chapter 5 addresses the importance of the stress history on the fracture closure potential. This stress-related closure potential is defined by the fracture stiffness. Different loading scenarios are used to demonstrate how repeated loading with progressive peak stress magnitudes impacts the sustainability of fracture permeability. Further, the underlying processes that impact the mechanical-hydraulic properties during loading are discussed. The general discussion and conclusion (chapter 6) aims to summarize the respective findings to provide recommendations for assessing the sustainability of the permeability of subsurface fractures.

REFERENCES

T. Agemar, J. Weber, and R. Schulz. Deep geothermal energy production in germany. *Energies*, 7(7):4397–4416, jul 2014. doi: 10.3390/en7074397.

S. Bandis, A. Lumsden, and N. Barton. Fundamentals of rock joint deformation. *International Journal of Rock Mechanics and Mining Sciences & Geomechanics Abstracts*, 20 (6):249–268, dec 1983. doi: 10.1016/0148-9062(83)90595-8.

S. Bauer, A. Dahmke, and O. Kolditz. Subsurface energy storage: geological storage of renewable energy—capacities, induced effects and implications. *Environmental Earth Sciences*, 76(20), oct 2017. doi: 10.1007/s12665-017-7007-9.

Y. Ben-Zion and C. G. Sammis. Characterization of fault zones. *Pure and Applied Geophysics*, 160(3):677–715, mar 2003. doi: 10.1007/PL00012554.

K. Bisdom, B. Gauthier, G. Bertotti, and N. Hardebol. Calibrating discrete fracture-network models with a carbonate three-dimensional outcrop fracture network: Implications for naturally fractured reservoir modeling. *AAPG Bulletin*, 98(7):1351–1376, jul 2014. doi: 10.1306/02031413060.

K. Bisdom, G. Bertotti, and H. M. Nick. The impact of different aperture distribution models and critical stress criteria on equivalent permeability in fractured rocks. *Journal of Geophysical Research: Solid Earth*, 121(5):4045–4063, may 2016a. doi: 10.1002/2015JB012657.

K. Bisdom, G. Bertotti, and H. M. Nick. The impact of in-situ stress and outcrop-based fracture geometry on hydraulic aperture and upscaled permeability in fractured reservoirs. *Tectonophysics*, 690:63–75, oct 2016b. doi: 10.1016/j.tecto.2016.04.006.

G. Blöcher, T. Reinsch, J. Henninges, H. Milsch, S. Regenspurg, J. Kummerow, H. Francke, S. Kranz, A. Saadat, G. Zimmermann, and E. Huenges. Hydraulic history and current state of the deep geothermal reservoir groß schönebeck. *Geothermics*, 63:27–43, sep 2016. doi: 10.1016/j.geothermics.2015.07.008.

G. S. Bödvarsson and C. F. Tsang. Injection and thermal breakthrough in fractured geothermal reservoirs. *Journal of Geophysical Research: Solid Earth*, 87(B2):1031–1048, feb 1982. doi: 10.1029/JB087iB02p01031.

K. Breede, K. Dzebisashvili, X. Liu, and G. Falcone. A systematic review of enhanced (or engineered) geothermal systems: past, present and future. *Geothermal Energy*, 1(1), nov 2013. doi: 10.1186/2195-9706-1-4.

M. Cacace and A. B. Jacquey. Flexible parallel implicit modelling of coupled thermal–hydraulic–mechanical processes in fractured rocks. *Solid Earth*, 8(5):921–941, sep 2017. doi: 10.5194/se-8-921-2017.

M. Cacace, G. Blöcher, N. Watanabe, I. Moeck, N. Börsing, M. Scheck-Wenderoth, O. Kolditz, and E. Huenges. Modelling of fractured carbonate reservoirs: outline of a novel technique via a case study from the molasse basin, southern bavaria, germany. *Environmental Earth Sciences*, 70(8):3585–3602, mar 2013. doi: 10.1007/s12665-013-2402-3.

J. S. Caine, J. P. Evans, and C. B. Forster. Fault zone architecture and permeability structure. *Geology*, 24(11):1025, 1996. doi: 10.1130/0091-7613(1996)024<1025:FZAAPS>2.3.CO;2.

T. Candela, F. Renard, M. Bouchon, A. Brouste, D. Marsan, J. Schmittbuhl, and C. Voisin. Characterization of fault roughness at various scales: Implications of three-dimensional high resolution topography measurements. *Pure and Applied Geophysics*, 166(10-11):1817–1851, jun 2009. doi: 10.1007/s00024-009-0521-2.

T. Candela, F. Renard, Y. Klinger, K. Mair, J. Schmittbuhl, and E. E. Brodsky. Roughness of fault surfaces over nine decades of length scales. *Journal of Geophysical Research: Solid Earth*, 117(B8):n/a–n/a, aug 2012. doi: 10.1029/2011JB009041.

G. Chambon, J. Schmittbuhl, A. Corfdir, N. Orellana, M. Diraison, and Y. Géraud. The thickness of faults: From laboratory experiments to field scale observations. *Tectonophysics*, 426(1-2):77–94, oct 2006. doi: 10.1016/j.tecto.2006.02.014.

C. R. Chamorro, J. L. García-Cuesta, M. E. Mondéjar, and A. Pérez-Madrazo. Enhanced geothermal systems in europe: An estimation and comparison of the technical and sustainable potentials. *Energy*, 65:250–263, feb 2014. doi: 10.1016/j.energy.2013.11.078.

L. Chen, J. F. Liu, C. Wang, J. Liu, R. Su, and J. Wang. Characterization of damage evolution in granite under compressive stress condition and its effect on permeability. *International Journal of Rock Mechanics and Mining Sciences*, 71:340–349, oct 2014. doi: 10.1016/j.ijrmms.2014.07.020.

Z. Chen, S. P. Narayan, Z. Yang, and S. S. Rahman. An experimental investigation of hydraulic behaviour of fractures and joints in granitic rock. *International Journal of Rock Mechanics and Mining Sciences*, 37(7):1061–1071, oct 2000. doi: 10.1016/S1365-1609(00)00039-3.

N. Cook. Natural joints in rock: Mechanical, hydraulic and seismic behaviour and properties under normal stress. *International Journal of Rock Mechanics and Mining Sciences & Geomechanics Abstracts*, 29(3):198–223, may 1992. doi: 10.1016/0148-9062(92)93656-5.

C. Cosma, O. Olsson, J. Keskinen, and P. Heikkinen. Seismic characterization of fracturing at the äspö hard rock laboratory, sweden, from the kilometer scale to the meter scale. *International Journal of Rock Mechanics and Mining Sciences*, 38(6):859–865, sep 2001. doi: 10.1016/S1365-1609(01)00051-X.

S. J. D. Cox and C. H. Scholz. On the formation and growth of faults: an experimental study. *Journal of Structural Geology*, 10(4):413–430, jan 1988. doi: 10.1016/0191-8141(88)90019-3.

N. Cuenot, J. Charléty, L. Dorbath, and H. Haessler. Faulting mechanisms and stress regime at the european HDR site of soultz-sous-forêts, france. *Geothermics*, 35(5-6):561–575, oct 2006. doi: 10.1016/j.geothermics.2006.11.007.

N. Deichmann and D. Giardini. Earthquakes induced by the stimulation of an enhanced geothermal system below basel (switzerland). *Seismological Research Letters*, 80(5):784–798, sep 2009. doi: 10.1785/gssrl.80.5.784.

M. Dombi, I. Kuti, and P. Balogh. Sustainability assessment of renewable power and heat generation technologies. *Energy Policy*, 67:264–271, apr 2014. doi: 10.1016/j.enpol.2013.12.032.

M. J. Economides and K. G. Nolte. *Reservoir stimulation*, volume 2. 1989.

T. C. Ekneligoda and K.-B. Min. Determination of optimum parameters of doublet system in a horizontally fractured geothermal reservoir. *Renewable Energy*, 65:152–160, may 2014. doi: 10.1016/j.renene.2013.08.003.

W. L. Ellsworth, D. Giardini, J. Townend, S. Ge, and T. Shimamoto. Triggering of the pohang, korea, earthquake (mw 5.5) by enhanced geothermal system stimulation. *Seismological Research Letters*, aug 2019. doi: 10.1785/0220190102.

R. Emmermann and J. Lauterjung. The german continental deep drilling program KTB: Overview and major results. *Journal of Geophysical Research: Solid Earth*, 102(B8): 18179–18201, aug 1997. doi: 10.1029/96JB03945.

J. P. Evans, C. B. Forster, and J. V. Goddard. Permeability of fault-related rocks, and implications for hydraulic structure of fault zones. *Journal of Structural Geology*, 19 (11):1393–1404, nov 1997. doi: 10.1016/S0191-8141(97)00057-6.

D. Faulkner and P. Armitage. The effect of tectonic environment on permeability development around faults and in the brittle crust. *Earth and Planetary Science Letters*, 375: 71–77, aug 2013. doi: 10.1016/j.epsl.2013.05.006.

D. Faulkner, C. Jackson, R. Lunn, R. Schlische, Z. Shipton, C. Wibberley, and M. Withjack. A review of recent developments concerning the structure, mechanics and fluid flow properties of fault zones. *Journal of Structural Geology*, 32(11):1557–1575, nov 2010. doi: 10.1016/j.jsg.2010.06.009.

Q. Fisher and R. Knipe. The permeability of faults within siliciclastic petroleum reservoirs of the north sea and norwegian continental shelf. *Marine and Petroleum Geology*, 18 (10):1063–1081, dec 2001. doi: 10.1016/S0264-8172(01)00042-3.

S. Follin and M. Stigsson. A transmissivity model for deformation zones in fractured crystalline rock and its possible correlation to in situ stress at the proposed high-level nuclear waste repository site at forsmark, sweden. *Hydrogeology Journal*, 22(2):299–311, dec 2013. doi: 10.1007/s10040-013-1078-9.

H. Fossen, R. A. Schultz, Z. K. Shipton, and K. Mair. Deformation bands in sandstone: a review. *Journal of the Geological Society*, 164(4):755–769, jul 2007. doi: 10.1144/0016-76492006-036.

A. Franco and M. Vaccaro. Numerical simulation of geothermal reservoirs for the sustainable design of energy plants: A review. *Renewable and Sustainable Energy Reviews*, 30: 987–1002, feb 2014. doi: 10.1016/j.rser.2013.11.041.

B. Fryer, G. Siddiqi, and L. Laloui. Injection-induced seismicity: strategies for reducing risk using high stress path reservoirs and temperature-induced stress preconditioning. *Geophysical Journal International*, 220(2):1436–1446, oct 2019. doi: 10.1093/gji/ggz490.

A. Genter, D. Fritsch, N. Cuenot, J. Baumgärtner, and J.-J. Graff. Overview of the current activities of the european EGS Soultz project: from exploration to electricity production. In *Proceedings, Thirty-Fourth Workshop on Geothermal Reservoir Engineering Stanford University, Stanford, California, February 9-11, 2009 SGP-TR-187*, 2009.

A. Ghassemi. A review of some rock mechanics issues in geothermal reservoir development. *Geotechnical and Geological Engineering*, 30(3):647–664, may 2012. doi: 10.1007/s10706-012-9508-3.

B. Haimson, M. Lee, N. Chandler, and D. Martin. Estimating the state of stress from subhorizontal hydraulic fractures at the underground research laboratory, manitoba. *International Journal of Rock Mechanics and Mining Sciences & Geomechanics Abstracts*, 30(7):959–964, dec 1993. doi: 10.1016/0148-9062(93)90052-F.

M. O. Häring, U. Schanz, F. Ladner, and B. C. Dyer. Characterisation of the basel 1 enhanced geothermal system. *Geothermics*, 37(5):469–495, oct 2008. doi: 10.1016/j.geothermics.2008.06.002.

H. Hofmann, G. Blöcher, N. Börsing, N. Maronde, N. Pastrik, and G. Zimmermann. Potential for enhanced geothermal systems in low permeability limesystem - stimulation strategies for the western malm karst (bavaria). *Geothermics*, 51:351–367, jul 2014. doi: 10.1016/j.geothermics.2014.03.003.

H. Hofmann, G. Zimmermann, M. Farkas, E. Huenges, A. Zang, M. Leonhardt, G. Kwiatek, P. Martinez-Garzon, M. Bohnhoff, K.-B. Min, P. Fokker, R. Westaway, F. Bethmann, P. Meier, K. S. Yoon, J. W. Choi, T. J. Lee, and K. Y. Kim. First field application of cyclic soft stimulation at the pohang enhanced geothermal system site in korea. *Geophysical Journal International*, 217(2):926–949, jan 2019. doi: 10.1093/gji/ggz058.

A. B. Jacquey, M. Cacace, G. Blöcher, N. Watanabe, E. Huenges, and M. Scheck-Wenderoth. Thermo-poroelastic numerical modelling for enhanced geothermal system performance: Case study of the groß schönebeck reservoir. *Tectonophysics*, 684:119–130, aug 2016. doi: 10.1016/j.tecto.2015.12.020.

A. B. Jacquey, L. Urpi, M. Cacace, G. Blöcher, G. Zimmermann, and M. Scheck-Wenderoth. Far field poroelastic response of geothermal reservoirs to hydraulic stimulation treatment: Theory and application at the groß schönebeck geothermal research facility. *International Journal of Rock Mechanics and Mining Sciences*, 110:316–327, oct 2018. doi: 10.1016/j.ijrmms.2018.08.012.

G. Kwiatek, P. Martínez-Garzón, K. Plenkers, M. Leonhardt, A. Zang, S. von Specht, G. Dresen, and M. Bohnhoff. Insights into complex subdecimeter fracturing processes occurring during a water injection experiment at depth in äspö hard rock laboratory, sweden. *Journal of Geophysical Research: Solid Earth*, aug 2018. doi: 10.1029/2017JB014715.

J. Limberger, P. Calcagno, A. Manzella, E. Trumpy, T. Boxem, M. P. D. Pluymaekers, and J.-D. van Wees. Assessing the prospective resource base for enhanced geothermal systems in europe. *Geothermal Energy Science*, 2(1):55–71, dec 2014. doi: 10.5194/gtes-2-55-2014.

J. A. López-Comino, S. Cesca, S. Heimann, F. Grigoli, C. Milkereit, T. Dahm, and A. Zang. Characterization of hydraulic fractures growth during the äspö hard rock laboratory experiment (sweden). *Rock Mechanics and Rock Engineering*, 50(11):2985–3001, jul 2017. doi: 10.1007/s00603-017-1285-0.

J. Mattila and E. Tammisto. Stress-controlled fluid flow in fractures at the site of a potential nuclear waste repository, finland. *Geology*, 40(4):299–302, apr 2012. doi: 10.1130/G32832.1.

M. W. McClure and R. N. Horne. An investigation of stimulation mechanisms in enhanced geothermal systems. *International Journal of Rock Mechanics and Mining Sciences*, 72:242–260, dec 2014. doi: 10.1016/j.ijrmms.2014.07.011.

T. M. Mitchell and D. R. Faulkner. Experimental measurements of permeability evolution during triaxial compression of initially intact crystalline rocks and implications for fluid flow in fault zones. *Journal of Geophysical Research*, 113(B11), nov 2008. doi: 10.1029/2008JB005588.

D. Moore and D. Lockner. The role of microcracking in shear-fracture propagation in granite. *Journal of Structural Geology*, 17(1):95–114, jan 1995. doi: 10.1016/0191-8141(94)E0018-T.

H. D. Murphy, J. W. Tester, C. O. Grigsby, and R. M. Potter. Energy extraction from fractured geothermal reservoirs in low-permeability crystalline rock. *Journal of Geophysical Research*, 86(B8):7145, 1981. doi: 10.1029/JB086iB08p07145.

R. Nair, E. Peters, S. Šliaupa, R. Valickas, and S. Petrauskas. A case study of radial jetting technology for enhancing geothermal energy systems at klaipėdageothermal demonstration plant. In *42nd Workshop on Geothermal Reservoir EngineeringStanford University, Stanford, California, February 13-15*, 2017.

C. Nussbaum, P. Bossart, F. Amann, and C. Aubourg. Analysis of tectonic structures and excavation induced fractures in the opalinus clay, mont terri underground rock laboratory (switzerland). *Swiss Journal of Geosciences*, 104(2):187–210, sep 2011. doi: 10.1007/s00015-011-0070-4.

S. Park, L. Xie, K.-I. Kim, S. Kwon, K.-B. Min, J. Choi, W.-S. Yoon, and Y. Song. First hydraulic stimulation in fractured geothermal reservoir in pohang PX-2 well. *Procedia Engineering*, 191:829–837, 2017. doi: 10.1016/j.proeng.2017.05.250.

D. Peacock and D. Sanderson. Displacements, segment linkage and relay ramps in normal fault zones. *Journal of Structural Geology*, 13(6):721–733, jan 1991. doi: 10.1016/0191-8141(91)90033-F.

E. Peters, J. Veldkamp, M. Pluymaekers, and F. Wilschut. Radial drilling for dutch geothermalapplications. Technical Report R10799, TNO, 2015.

E. Peters, G. Blöcher, S. Salimzadeh, P. J. P. Egberts, and M. Cacace. Modelling of multilateral well geometries for geothermal applications. *Advances in Geosciences*, 45:209–215, aug 2018. doi: 10.5194/adgeo-45-209-2018.

S. Portier, L. André, and F.-D. Vuataz. Review on chemical stimulation techniques in oil industry and applications to geothermal systems. 2007.

S. Portier, F.-D. Vuataz, P. Nami, B. Sanjuan, and A. Gérard. Chemical stimulation techniques for geothermal wells: experiments on the three-well EGS system at soultz-sous-forêts, france. *Geothermics*, 38(4):349–359, dec 2009. doi: 10.1016/j.geothermics.2009.07.001.

L. Rybach. Geothermal energy: sustainability and the environment. *Geothermics*, 32(4-6): 463–470, aug 2003. doi: 10.1016/S0375-6505(03)00057-9.

L. Rybach. Geothermal power growth 1995–2013—a comparison with other renewables. *Energies*, 7(8):4802–4812, jul 2014. doi: 10.3390/en7084802.

S. Salimzadeh, M. Grandahl, M. Medetbekova, and H. Nick. A novel radial jet drilling stimulation technique for enhancing heat recovery from fractured geothermal reservoirs. *Renewable Energy*, 139:395–409, aug 2019. doi: 10.1016/j.renene.2019.02.073.

M. Scheck-Wenderoth, M. Cacace, Y. P. Maystrenko, Y. Cherubini, V. Noack, B. O. Kaiser, J. Sippel, and L. Björn. Models of heat transport in the central european basin system: Effective mechanisms at different scales. *Marine and Petroleum Geology*, 55:315–331, aug 2014. doi: 10.1016/j.marpetgeo.2014.03.009.

M. Schindler, P. Nami, R. Schellschmidt, D. Teza, and T. Tischner. Summary of hydraulic stimulation operations in the 5 km deep crystalline HDR/EGS reservoir at Soultz-sous-Forêts. In *Thirty-Second Workshop on Geothermal Reservoir Engineering, Stanford University, Stanford, California, January 28-30*, 2008.

H. Tenzer, C.-H. Park, O. Kolditz, and C. I. McDermott. Application of the geomechanical facies approach and comparison of exploration and evaluation methods used at soultz-sous-forêts (france) and spa urach (germany) geothermal sites. *Environ Earth Sci*, 61(4): 853–880, jan 2010. doi: 10.1007/s12665-009-0403-z.

L. W. Teufel. Permeability changes during shear deformation of fractured rock. In *28. U.S. Symposium on Rock Mechanics. Tucson, AZ, USA, 29 June*, 1987.

T. Tischner, M. Schindler, R. Jung, and P. Nami. Hdr project soultz: Hydraulic and seismic observations during stimulation of the 3 deep wells by massive water injections. In *Thirty-Second Workshop on Geothermal Reservoir Engineering, Stanford University, Stanford, California*, 2007.

T. Tischner, S. Krug, E. Pechan, A. Hesshaus, R. Jatho, M. Bischoff, and T. Wonik. Massive hydraulic fracturing in low permeable sedimentary rock in the genesys project. In *Proceedings Thirty-Eighth Workshop on Geothermal Reservoir Engineering, Stanford University, Stanford, California*, 2013.

J. M. Vermilye and C. H. Scholz. Fault propagation and segmentation: insight from the microstructural examination of a small fault. *Journal of Structural Geology*, 21(11): 1623–1636, nov 1999. doi: 10.1016/S0191-8141(99)00093-0.

J. Walsh. Effect of pore pressure and confining pressure on fracture permeability. *International Journal of Rock Mechanics and Mining Sciences & Geomechanics Abstracts*, 18 (5):429–435, oct 1981. doi: 10.1016/0148-9062(81)90006-1.

N. Watanabe, N. Hirano, and N. Tsuchiya. Diversity of channeling flow in heterogeneous aperture distribution inferred from integrated experimental-numerical analysis on flow through shear fracture in granite. *Journal of Geophysical Research*, 114(B4), apr 2009. doi: 10.1029/2008JB005959.

C. A. Wibberley, J.-P. Petit, and T. Rives. Micromechanics of shear rupture and the control of normal stress. *Journal of Structural Geology*, 22(4):411–427, apr 2000. doi: 10.1016/S0191-8141(99)00158-3.

Z. Ye and A. Ghassemi. Injection-induced shear slip and permeability enhancement in granite fractures. *Journal of Geophysical Research: Solid Earth*, 123(10):9009–9032, oct 2018. doi: 10.1029/2018JB016045.

C. H. Yew. *Mechanics of Hydraulic Fracturing*. Gulf Publishing Co., Houston, TX, USA, 1997.

A. Zang, F. C. Wagner, S. Stanchits, C. Janssen, and G. Dresen. Fracture process zone in granite. *Journal of Geophysical Research: Solid Earth*, 105(B10):23651–23661, oct 2000. doi: 10.1029/2000JB900239.

G. Zimmermann, I. Moeck, and G. Blöcher. Cyclic waterfrac stimulation to develop an Enhanced Geothermal System (EGS) - Conceptual design and experimental results. *Geothermics*, 39(1):59 – 69, 2010. ISSN 0375-6505. doi: 10.1016/j.geothermics.2009.10.003.

G. Zimmermann, G. Blöcher, A. Reinicke, and W. Brandt. Rock specific hydraulic fracturing and matrix acidizing to enhance a geothermal system - concepts and field results. *Tectonophysics*, 503(1-2):146–154, 2011. ISSN 0040-1951. doi: 10.1016/j.tecto.2010.09.026.

2

On the validity of the cubic law

Flow along fractures becomes increasingly important in the context of geo-engineering applications. Commonly, the permeability of fractures is approximated using the cubic law assumption. However, fracture flow is influenced by the surface roughness and the relative shear displacement. A numerical approach was used which calculates the flow pattern within a rough fracture. Therefore, fracture surfaces are generated using a power spectral density function and fracture flow is simulated under the incompressible Navier Stokes approximation. It is shown that the cubic law solution overestimates the permeability as modeled by the 3D numerical simulation of flow in fractures.

This chapter is based on: C. Kluge, H. Milsch, G. Blöcher, *Permeability of displaced fractures*, Energy Procedia **125**, 88-97 (2017).

2.1. INTRODUCTION

Flow along fractures or in fissured systems becomes increasingly important in the context of Enhanced Geothermal Systems (EGS), shale gas recovery or nuclear waste disposal. Fault zones and natural fracture networks are more and more considered as main reservoir targets, for example the geothermal exploitation in the Southern German Molasse Basin (Hofmann et al., 2014). An approximation of the potential of fracture transmissivity is therefore an important topic. In reservoir simulations, commonly, a constant fracture aperture is used to describe permeability in a fracture or in fracture networks. The permeability of fractures is approximated using the Hagen-Poiseuille solution of the Navier Stokes equation. Flow in fractures is assumed to be laminar between two parallel plates separated by a constant distance a, such that the fracture permeability k_f can be derived from the cubic law approximation Witherspoon et al. (1980):

$$k_{f,cubic} = \frac{a^2}{12} \tag{2.1}$$

However, it is a well-known fact, that fracture flow is strongly influenced by the fracture surface roughness and the shear displacement along the fracture planes (Jin et al., 2017, Walsh et al., 2008, Zimmerman and Bodvarsson, 1996). Furthermore, the orientation of the pressure gradient in respect to the aperture field is causing a strong variability of the hydraulic behaviour of a rough fracture (Méheust and Schmittbuhl, 2001). Correction factors for the aperture to calculate the cubic law permeability were therefore introduced by several authors. Méheust and Schmittbuhl (2000) studied the deviation of the cubic law for a natural fracture surface and plexiglas, observing higher deviations from the cubic law for small apertures, which are correlating to the same trend in experimental investigations. Zimmerman and Bodvarsson (1996) corrected the aperture a, considering the mean aperture, $\langle a \rangle$, a surface roughness factor, C_r, and a tortuosity factor, C_t, that was later modified by Walsh et al. (2008):

$$a = \langle a \rangle \cdot C_r \cdot C_t \tag{2.2}$$

Jin et al. (2017) introduced a semi-empirical function using fitted parameters depending on the surface geometry accounting for the surface roughness, as well as for the hydraulic and surface tortuosity effect. We are providing a fracture flow simulation considering 3D Navier Stokes flow for rough and displaced fractures. We further provide a quantification of the deviation from the cubic law permeability. The controlling parameters on fracture permeability of rough and displaced fractures are discussed.

2.2. METHODS

The workflow for the fracture flow simulation in a 3D fracture comprises three main steps: (1) generating fracture topographic surfaces with varying roughness and displacement, (2) generating a finite element mesh to produce a 3D model of a fracture, (3) perform fracture

flow simulations using Navier Stokes flow in the finite element software Comsol Multiphysics (www.comsol.de), to derive fracture permeability from the pressure and velocity field using Darcy's law.

2.2.1. FRACTURE TOPOGRAPHY GENERATION

Rock fracture surface anisotropy can be captured by power spectral density formulations (Zhou and Xie, 2004). The following simplified equations were used to generate fracture topographies following a power law with a uniform random signal:

$$h = P_0^{0.5} \cdot \frac{h_0}{S} \tag{2.3}$$

$$S = i(x,y)^{B/2} \tag{2.4}$$

where h is the asperity height, P_0 the multiplier amplitude, h_0 is the normalised random height distribution i the location of a point and B the amplitude scaling factor influencing the roughness. A small B value produces rough fractures, whereas large B values produce smooth fracture topographies. The power $B/2$ is used because the power spectral density is proportional to the amplitude squared. The fracture aperture distribution is a normalized Gaussian distribution as it is commonly observed for natural fracture surfaces. The script allows to produce fracture surfaces of 100x100 mm or any other quadratic size.

Assuming that tensile fracturing will naturally produce two fracture surfaces that are perfectly matching and equal in shape, two equal surfaces are generated and super-positioned based on their minimum contacting points. The aperture is calculated as the subtraction of the upper and the lower asperity height at each point. When both fracture surfaces have no displacement relative to each other, the overall aperture is zero, since both fracture are perfectly matching. To implement a shear displacement, the top surface is displaced relative to the bottom surface by shifting the spatial point cloud data by a 1 mm increment in the y-direction to a maximum displacement of 50 mm. Every point that has no spatial correlation on the bottom surface is again added to the opposite side of the fracture using the "circshift" function in Matlab (figure 2.1a). This means that by displacing the upper fracture surface by 100 mm, both surfaces are again matching. The distance between the two surfaces, i.e. the aperture, is recalculated at every step based on the minimum contacting points. Therefore, each change in displacement leads to a change in mean aperture (figure 2.1b). The advantage of this approach is that the length of the fracture stays constant. However, this approach excludes any mechanical deformation of the fracture asperities, i.e. fracture asperities have an infinite stiffness. The fracture apertures in our models are in the range of a few 0.5 to 2.5 mm in our study, which describe a lower bound of the real spectra. Hydraulic apertures filled with proppants in reservoirs range from 0.2 mm to 2 cm (Blöcher et al., 2010, Zimmermann et al., 2010). On laboratory scale, however, fracture apertures are some μm and therefore not comparable to our results (Hofmann et al., 2016, Milsch et al., 2016).

The spatial point cloud data is then exported to the software "MeshIt" (Cacace and Blöcher, 2015). MeshIt allows to create a 3D finite element mesh based on spatial point cloud data. The fracture topographic surface is interpolated using the Inverse Distance Weighting method (IDW). The mesh was refined at the inflow and outflow boundaries to allow for a more precise calculation of the pressure field. The element size of the respective fracture models was around 150000-300000 elements.

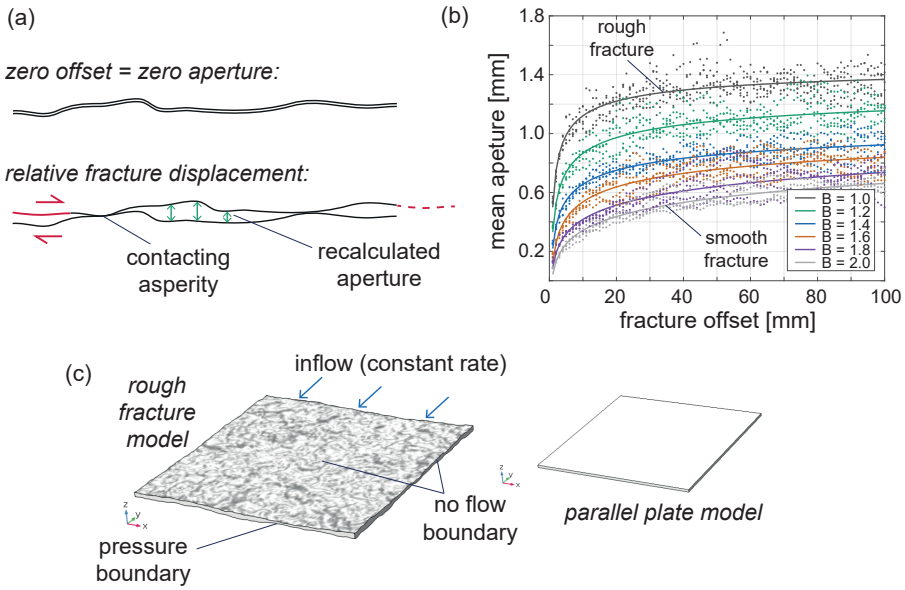

Figure 2.1: (a) Illustration of the applied method to create a shear displacement between two equal fracture topographic surfaces. (b) The mean aperture increases strongly at low fracture offset, but is changing less after around 15 mm of fracture displacement, i.e. when the elevations of the initially neighbouring asperities are overcome. (c) 3D model of a rough fracture with constant flow applied at the inlet and a pressure boundary at the outlet, as well as the parallel plate model for the verification of results.

2.2.2. FLUID FLOW SIMULATIONS

Comsol Multiphysics (www.comsol.de) allows to simulate the flow in saturated void space using the free flow physics tool, which is based on the Navier Stokes approximation using the continuum equation for incompressible flow (with $\nabla \cdot u = 0$):

$$\underbrace{\rho\left(\frac{\partial u}{\partial t} + u \cdot \nabla u\right)}_{\text{inertial forces}} = \underbrace{-\nabla p}_{\text{pressure forces}} \underbrace{+\nabla \cdot (\mu(\nabla u + (\nabla u)^T) - \frac{2}{3}\mu(\nabla \cdot u) I)}_{\text{viscous forces}} + \underbrace{F}_{\text{external forces}} \tag{2.5}$$

where u is the fluid velocity, p is the fluid pressure, ρ is the fluid density, μ is the fluid

dynamic viscosity, I is the identity matrix and F are the external forces. The first term describes the inertial forces, which is assumed to be negligible in our models, the second term the pressure forces, the third term the viscous forces and F the external forces applied to the fluid, i.e. gravity. However, gravity has almost no impact for the apertures of a few millimeters. The 3D finite element mesh was imported to Comsol and the following boundary conditions were applied to the model: (1) constant flow rate at the inlet, (2) zero bar pressure boundary at the outlet (relative to atmospheric pressure) and (3) no flow (no slip) condition at the boundaries (figure 2.1c). The parameters used for the simulation are a constant inflow velocity v or u of 1e-3, 1e-4 and 1e-5 m/s, as well as a temperature dependent fluid density ρ and dynamic fluid viscosity μ (constant room temperature). Flow was imposed parallel to the displacement direction of the fracture along the y-axis. The simulation is a time dependent, transient solution, calculating results every 60 sec up to a total simulation time of 3600 sec. A steady state pressure regime was observed within the first 60 sec in all simulations. The permeability of the fracture was calculated using Darcy's law for laminar flow. The pressure gradient was calculated using the mean inflow and outflow pressure at the boundaries. Three different inflow velocities were chosen such that laminar flow conditions are met ($Re < 1400$) by calculating the Reynolds number for two parallel plates:

$$Re = \frac{a v \rho}{\mu} \tag{2.6}$$

where a is the aperture at each point of the fracture, v the flow velocity at each point of the fracture, ρ the fluid density (constant) and μ the fluid viscosity (constant). The aperture distribution $a(x, y)$ was taken from the generated fracture topography model and the velocity $v(x, y)$ was exported from the Comsol simulation. Interpolation of the x and y coordinates of the velocity field to those of the aperture field gives a spatial model for the Reynolds number using equation 2.6. Two examples for a spatial distribution of the Reynolds number are shown in figure 2.2. Although increasing the inflow velocity and therefore the Reynolds number led to numerical instability of the simulations, the Reynolds number never exceeded conditions for laminar flow ($Re < 1400$). Five models at five different displacement levels (d = 1 mm, d = 5 mm, d = 10 mm, d = 25 mm and d = 50 mm) were used for the simulation. Furthermore, three different roughness levels were used (B = 1, B = 1.5, B = 2). A total of 45 flow simulations have been performed. However, not all simulations were successful due to numerical instability for certain cases.

2.2.3. MODEL VERIFICATION

To verify the results from the numerical simulations, flow through two parallel plates, separated by a constant distance of a = 1.5 mm, representing about the average aperture of all simulations, was simulated. The same boundary conditions as for the rough fractures were used. Comparing the results of flow through two parallel plates in a 3D simulation and the analytical solution given by the cubic law (equation 2.1), the simulation provides an accuracy within 1 % (see table 2.1).

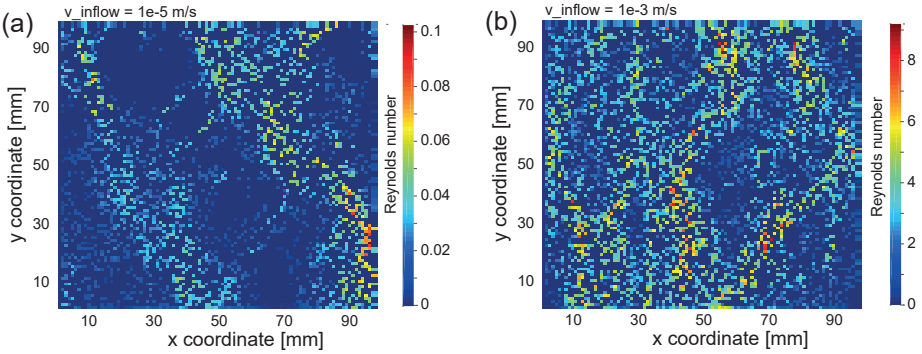

Figure 2.2: Spatial distribution of the Reynolds number for (a) 50mm displacement, medium roughness (B = 1.5), inflow velocity 1e-5 m/s and (b) 50mm displacement, high roughness (B = 1), inflow velocity 1e-3 m/s. The maximum Reynolds number is less than 10, such that flow is laminar in all simulations.

2.3. RESULTS

The simulations were evaluated in terms of the dependence of fracture permeability on fracture roughness and displacement. The fluid pressure distribution and velocity field is used to demonstrate the change in flow pattern from the 3D flow simulations. The permeability obtained from the simulations were compared to the fracture permeability calculated from the cubic law approximation (equation 2.1). The results are summarized in table 2.1. The maximum Reynolds number Re is given for the inflow velocity of 1e-4 m/s (range of Re is always between 0 and Re_{max}).

Table 2.1: Parameters and results for simulations at various displacement and for fractures of different roughness.

d (mm)	B $(-)$	Re_{max} $(-)$	$\bar{a}$ (mm)	$\mathrm{k}_{f,cub}$ (m^2)	$\mathrm{k}_{f,num}$ (m^2)	$\mathrm{k}_{f,num}$ / $\mathrm{k}_{f,cub}$
5	1.0	0.83	1.79	$2.67e^{-7}$	$8.47e^{-8}$	0.32
	1.5	0.51	0.97	$7.91e^{-8}$	$1.72e^{-8}$	0.22
	2.0	0.15	0.55	$2.55e^{-8}$	$5.56e^{-9}$	0.22
10	1.0	0.85	1.83	$2.81e^{-7}$	$1.08e^{-7}$	0.38
	1.5	0.89	1.22	$1.24e^{-7}$	$3.00e^{-8}$	0.24
	2.0	0.89	0.73	$4.51e^{-8}$	-	-
25	1.0	0.78	2.06	$3.53e^{-7}$	$1.58e^{-7}$	0.45
	1.5	0.99	1.57	$2.06e^{-7}$	$7.65e^{-8}$	0.37
	2.0	0.57	1.08	$9.67e^{-7}$	$1.73e^{-8}$	0.18
50	1.0	0.91	2.38	$4.71e^{-7}$	$2.18e^{-7}$	0.46
	1.5	1.03	1.68	$2.36e^{-7}$	$1.10e^{-7}$	0.47
	2.0	0.95	1.16	$1.11e^{-7}$	$2.39e^{-8}$	0.21
par. plates	-	0.15	1.50	$1.88e^{-7}$	$1.87e^{-7}$	0.99

2.3.1. APERTURE DISTRIBUTION

The aperture distribution across one fracture is a normal Gaussian distribution by definition of the power spectral density function used for the fracture surface generation. However, the range of aperture distribution is changing with the relative fracture displacement. Generally, the higher the fracture displacement the higher the mean aperture (figure 2.1) and the wider the range or distribution of the aperture (figure 2.3). This behaviour is different for different fracture roughnesses, but the trend is similar in all cases. After a certain threshold in displacement, i.e. $d = 15$ mm in our simulations, the mean aperture magnitude and the distribution are not changing significantly anymore. The magnitude of the aperture is dependent on fracture roughness. Rough fractures have a higher mean aperture than smooth fractures when being displaced.

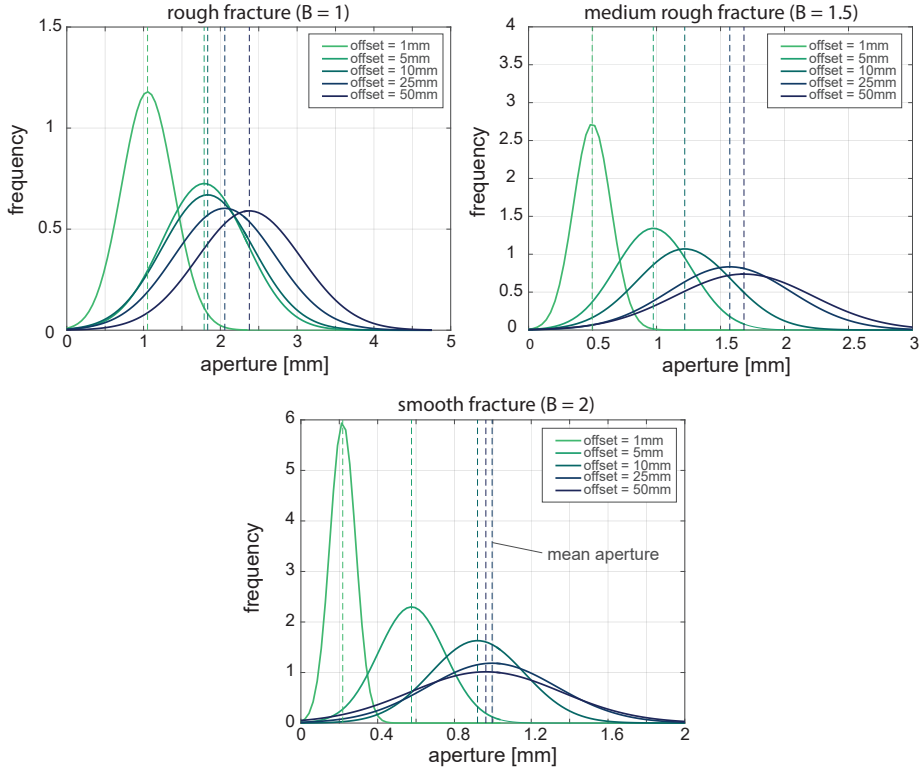

Figure 2.3: Probability density function of aperture distribution for different fracture offsets showing and increase in mean aperture and an increase in aperture range for increasing offsets.

2.3.2. VARIATIONS IN FRACTURE DISPLACEMENT

The flow velocity magnitude field allows to describe the flow pattern within a rough fracture. The velocity and pressure distribution of a fracture with constant roughness ($B = 1.5$)

and increasing displacement was analysed. Figure 2.4 shows a cut through the middle of the fracture plane, displaying pressure and fluid velocity. For small displacements small flow channels with low velocities were simulated. With increasing displacement, channels become wider and are getting connected having higher flow velocities. At a displacement of $d = 25$ mm the flow field already covers large areas of the fracture. The pressure gradient is very small in all simulations. The reason for that is the large aperture and therefore the high hydraulic permeability. However, higher inflow velocities led to some numerical instability. Calculating the fracture permeability from the simulation data, permeability follows the same general trend as the aperture with increasing displacement, i.e. the more displaced a fracture the higher its permeability.

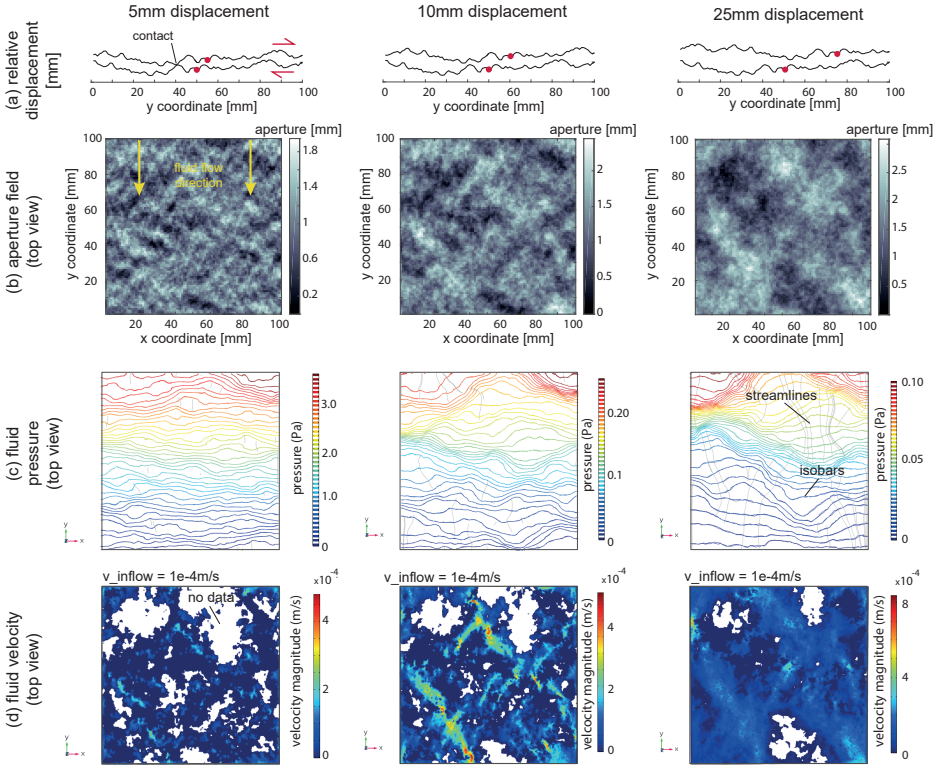

Figure 2.4: (a) Fracture aperture profiles showing a profile of the displaced fracture, (b) aperture distribution across the fracture, (c) fluid pressure distribution (zero pressure = atmospheric pressure) with stream lines and (d) velocity magnitude field across the fracture. The roughness is constant with $B = 1.5$ for all fracture models, whereas displacement was varied. Generally, the flow velocity is zero or close to zero in areas of low aperture. The distribution of low and high aperture regions depends on the displacement. Higher displacement causes continuous flow with higher velocity distributed all over the fracture void space. Less displaced fractures, in contrast, show very localised flow with small channels and discontinuous streamlines.

2.3.3. VARIATIONS IN FRACTURE ROUGHNESS

The dependence of fracture roughness on the flow behaviour was analysed, as well. For these simulations, the displacement of all fractures was set to 50 mm and roughness levels of $B = 1$, $B = 1.5$ and $B = 2$ were used. Figure 2.5 shows a cut through the middle of the fracture plane, displaying pressure and fluid velocity. For rough fractures, large and continuous channels are distributed over the entire area of the fracture void space. Smooth fractures, in contrast, show very localised flow since aperture in some local areas is either high, or close to zero. The evaluation shows that the effective fracture permeability is only between 20% and 50% of the analytical solution without corrections (figure 2.6). Rough fractures show a systematic decrease in deviation with increasing fracture offset, whereas smooth fractures show no clear trend. The permeability is generally lower for smooth and displaced fractures compared to rough and displaced fractures.

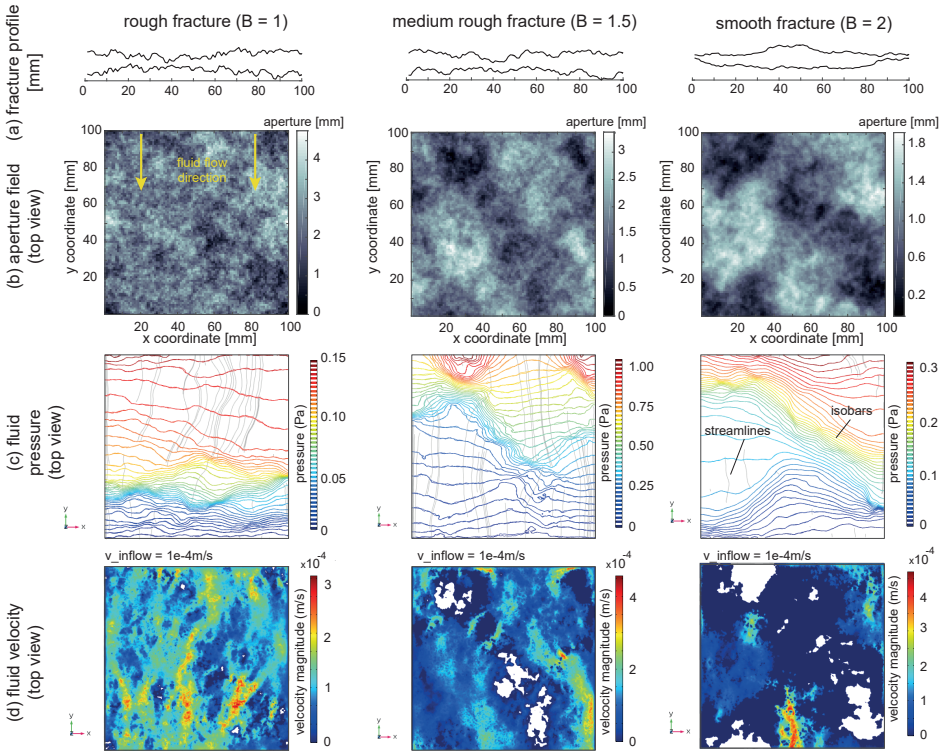

Figure 2.5: (a) Fracture aperture profiles showing a profile of the the fractures with different roughness, (b) aperture distribution across the fracture, (c) fluid pressure distribution (zero pressure = atmospheric pressure) with stream lines and (d) velocity magnitude field across the fracture. The displacement d is constant at 50 mm for all fracture models, whereas roughness was varied. Generally, the flow velocity is zero or close to zero in areas of low aperture. The distribution of low and high aperture regions depends on the roughness. Higher roughness causes continuous flow with higher velocity distributed all over the fracture void space. Smooth fractures, in contrast, show very localised flow and discontinuous streamlines.

2.3.4. CORRECTION FACTORS FOR THE CUBIC LAW

The fracture permeability obtained from our simulations is 50 to 80 % less than that calculated using the cubic law approximation. Several authors have tried to establish correction factors, accounting for parameters such as surface roughness and tortuosity. Zimmerman and Bodvarsson (1996) defined correction factors for the aperture (equation 2.2). The roughness correction factor C_r depends on the standard deviation of the aperture. The tortuosity factor C_t depends on the fracture closure ratio, i.e. the proportion of the fracture plane that is occupied by obstructions. This factor was modified by Walsh et al. Walsh et al. (2008) due to a percolation threshold at contact ratios of 50 % and above. The general trend is, that the higher the closure ratio, the higher the deviation from the cubic law. The closure ratio required to obtain the same deviation from the cubic law in our simulations and including the correction factor by Zimmerman and Bodvarsson (1996) is around 0.2 to 0.3. Looking at the dependence of fracture permeability on mean aperture and standart deviation of the mean aperture, i.e. the spread of the aperture distribution, there is a clear trend that the deviation from the cubic law is decreasing with increasing mean aperture and increasing standart deviation (figures 2.6 d,e).

2.4. DISCUSSION

The mean aperture $\langle a \rangle$ and the aperture distribution for one single fracture is dependent on the fracture offset (figure 2.3). Since permeability is a function of the aperture, it is dependent on the fracture offset as well. However, the simulations show that this relation cannot be simply addressed with the Hagen Poiseulle solution of the cubic law (Witherspoon et al., 1980). The cubic law assumption of two parallel plates with a constant aperture and laminar flow conditions will be violated in fractures with rough surfaces. Natural fractures with rough surfaces always have a smaller permeability than approximated by the cubic law (figure 2.6). Intuitively, the rougher a fracture, the more deviation from the cubic law can be expected. Our simulations show, that rough and displaced fractures have a smaller deviation from the cubic law due to the higher overall aperture which is distributed more equally over the area of the fracture. Similar to the observations by Méheust and Schmittbuhl Méheust and Schmittbuhl (2000), roughness becomes less meaningful at larger apertures, giving closer results to the cubic law.

Comparing correction factors for the cubic law provided in other studies, for example Zimmerman and Bodvarsson (1996) or Jin et al. (2017), the calculation of the required parameters from our models remains difficult. The tortuosity factor, i.e. the closure ratio, in Zimmerman and Bodvarsson (1996) cannot be calculated correctly. This is because the number of contacting points is very little due to the superposition principle of two fracture surfaces based on the numerical surface heights and the neglected mechanical deformation of the asperities. To obtain the same deviation from the cubic law as provided by the numerical simulation results, the fracture closure ratio would need to be around 0.2 to 0.3. This means, that for a our fracture models, i.e. a model with the mean aperture of 1.8 mm, all apertures below 1.5 mm must be regarded as closed. It remains difficult to relate this value to a possible closure rate under normal stresses acting perpendicular to the fracture planes in real systems.

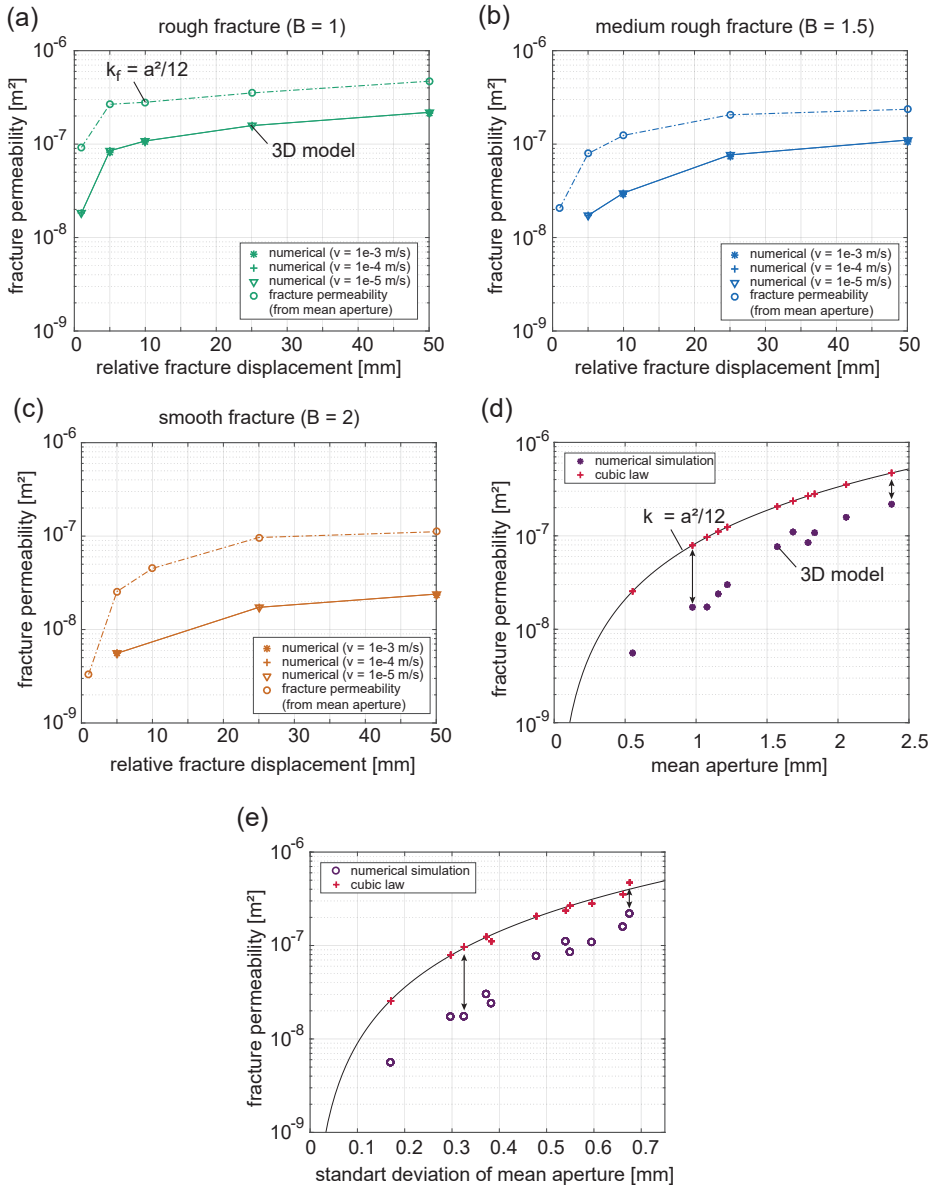

Figure 2.6: Fracture permeability depending on relative fracture displacement calculated using the cubic law and the numerically derived permeability for three different levels of roughness: (a) $B = 1$, (b) $B = 1.5$, (c) $B = 2$. (c) Simulated fractured permeability highly depends on the mean aperture. (d) Fracture permeability depending on the mean aperture and (e) standard deviation of mean aperture.

Looking at the relation of roughness and displacement, one might argue that the higher the displacement, the higher the permeability. Considering the fact that no mechanical defor-

mation of asperities is involved in our simulations, real fracture asperities will be damaged, due to the normal stress acting perpendicular to a fracture (Crawford, 1998, Elkhoury et al., 2011, Watanabe et al., 2009). This will effectively reduce permeability. Asperity deformation in smooth fractures is most likely reduced compared to rough fractures, due to the higher contact area ratio. A balance between displacement and deformation needs to be found for an optimum permeability prediction. Furthermore, no leak-off of fluid from the fracture into the surrounding rock is considered in the models presented in this studies.

2.5. CONCLUSIONS

In this study, 3D numerical flow simulations were performed to investigate the flow behaviour in rough fractures. By use of this approach, correlation between shear displacement and mean aperture, shear displacement and permeability, as well as surface roughness and permeability can be obtained. This hydraulic modeling approach can be applied for artificial as well as real systems. We found in our study, that the mean aperture is increasing with increasing shear displacement when the deformation of the fracture asperities is neglected. Furthermore, the lower the shear displacement, a larger number of small channels with low velocity form. Localizing of flow in smooth and displaced fractures causes a discontinuous flow velocity field. Furthermore, the more smooth a displaced fracture, the higher the deviation from the cubic law. The main controlling parameter on fracture permeability is the mean aperture. Including numerical errors and errors caused by the permeability calculation using mean pressures from the flow simulations, the real fracture permeability is 50 to 80% lower than that calculated using the cubic law approximation. In the future, we aim to include fracture-matrix systems in our simulations to allow for the quantification of the flow volumes in the matrix and the fracture, as well as to quantify the impact of fluid leak-off from the matrix into the host rock.

REFERENCES

G. Blöcher, G. Zimmermann, I. Moeck, W. Brandt, A. Hassanzadegan, and F. Magri. 3d numerical modeling of hydrothermal processes during the lifetime of a deep geothermal reservoir. *Geofluids*, 10(3):406–421, aug 2010. doi: 10.1111/j.1468-8123.2010.00284.x.

M. Cacace and G. Blöcher. MeshIt—a software for three dimensional volumetric meshing of complex faulted reservoirs. *Environmental Earth Sciences*, 74(6):5191–5209, may 2015. doi: 10.1007/s12665-015-4537-x.

B. R. Crawford. Experimental fault sealing: shear band permeability dependency on cataclastic fault gouge characteristics. *Geological Society, London, Special Publications*, 127(1):27–47, 1998. doi: 10.1144/gsl.sp.1998.127.01.04.

J. E. Elkhoury, A. Niemeijer, E. E. Brodsky, and C. Marone. Laboratory observations of permeability enhancement by fluid pressure oscillation of in situ fractured rock. *Journal of Geophysical Research*, 116(B2), feb 2011. doi: 10.1029/2010JB007759.

H. Hofmann, G. Blöcher, N. Börsing, N. Maronde, N. Pastrik, and G. Zimmermann. Potential for enhanced geothermal systems in low permeability limesystem - stimulation strategies for the western malm karst (bavaria). *Geothermics*, 51:351–367, jul 2014. doi: 10.1016/j.geothermics.2014.03.003.

H. Hofmann, G. Blöcher, H. Milsch, T. Babadagli, and G. Zimmermann. Transmissivity of aligned and displaced tensile fractures in granitic rocks during cyclic loading. *International Journal of Rock Mechanics and Mining Sciences*, 87:69–84, sep 2016. doi: 10.1016/j.ijrmms.2016.05.011.

Y. Jin, J. Dong, X. Zhang, X. Li, and Y. Wu. Scale and size effects on fluid flow through self-affine rough fractures. *International Journal of Heat and Mass Transfer*, 105:443–451, feb 2017. doi: 10.1016/j.ijheatmasstransfer.2016.10.010.

Y. Méheust and J. Schmittbuhl. Flow enhancement of a rough fracture. *Geophysical Research Letters*, 27(18):2989–2992, sep 2000. doi: 10.1029/1999GL008464.

Y. Méheust and J. Schmittbuhl. Geometrical heterogeneities and permeability anisotropy of rough fractures. *Journal of Geophysical Research: Solid Earth*, 106(B2):2089–2102, feb 2001. doi: 10.1029/2000JB900306.

H. Milsch, H. Hofmann, and G. Blöcher. An experimental and numerical evaluation of continuous fracture permeability measurements during effective pressure cycles. *International Journal of Rock Mechanics and Mining Sciences*, 89:109–115, nov 2016. doi: 10.1016/j.ijrmms.2016.09.002.

R. Walsh, C. McDermott, and O. Kolditz. Numerical modeling of stress-permeability coupling in rough fractures. *Hydrogeology Journal*, 16(4):613–627, mar 2008. doi: 10.1007/s10040-007-0254-1.

N. Watanabe, N. Hirano, and N. Tsuchiya. Diversity of channeling flow in heterogeneous aperture distribution inferred from integrated experimental-numerical analysis on flow through shear fracture in granite. *Journal of Geophysical Research*, 114(B4), apr 2009. doi: 10.1029/2008JB005959.

P. A. Witherspoon, J. S. Y. Wang, K. Iwai, and J. E. Gale. Validity of cubic law for fluid flow in a deformable rock fracture. *Water Resources Research*, 16(6):1016–1024, dec 1980. doi: 10.1029/WR016i006p01016.

H. Zhou and H. Xie. Anisotropic characterization of rock fracture surfaces subjected to profile analysis. *Physics Letters A*, 325(5-6):355–362, may 2004. doi: 10.1016/j.physleta.2004.04.006.

R. Zimmerman and G. Bodvarsson. Hydraulic conductivity of rock fractures. *Transport in Porous Media*, 23(1), apr 1996. doi: 10.1007/BF00145263.

G. Zimmermann, I. Moeck, and G. Blöcher. Cyclic waterfrac stimulation to develop an Enhanced Geothermal System (EGS) - Conceptual design and experimental results. *Geothermics*, 39(1):59 – 69, 2010. ISSN 0375-6505. doi: 10.1016/j.geothermics.2009.10.003.

3

HYDRO-MECHANICAL PROPERTIES OF MICROFAULTS

Fault zones are key features in crystalline geothermal reservoirs or in other subsurface environments due to the fact that they act as main fluid pathways. An adequate experimental description of the evolution of permeability of a realistic microscopic fault zone under in-situ reservoir and fracture parallel flow conditions is required. To address this topic, we demonstrate a novel experimental set up (Punch-Through Shear test) that is able to generate a realistic shear zone (microfault) under in-situ reservoir conditions while simultaneously measuring permeability and dilation. Three samples of intact granite from the Odenwald (Upper Rhine Graben) were placed into a MTS 815 tri-axial compression cell, where a self-designed piston assembly punched down the inner cylinder of the sample creating the desired microfault geometry with a given offset. Permeability was measured and fracture dilation was inferred from an LVDT extensometer chain, as well as the balance of fluid volume flowing in and out of the sample. After fracture generation, the shear displacement was increased to 1.2 mm and pore pressure changes of ± 5 or ± 10 MPa were applied cyclically to simulate injection and production scenarios. Formation of a microfault increased the permeability of the granite rock by 2 to almost 3 orders of magnitude. Further shear displacement led to a small increase in permeability by a factor of 1.1 to 4.0, but permeability was reduced by a factor of 2.5 to 4 within 16 h due to compaction and fault healing. Effective pressure cycling led to reversible permeability changes. CT images showed that the fracture network is rather complex, but depicts all features commonly observed in larger scale fault zones.

This chapter is based on: C. Kluge, G. Blöcher, A. Barnhoorn, D. Bruhn, *Hydraulic-mechanical properties of microfaults in granitic rock using the Punch-Through Shear test*, International Journal of Rock Mechanics and Mining Sciences **134**, (2020).

3.1. INTRODUCTION

The permeability of fractures and faults, or, more generally, shear fractures in crustal rocks has been a substantial research topic in the past. It is not only important in crustal faulting processes or earthquake mechanisms, but is also key in understanding the fluid flow in faulted or enhanced geothermal systems (Cuenot et al., 2006, Evans et al., 2005, Hofmann et al., 2018, McClure and Horne, 2014), as well as the stability of underground constructions, such as tunnels or nuclear waste repositories. Fractures control the hydrological and mechanical behaviour of rock masses, such that any changes in fracture properties have a large impact on the bulk transport properties. Laboratory experiments with fractured rock samples are a substantial element to better understand and physically characterise fractures in order to imply physical relationships for the larger scale.

Conventional tri-axial compression tests are classically used to generate shear fractures or shear zones. Since measuring fracture permeability in such experiments is difficult and fracture permeability cannot be isolated from the rock matrix, other experimental approaches are required. The fractures used for experiments are commonly generated in tensile mode, for example by Brazilian Disk splitting (Hofmann et al., 2016, Milsch et al., 2016, Watanabe et al., 2008), or existing, as well as artificial joints are used (Develi and Babadagli, 2015, Fang et al., 2018, Vogler et al., 2016). The sample halves are then placed together at a certain offset and are installed in a tri-axial cell or shear-box tool to study the permeability evolution. Although the term shear fracture is often applied to such geometries, they do not represent the complex structure of a single shear or fault zone. Several attempts have been made in the past to reproduce a single realistic fault zone in the laboratory. Watanabe et al. (2009) used a shear-box tool to apply mode II loading to an intact rock sample, but pointed out that it is difficult to generate a single shear fracture from shear-box experiments due to the occurrence of multiple fractures. However, experiments by Frash et al. (2019) using shale and anhydrite samples highlighted the importance of features, such as en echelon structures, for the aperture anisotropy. Recently, Ye and Ghassemi (2018b) used a conventional tri-axial setup with cylindrical double-flawed samples connected to pumps using two injection holes. By increasing the injection pressure, they generated a complex fracture network including shear and tensile fractures and compared the permeability before and after fracture generation. Besides the challenge to generate a single shear zone while flowing fluid through the sample, permeability is rarely measured during the initiation and propagation of a fracture under in-situ pressure conditions. First attempts to measure permeability while generating a shear fracture in high permeable rocks have been made for example by Zhu and fong Wong (1997) or Crawford (1998). Paola et al. (2009) measured the permeability of anhydrite samples during tri-axial testing and subdivided the permeability evolution into three stages of compaction, dilation and brittle failure. Others measured the permeability in tri-axial tests using the pore pressure oscillation method (Carey et al., 2018, Elkhoury et al., 2011, Shokouhi et al., 2020). Mitchell and Faulkner (2008) quantified the permeability enhancement to about 2 orders of magnitude with the same experimental procedure for granite and granodiorite. However, the shear fractures in these tests were not parallel to the flow direction or the entire sample integrity was lost during failure, which makes it difficult to isolate the mechanical and hydraulic behaviour of the fracture from the surrounding rock mass. Watanabe et al. (2009) tested fractured granite samples in a shear-

box tool and measured the permeability of these samples in another flow-through apparatus. Although a flow parallel fracture geometry is given, no fluid flow was applied during fracturing and the sample had to be removed from the shear apparatus after fracture generation, which highly alters the hydraulic-mechanical fracture properties.

The permeability during shearing is substantial for the understanding of the processes involved in hydro-shearing or the permeability evolution in active faults. In some experimental studies, asymmetric loading conditions on a pre-existing tensile fracture in cylindrical samples with different end cap designs were used to displace a fracture while measuring permeability (Elkhoury et al., 2011, Kluge et al., 2017, Zhang et al., 2019). Shear-box tools were also used to displace a fracture under normal loading conditions (Lee and Cho, 2002, Yeo et al., 1998), but the normal effective pressures in these tests were too low to make meaningful conclusions or additional fractures formed. Watanabe et al. (2009) compared the permeability of displaced tensile fractures and fractures generated by shearing and found that displaced tensile fractures have a higher permeability and a higher resistance to closing compared to shear fractures when increasing normal stress. More frequently, tri-axial set ups with injection-holes are used to generate a shear displacement on a pre-existing planar shear plane in different materials (Rutter and Mecklenburgh, 2017, Sheng et al., 2018). Other authors performed performed stick-slip experiments with artificial surfaces (Im et al., 2018, Ye and Ghassemi, 2018a), which are sheared while measuring permeability. Although it is possible to accurately quantify permeability, the experimental set ups mentioned involve unrealistic planar fracture surfaces, which lead to only marginal permeability changes or are performed at very low normal stress.

The longevity or sustainability of the generated permeability enhancement by fracturing is crucial for engineering applications, in which, for example, pore pressures change due to production and injection schemes, or the fracture aperture changes due to stress relaxation when the well is not operated. In experimental studies with granite (Chen et al., 2000, Hofmann et al., 2016, Pyrak-Nolte and Morris, 2000, Watanabe et al., 2009), the effective pressure was varied by changing the confining pressure cyclically using displaced tensile fractures in granite and found a progressive reduction in permeability with each cycle. However, manually displaced tensile fractures might have a different initial strength during the first loading stages compared to faults. Furthermore, a variation in confining pressure is different compared to changing the pore pressure when considering effective pressure coefficients (Walsh, 1981). Zangerl et al. (2008) evaluated the fracture normal stiffness of several granite samples and provided a range of values, without finding systematic changes, but highlighted the importance of surface geometry and asperity deformability. Lastly, permeability losses are often observed in experiments and are related to mechanical compaction (Elkhoury et al., 2011, Im et al., 2018) or fluid-rock interactions (Yasuhara and Elsworth, 2008). Therefore, effective pressure cycling, fracture stiffness characterisation, as well as compaction induced permeability reductions need to be considered for complex shear fracture or fault geometries. There is too little quantification of permeability enhancement in granite during shear fracture generation or permeability evolution during shearing and only a few of those studies account for a realistic shear zone geometry, or they are limited in terms of the displacement magnitude.

We present an approach to combine most of the above-mentioned experimental technolo-

gies in a single experiment. The evolution of permeability during initiation and propagation of a circular shear fracture (referred to as a microfault in the following) is presented, using the Punch-Through-Shear (PTS) test, originally developed to measure mode II fracture toughness (Backers, 2004, Backers and Stephansson, 2012, Meier, 2009, Wu et al., 2017, Yoon and Jeon, 2004). The existing experimental setup has been supplemented with the possibility of saturating the sample and allowing fluid flow-through to measure the pressure gradient across the sample. This enables us to determine the permeability of an artificially-generated microfault with flow oriented parallel to the fracture. The PTS test allows for the quantification of the permeability during fracture initiation, propagation and effective pressure changes, an analysis of fracture properties and geometry, as well as an assessment of its hydraulic-mechanical sustainability.

3.2. MATERIALS & METHODS

3.2.1. TESTING EQUIPMENT

The Punch-Through-Shear (PTS) test was carried out in a conventional MTS tri-axial compression cell. The stiff, servo-controlled loading frame (MTS 815, Material Testing Systems Corporation) holds a loading capacity of up to 4600 kN (load cell calibrated to 1000 kN, calibration error <1 %) and a servo-controlled maximum hydrostatic confining pressure of 140 MPa applied via an oil-filled pressure vessel coupled to an external pressure intensifier. The pore fluid pressure was applied via four Quizix fluid pressure pumps (Model C6000-10K-HC-AT) with a maximum fluid pressure of 70 MPa. Flow-through was continuously applied at a minimum of 2 MPa confining pressure using two paired upstream pumps and two paired downstream pumps. The differential fluid pressure, which is the difference between in- and outflow pressure, was measured using a differential pressure sensor (Honeywell HL-Z; range: 1 MPa; line pressure max. 35 MPa; precision: ~1 %). Changes in circumferential strain were measured using a LVDT extensometer chain. All experiments have been performed at ambient conditions, i.e. temperatures of 25 to 30 °C. Data were recorded at a frequency of 1 Hz. A detailed description of the machine is found in Pei et al. (2016).

3.2.2. SAMPLE MATERIAL

The testing material is a granite from the Odenwald region (International Geo Sample Number, IGSN: GFTRE0033) taken from a quarry in Rimbach, Germany. The fresh granite shows no signs of strong alterations or microfracturing (figure 3.1c to f). It is composed of quartz (Qtz) with a grain size ranging from 1 to 3 mm, feldspar (Fsp) between 2 to 3 mm and mica (Mca) between 1 to 3 mm, suggesting a very even size distribution of minerals. Quartz, as well as the darker and brighter mica are the main constituents, feldspars have a less frequent occurrence. Microfractures are only partially present and either cut through grains, or propagate along grain boundaries with no visible shear offset. The porosity of less than 0.6 % is mostly intra-granular and rarely connected. The intact rock properties of the Odenwald granite, in the following labelled as PGR6-RI,40 are summarized in table 3.1. Three granite samples have been tested with their testing conditions and sample dimensions

listed in table 3.2.

Table 3.1: Intact rock properties of sample PGR6-RI according to Blöcher et al. (2019).

rock sample ID	*TS* [MPa]	K_{IC} [MPa*m$^{0.5}$]	*UCS* [MPa]	*E* [GPa]	*ν* [-]	*ϕ* [%]	*k* [m^2]
IGSN: GFTRE0033	11.8	1.347	120 - 142	39.9 - 47.6	0.19 - 0.26	<0.5	$<10^{-18}$

TS: tensile strength, K_{IC}: mode I fracture toughness, *UCS*: uniaxial compressive strength, *E*: Young's modulus, *ν*: Poisson ratio, *ϕ*: porosity, k_{ini}: initial permeability

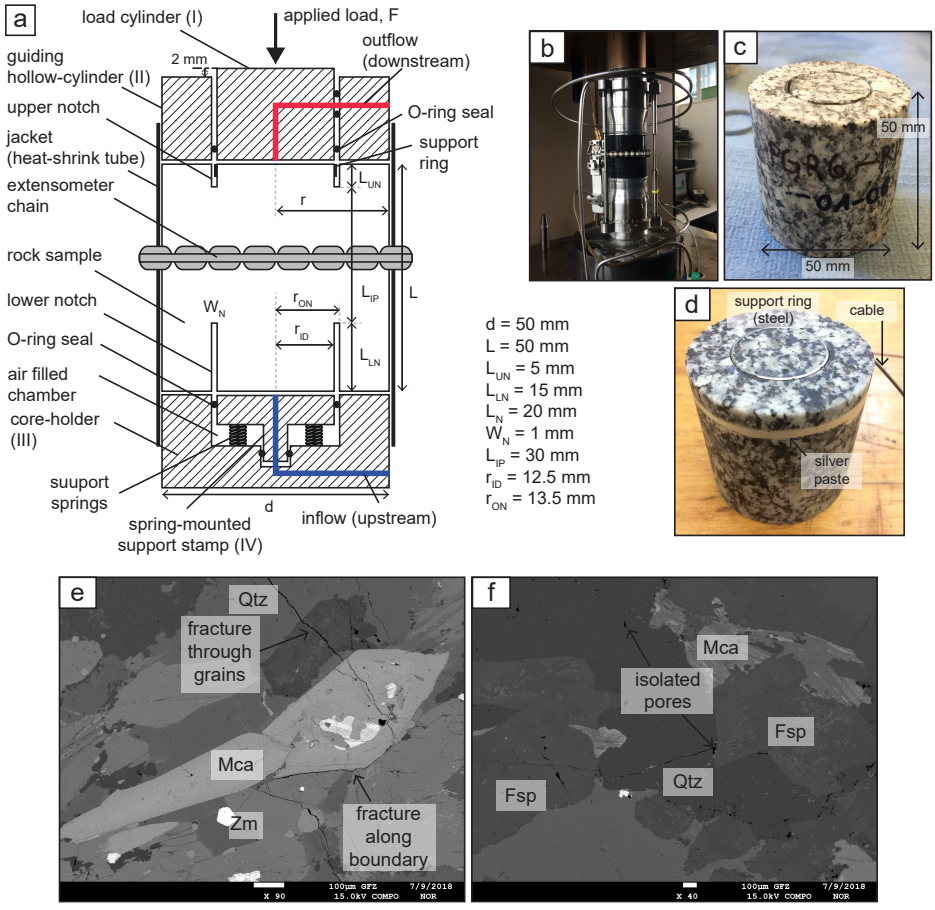

Figure 3.1: a) Experimental set up and dimensions, b) Experimental set up, c) Odenwald granite sample (PGR6-RI), d) integrity test, e) and f) electron probe microanalyzer (EPMA) images of the intact rock.

3.2.3. SAMPLE GEOMETRY & EXPERIMENTAL SETUP

The idea of the Punch-Through-Shear (PTS) test is to have a notched intact cylindrical sample, of which a smaller inner part (inner cylinder) is punched through the surrounding hollow cylinder. The main objective is to generate a shear stress concentration at the notch tips generating a circular shear fracture (microfault) connecting the bottom and top notch of a cylindrical rock sample. The experimental set up and sample geometry are illustrated in figures 3.1a, b. The set up consists of a piston assembly that applies a load to the top inner cylinder and the bottom outer annulus of the sample, as well as a core-holder system supporting the sample at the bottom, both made of stainless steel. The cylindrical samples were drilled from larger blocks to a diameter, d, of 50 mm using a diamond drill bit and water as lubricant. The samples were cut to length, L, of 50 mm using a diamond saw, and the end-surfaces were ground plan-parallel. The notches were then drilled using a diamond drill bit with an inner diameter, r_{ID}, of 25 mm and a wall thickness, i.e. notch width, W_N, of 1 mm. Top notch depth and lower notch depth were 5 and 15 mm respectively, resulting in an intact portion, L_{IP}, of 30 mm. This intact portion, L_{IP}, was larger compared to the 15 mm suggested by the ISRM International Society for Rock Mechanics and Rock Engineering (Backers and Stephansson, 2012), but was used to enable the proper characterisation of the hydraulic, mechanical and geometrical properties of the microfault. This deviation from the recommended design is acceptable, as no variations in fracture toughness up to a length of 35 mm were previously found (Backers, 2004, Backers and Stephansson, 2012, Yoon and Jeon, 2004). The mechanical integrity of the top-notch walls was supported by a 0.3 mm strong steel ring (2 mm shorter than the top notch length L_{UN}) to prevent breakouts and compaction that were observed in pre-tests without a supporting ring (figure 3.1d). Due to its shorter length the ring is assumed to not cause axial stress to the rock sample itself. The sample was covered with a heat-shrink tube to prevent confining fluid from entering the sample. The loading assembly, shown in figure 3.1a, consists of a mobile steel cylinder of 25 mm in diameter (I), guided by a surrounding hollow cylinder (II), which is 2 mm shorter than the mobile inner cylinder. The space in between the two parts is sealed by O-rings to prevent oil from entering the sample. The lower part of the assembly consists of a rigid core-holder system with a hollow cylindrical shape to counteract the applied load from the top (III). A movable smaller core-holder in the middle (IV), also sealed with O-rings, is mounted on a set of springs in an air-filled chamber. This is to prevent the inner cylinder from falling down instantly after failure and allows for a controlled displacement along the fracture. Fluid ports were incorporated within the loading assembly and core-holder system, sealed from the confining fluid by O-rings. A grid across the surface of the end caps allows for uniform in- and outflow across the entire cross-sectional area (top and bottom) of the sample. An extensometer chain (LVDT) attached at the centre between upper and lower notch is used to record the bulk circumferential strain throughout the entire duration of the test. Furthermore, the integrity of the sample wall during one experiment was monitored (PGR6-RI-01-07). Silver paste was applied to the circumference of the sample connected to an electronic circuit, such that any fracturing of the wall would result in an interruption of the electric signal (figure 3.1d).

Table 3.2: List of samples, sample dimensions and testing conditions.

sample ID	testing conditions	L_{IP} [mm], L [mm], d [mm]	Additional measurements
PGR6-RI-01-07	Failure at P_c = 40 MPa and P_p = 20 MPa, pressure cycling: none	31.40, 49.40, 50.05	Integrity test, fluid leak no LVDT chain
PGR6-RI-01-08	Failure: P_c = 40 MPa and P_p = 20 MPa, pressure cycling: 5 MPa	30.15, 50.15, 50.10	LVDT chain, x-ray CT
PGR6-RI-01-09	Failure: P_c = 40 MPa and P_p = 20 MPa, pressure cycling: 10 MPa	30.18, 50.19, 50.10	LVDT chain, x-ray CT

P_c: confining pressure, P_p: pore pressure, L_{IP}: length of intact portion, L: sample length, d: sample diameter

3.3. EXPERIMENTAL PROCEDURES

The sample was installed in the measuring assembly and an absolute pore pressure of 1 kPa was generated using a vacuum pump (Laboxact SEM 820). The confining pressure was increased from 0 to 2 MPa at a rate of 0.5 MPa/min with the dry sample. After applying the vacuum, the system was saturated by applying a constant fluid pressure of 0.2 MPa from the upstream side. That way, water flew into the sample under nearly vacuum conditions, such that all pores were saturated. Saturation was finished when no more water flew into the sample to avoid effects of the saturation process to govern the permeability at later stages of the experiments (Hofmann et al., 2016). For all permeability measurements, a constant flow rate (0.4 to 1 ml/min) was applied to the bottom of the sample and a constant pressure was applied at the downstream side (10 to 30 MPa) to determine the sample permeability. Steady-state conditions were reached when the flow rates and pressure difference reach a constant value. Sample permeability, k, was calculated by equation 3.1 using Darcy's law (Darcy, 1856), where the length, L_{IP}, is the distance between the lower and upper notch which corresponds to the maximum pressure gradient in the microfault. The sample permeability, k, corresponds to the permeability of the rock portion between the notches, assuming there is no pressure gradient along the 1 mm wide notches:

$$k = \frac{Q}{A}\frac{\mu L_{IP}}{dP} \tag{3.1}$$

where Q is the volumetric inflow rate in m^3/s, A is the cross-sectional area of the sample in m^2 μ is the dynamic viscosity of the fluid (Pa·s), L_{IP} is the distance between the notches of the sample in m and dP is the differential fluid pressure in Pa. The minimum measurable permeability of our apparatus is around $k = 10^{-18}$. It is important to note, that steady-state permeability, k_{ss}, was measured during the hold phase (C), during shearing (D) and before pressure cycling (E), as well as during the constant pressure phases during cyclic loading (F). In contrast, flow conditions were transient, k_{trans}, during the fracturing process (B) and during pore pressure ramping (F). These measurements were labelled as apparent permeability in the results, although they were calculated using equation (1). Comparing the minimum measurable permeability and the permeability after the hold phase, the fold

of increase in permeability, $k_{FOI} = k_{ss,hold}/10^{-18}$, was calculated to infer the permeability enhancement by fracturing.

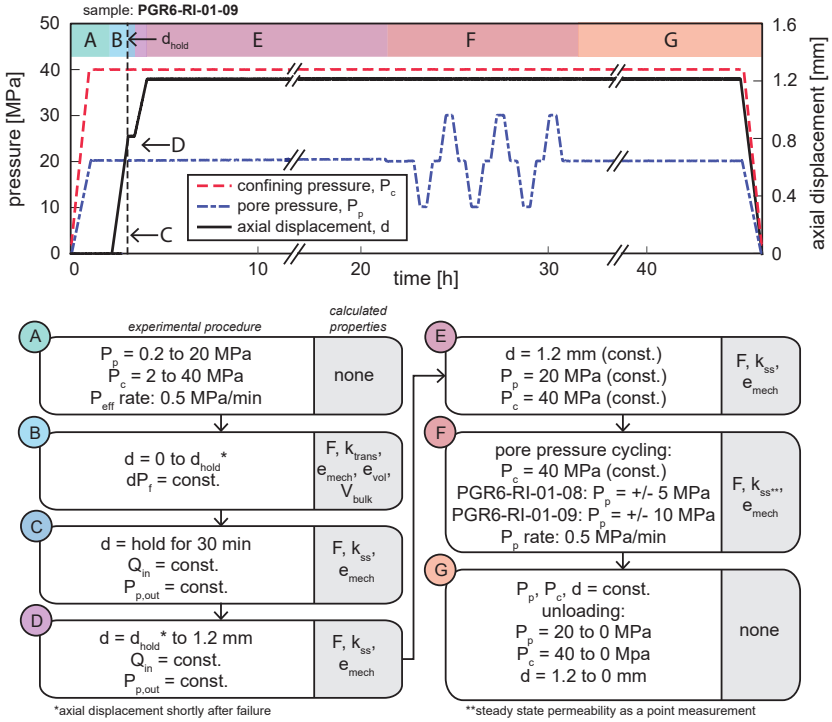

Figure 3.2: Experimental procedure and flow chart of the respective phases (A–G).

During the fracturing process, an elevated effective pressure state is desired, where Terzaghi's effective pressure (Terzaghi, 1925), P_e (equation 3.2), is defined as the confining pressure, P_c, minus fluid pressure, P_p. The pore fluid pressure was estimated by the outflow pressure, $P_{p,out}$, and the differential fluid pressure, $P_{p,in}$–$P_{p,out}$, divided by two (equation 3.3), assuming a linear pressure distribution (Hofmann et al., 2016, Milsch et al., 2016):

$$P_e = P_c - P_p \tag{3.2}$$

$$P_p = P_{p,out} + \frac{P_{p,in} - P_{p,out}}{2} \tag{3.3}$$

The change of volume of fluid in the sample, V_b (bulk volume) was determined according to equation 3.4 from the difference of cumulative inflow (V_{in}) and cumulative outflow volume (V_{out}) in ml:

$$V_b = V_{in} - V_{out} \tag{3.4}$$

After saturating the sample at 2 MPa confining pressure, the fluid pressure and confining pressure were simultaneously increased to 20 MPa and 40 MPa, respectively, within 1 h to an effective pressure of 20 MPa (figure 3.2, A). Afterwards, an axial displacement rate of 0.001 mm/s was applied to the top of sample (figure 3.2, B), which pushed the inner loading cylinder down relative to the guiding hollow cylinder until the point of failure. A drop in axial load, F, indicated the formation of a fracture. Up to this point, the inflow and outflow pressure were kept constant at a differential fluid pressure of 0.5 MPa. The fracture geometry was intended to initiate from the outer lower notch tip to the inner upper notch tip (Backers and Stephansson, 2012), resulting in an overall conical shape.

The mode II fracture toughness, K_{IIc}, or critical stress intensity factor, is a material parameter obtained by the PTS test, and depends on the type of rock material and its physical boundary conditions, such as confining pressure and temperature (Backers, 2004, Meier, 2009). The fracture toughness (K_{IIc}) was calculated at the point of failure by the following empirical relation (equation 3.5) based on the ISRM Suggested Methods (Backers and Stephansson, 2012):

$$K_{IIc} = 7.74 \cdot 10^2 F_{max} - 1.80 \cdot 10^3 P_e \cdot 10^3 \tag{3.5}$$

where F_{max} is the peak load in kN and P_e is the effective pressure in MPa. Using the circumferential extensometer, the mechanical fracture dilation (e_{mech}) can be calculated by converting the change in circumference (d_U) in mm to a change in radius:

$$e_{mech} = \frac{dU}{2\pi} \tag{3.6}$$

The fracture dilation is assumed to approximate the fracture aperture during the test. In addition, the changes in volume (equation 3.4) were used to calculate the volume balance-based dilation e_{vol}. This was only possible during phase B, since the change of cumulative fluid volume could be measured when a constant differential fluid pressure was applied. During fracture generation, additional void is generated. This is composed by the opening of the fracture itself, as well as the widening of the notches. The widening of the two notches is considered at the outer notch radius, r_{ON}. The additional volume can then be approximated as follows:

$$\Delta V_{notch} = \Delta e 2 r_{ON} \pi L_N \tag{3.7}$$

where r_{ON} is the radius to the outer notch, L_N is the total length of the upper and lower notch and e is the dilation with all units in m. The fracture has a shape of a truncated cone with a mantle surface area of $(r_{ON}+r_{ID})\pi L_{frac}$. Here, L_{frac} is the fracture length measured from the lower outer and top inner notch, r_{ID} is the inner radius and r_{ON} the radius to the

outer notch wall (figure 3.6c). The additional volume due to fracture generation can then be calculated as follows:

$$\Delta V_{frac} = \Delta e(r_{ON} + r_{ID})\pi L_{frac} \tag{3.8}$$

The total volume change measured $V_{measured} = V_{notch} + V_{frac}$, can be used to estimate the fracture dilation, e_{vol}:

$$e_{vol} = \frac{V_{bulk}}{2r_{ON}\pi L_N + (r_{ON} + r_{ID})\pi L_{frac}} \tag{3.9}$$

After failure, the axial displacement ramp was stopped (hold phase) and the constant pressure boundaries for the fluid flow were changed to a constant inflow rate and a constant downstream pressure until a constant differential pressure of at least 0.1 MPa was reached and permeability was measured (figure 3.2, C). After that, the axial displacement was again increased at a slower rate of 0.0001 mm/s leading to an increase in shear displacement until a maximum of around 1.2 mm was reached (figure 3.2, D). Finally, the axial displacement of the loading cylinder at the top was maintained to measure changes in stress and was kept in this position for at least 16 h (figure 3.2, E).

After that, the effective pressure was varied cyclically by changing the mean fluid pressure in the sample by ± 5 or ± 10 MPa (figure 3.2, F). A constant ramp operation of fluid pressure (0.5 MPa/min) was applied to the outflow side of the sample with the inflow pressure following the given ambient pressure change without active operation. Steady state flow conditions were achieved when the inflow and outflow pressure and rates reached a constant value, which took about 10 min considering a hydraulic diffusivity of about $4.5{\cdot}10^{-6}$ m^2/s for a length of 0.05 m calculated according to Nicolas et al. (2020) For the diffusivity we used a conservative matrix permeability of $1{\cdot}10^{-19}$ m^2, Biot and Skempton coefficients of 0.4 and 0.6 and a bulk compressibility of 30 GPa reported for granite (Tan et al., 2014). During pressure cycling, the vertical load, F, was transformed into shear stress (Backers and Stephansson, 2012), τ using equation 3.10:

$$\tau = \frac{F}{\pi r_{ID} L_{frac}} \tag{3.10}$$

where r_{ID} is the inner diameter in m and L_{frac} is the fracture length in m. This equation assumes and simplifies that the fracture to be a single plane. The fracture stiffness describes the fracture closure behaviour under increasing effective normal pressure. For a semi-logarithmic closure law (Barton et al., 1985) only one free parameter, the fracture stiffness characteristic, χ, is required and was obtained from the slope of the effective normal pressure versus fracture aperture change (Crawford et al., 2017, Zangerl et al., 2008) following equation 3.11:

$$\ln P_e = \chi \Delta e_{mech} + \ln \sigma_n^{ref} \tag{3.11}$$

P_e is the normal effective pressure in MPa, χ, the fracture stiffness characteristic in mm^1, Δe_{mech} is the change in mechanical dilation in mm and σ_{ref} n is any arbitrary reference value of normal stress in MPa. After effective pressure cycling was finished, the testing conditions were kept constant for another 12 h, until the axial displacement, fluid and confining pressure were decreased simultaneously at similar rates as at the loading stage (figure 3.2, G).

3.4. EXPERIMENTAL RESULTS

In the following, the process of microfault generation and propagation is described and the results for permeability evolution, flow rate changes, fracture dilation and volume balance during loading are given (figures 3.3 to 3.5). The evolution of shear stress, dilation, permeability and fracture stiffness for cyclic effective pressure loading are also presented (figures 3.7 to 3.9). Furthermore, the fracture geometry is described using the computed x-ray CT imaging (figure 3.10). The overall results are summarized in table 3.3.

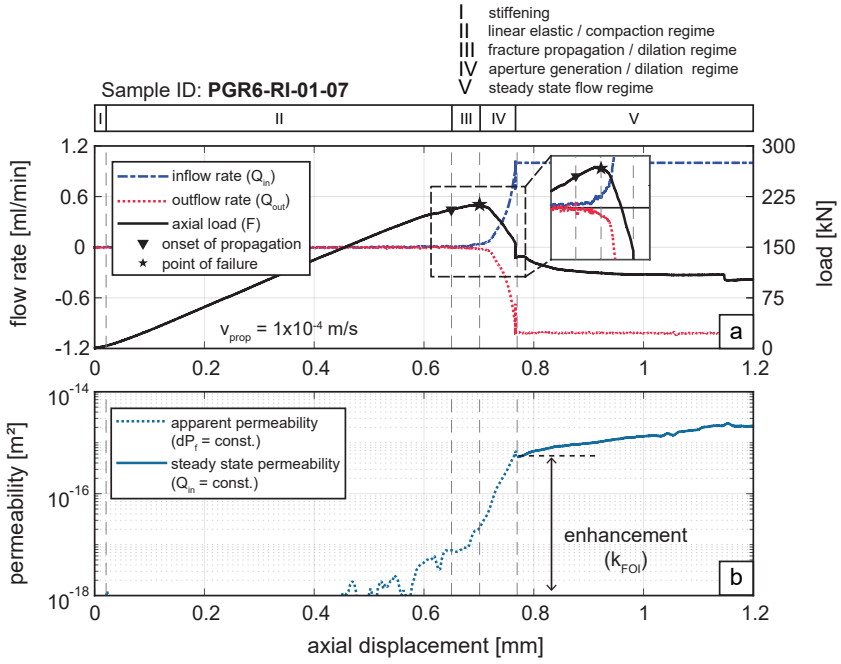

Figure 3.3: The change in inflow and outflow rate and axial load vs. the axial displaced (a) and sample permeability during fracturing and shearing (b).

3.4.1. FRACTURE GENERATION

The loading and failure process can be subdivided into five regimes with different dominant processes (figures 3.3 to 3.5). The stages of fracture initiation and propagation are illustrated in figure 3.6.

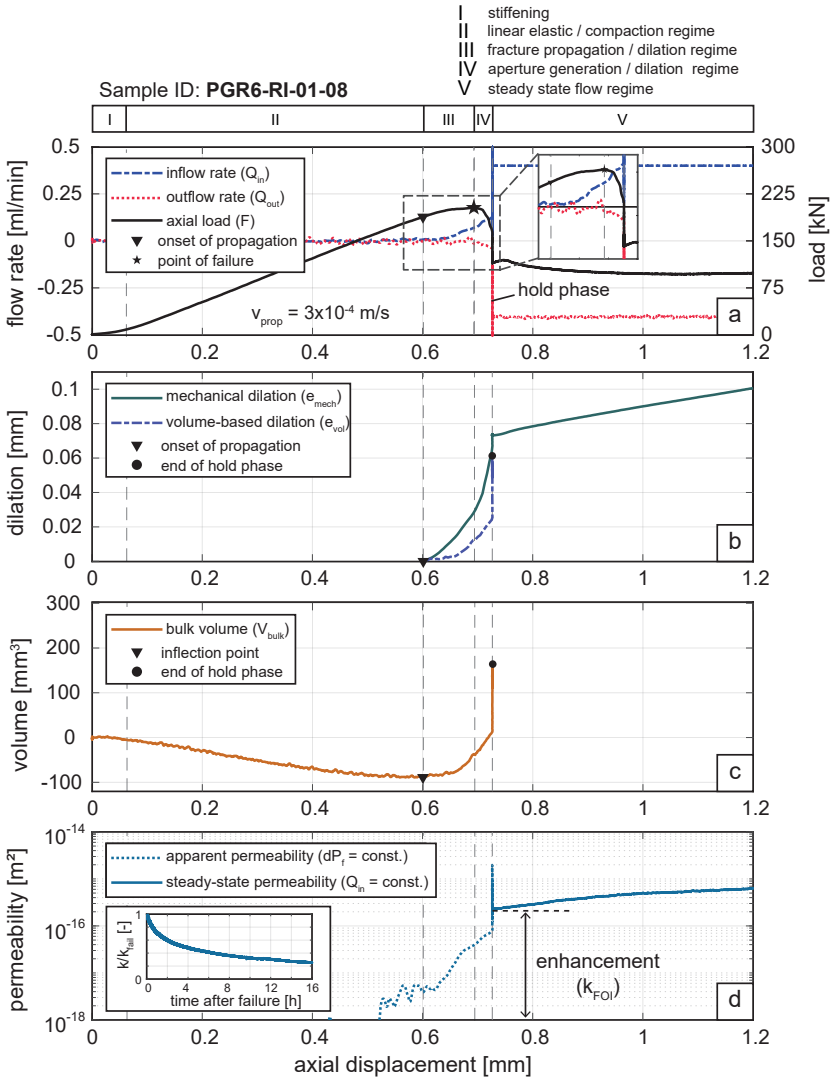

Figure 3.4: The change in inflow and outflow rate and axial load vs. the axial displaced (a), mechanical and volume-based aperture (b), fracture volume (c) and sample permeability (d).

During stiffening and compaction at the first stage of loading, the volume of the sample was reduced and water was squeezed out of the sample. Between 0.60 to 0.65 mm of

axial displacement, the inflow rate started to increase, the load curve flattened and the volume balance reached an inflection point (figures 3.3a, b; 3.4a, b, c and 3.5a, b, c). At this point, fracture initiation took place from the bottom of the sample, indicated by an increased inflow rate and a imbalance between in- and outflow, leading to dilation and a consequent increase of fracture volume of the sample (figure 3.6). Using equations 3.6 and 3.9, the mechanical fracture dilation and the volume balance-based dilation was calculated, respectively, since it was assumed that a fracture is introduced into the sample. The mechanical dilation, which represents the change in mechanical aperture, increased faster than the volume-based dilation, since it took longer for the pore fluid to progress through the sample and the circumferential strain was only measured at the centre of the intact portion.

At the point of failure, the axial load reached values of about 212, 203 and 197 kN which is equal to 424, 406 and 394 MPa axial stress, which corresponds to 384, 366 and 354 MPa differential stress for sample PGR6-RI-01-07, PGR6-RI-01-08 and PGR6-RI-01-09, respectively. The load then dropped and the increase in outflow rate indicated a hydraulic short-cut between the lower and upper notch, suggesting a fully developed fracture system. Calculating the mean fracture propagation velocity, v_{prop}, which is simply the length of the fracture, L_{frac}, over the time span of fracture initiation to the point of failure, t_{prop}, the velocity was in the range of 0.1 to 0.3 mm/s ($v_{prop} = L_{frac}/t_{prop}$). After failure, at a displacement of about 0.7 to 0.8 mm, the inner cylinder was punched down and most of the aperture was created, indicated by a rapid increase in mechanical and volume-based dilation. The measured load was now controlled by the frictional properties of the fracture. Shortly after the point of failure the displacement was put on hold for about 30 min (hold phase) such that the fluid pressure field could reach steady state flow conditions. The final value for dilation and fracture volume were reached during the hold phase when fluid pressure diffusion was finished. After restarting the displacement up to a maximum of 1.2 mm all samples showed no drop or rapid increase in axial load, i.e. no "stick slip" behaviour, but rather approached a limiting value of about 75 and 100 kN. This behaviour of fracture generation and propagation was similar in all three experiments. The fracture toughness values (equation 3.5) for the saturated granite samples ranged between 15.3 and 16.4 MPa·m$^{0.5}$ (table 3.3).

Table 3.3: Experimental results.

sample ID	P_e [MPa]	v_{prop} [mm/s]	K_{IIc} [MPa·m$^{0.5}$]	k_{FOI} [-]	e_{mech} [mm]
PGR6-RI-01-07	20	0.1	16.42	520	-
PGR6-RI-01-08	20	0.3	15.71	230	0.07 (0.09 – 0.1)*
PGR6-RI-01-09	20	0.3	15.34	230	0.08 (0.07 – 0.1)*

*during pore pressure cycles, P_e: effective pressure, v_{prop}: fracture propagation velocity, K_{IIc}: mode II fracture toughness, k_{FOI}: permeability fold of increase, e_{mech}: mechanical dilation after failure.

3.4.2. PERMEABILITY & DILATION EVOLUTION DURING FAILURE

During all tests, the permeability was measured simultaneously during loading and failure. The flow conditions during failure were regarded as transient (apparent permeability, k_{trans}), but steady state after the hold phase (steady-state permeability, k_{ss}). The perme-

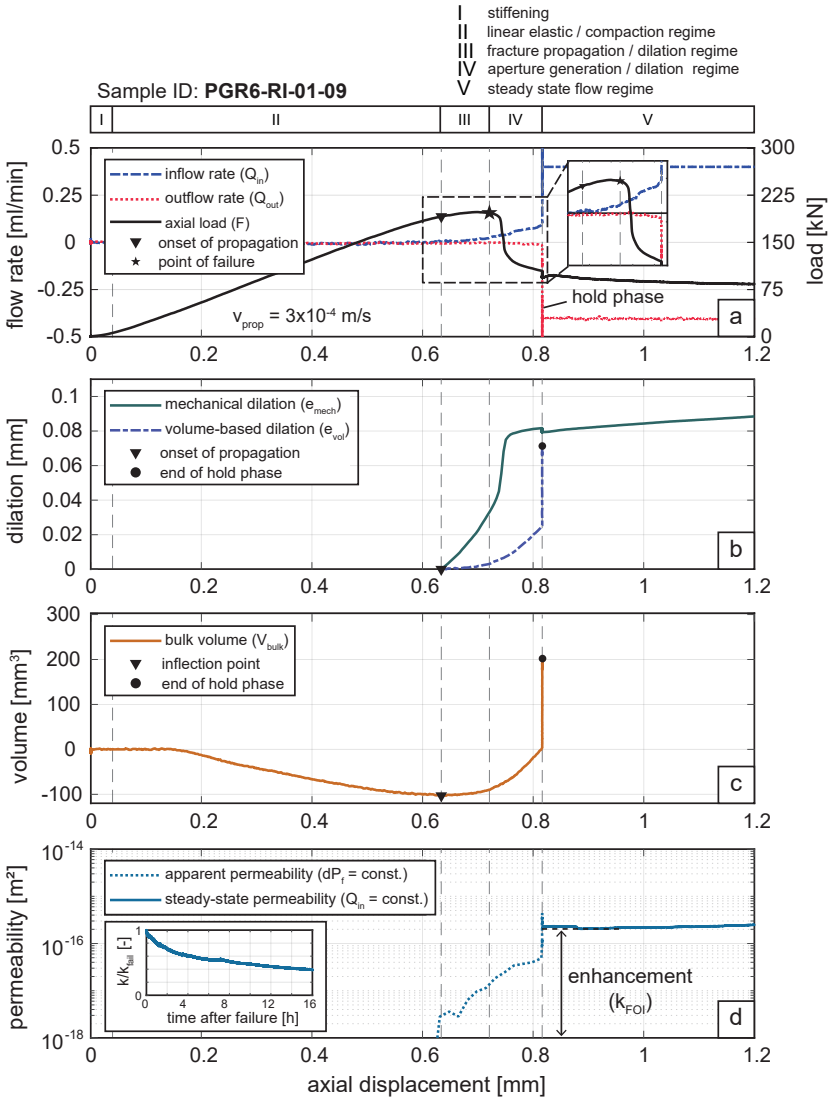

Figure 3.5: The change in inflow and outflow rate and axial load vs. the axial displaced (a), mechanical and volume-based aperture (b), fracture volume (c), sample permeability (d).

ability evolution during fracture generation is shown in figures 3.3b, 3.4d and 3.5d, where all experiments showed a pre-failure increase in apparent permeability of half to almost one order of magnitude, coinciding roughly with the inflection point of the volume balance as well as with the onset of yielding. For all granite samples, the increase in permeability was about 2 to almost 3 orders of magnitude at an effective pressure of 20 MPa (P_c = 40 MPa, P_p = 20 MPa), comparing the pre-failure permeability and the permeability

during the hold phase (k_{FOI}, table 3.3). As explained before, the main dilation and consequent permeability was generated after the point of failure, with values of 0.06 to 0.07 mm (PGR6-RI-01-08) and 0.07 to 0.08 mm (PGR6-RI-01-09), while mechanical dilation and volume-based dilation were in very good agreement, suggesting that the measured dilation corresponds to the mechanical aperture. After the hold phase, the microfault was displaced up to 1.2 mm, resulting in a gentle increase in mechanical dilation to about 0.1 mm for sample PGR6-RI-01-08 and 0.09 mm in sample PGR6-RI-01-09, while permeability was consequently relatively constant. The maximum additional increase was between a factor of 4.0 for sample PGR6-RI-01-07 and 1.1 for sample PGR6-RI-01-09. No additional fracturing was inferred from the mechanical-hydraulic and electrical data (PGR6-RI-01-07) during this period. Permeability decay curves measured for about 16 h were similar for two granite samples at 20 MPa effective pressure and showed a reduction by a factor of 2.5 to 4 (inset figures 3.4d and 3.5d).

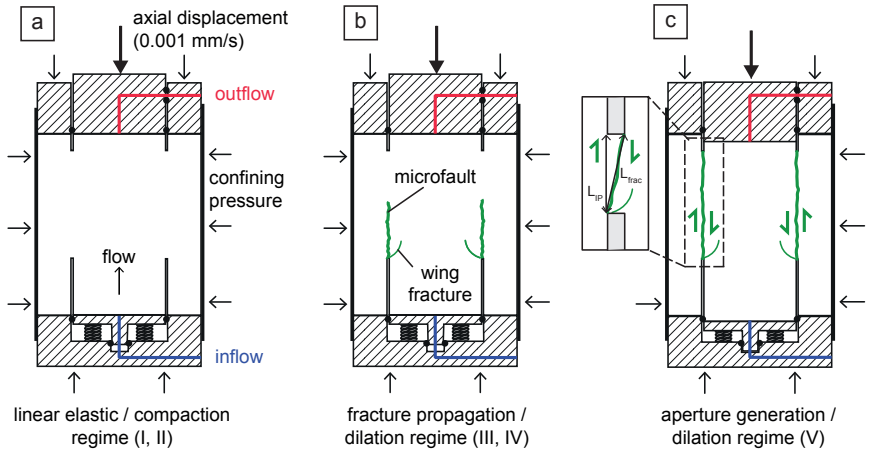

Figure 3.6: Illustration of the fracture propagation process during the different stages: a) linear elastic phase, b) fracture propagation, c) shear displacement along a principal shear plane.

3.4.3. PERMEABILITY EVOLUTION DURING PORE PRESSURE CYCLING

To simulate reservoir operation procedures, such as injection or production, the pore pressure was cycled in two samples in order to monitor possible changes in shear stress due to slipping of the fault, permeability and strain at varying effective pressure (figures 3.7 and 3.8). The starting pore pressure of 20 MPa was varied by ± 5 MPa (PGR6-RI-01-08) and ± 10 MPa (PGR6-RI-01-09), corresponding to a change of around 500 to 1000 m in the water column in a geothermal well. In total, six cycles of pore pressure increase and decrease were performed for each experiment.

The permeability was reduced when the pore pressure was reduced increasing pore pressure (effective pressure decrease). The total variations in permeability for the pressure changes of ± 5 MPa (PGR6-RI-01-08, figure 3.7b) ranged from $8.53 \cdot 10^{-17}$ m^2 to $2.57 \cdot 10^{-16}$ m^2,

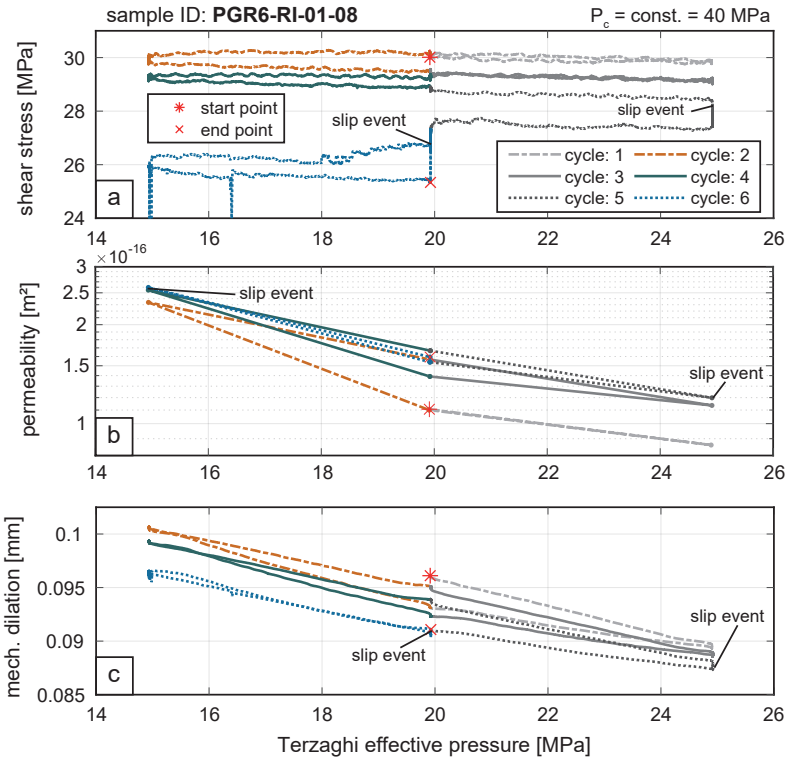

Figure 3.7: Shear stress (a), permeability (b) and mechanical aperture (c) evolution during effective pressure changes of 5 MPa (sample PGR6-RI-01-08).

while permeability varied from $3.84 \cdot 10^{-16}$ m^2 to $6.0 \cdot 10^{-17}$ m^2 for pressure variations of ± 10 MPa (PGR6-RI-01-09, figure 3.8b). Permeability was slightly increased from $1.10 \cdot 10^{-16}$ m^2 to $1.58 \cdot 10^{-16}$ m^2 after six pressure cycles for the variations of 5 MPa (PGR6-RI-01-08). Similar, a minor permanent increase from $8.65 \cdot 10^{-17}$ m^2 to $1.17 \cdot 10^{-16}$ m^2 was observed for the effective pressure variations of 10 MPa (PGR6-RI-01-09). Comparing the mechanical dilation evolution (figures 3.7c and 3.8c), both samples showed a similar behaviour, which is opening during the pore pressure increase (effective pressure decrease) and closure during the pore pressure decrease (effective pressure increase). Doubling the pore pressure change led to a doubling in magnitude of the dilation change.

During the pore pressure changes, the load cylinder was maintained at a constant vertical position after the maximum displacement was reached. This way, the shear stress evolution was obtained from the measured vertical load (equation 3.10, figures 3.7a and 3.8a). When the pore pressure is varied, the effective normal stress is also changed, which can lead to slip events when a failure criterion is exceeded, resulting in a change in shear stress. For the 5 MPa effective pressure variation, a reduction in shear stress ("slip event") was observed in the 5th and 6th cycle, reducing the shear stress by about 5 MPa. For the 10 MPa effective

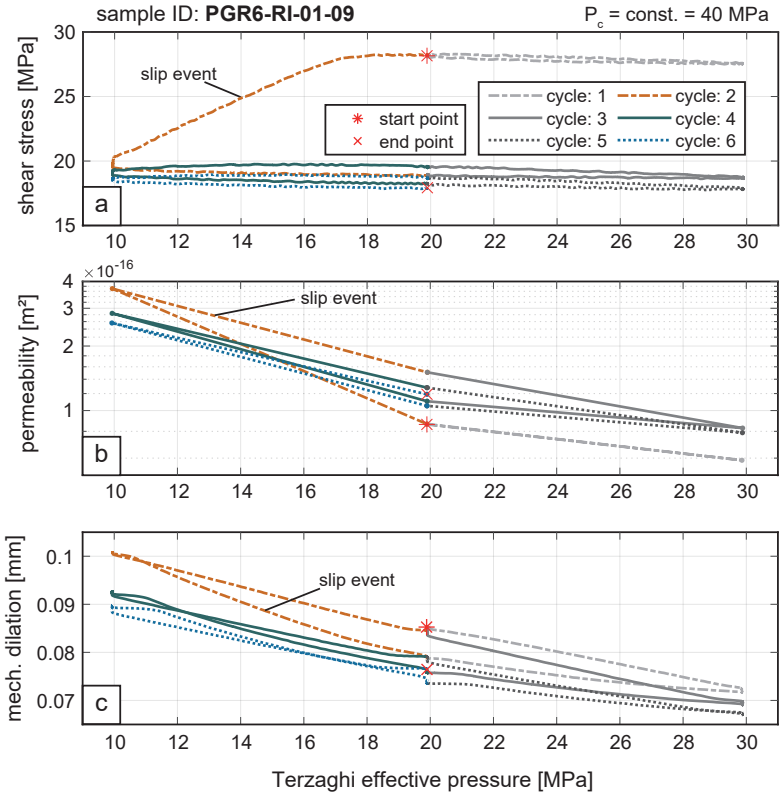

Figure 3.8: Shear stress (a), permeability (b) and mechanical aperture (c) evolution during effective pressure changes of 10 MPa (sample PGR6-RI-01-09).

pressure variation the decrease in shear stress occurred in the 2nd cycle already with a larger magnitude of reduction of about 10 MPa. The vertical stress in the system could only be released towards the bottom of the sample, where the core of the sample was mounted on springs (top load piston was fixed). Since the dilation change suggested only small changes in lateral direction (figures 3.7c and 3.8c), we assume that this stress release resulted in a downward movement of the inner cylinder, such as a "slip event", i.e. a small vertical displacement along the microfault. The friction coefficient could not be calculated since the normal stress was possibly disturbed by the sample and fracture geometry and needed to be determined numerically. The slip events resulted in a small reduction of permeability for a change of 5 MPa in pore pressure, accompanied by further fracture closure. Conversely, the slip event for the 10 MPa pore pressure change resulted in a slight increase in permeability and a dilation increase. However, the mechanical dilation was only measured at the centre of the intact portion (L_{IP}), such that opening or closing during slip depends on the orientation of the fracture at this location.

The fracture stiffness, χ, was obtained at each loading cycle during pore pressure reduction

(equation 3.11). It was observed that the fracture stiffness increases with each loading cycle and that fractures stiffness was higher when the initial effective pressure level was higher (figure 3.9), while the permeability was not significantly changing with an increasing number of pressure cycles. Generally, the permeability changes and fracture stiffness suggested a mechanically and hydraulically sustainable fracture.

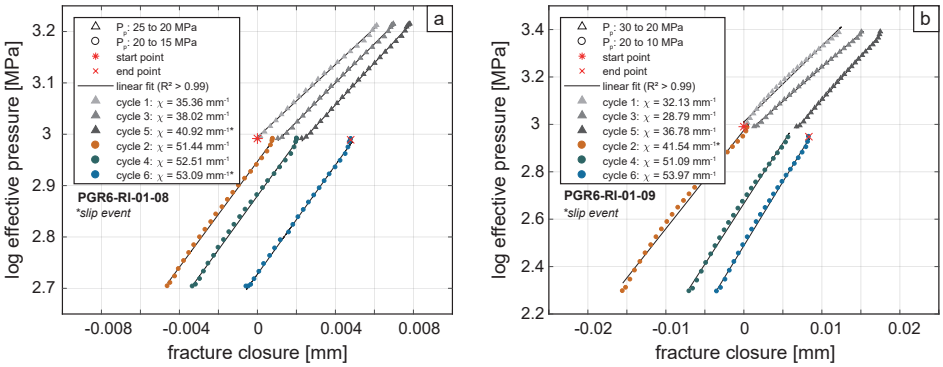

Figure 3.9: Relative fracture closure vs. the logarithmic effective pressure change during the six effective pressure cycles (only pore pressure reduction) for sample PGR6-RI-01-08 (a) and sample PGR6-RI-01-09 (b).

3.4.4. FRACTURE GEOMETRY FROM X-RAY μ-CT SCAN ANALYSIS

Computed x-ray CT scanning was performed using the entire sample after testing to visualize the deformation within the sample. We used a nanotom™ ultra-high resolution nanoCT system with a 360° scanning projection, providing a resolution for our sample size (50 by 50 mm) of about 25 μm. Computed x-ray CT scanning images of the microfaults in samples PRG6-RI-01-08 and PGR6-RI-01-09 revealed a complex microfault zone connecting the upper and lower notch of the sample (figure 3.10). The major fault zone was characterised by step-over structures, clearly displaced fracture faces with a visible self-propping effect, fracture branching, as well as particles or breccia distributed across the shear zone. Radial fractures and horizontal fractures were secondary features that formed during the unloading to atmospheric pressure at the end of the test and therefore do not contribute to permeability. They usually terminate against fracture branches of the central shear zone and are found in areas where the two fracture faces are in contact, thus minimising permeability.

True apertures were measured at defined distances of about 0.5 to 0.8 mm along the fracture in x-y oriented cross sections at different height levels (21 levels with about 2300 measured apertures, N, for each sample) between the bottom and top notch (figure 3.10). Closed sections (apertures smaller 0.01 mm), as well as open sections were measured in order to obtain a contact-area ratio, R_c, which was defined as the amount of contact points (zero aperture) over the total number of measurements, N. Based on the aperture distribution, mean aperture, contact area ratio and the structural features of specific areas along the vertical fracture, three specific zones were identified (zone I, II and III).

For sample PGR6-RI-01-08, zone I showed mostly apertures between 0.05 and 0.2 mm with mean apertures indicated in figure 3.10. The top part of the fracture was highly damaged and crushed. Below, a zone of transpressional features was visible with a mean aperture of 0.087 and a contact area ratio of 20 % indicated as zone I. Zone II was characterised by almost vertically oriented fractures (simple shear zone) showing the highest contact area ratio of about 34 % and a mean aperture of 0.089 mm. The largest zone was zone III characterised by an inclined fracture orientation and consequent transtension showing a highest mean aperture of 0.17 mm and a contact-area ratio of 31 %.

Sample PGR6-RI-01-09 showed a similar distribution of zone I (transpression), zone II (simple shear) and zone III (transtension). However, the mean apertures were overall higher (0.175 mm), with zone II showing the smallest mean aperture of 0.110 mm and highest contact area-ratio of 41 %. Furthermore, zone II was largest, meaning that the largest portion of the fracture was oriented vertically with simple shear features, and only small portions at the bottom show transtensional features.

Comparing samples PGR6-RI-01-08 and PGR6-RI-01-09, the latter had an overall lower mean aperture and higher contact-area ratio with the largest portion showing simple shearing, while the other had a larger zone of transtension with overall higher mean apertures and smaller contact area ratios. For both, shear zones cutting through feldspar minerals resulted in apertures of mostly zero while the largest open zones were found in quartz dominated areas. Fracture breccias or other fine and detached particles were found in every sample. The fact that they were located mostly in the bottom part of the fracture at the inflow zone indicates, that the particles were distributed and transported along the fracture, causing a further reduction in permeability.

Comparing the mechanical dilation (equation 3.6) and volume-based dilation (equation 3.9) with the aperture measured from the x-ray CT scan images, the post-testing CT images gave the largest mean aperture ranging from 0.09 to 0.18 mm while the mechanical dilation measured in-situ with extensometers gave 0.08 to 0.1 mm after failure.

3.5. DISCUSSION

3.5.1. MICROFAULT GENERATION

Shear fracture geometries generated in conventional fracture permeability experiments sometimes do not represent the complex geometry of single fault zone on a laboratory scale. In this section, the fracture properties, the fracture geometry regarding structural features, as well as implications of the aperture distribution for the overall permeability and strength, obtained by the PTS test, will be discussed.

Our results suggest a sufficient reproducibility for this testing procedure in terms of mode II fracture toughness, yield point, as well as permeability and dilation evolution. Monitoring the changes in inflow and outflow volume of the pore fluid during failure allows for a good control of the fracturing process and reveals similar processes as described by Backers (2004), where the fracture initiated from the outer bottom notch and propagated towards the inner top notch. However, it is not clear from the experiments whether wing fractures,

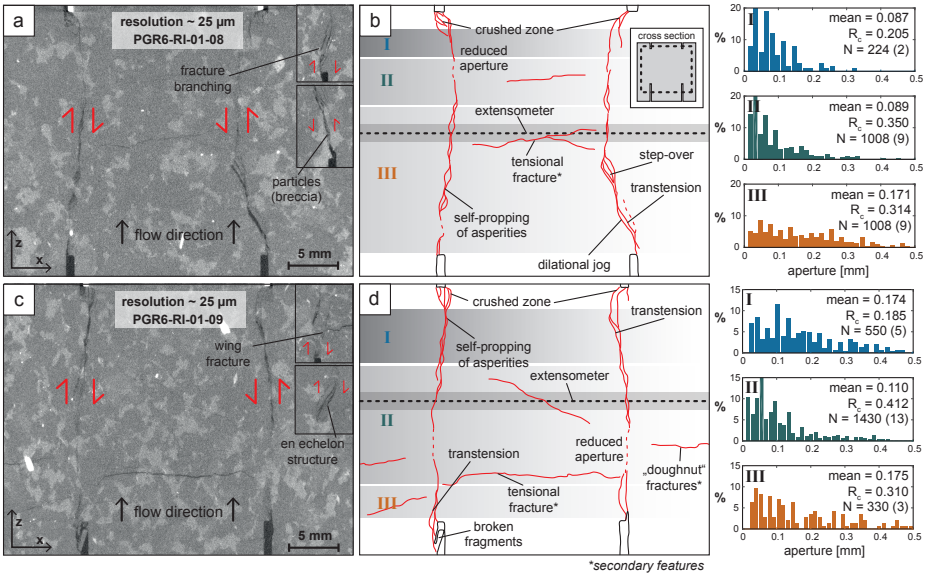

Figure 3.10: Computed x-ray CT images and the reconstruction of the fracture system of sample PGR6-RI-01-08 (a, b) and sample PGR6-RI-01-09 (c, d).

as described by Backers (2004), cause the initial increase in inflow rate and that the actual shear fracture might form later and more rapidly at the point of failure. The fracture toughness values of about 15.3 to 16.4 MPa·m$^{0.5}$ were slightly higher compared to other granites, for example Ävrö, Aue or Mizunami granite with values between 10.9 to 11.5 MPa·m$^{0.5}$, tested under dry conditions (Backers and Stephansson, 2012). While these experiments were performed at non-hydrostatic conditions, our experiments were performed with a confining stress acting on the top and bottom annulus of the sample. Furthermore, we were able to produce a single fracture at high effective pressures, which has been proven to be difficult in the past when applying mode II loading conditions in, for example, shear-box experiments (Watanabe et al., 2009).

We favour the term "microfault" for the structures produced in our experiments, although (Crider, 2015) suggested differentiating between shear fractures (experimentally produced) and faults (field structures). The reason is, that most of the existing experimental studies applied the term "shear fracture" to describe tensile fractures with offset, which is not adequate. Although there is a discussion about whether fracture initiation in PTS experiments is in shear mode (Wu et al., 2017), the ongoing displacement of up to 1.2 mm clearly generated a principle shear plane with common features found in larger scale faults (Faulkner et al., 2010, Peacock et al., 2016). The microfault geometry of the PTS test is rather complex and can be subdivided into three domains that are also found in natural fault systems: transpression, simple shear zones, transtension (Dewey et al., 1998, Jones and Tanner, 1995). The location of these systems along the fracture are assumed to control local permeability variation and depend on the fracture orientation, as well as on the degree

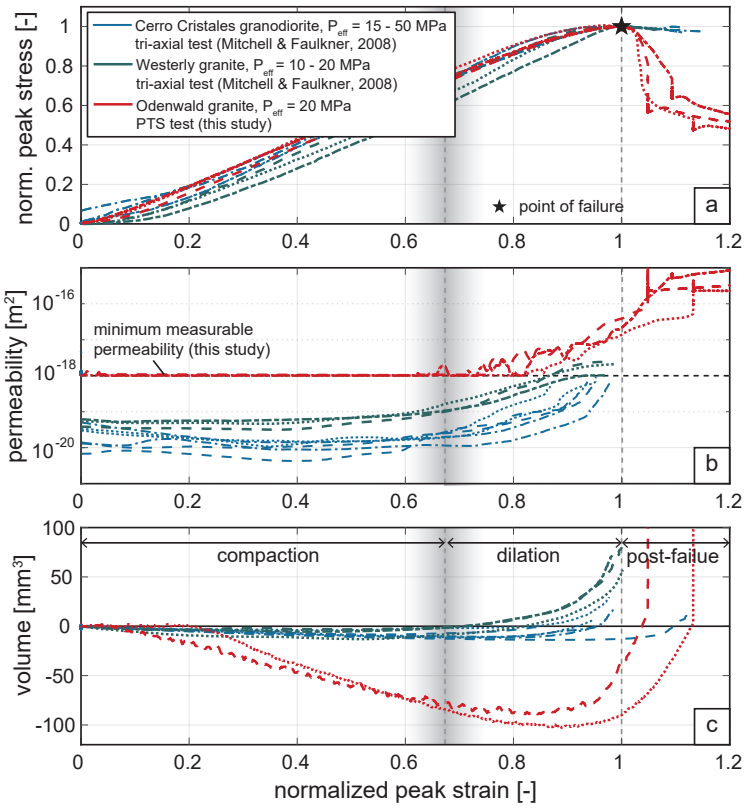

Figure 3.11: Normalized stress-strain curves (a), permeability evolution (b) and volume changes (c) during failure for the Odenwald granite and the experiments with granite and granodiorite by Mitchell & Faulkner.20

of bending of the fault zone between top and bottom notch, and can also occur very locally. Transpression occurred mostly at the top of the sample, while transtension was found in the middle and lower section of the fracture zone. The fault zone structure is highly dependent on the stress and displacement magnitude, protolith and fluid flow (Faulkner et al., 2010). A fine grained fault core (zone of reduced aperture), a fracture dominated damage zone and damage of linking damage structures (Faulkner et al., 2010) or “dilational jogs” (Peacock et al., 2016) were found in both our samples (figure 3.10). Detailed thin section analysis and a comparison with other rock types might provide more insights into the development of a fault zone, microfracture density or fault zone dimensions using the PTS test, to be able to compare this to general shear zone developments (Cho et al., 2008). In addition, the permeability can be adequately quantified due to the flow parallel orientation of fracture, meaning that compared to conventional tri-axial testing geometries, the fluid is not required to flow through a matrix before entering the fracture. Computed x-ray CT images also did show additional fractures such as radial fractures present in the matrix (figure 3.10). Due to the displacement and the interlocking of asperities the inner cylinder was pushing against

the outer cylinder, which resulted in brittle radial fracturing exclusively during unloading to atmospheric pressure at the end of the experiment (secondary feature). There was no indication of radial fracturing during displacement or pore pressure cycling since they would result in a larger permeability increase. Monitoring the electric conductivity of a silver paste applied to the circumference of the sample suggests an intact sample wall during fracture generation. To reduce the possibility of radial fracture generation, we recommend to increase the diameter of the sample while keeping the diameter of the notches. Furthermore, the top of the inner diameter needs support (steel ring) for hydrostatic pressure conditions, as hydrostatic conditions reduce the difference of compressional and tensile forces at the bottom notch, which are required to initiate shear fracture growth (Backers, 2004). This possibly also explains the slightly higher load, or more precise, higher fracture toughness values, required for fracture generation.

3.5.2. PERMEABILITY & DILATION DURING FRACTURING & SHEARING

Quantifying and understanding the physical properties and processes that control the hydraulic-mechanical properties of fractured rocks are crucial for any engineering application in the subsurface. Experimental data of the generation and displacement of a single shear fracture zone under in-situ reservoir and fracture parallel flow conditions while measuring permeability are limited in the present literature. In the following, we will discuss our results of the permeability of microfaults framed in the context of existing approaches and outcomes in existing literature (figure 3.11).

In order to compare the measured permeability pre-, during and post-failure, the measured value should represent a pseudo steady-state value. To ensure these conditions we calculated the hydraulic diffusivity and the additional fluxes caused by the fracture formation. The diffusivity of $4.5 \cdot 10^{-6}$ m^2/s was calculated according to Nicolas et al. (2020), resulting in a pore pressure diffusion to take less than 10 min. Furthermore, the generated fracture volume was measured to be maximum 0.2 ml within 90 min, while the applied flow rates varied between 0.4 ml/min and 1 ml/min. We concluded that both effects could be neglected for the permeability evolution during shearing, but consider the permeability during fracturing as transient.

Our results show that the magnitude of permeability enhancement is about 2 to almost 3 orders of magnitude, from less than 10^{19} m^2 to more than 10^{16} m^2 for a medium grained fresh granite such as the Odenwald granite with a sample diameter of 50 mm. This is more than the 17 to 35 times permeability increase reported by Ye and Ghassemi (2018a) on Sierra White Granite for their double flawed samples with a complex shear zone. However, it is similar to the experiments on Westerly granite and Cerro Cristales granodiorite by Mitchell and Faulkner (2008) (figure 3.11b) using the pore pressure oscillation technique in conventional tri-axial testing at effective pressures of 10 to 50 MPa. Similar to their study, we assume that the damage in the surrounding rock matrix is negligible and that permeability is exclusively controlled by the generated microfault. The fracture volume evolution in the experiments by Mitchell and Faulkner (2008) shows a similar inflection at about 70 to 90 % of the peak stress, although permeability increases already at lower strain, i.e. at about 60 % of peak strain. The differences in fracture volume (figure 3.11c)

arise from the sample and fracture geometry, or more precise, the fact that pore fluid can hardly travel through the rock matrix at the bottom and top of the sample in a tri-axial test, while there is an instant hydraulic connection and flow-parallel conditions in the PTS test. Generally, both results demonstrate that measuring permeability over more than three orders of magnitude experimentally during fracture initiation and propagation remains technically difficult. Still, similar to the experiments by Paola et al. (2009) show, the permeability evolution can be subdivided into three stages: compaction, dilation and post-failure, with the transition from compaction to dilation between 60 to 80 % of peak strain. Assuming that Mitchell and Faulkner (2008) rather measured pre-failure permeability evolution and that our results show the permeability increase during failure and at post-failure state, the total increase by brittle faulting can exceed 3 orders of magnitude (figure 3.10).

The bulk permeability of a fault is controlled by the size of the fault zone and the aperture resulting from shear dilation. The mechanical and volume based dilation, as well as fracture volume, are commonly used to determine the aperture changes in fractures due to changes in load (Hofmann et al., 2016), but present only bulk measurements for certain locations along the fracture. The x-ray CT images (figure 3.11) showed that local permeability is controlled by the distribution of aperture, which is again controlled by the fracture geometry and grain size. Similar to the study by (Frash et al., 2019), aperture and therefore permeability are highly controlled by the presence of en-echelon or step-over structures, as well as fault particle transportation along the fault. Experimental studies with planar structures might simplify the processes involved (Im et al., 2018, Rutter and Mecklenburgh, 2017, Sheng et al., 2018), but do not reflect the evolution of permeability in active faults.

We demonstrated the ability to shear a fracture at an effective pressure of 20 MPa using the PTS test. Permeability increased by a factor of 1.1 to 4.0 by shearing under in-situ conditions right after producing the shear zone. Such an increase is comparable to experiments with sheared tensile fractures in other studies (Lee and Cho, 2002, Zhang et al., 2019). A high dependence on the grain size is involved in the mechanical processes during shearing of a microfault, due to the sample size on a laboratory scale. The applied displacement did not exceed the grain size of the material and therefore no stick-slip behaviour, commonly observed in large scale fault mechanisms, was observed in our experiments. The realistic microfault geometry causes a heterogeneous aperture distribution, which highlights the importance of structural features, such as en-echelon or step-over structures, in faults during the displacement. We therefore also support the assumption that local pressure gradients play an critical role in controlling local permeability perturbations, when fluid is directly injected into a fault zone (Passelègue et al., 2018), as well as when fluid is injected in an adjacent well.

3.5.3. SUSTAINABILITY OF PERMEABILITY

The sustainability of the permeability of fault structures, in other words, the resistance of a fracture towards closing caused by pressure changes, is crucial for several underground applications. In the following chapter, we will discuss our results of longevity for microfault permeability and compare those with data from tensile and displaced tensile fractures published in literature (figures 3.12a, b).

Fault compaction due to elevated normal stress can significantly reduce the permeability of a microfault. Because of the relatively short testing period, we assume that no chemical rock-fluid interactions impact the hydraulic properties of the fracture. However, we could not consider possible particle redistribution affecting permeability. We therefore recommend to analyse the effluent in future studies. The observed reduction in permeability over time after shear fracture formation by a factor of 2.5 to 4 might be related to three possible mechanisms: (a) chemical rock-fluid interactions, i.e. dissolution or precipitation of minerals, (b) fines migration leading to a blockage of fluid pathways within the fault, and (c) mechanical creep, i.e. compaction or rearrangement of fault gouge particles. Mechanical back-slip is not possible, since the axial displacement piston was held in place after reaching a maximum of 1.2 mm.

Rock-fluid interactions, re-crystallizations or cementations are unlikely to influence permeability in our short-term experiments (several hours). Such processes evolve over long time-scales of several weeks (Yasuhara and Elsworth, 2008) and require saline solution as the pore fluid while we used distilled water, such it is unlikely that this impacted permeability. For longer term experiments, such processes should be considered to impact fault permeability. Possible fines migration cannot be assessed in this study since it requires a microstructural analysis of the microfault. Comparing our data to literature data, the permeability decay curves over time are similar to those in literature (Hofmann et al., 2016, Im et al., 2018) for exponential or power law decay, although the normal effective stress range conditions (from 3 to 60 MPa) and fracture type (smooth saw-cut or displaced tensile type) differ to our study (figure 3.12a). Other authors suggest a linear decay (Caulk et al., 2016) of permeability over several days, which did not fit our data. This might be caused by an insufficient resolution of permeability of the first 24 h in these tests. The main factor controlling the permeability decay cannot be explained by the data we obtained, but permeability losses up to one order of magnitude are possible within the first 16 h.

Considering pore pressure changes of ± 5 MPa to ± 10 MPa that simulate injection and production procedures in geothermal systems, permeability increased with decreasing effective pressure and decreased by less than one order of magnitude. This process was rather reversible.

In figure 3.12b we compared our permeability during the effective pressure loading to fracture permeability data from literature for displaced and non-displaced tensile fractures. To be able to compare our sample permeability data, we need to calculate the fracture permeability, k_f, assuming that the permeability relates to the area of flow following Hofmann et al. (2016):

$$A_s k_s = A_m k_m + A_f k_f \tag{3.12}$$

where k is permeability, A is area of flow and the subscripts s, m, f relate to sample, matrix and fracture, respectively. The area of the sample is approximated by $A_s = \pi r^2$ and the fracture area is calculated from the circumference of the fracture multiplied by the aperture $A_f = a_h \pi (2r_{ID})2$, with $2r_{ID} = r$. If we now assume that the matrix permeability of the granite is negligible ($k_m = 0$), we can rearrange equation 3.12 for the fracture permeability,

which is given by the cubic law ($k_f = a^2/12$):

$$\frac{a^2}{12} = \frac{k_s \pi r^2}{r \pi a_h} \tag{3.13}$$

This provides an equation for the hydraulic aperture similar to Hofmann et al. (2016), but for a circular fracture:

$$a_h = \sqrt[3]{12 k_s r} \tag{3.14}$$

Inserting the hydraulic aperture, a_h, into the cubic law we obtain the fracture permeability ($k_f = a^2/12$), that we can now compare to the fracture permeability from the literature. The permeability reference value for normalisation at 10 MPa for our data is $1.97 \cdot 10^{-12}$ m^2.

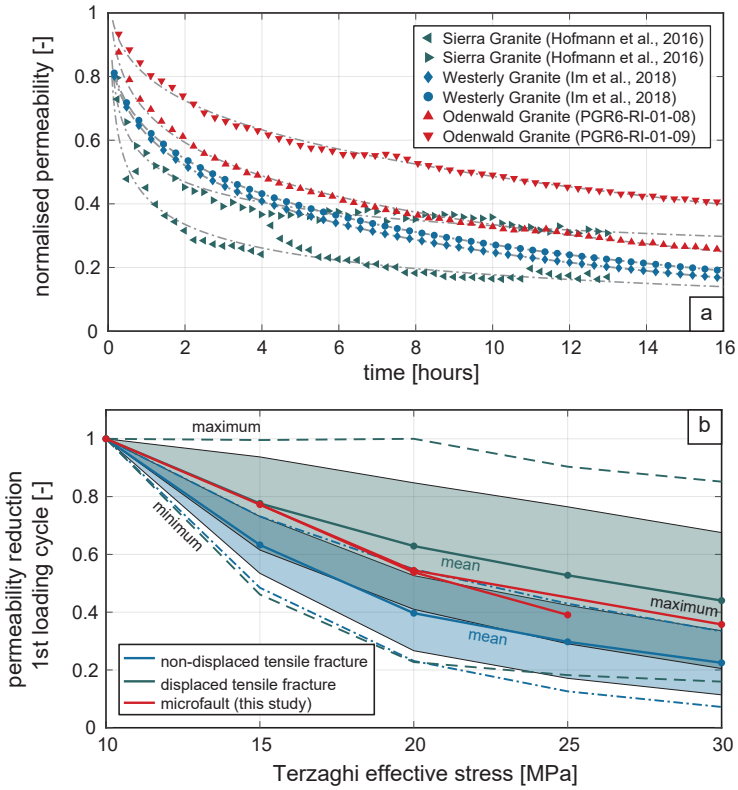

Figure 3.12: Comparison of the permeability decay curves over time for different granites and fracture types reported from literature (Im et al., 2018, Ye and Ghassemi, 2018a) (a). Permeability reduction due to increasing effective pressure of non-displaced (Hofmann et al., 2016, Pyrak-Nolte and Morris, 2000, Watanabe et al., 2009) and displaced tensile fractures (Chen et al., 2000, Hofmann et al., 2016, Watanabe et al., 2009) from literature and the microfaults from our study (b).

Comparing the permeability loss during the first loading cycle to other studies (Chen et al., 2000, Hofmann et al., 2016, Pyrak-Nolte and Morris, 2000, Watanabe et al., 2009) the permeability loss at the respective effective pressures are similar in magnitude with displaced fractures, during the first loading cycle when normalizing permeability to the permeability at 10 MPa effective pressure (figure 3.12b). Permeability loss at lower effective pressure is strongly affected by the experimental set up and is usually higher, such that those pressures are not considered here. Generally, displaced fractures and the microfaults in our study have a higher resistance to fracture closure compared to fractures without displacement. Higher displacements result in a higher sustainability of fracture permeability when comparing our results to those by (Watanabe et al., 2009) and Chen et al. (2000) This implies, that the type of fracturing (matched tensile, displaced tensile or shear fracturing) is a key aspect when assessing the performance and sustainability of, for example, a geothermal reservoir. Moreover, all literature values presented here (Chen et al., 2000, Hofmann et al., 2016, Pyrak-Nolte and Morris, 2000, Watanabe et al., 2009) result from increasing confining pressure while in our experiments the pore pressure was decreased at constant confining pressure.

In this context, we recommend to consider effective pressure coefficients (Walsh, 1981, Zoback and Byerlee, 1975) instead of using Terzaghi's effective pressure. However, these coefficients are highly dependent on the rock type used and need to be determined experimentally (Walsh, 1981). Changes in pore pressure, as in our experiments, are likely to have a smaller impact on fracture permeability, meaning that the change in permeability per step effective pressure is larger, assuming a coefficient of 0.9 for granite (Kranzz et al., 1979). Considering several pressure cycles, the permanent permeability change in the presented experiments with six pressure cycles was an increase by a factor less than 1.4. Other studies suggested a reduction in permeability of up to one order of magnitude after two cycles, with the highest permeability damage during the first loading stage (Hofmann et al., 2016). We argue that the permeability of a microfault generated under in-situ conditions might be reversible due to the lack of plastic energy in the system. In experiments with displaced tensile fractures (Hofmann et al., 2016) for example, the fracture preparation, i.e. placing two sample halves together by hand, causes a high amount of plastic energy. Under external load asperities break and the fracture re-arranges itself, causing a permanent permeability decrease in every loading cycle. This is not the case for in-situ fracture generation in the PTS test. Furthermore, aperture closure analysis suggests a stiffening of the fracture zone, i.e. less closure at similar stress (Zangerl et al., 2008), with an increasing number of cycles, indicating compaction and stiffening effects during pressure cycling. The observed slip events when increasing the pore pressure lead to a minor permeability increase, as well as in a further stiffening of the fracture. Long-term permeability changes at high pressure and temperature of such small faults are required in the future to compare their behaviour to, for example, displaced tensile fractures (Caulk et al., 2016).

3.6. CONCLUSIONS

Our experiments demonstrated an innovative technique to quantify the changes in permeability by introducing a shear fracture (microfault) in a previously intact rock sample simul-

taneous to fluid flow and at elevated effective pressure (pore and confining pressure). We modified the PTS setup by allowing for hydrostatic loading conditions, for the application of a controlled displacement after failure using a springsupported core holder system, and for continuous fluid flow by introducing fluid ports to the end caps. A meaningful interpretation of the magnitude of fracture permeability change by introducing a realistic microscopic fault zone was therefore possible. Our results help to better understand and characterise the hydraulic and mechanical properties, as well as the sustainability of faulted reservoirs in general. The following general conclusions can be drawn from our results: (1) the microfault geometry produced is rather complex but contains features that are commonly found in large scale fault zones, (2) the spatial distribution of aperture suggests a very local permeability distribution along the central shear zone, (3) permeability enhancement by brittle faulting in crystalline rock is about 2 to almost 3 orders of magnitude, while permeability increases at 60 to 80 % of peak load, (4) shearing causes a slight increase in permeability by a factor of 1.1 to 4.0 which is possibly caused by the displacement magnitude being below grain size, (5) after compaction has ceased, which can cause reductions in permeability by a factor of 2.5 to 4, the generated microfault is hydraulically and mechanically sustainable when varying pore pressure by ± 5 to ± 10 MPa, (6) permeability is rather reversible and slight changes during pressure cycling are mainly caused by processes altering shear stress, (7) the resistance of a microfault to fracture closure at increasing effective pressure is in the range of displaced tensile fractures, and (8) the fracture types are a significant aspect when assessing the reservoir performance on a larger scale.

In the future, the dependence of fracture permeability on confining pressure and different rock types should be tested in order to quantify microfault permeability depending on rock type and rock physical properties. Additionally, acoustic emission monitoring would allow for better description on possible induced seismicity and permeability distribution of brittle fault zones in crystalline rock during effective pressure change.

REFERENCES

T. Backers. *Backers T. Fracture toughness determination and micromechanics of rock undermode I and mode II loading*. PhD thesis, University of Potsdam, 2004.

T. Backers and O. Stephansson. ISRM suggested method for the determination of mode II fracture toughness. *Rock Mechanics and Rock Engineering*, 45(6):1011–1022, jul 2012. doi: 10.1007/s00603-012-0271-9.

N. Barton, S. Bandis, and K. Bakhtar. Strength, deformation and conductivity coupling of rock joints. *International Journal of Rock Mechanics and Mining Sciences & Geomechanics Abstracts*, 22(3):121–140, jun 1985. doi: 10.1016/0148-9062(85)93227-9.

G. Blöcher, C. Kluge, T. Goense, L. Pei, R. R. Bakker, and D. F. Bruhn. Hydraulic-mechanical characterization of geothermal reservoir rocks. In *European Geothermal Congress 2019, Den Haag, The Netherlands, 11-14 June*, 2019.

J. W. Carey, L. P. Frash, and T. Ickes. Experimental investigation of shear fracturedevelop-

ment and fluid flow in dolomite. In *52nd US Rock Mechanics/Geomechanics Symposium, American Rock Mechanics Association; Seattle,Washington, USA, 17–20 June*, 2018.

R. A. Caulk, E. Ghazanfari, J. N. Perdrial, and N. Perdrial. Experimental investigation of fracture aperture and permeability change within enhanced geothermal systems. *Geothermics*, 62:12–21, jul 2016. doi: 10.1016/j.geothermics.2016.02.003.

Z. Chen, S. P. Narayan, Z. Yang, and S. S. Rahman. An experimental investigation of hydraulic behaviour of fractures and joints in granitic rock. *International Journal of Rock Mechanics and Mining Sciences*, 37(7):1061–1071, oct 2000. doi: 10.1016/S1365-1609(00)00039-3.

N. Cho, C. Martin, and D. Sego. Development of a shear zone in brittle rock subjected to direct shear. *International Journal of Rock Mechanics and Mining Sciences*, 45(8):1335–1346, dec 2008. doi: 10.1016/j.ijrmms.2008.01.019.

B. R. Crawford. Experimental fault sealing: shear band permeability dependency on cataclastic fault gouge characteristics. *Geological Society, London, Special Publications*, 127(1):27–47, 1998. doi: 10.1144/gsl.sp.1998.127.01.04.

B. R. Crawford, M. C. Tsenn, J. M. Homburg, R. C. Stehle, J. A. Freysteinson, and W. C. Reese. Incorporating scale-dependent fracture stiffness for improved reservoir performance prediction. *Rock Mechanics and Rock Engineering*, 50(12):3349–3359, sep 2017. doi: 10.1007/s00603-017-1314-z.

J. G. Crider. The initiation of brittle faults in crystalline rock. *Journal of Structural Geology*, 77:159–174, aug 2015. doi: 10.1016/j.jsg.2015.05.001.

N. Cuenot, J. Charléty, L. Dorbath, and H. Haessler. Faulting mechanisms and stress regime at the european HDR site of soultz-sous-forêts, france. *Geothermics*, 35(5-6):561–575, oct 2006. doi: 10.1016/j.geothermics.2006.11.007.

H. P. G. Darcy. *Les Fontaines publiques de la ville de Dijon. Exposition et application des principes á suivre et des formules 'a employer dans les questions de distribution d'eau, etc.* V. Dalamont, 1856.

K. Develi and T. Babadagli. Experimental and visual analysis of single-phase flow through rough fracture replicas. *International Journal of Rock Mechanics and Mining Sciences*, 73:139–155, jan 2015. doi: 10.1016/j.ijrmms.2014.11.002.

J. F. Dewey, R. E. Holdsworth, and R. A. Strachan. Transpression and transtension zones. *Geological Society, London, Special Publications*, 135(1):1–14, 1998. doi: 10.1144/GSL.SP.1998.135.01.01.

J. E. Elkhoury, A. Niemeijer, E. E. Brodsky, and C. Marone. Laboratory observations of permeability enhancement by fluid pressure oscillation of in situ fractured rock. *Journal of Geophysical Research*, 116(B2), feb 2011. doi: 10.1029/2010JB007759.

K. F. Evans, A. Genter, and J. Sausse. Permeability creation and damage due to massive fluid injections into granite at 3.5 km at soultz: 1. borehole observations. *Journal of Geophysical Research: Solid Earth*, 110(B4), apr 2005. doi: 10.1029/2004JB003168.

Y. Fang, D. Elsworth, T. Ishibashi, and F. Zhang. Permeability evolution and frictional stability of fabricated fractures with specified roughness. *Journal of Geophysical Research: Solid Earth*, 123(11):9355–9375, nov 2018. doi: 10.1029/2018JB016215.

D. Faulkner, C. Jackson, R. Lunn, R. Schlische, Z. Shipton, C. Wibberley, and M. Withjack. A review of recent developments concerning the structure, mechanics and fluid flow properties of fault zones. *Journal of Structural Geology*, 32(11):1557–1575, nov 2010. doi: 10.1016/j.jsg.2010.06.009.

L. P. Frash, J. W. Carey, and N. J. Welch. Scalable en echelon shear-fracture aperture-roughness mechanism: Theory, validation, and implications. *Journal of Geophysical Research: Solid Earth*, 124(1):957–977, jan 2019. doi: 10.1029/2018JB016525.

H. Hofmann, G. Blöcher, H. Milsch, T. Babadagli, and G. Zimmermann. Transmissivity of aligned and displaced tensile fractures in granitic rocks during cyclic loading. *International Journal of Rock Mechanics and Mining Sciences*, 87:69–84, sep 2016. doi: 10.1016/j.ijrmms.2016.05.011.

H. Hofmann, G. Zimmermann, A. Zang, and K.-B. Min. Cyclic soft stimulation (CSS): a new fluid injection protocol and traffic light system to mitigate seismic risks of hydraulic stimulation treatments. *Geothermal Energy*, 6(1), dec 2018. doi: 10.1186/s40517-018-0114-3.

K. Im, D. Elsworth, and Y. Fang. The influence of preslip sealing on the permeability evolution of fractures and faults. *Geophysical Research Letters*, 45(1):166–175, jan 2018. doi: 10.1002/2017GL076216.

R. R. Jones and P. G. Tanner. Strain partitioning in transpression zones. *Journal of Structural Geology*, 17(6):793–802, jun 1995. doi: 10.1016/0191-8141(94)00102-6.

C. Kluge, H. Milsch, and G. Blöcher. Permeability of displaced fractures. *Energy Procedia*, 125:88–97, sep 2017. doi: 10.1016/j.egypro.2017.08.077.

R. Kranzz, A. Frankel, T. Engelder, and C. Scholz. The permeability of whole and jointed barre granite. *International Journal of Rock Mechanics and Mining Sciences & Geomechanics Abstracts*, 16(4):225–234, aug 1979. doi: 10.1016/0148-9062(79)91197-5.

H. S. Lee and T. F. Cho. Hydraulic characteristics of rough fractures in linear flow under normal and shear load. *Rock Mechanics and Rock Engineering*, 35(4):299–318, oct 2002. doi: 10.1007/s00603-002-0028-y.

M. W. McClure and R. N. Horne. An investigation of stimulation mechanisms in enhanced geothermal systems. *International Journal of Rock Mechanics and Mining Sciences*, 72:242–260, dec 2014. doi: 10.1016/j.ijrmms.2014.07.011.

T. Meier. The influence of temperature on mode II fracture toughness using the punch-through shear with confining pressure experiment. 2009. doi: 10.3997/2214-4609.201400344.

H. Milsch, H. Hofmann, and G. Blöcher. An experimental and numerical evaluation of continuous fracture permeability measurements during effective pressure cycles. *International Journal of Rock Mechanics and Mining Sciences*, 89:109–115, nov 2016. doi: 10.1016/j.ijrmms.2016.09.002.

T. M. Mitchell and D. R. Faulkner. Experimental measurements of permeability evolution during triaxial compression of initially intact crystalline rocks and implications for fluid flow in fault zones. *Journal of Geophysical Research*, 113(B11), nov 2008. doi: 10.1029/2008JB005588.

A. Nicolas, G. Blöcher, C. Kluge, Z. Li, H. Hofmann, L. Pei, H. Milsch, J. Fortin, and Y. Guéguen. Pore pressure pulse migration in microcracked andesite recorded with fibre optic sensors. *Geomechanics for Energy and the Environment*, 24:100183, dec 2020. doi: 10.1016/j.gete.2020.100183.

N. D. Paola, D. R. Faulkner, and C. Collettini. Brittle versus ductile deformation as the main control on the transport properties of low-porosity anhydrite rocks. *Journal of Geophysical Research*, 114(B6), jun 2009. doi: 10.1029/2008JB005967.

F. X. Passelègue, N. Brantut, and T. M. Mitchell. Fault reactivation by fluid injection: Controls from stress state and injection rate. *Geophysical Research Letters*, 45(23), dec 2018. doi: 10.1029/2018GL080470.

D. Peacock, C. Nixon, A. Rotevatn, D. Sanderson, and L. Zuluaga. Glossary of fault and other fracture networks. *Journal of Structural Geology*, 92:12–29, nov 2016. doi: 10.1016/j.jsg.2016.09.008.

L. Pei, G. Blöcher, H. Milsch, F. Deon, G. Zimmermann, W. Rühaak, I. Sass, and E. Huenges. Thermal strain in a water-saturated limestone under hydrostatic and deviatoric stress states. *Tectonophysics*, 688:49–64, oct 2016. doi: 10.1016/j.tecto.2016.09.020.

L. Pyrak-Nolte and J. Morris. Single fractures under normal stress: The relation between fracture specific stiffness and fluid flow. *International Journal of Rock Mechanics and Mining Sciences*, 37(1-2):245–262, jan 2000. doi: 10.1016/S1365-1609(99)00104-5.

E. H. Rutter and J. Mecklenburgh. Hydraulic conductivity of bedding-parallel cracks in shale as a function of shear and normal stress. *Geological Society, London, Special Publications*, 454(1):67–84, 2017. doi: 10.1144/sp454.9.

M. Sheng, Z. Xu, X. Wang, and P. Li. Experimental study on hydro-shearing propagation ofan embedded fracture in hot dry granite rock. *GRC transactions*, 42, 2018.

P. Shokouhi, J. Jin, C. Wood, J. Rivière, B. Madara, D. Elsworth, and C. Marone. Dynamic stressing of naturally fractured rocks: On the relation between transient changes in permeability and elastic wave velocity. *Geophysical Research Letters*, 47(1), jan 2020. doi: 10.1029/2019GL083557.

X. Tan, H. Konietzky, and T. Frühwirt. Experimental and numerical study on evolution of biot's coefficient during failure process for brittle rocks. *Rock Mechanics and Rock Engineering*, 48(3):1289–1296, jun 2014. doi: 10.1007/s00603-014-0618-5.

K. Terzaghi. *Erdbaumechanik Auf Bodenphysikalischer Grundlage*. Leipzig u. Wien, F. Deuticke, 1925.

D. Vogler, F. Amann, P. Bayer, and D. Elsworth. Permeability evolution in natural fractures subject to cyclic loading and gouge formation. *Rock Mechanics and Rock Engineering*, 49(9):3463–3479, jun 2016. doi: 10.1007/s00603-016-1022-0.

J. Walsh. Effect of pore pressure and confining pressure on fracture permeability. *International Journal of Rock Mechanics and Mining Sciences & Geomechanics Abstracts*, 18 (5):429–435, oct 1981. doi: 10.1016/0148-9062(81)90006-1.

N. Watanabe, N. Hirano, and N. Tsuchiya. Determination of aperture structure and fluid flow in a rock fracture by high-resolution numerical modeling on the basis of a flow-through experiment under confining pressure. *Water Resources Research*, 44(6), jun 2008. doi: 10.1029/2006WR005411.

N. Watanabe, N. Hirano, and N. Tsuchiya. Diversity of channeling flow in heterogeneous aperture distribution inferred from integrated experimental-numerical analysis on flow through shear fracture in granite. *Journal of Geophysical Research*, 114(B4), apr 2009. doi: 10.1029/2008JB005959.

H. Wu, J. Kemeny, and S. Wu. Experimental and numerical investigation of the punch-through shear test for mode II fracture toughness determination in rock. *Engineering Fracture Mechanics*, 184:59–74, oct 2017. doi: 10.1016/j.engfracmech.2017.08.006.

H. Yasuhara and D. Elsworth. Compaction of a rock fracture moderated by competing roles of stress corrosion and pressure solution. *Pure and Applied Geophysics*, 165(7): 1289–1306, jul 2008. doi: 10.1007/s00024-008-0356-2.

Z. Ye and A. Ghassemi. Injection-induced shear slip and permeability enhancement in granite fractures. *Journal of Geophysical Research: Solid Earth*, 123(10):9009–9032, oct 2018a. doi: 10.1029/2018JB016045.

Z. Ye and A. Ghassemi. Experimental study on injection-induced fracture propagation andcoalescence for egs stimulation. In *43rd Workshop on Geothermal Reservoir Engineering, Stanford University, California*, 2018b.

I. Yeo, M. de Freitas, and R. Zimmerman. Effect of shear displacement on the aperture and permeability of a rock fracture. *International Journal of Rock Mechanics and Mining Sciences*, 35(8):1051–1070, dec 1998. doi: 10.1016/S0148-9062(98)00165-X.

J. Yoon and S. Jeon. Experimental verification of a pts mode II test for rock. *International Journal of Rock Mechanics and Mining Sciences*, 41:8–13, may 2004. doi: 10.1016/j.ijrmms.2004.03.012.

C. Zangerl, K. Evans, E. Eberhardt, and S. Loew. Normal stiffness of fractures in granitic rock: A compilation of laboratory and in-situ experiments. *International Journal of Rock Mechanics and Mining Sciences*, 45(8):1500–1507, dec 2008. doi: 10.1016/j.ijrmms.2008.02.001.

Q. Zhang, X. Li, B. Bai, L. Pei, L. Shi, and Y. Wang. Development of a direct-shear apparatus coupling with high pore pressure and elevated temperatures. *Rock Mechanics and Rock Engineering*, 52(9):3475–3484, feb 2019. doi: 10.1007/s00603-019-1735-y.

W. Zhu and T. fong Wong. The transition from brittle faulting to cataclastic flow: Permeability evolution. *Journal of Geophysical Research: Solid Earth*, 102(B2):3027–3041, feb 1997. doi: 10.1029/96jb03282.

M. D. Zoback and J. D. Byerlee. The effect of microcrack dilatancy on the permeability of westerly granite. *Journal of Geophysical Research*, 80(5):752–755, feb 1975. doi: 10.1029/jb080i005p00752.

4

ENHANCEMENT POTENTIAL & SUSTAINABILITY OF MICROFAULTS

Using an innovative experimental set up (Punch-Through Shear test), we initiated a shear zone (microfault) in Flechtingen sandstone and Odenwald granite under in-situ reservoir conditions while monitoring permeability and fracture dilation evolution. The shear zone, which has a cylindrical geometry, is produced by a self-designed piston assembly that punches down the inner part of the sample. Permeability and fracture dilation were measured for the entire duration of the experiment. After the shear zone generation, the imposed shear displacement was increased to 1.2 mm and pore pressure changes of ± 5 or ± 10 MPa were applied cyclically to simulate injection and production scenarios. Thin sections and image analysis tools were used to identify microstructural features of the shear zone. The geometry of the shear zone is shown to follow a self-affine scaling invariance, similar to the fracture surface roughness. The permeability evolution related to the onset of the fracture zone is different for both rocks: almost no enhancement for the Flechtingen sandstone and an increase of more than 2 orders of magnitude for the Odenwald granite. Further shear displacement resulted in a slight increase in permeability. A fault compaction is observed after shear relaxation which is associated to a permeability decrease by a factor more than 3. Permeability changes during pressure cycling are reversible when varying the effective pressure. The difference in permeability enhancement between the sandstone and the granite is related to the larger width of the shear zones.

This chapter is based on: C. Kluge, G. Blöcher, A. Barnhoorn, J. Schmittbuhl, D. Bruhn, *Permeability evolution during shear zone initiation in low-porosity rocks*, Rock Mechanics and Rock Engineering, (2021).

4.1. INTRODUCTION

Discontinuities in the upper crust control the hydro-mechanical behaviour of rock masses. They are essential to understand the potentials and limitations of subsurface engineering applications, as well as the structural evolution of geological environments. Laboratory experiments are a substantial element to characterise subsurface discontinuities at a small scale. They are also important for providing reliable data to support the growing number of numerical studies and to describe the complexity of geologic features.

Faulkner et al. (2010) reviewed the advances in studies about fault zones and emphasized that structure, mechanics and fluid flow properties cannot be studied separately. Faults in the field are classically studied from outcrops where the dimensions of faults range from millimetres to decameters, and even kilometre-scale (e.g. Candela et al., 2012, Myers and Aydin, 2004). From structural features, qualitative assumptions on hydraulic properties of faults are usually made (e.g. Evans et al., 1997, Faulkner et al., 2010, Fisher and Knipe, 2001, Fossen et al., 2007). On the laboratory scale, fault properties at scales ranging from μm to cm, such as microstructural features of fault zones, can be studied. Several studies describe fault initiation and propagation, as well as the fault properties on the microscale (e.g. Chambon et al., 2006, Janssen et al., 2001, Moore and Lockner, 1995, Vermilye and Scholz, 1999, Wibberley et al., 2000, Wong, 1982, Zang et al., 2000).

Tri-axial compression tests are the most common testing procedure to generate a shear zone in a previously intact rock sample. They enable to measure the related hydraulic-mechanical properties, such as permeability and dilation (e.g. Chen et al., 2014, Faulkner and Armitage, 2013, Mitchell and Faulkner, 2008, Teufel, 1987). In tri-axial testing, conjugated shear fractures at a certain angle with respect to the loading direction are generated. By its inclination, the conjugated shear fractures are subjected to a displacement in a compressional direction. To apply a normal stress to a shear fracture with a displacement parallel to the shear loading direction, shear box tests were often used but proved difficult to generate a single shear fracture (e.g. Elkhoury et al., 2011, Faoro et al., 2009, Zhang et al., 2019). Direct-shear experiments on core samples with saw-cut fractures or 3D-printed fractures were also used in the past (Fang et al., 2017, 2018, Im et al., 2018, Ishibashi et al., 2020). Such simplified surfaces geometries allow for an isolation of specific physical processes that control, for example, frictional properties or permeability during shearing. However, they cannot depict the variety of structural features commonly found in a natural shear zone (Kluge et al., 2020, Ye and Ghassemi, 2019).

The micro-structure of faults has been studied extensively on outcrops and laboratory samples in all types of rocks. In crystalline rocks such as granite, the properties depend on the mineralogy, grain size and mineral strength, as well as the existence of links between microfractures and joints (e.g. Amitrano and Schmittbuhl, 2002, Hansen and Schmittbuhl, 2003, Lockner et al., 1991, Pollard, 2005). Fracture initiation and propagation is assumed to be caused by the coalescence of tensile microfractures formed during loading, oriented parallel to the maximum principal stress (Barnhoorn et al., 2010, Cox and Scholz, 1988). The microstructure of a fault is highly dependent on the amount of deformation or displacement (Cox and Scholz, 1988) and involves different deformation mechanisms. This includes mode I and II cracks, inter- or intragranular fractures, cataclastic flow and sub-shear band

localisation (Amitrano and Schmittbuhl, 2002). For sandstones, a distinction between low and high porosity rock is commonly made. This is because porosity and consequently grain size and grain distribution have the largest impact on the structural features forming during shearing (Dunn et al., 1973, Faulkner et al., 2010). But also the phyllosilicate content, lithification and diagenesis are important parameters (Fisher and Knipe, 1998).

Permeability differences between deformation bands, the most common feature of faults in porous sandstones, and intact rocks can be up to five orders of magnitude (Fossen et al., 2007). In low-permeability rocks like clay-bearing sandstones, two competitive mechanisms control the permeability of faults: clay-coating and grain-contact cementation and the existence of fault smear from cataclasis and grain crushing during shear (Fisher and Knipe, 2001). These microstructural observations are actually rarely related to the hydraulic properties during fracture generation. This is why there is need for relating the development of small-scale fault architecture to the evolution of the permeability.

The sustainability of shear fracture permeability is crucial for understanding the long-term performance of fault zones or induced shear fractures in, for example, deep geothermal applications. Commonly, the behaviour of shear fractures is approximated from shear displaced tensile fractures in the laboratory. The fracture closure and the related permeability behaviour under varying normal and shear stresses can thus be determined (e.g. Barton et al., 1985, Hofmann et al., 2016, Milsch et al., 2016, Watanabe et al., 2009). Typically, an artificial shear displacement is applied to a tensile fracture generated independently. This results in the absence of a damage zone and the asperity deformation related to shear dilation. Therefore, innovative experimental set-ups are needed to be able to generate realistic fault zones and to monitor the evolution of their hydraulic properties.

The Punch-Through Shear (PTS) test was originally developed to obtain the mode II fracture toughness of rocks (Backers and Stephansson, 2012). This testing set-up has been adapted to quantify the permeability evolution during fault generation under saturated conditions with a rate or pressure controlled fluid flow (Kluge et al., 2020). In our experiments, we relate the evolution of hydraulic properties, such as permeability, to microstructural observations in shear zones on a laboratory scale (microfault). We will first describe the experimental procedures of the PTS test and present the laboratory results. After that, we will show the procedures and results of the microstructural analysis. Finally, we will discuss the microfault propagation and architecture, their impact on the measured hydraulic properties, as well as their impact on the sustainability of fracture permeability.

4.2. MATERIALS & METHODS

4.2.1. TESTING EQUIPMENT

The Punch-Through-Shear (PTS) tests were carried out in a conventional MTS tri-axial compression cell. The stiff, servo-controlled loading frame (MTS 815, Material Testing Systems Corporation) holds a loading capacity of up to 4600 kN (load cell calibrated to 1000 kN, calibration error <1 %) and a servo-controlled maximum hydrostatic confining pressure of 140 MPa applied via an oil-filled pressure vessel coupled to an external pres-

sure intensifier. The pore fluid pressure was applied via four Quizix fluid pressure pumps (Model C6000-10K-HC-AT) with a maximum fluid pressure of 70 MPa. Flow-through was continuously applied at a minimum of 2 MPa confining pressure using two paired upstream pumps and two paired downstream pumps. The differential fluid pressure, which is the difference between in- and outflow pressure, was measured using a differential pressure sensor (Honeywell HL-Z; range: 1 MPa; line pressure max. 35 MPa; precision: ~ 1%). Changes in circumferential strain were measured using a LVDT extensometer chain. All experiments have been performed at ambient temperatures of 25 to 30 °C. Data were recorded at a frequency of 1 Hz. A detailed description of the machine can be found in Pei et al. (2016).

4.2.2. SAMPLE MATERIAL

Samples were cored from two different rocks: Odenwald granite and Flechtingen sandstone. All hydro-mechanical parameters of these two types of rocks are listed in table 4.1 (data are from Blöcher et al. (2019)).

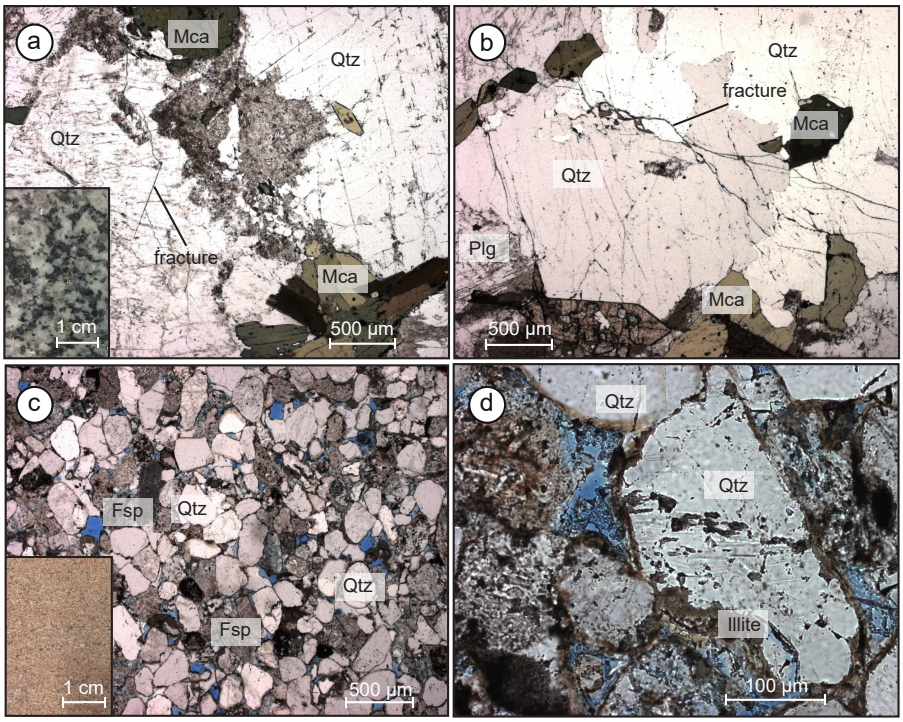

Figure 4.1: Thin section images of the intact sample material of Odenwald granite (PGR6-RI) and Flecthingen sandstone (SBT6-BE).

The Odenwald Granite (PGR6-RI) was taken from a quarry near Rimbach in the Upper Rhine Graben, Germany. It is a Carboniferous, fresh granite showing no sign of alterations

or strong micro-fracturing (figure 4.1a, b). It is composed of quartz (Qtz) with a grain size ranging from 1 to 3 mm, feldspar (Fsp) between 2 to 3 mm and mica (Mca) between 1 to 3 mm. The minerals are evenly distribution and size of minerals. Quartz, as well as the darker and brighter mica are the main constituents within our samples. Feldspars have a smaller occurrence. Micro-fractures are sparse and are cutting through grains. They were mostly found within the less compliant Quartz, or exist along grain boundaries with no visible shear offset. The porosity is less than 0.6 % and the permeability is less than $1 \cdot 10^{-18}$ m^2.

The Flechtingen Sandstone (SBT6-BE) was taken from a quarry near Magdeburg in the North German Basin, Germany. It is a Permian, arkosic litharenite with quartz, feldspars and rock fragments of mainly volcanic origin, about 8% of clay, predominantly illite and chlorite (figure 4.1c, d). This Rotliegend rock is used as an analogue to the sedimentary geothermal reservoirs in the Northern German Basin (Blöcher et al., 2014, 2016). Grain sizes range between 0.05 and 0.2 mm for the feldspar and 0.1 to 0.5 mm for the quartz, and are partly rounded and well sorted. Contrary to the findings by Hassanzadegan et al. (2014), almost no micro-fractures were found. The low porosity derives from dense packing of grains, as well as illite-clay partially blocking the pore space by coating the quartz grains. Still, some grain-contact quartz dissolution is present which additionally reduces permeability. The sandstone is layered, such that all cores were taken perpendicular to the bedding. The porosity of this rock varies between 6 and 10 %, while the intact matrix permeability at 2 MPa is given with $2 \cdot 10^{-16}$ m^2.

Table 4.1: Intact rock properties of samples PGR6-RI & SBT6-BE (Blöcher et al., 2019).

	TS [MPa]	K_{IC} [MPa· m$^{0.5}$]	UCS [MPa]	E [GPa]	ν [-]	ϕ [%]	k_0 [m^2]
PGR6-RI	11.8	1.347	131	43.8	0.22	< 0.6	$< 1 \cdot 10^{-18}$
SBT6-BE	3.82	0.480	56	14.9	0.28	8.5	$2 \cdot 10^{-16}$

TS: tensile strength, K_{IC}: mode I fracture toughness, UCS: uni-axial compressive strength, E: Young's modulus, ν: Poisson ratio, ϕ: porosity, k_0: initial permeability

4.2.3. SAMPLE GEOMETRY & EXPERIMENTAL SETUP

The Punch-Through-Shear (PTS) test allows to induce a cylindrical shear fracture into an intact sample during fluid flow injection along the fracture direction. The stress concentrates at the notch tips when loading the sample causes a circular shear fracture (microfault) to propagate from the bottom to the top notch. The experimental setup and sample geometry are illustrated in figure 4.2a. A full description of the experimental testing procedure can be found in Kluge et al. (2020). Four tests were performed and are listed with their respective dimensions and testing conditions in table 4.2.

4.2.4. EXPERIMENTAL PROCEDURE

The dry samples were jacketed in a heat-shrink tube and installed into the tri-axial compression cell while being subjected to nearly vacuum conditions of 1 kPa using a vacuum pump

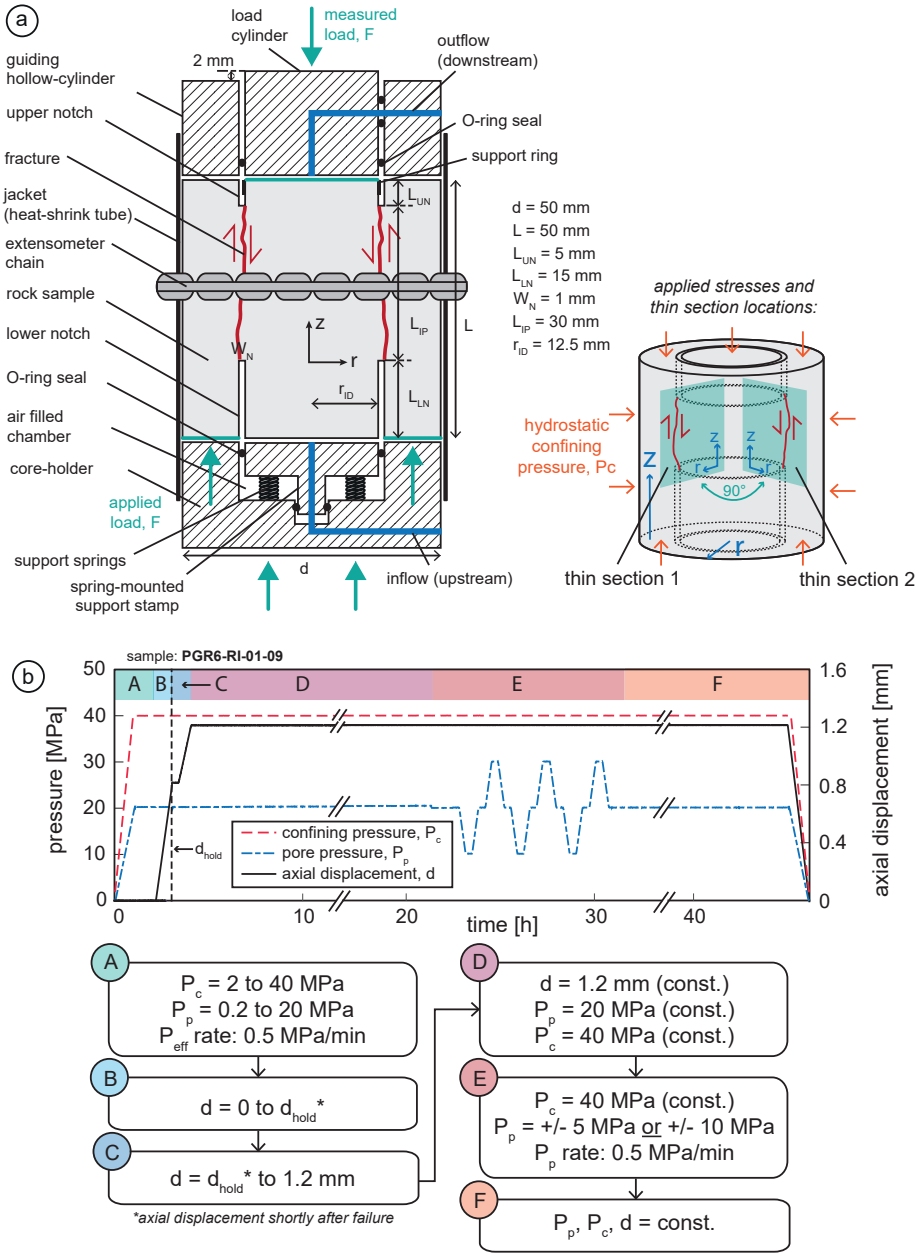

Figure 4.2: Experimental setup and sample dimension of the Punch-Through-Shear test (a) and experimental procedure for all tests (b).

Table 4.2: List of samples, sample dimensions and testing conditions.

sample ID	L_{IP}, L, d [mm]	testing conditions
PGR6-RI-01-08	30.15, 50.15, 50.10	faulting: P_c = 40 MPa, P_p = 20 MPa pressure cycling: $P_p \pm 5$ MPa
PGR6-RI-01-09	30.18, 50.18, 50.10	faulting: P_c = 40 MPa, P_p = 20 MPa pressure cycling: $P_p \pm 10$ MPa
SBT6-BE-03-01	30.00, 50.00, 50.10	faulting: P_c = 40 MPa, P_p = 20 MPa pressure cycling: $P_p \pm 5$ MPa
SBT6-BE-03-02	30.07, 50.07, 50.10	faulting: P_c = 40 MPa, P_p = 20 MPa pressure cycling: $P_p \pm 10$ MPa

L_{IP}: length of intact portion, L: sample length, d: sample diameter
P_c: confining pressure, P_p: pore pressure,

(Laboxact SEM 820). Then they are saturated with distilled water under vacuum conditions and a confining pressure of 2 MPa and a constant pore fluid pressure of 0.2 MPa. Saturation was ended when no more fluid flowed into the sample. This took at least three days for the granite samples and at least 24 hours for the sandstone. A constant inflow rate of 0.2 to 1 ml/min was applied to measure permeability. The fluid was injected from the bottom over the entire cross-sectional area of the sample, A, via an injection grid in the end caps. When the in- and outflow pressure and flow rate was constant, the Darcy permeability was measured. Sample permeability, k, was calculated from equation 4.1 using Darcy's law (Darcy, 1856), where the length, L_{IP}, is the distance between the lower and upper notch (figure 4.2a). This distance corresponds to the maximum pressure difference, Δp_f, along the micro-fault (Kluge et al., 2020):

$$k = \frac{Q}{A} \frac{\mu L_{IP}}{\Delta p_f} \tag{4.1}$$

Here, Q is the volumetric inflow rate in m^3/s, A is the cross-sectional area of the entire sample in m^2, μ is the dynamic viscosity of the fluid (Pa·s), L_{IP} is the distance between the notches of the sample in meter and Δp_f is the differential fluid pressure in Pa. To verify laminar flow conditions, three different flow rates were applied and the resulting differential fluid pressure was obtained. Flow rate and differential fluid pressure were then checked for linearity at experimental stages of constant stress and displacement. The minimum measurable permeability of our apparatus is around $k = 10^{-18}$ m^2. During the entire duration of the experiment the change in circumference, dU, was measured using the LVDT extensometer chain around the sample. This enables to calculate the mechanical fracture dilation, e_{mech}, related to the mechanical fracture aperture:

$$e_{mech} = dU/2\pi \tag{4.2}$$

It is important to note, that the fracture dilation is a measure of the bulk deformation of rock matrix and fracture. Terzaghi's effective pressure, p_e, is defined as the confining pressure,

p_c, minus fluid pressure, p_p (equation 4.3) (Terzaghi, 1925). The pore fluid pressure was estimated by the outflow pressure, $p_{p,out}$, and the difference in fluid pressures, $p_{p,in}$ - $p_{p,out}$, divided by two (equation 4.4), assuming a linear pressure distribution (Kluge et al., 2020):

$$p_e = p_c - p_p \tag{4.3}$$

$$p_p = p_{p,out} + \frac{p_{p,in} - p_{p,out}}{2} \tag{4.4}$$

The experimental procedure and a flow chart are illustrated in figure 4.2b. Before loading the sample axially to generate the fracture, pore and confining pressure were increased simultaneously to 20 and 40 MPa, respectively, within one hour. An axial load was then applied by a constant axial displacement at a rate of 0.001 mm/s, pushing the inner loading cylinder down and generating a shear fracture. A drop in the axial load, F, indicated the loss of sample integrity and the consequent existence of a fracture connecting bottom and top notches. The fracturing process is described in detail in Kluge et al. (2020). To allow the pore pressure to reach steady state conditions, the axial displacement was stopped after a clear indication of failure given by the load curve. During loading and until the hold phase, permeability was assumed to be non-steady state. Assuming that the hydraulic diffusivity of the rock matrix itself, D_r, was constant during the experiments, it was calculated from equation 4.5 using the permeability, k, the Skempton coefficient, B, the drained bulk modulus, K_d, the fluid viscosity, η, and the Biot coefficient, α (Nicolas et al., 2020):

$$D_r = \frac{kBK_d}{\eta\alpha} \tag{4.5}$$

This results in a hydraulic matrix diffusivity of 4.5 $\cdot 10^{-6}$ m^2/s and 1.1 $\cdot 10^{-4}$ m^2/s for the Odenwald granite and Flechtingen sandstone, respectively. The diffusion process over the length of the sample, L, was therefore about 10 min for the Odenwald granite and 0.4 min for the Flechtingen sandstone. We used a time range of about 30 min to reach steady state flow conditions. After that, the axial displacement was again increased at a slower rate of 0.0001 mm/s leading to an increase in shear displacement until a maximum of around 1.2 mm. Finally, the axial displacement of the upper loading cylinder was maintained to measure changes in stress. The piston position was constant for at least 14 h, while continuously measuring Darcy permeability and dilation. The cyclic effective pressure changes were applied by varying the outflow pressure by ± 5 or ± 10 MPa at a rate of 0.5 MPa/min. The permeability measurements during the pore pressure cycling were therefore point measurements at the respective stress levels, i.e. after 20 to 30 min of holding (figure 4.2).

4.3. EXPERIMENTAL RESULTS

In the following sections, we will present the evolution of the axial load, F, the sample permeability, k, and the mechanical fracture dilation, e_{mech}. Their evolution is shown during

fracture generation and shearing (figures 4.3a, c, e), as well as during the constant displacement phase of about 14 hours (figures 4.3b, d, f). After that, we show the permeability and fracture dilation evolution during the pore pressure cycling (figure 4.4).

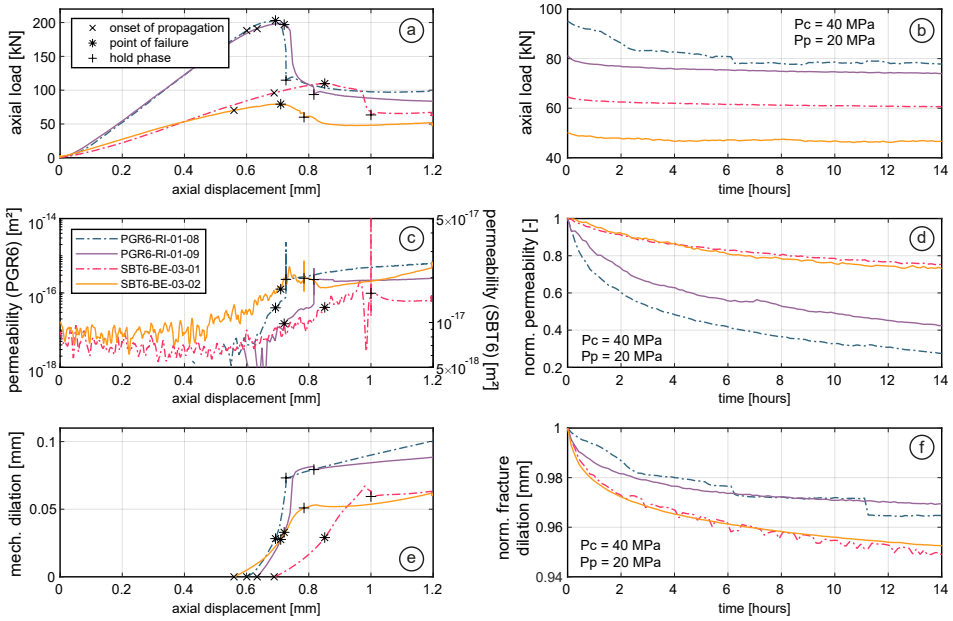

Figure 4.3: Axial load (a), the permeability (b) and mechanical fracture dilation (c) evolution vs. axial displacement of the Odenwald granite (PGR6-RI-01-08 & PGR6-RI-01-09) and Flechtingen sandstone samples (SBT6-BE-03-01 & SBT6-BE-03-02) during loading, failure and shearing. Axial load (d), normalised permeability (e) and mechanical fracture dilation (f) evolution of all samples during the constant displacement phase over 14 hours.

4.3.1. FRACTURE GENERATION

The loading curves of the granite and sandstone samples tested showed a similar behaviour (figure 4.3a). The loading amplitude and the slope in the linear elastic region differed. It shows a higher strength and higher elasticity of the granite samples compared to the sandstone. The onset of fracture initiation in the PTS test can usually be determined by the change in inflow and outflow rate, as well as the volume change in combination with the change in slope of the load curve (Kluge et al., 2020). The change in inflow rate indicated an increase in fracture porosity being flooded. The increase in outflow rate shortly before failure indicated a through-going fracture connecting bottom and top notch.

The apparent permeability, calculated from equation 4.1, of the two granite samples (PGR6-RI-01-08 and 09) started to increase at about 70 % of the peak load, i.e. an axial displacement of about 0.6 mm. This corresponded to the change in slope of the load-displacement curve (figure 4.3a). The sample integrity was lost after the load started to decrease indicating the development of a through-going fracture at a displacement of about 0.7 mm. Sample

SBT6-BE-03-01 started yielding at about 0.55 mm, with failure at about 0.7 mm, similar to the granite samples. SBT6-BE-03-01 failed at a displacement of 0.85 mm, which was higher compared to all other samples. The peak load was rather plateau-like and the drop in load at about 0.95 mm was also delayed (figure 4.3a).

4.3.2. PERMEABILITY & FRACTURE DILATION DURING FAULTING

The point of failure of the granites (PGR6-RI-01-08 and 09) coincided with a sharp increase in fracture dilation calculated from the lateral extensometer data. During fracturing, a continuous increase in dilation was observed even after peak load (figure 4.3e). During the hold phase, the Darcy permeability was first measured at steady state conditions. The increase in permeability was more than 2 orders of magnitude, from below $1 \cdot 10^{-18}$ m^2 to about $2.3 \cdot 10^{-16}$ m^2 for both samples (figure 4.3c). The mechanical fracture dilation reached a value of 0.07 mm and 0.08 mm (table 4.3). During shearing, the permeability of sample PGR6-RI-01-08 increased from $2.3 \cdot 10^{-16}$ m^2 to $6.0 \cdot 10^{-16}$ m^2, while the permeability of sample PGR6-RI-01-09 remained relatively constant at around $2.3 \cdot 10^{-16}$ m^2. A similar trend as for permeability was observed for the fracture dilation. Here, sample PGR6-RI-01-08 showed an increase from 0.07 mm to 0.1 mm, while sample PGR6-RI-01-09 showed an increase from 0.08 mm to a bit less than 0.09 mm.

The pre-failure permeability of both sandstone samples (SBT6-BE-03-01 and 02) were about $1 \cdot 10^{-17}$ m^2. The permeability of both samples decreased during the linear elastic loading phase (figure 4.3c). At about 0.6 mm, similar to the granite, the permeability started to increase. Sample SBT6-BE-03-01 showed a delayed increase. The permeability in both sandstone samples increased to $1.6 \cdot 10^{-17}$ m^2 and $2.0 \cdot 10^{-17}$ m^2 for sample SBT6-BE-03-01 and 02, respectively. The mechanical fracture dilation reached a value of 0.05 mm and 0.06 mm, which was lower compared to the granite (figure 4.3e). During further shearing the permeability remained constant for both samples at about $1.5 \cdot 10^{-17}$ m^2 and $2.0 \cdot 10^{-17}$ m^2. Fracture dilation during shearing again followed the same trend as for the permeability: it remained relatively constant for sample SBT6-BE-03-01 at around 0.06 mm. A slight increase from 0.05 mm to 0.06 mm was measured for sample SBT6-BE-03-02.

After that, the axial displacement was stopped and kept constant until the end of the experiment. Permeability was measured over the time span of at least 14 hours to monitor possible longer term changes in stress, permeability and dilation (figure 4.3b,d,f). The reduction of the measured axial load after fracture generation and shearing was largest in the first two hours. The axial load then reached an almost stable value and was overall higher for the granites (figure 4.3b). Figure 4.3d shows, that the permeability of the granites was reduced by a factor of about 3.3 and 2.5. Permeability of the two sandstone samples was reduced by a factor of about 1.4. Still, the dilation of the sandstone was larger compared to the granite (figure 4.3f).

The results of the permeability changes during the respective experimental stages were summarized in table 4.3.

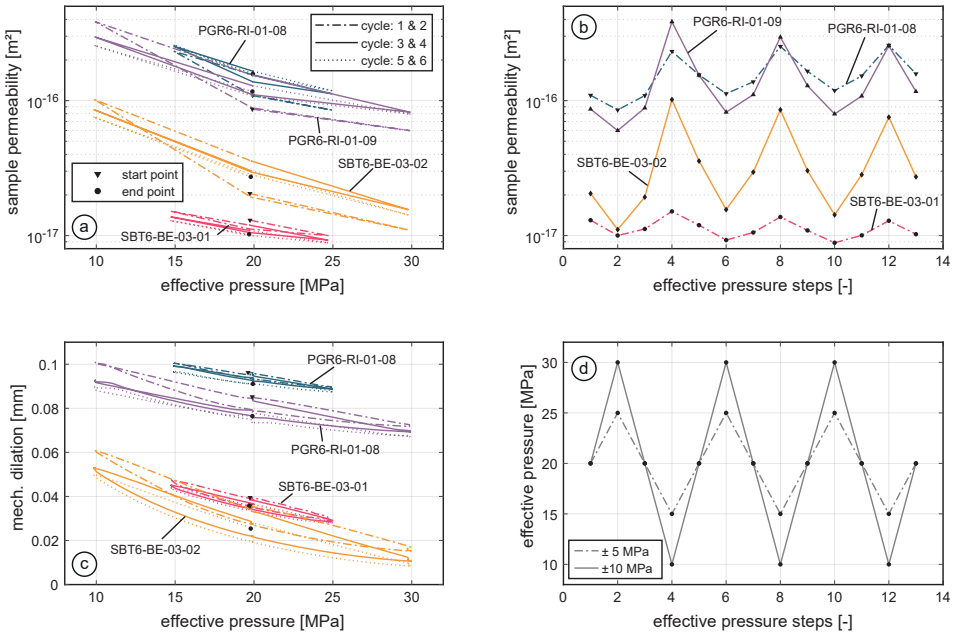

Figure 4.4: Permeability and mechanical fracture dilation evolution vs. the effective pressure (a,b) and vs. the effective pressure steps (c,d).

4.3.3. PERMEABILITY EVOLUTION DURING PORE PRESSURE CYCLING

The change in permeability and fracture dilation during effective pressure changes is crucial for an understanding of the sustainability of fractured reservoirs. Therefore, the pore pressure was varied at a constant confining pressure by ± 5 MPa and ± 10 MPa for one sandstone and one granite sample, respectively (figure 4.4). The permeability in figures 4.4a, b is given as a point measurement at the respective effective pressure level.

During the pore pressure changes of ± 5 MPa, the permeability magnitude was in the range of $8.5 \cdot 10^{-17}$ m^2 to $2.5 \cdot 10^{-16}$ m^2 for the Odenwald granite and between $8.8 \cdot 10^{-18}$ m^2 and $1.5 \cdot 10^{-17}$ m^2 for the Flechtingen sandstone. Permeability changes of the granite and sandstone were rather reversible. A slight permanent reduction in permeability for the sandstone and a slight increase for the granite after six loading cycles was found (table 4.3). The fracture dilation showed a similar reversible behaviour, although the fracture dilation of the sandstone was half compared to the dilation of the granite (figure 4.4c). The mean dilation calculated from the lateral extensometer data represents the bulk changes in circumference caused by matrix and fracture.

During pore pressure changes of ± 10 MPa, the reversible change in permeability was larger (figure 4.4a). The granite sample was measured with a permeability between $6.0 \cdot 10^{-17}$ m^2 and $3.8 \cdot 10^{-16}$ m^2. The sandstone was measured with $1.1 \cdot 10^{-17}$ m^2 to $1.0 \cdot 10^{-16}$ m^2 which corresponds to a change of about 1 order of magnitude. Interestingly,

the permeability after six pressure cycles was slightly increased for the granite and the sandstone compared to before the pressure changes (table 4.3). The change in mean fracture dilation was larger compared to pressure changes of ± 5 MPa, with a slight permanent reduction after six pressure changes (figure 4.4c). The total range of dilation was larger for the sandstone compared to the granite. This implicates a higher deformability of the sandstone matrix and fracture system.

Considering the slopes of the permeability changes (figure 4.4b), the magnitude of the effective pressure dependent permeability change depends on the previous stress level (figure 4.4d). When the effective pressure reduced from 25 or 30 MPa to 20 MPa, permeability changes were larger compared to unloading from 20 MPa to 15 or 10 MPa. Loading the sample from lower effective pressure (10 or 15 MPa to 20 MPa) led to larger changes in permeability compared to loading from 20 MPa to 25 or 30 MPa. Permeability changes of the Odenwald granite were always larger compared to changes of the Flechtingen sandstone.

Table 4.3: Summary of permeability evolution during the respective experimental stages.

sample ID	k_f/k_0	k_s/k_f	k_c/k_s	k_p/k_c	k_p/k_0*
PGR6-RI-01-08	231.1	2.8	0.3	1.4	158.0
PGR6-RI-01-09	229.5	1.0	0.4	1.4	116.8
SBT6-BE-03-01	1.8	0.8	0.7	0.8	1.2
SBT6-BE-03-02	2.0	1.2	0.7	1.3	2.7

k_0: intact sample permeability, k_f: after faulting, k_s: after shearing,
k_c: after compaction, k_p: after cyclic pressure loading,
*total enhancement before and after the experiment

4.4. MICROSTRUCTURAL ANALYSIS OF FAULT GEOMETRY

Two thin sections were cut from each sample, both vertically in the r and z-direction (cylindrical coordinates, see figure 4.2a). They depict the entire microfault between both notches (~ 30 mm). Blue epoxy was injected into the sample before preparing the thin sections to visualize the void spaces and microfractures. The fault zone geometry was analysed with and without polarized light to identify the fault zone dimensions and geometrical features. Image analysis was performed to quantify the fault properties (table 4.4).

4.4.1. FAULT GEOMETRY IN ODENWALD GRANITE

Two thin sections from each sample were prepared along the z-direction to show the full extent of the fault between the two notches. The inferred direction of maximum principal stress, the flow direction, as well the orientation of the thin section images within the sample are shown in figures 4.5a, b.

A fault core, i.e. a zone where the two fracture faces were clearly separated and displaced, and a surrounding damage zone was visible. The fractures in the damage zone were oriented mainly 20° to 30° to the displacement direction. They were therefore not typical Riedel

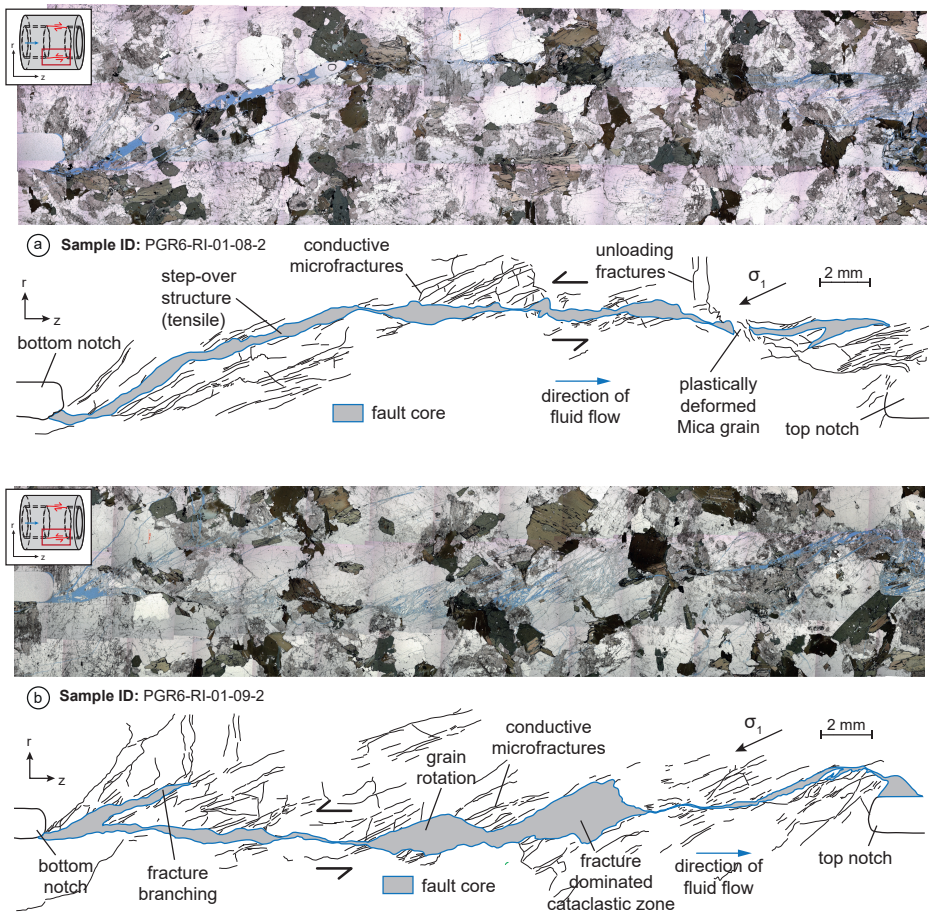

Figure 4.5: Overview of the microfault connecting the lower and upper notch of the sample in thin section and interpretative drawings below indicating the structural features of a granite sample PGR6-RI-01-08-2 (a) and PGR6-RI-01-09-2 (b).

structures (10° to 20°) and occurred mainly as intragranular fractures. The absence of shear displacement led us assume tensile mode they are tensile mode fractures with apertures in the μm range. Some small fractures connected the tensile fractures in the damage zone.

Other fractures grew radially in r-direction and were stress-relaxation fractures formed during unloading in tensile mode (Kluge et al., 2020). Damage zone fractures were highly present in quartz and plagioclase grains, but rather localized or absent in mica grains. Fault particles were brecciated, mostly elongated and very different in size. In plagioclase, identified by their striations, a similar brecciatic fault core could be observed with a maximum width of about 2 mm (figure 4.6a). K-feldspar minerals, without striations, were locally weathered and produced very fine-grained and thin fault gouge (figure 4.6b). Micas were

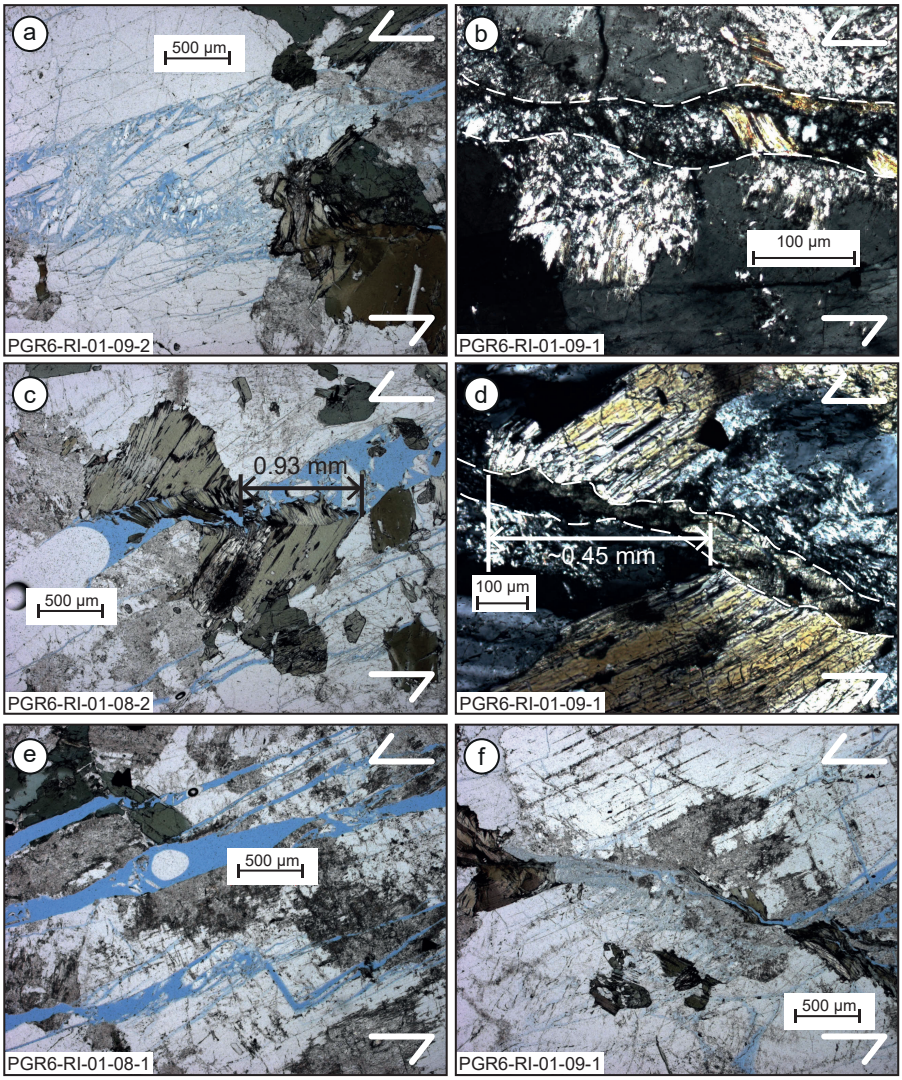

Figure 4.6: Detailed view of cataclastic rock fragments in quartz (a), fine fault gouge filling the fault core (b), displaced mica minerals (c,d), tensional fractures (e) and fault core compression (f) in the Odenwald granite thin sections.

deformed in three different modes: brittle, plastic or smeared out (figures 4.6c, d). Although some mica grains were clearly displaced, they were partly deformed without showing any clear microfractures or void spaces. The plastic deformation of micas resulted in a discontinuous fault core, i.e. no visible void space, at some locations (figure 4.5).

Larger tensile fractures in mainly stiff minerals formed transtensional wedges that lack features of brittle deformation (figure 4.6e). These wedges can be understood as step-over structures connecting zones of simple shear. In weaker minerals, such as mica or feldspar, the fault was characterized by simple shear. In simple shear, faulting was parallel to the displacement direction, which produced a very fine fault gouge (figure 4.6f). In some areas, the orientation changed into compressional or transpressional regimes. Here, the fault core was very thin and shows several splay fractures (figure 4.6f).

The formation of joints, wedges and cavities enabled additional slip accommodation (Segall and Pollard, 1983). The relative displacement was measured at displaced mica minerals at certain locations and varied from 0.45 mm to 0.93 mm (figures 4.6c, d). This was less than the applied axial displacement of 1.2 mm. The fracture branches were hydraulically isolated from the main fault zone, since no microfractures were found connecting them to the main fault.

4.4.2. FAULT GEOMETRY IN FLECHTINGEN SANDSTONE

Two thin sections from the Flechtingen sandstone samples were taken along the z-direction. They showed a narrower, but also continuous fault zone connecting the upper and lower notches of the sample. The inferred direction of maximum principal stress, the flow direction, as well the orientation of the thin section images within the sample are shown for an overview in figures 4.7a, b.

In areas where the fault core was straight it showed a rather constant width (figure 4.8a). The fractures in the damage zone were either intragranular or intergranular and were thus isolated from each other, since clay was found in between the grains (figures 4.1c, d). Furthermore, intragranular fractures were mainly extensional fractures sub-parallel to the maximum compressive stress direction. The clay that originally coated the quartz minerals was smeared across the fault core and produced a very fine gouge (figure 4.8b). The fault mostly propagated along grain boundaries (intergranular). Only in some locations, the quartz grains were brecciated and partially rotated (figures 4.8c, d).

In areas of transpression and simple shear, the fault zone was extremely narrow with clay smear and other fine particles being found along the fault zone (figure 4.8c, d). The fault was wider and more open for fluids when the fault core was oriented similar to the damage zone fractures, i.e. 20° to 30° to the axial displacement direction (figure 4.8e). Splay fractures, typical for large scale faults (Myers and Aydin, 2004), were found to develop in areas of fault compression (figure 4.8f). Step-over structures were absent in the sandstone samples, contrary to the granite fault. Furthermore, most of the displacement was accommodated by the fault core or shear band itself. Rarely any deformation or displacement accommodation was found in the damage zone. Still, strain accommodation within the surrounding rock matrix was hard to identify from our images, but was likely to be a contributing factor.

4.4.3. IMAGE ANALYSIS & SHEAR ZONE WIDTH

To compute the width of the shear zone perpendicular to the flow direction (in z-direction) from the thin section images, we used a combined approach using the software tools IMAGEJ (Schneider et al., 2012) and MATLAB (see appendix for detailed description). The width, w, was defined as the open area of a profile perpendicular to the fracture and corresponds to the measured mechanical fracture dilation, e_{mech}, i.e. the opening of the fault perpendicular to flow. First, the blue epoxy in the thin section images was extracted by separating the respective Hue Saturation Brightness (HSB) color range from the remaining colors present. We assume that the epoxy filled the entire void space. The extracted binary image of the pore space was then imported to Matlab. A sliding square filter was applied

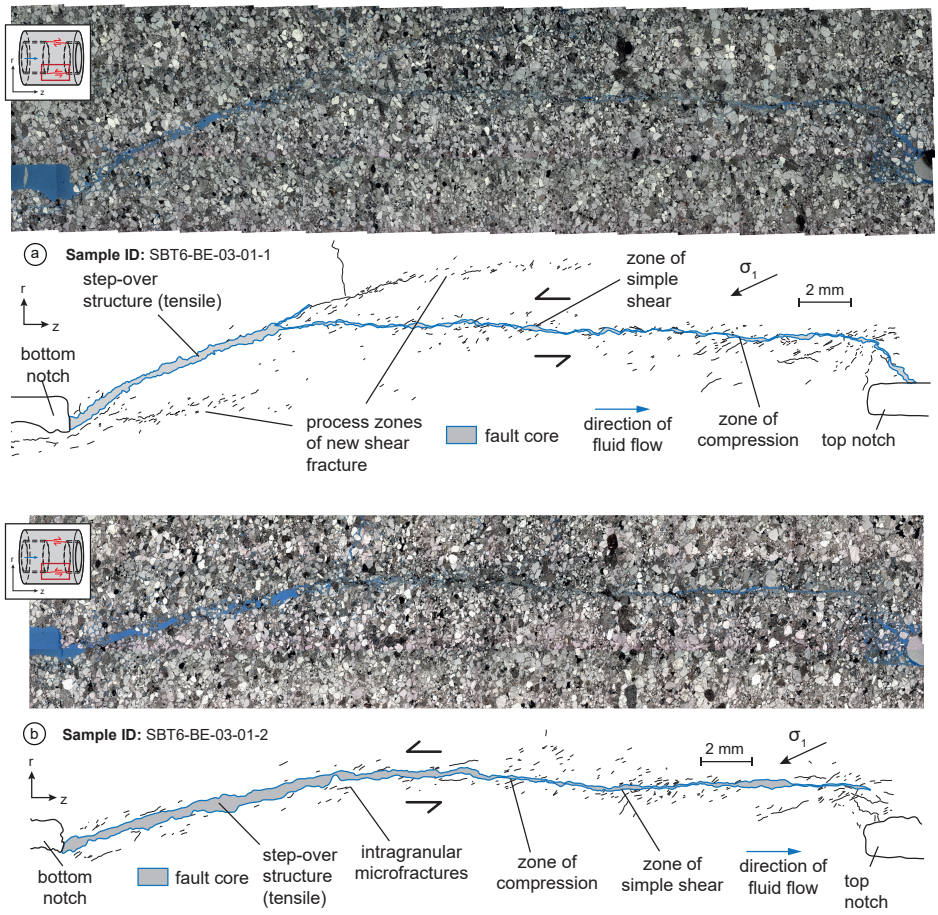

Figure 4.7: Overview of the microfault connecting the lower and upper notch of the sample in thin section and interpretative drawings below indicating the structural features of a sandstone sample SBT6-BE-03-01-1 (a) and SBT6-BE-03-01-2 (b).

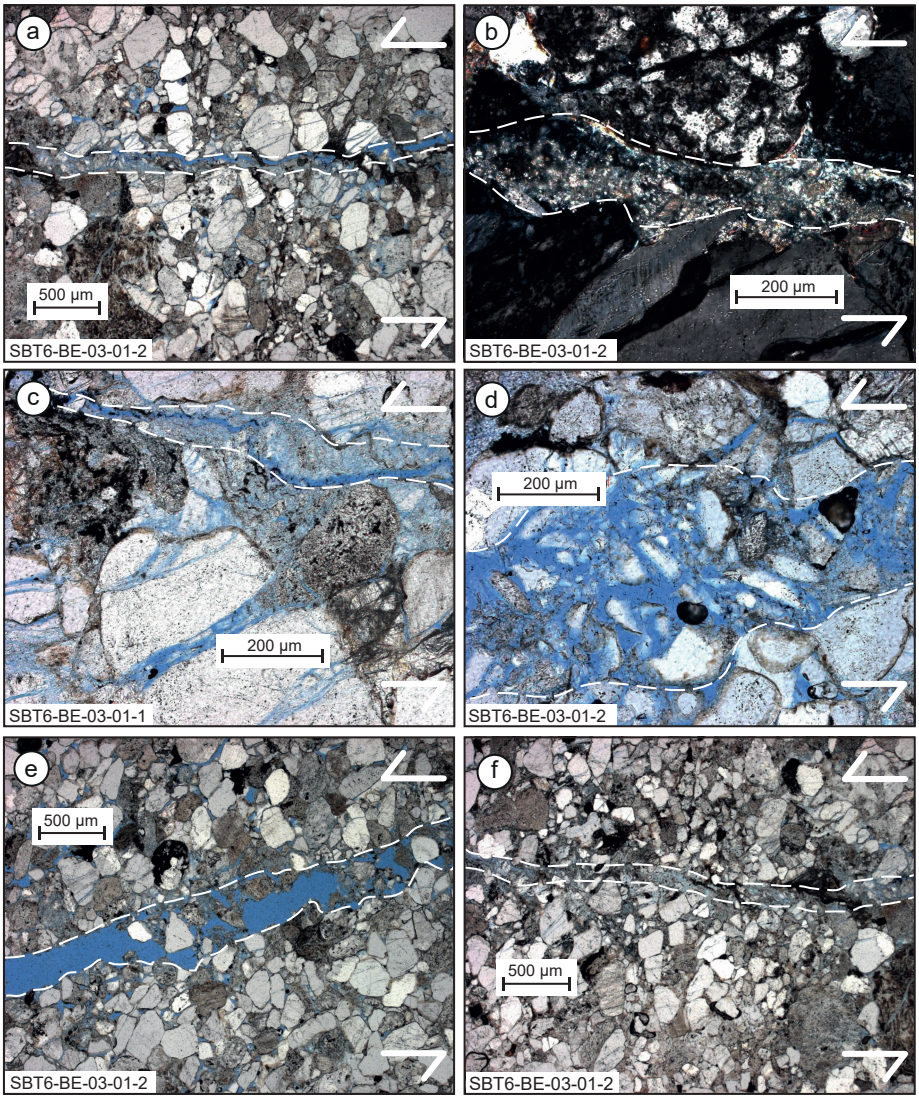

Figure 4.8: Detailed view of the narrow fault core (a), fine fault gouge filling the fault core (b), grain splitting (c), grain fragmentation (d), tensional fractures(e) and fault core compression (f) in the Flechtingen sandstone thin sections.

to calculate the fracture density, n_f, defined as the numbers of black pixels (void space) divided by the number of total pixels inside one window (144). We used a window size of 12 by 12 pixels, corresponding to 3.5 μm by 3.5 μm. This resulted in a fracture density distribution of the fault zone and the surrounding damage zone (figures 4.9a, b). To obtain

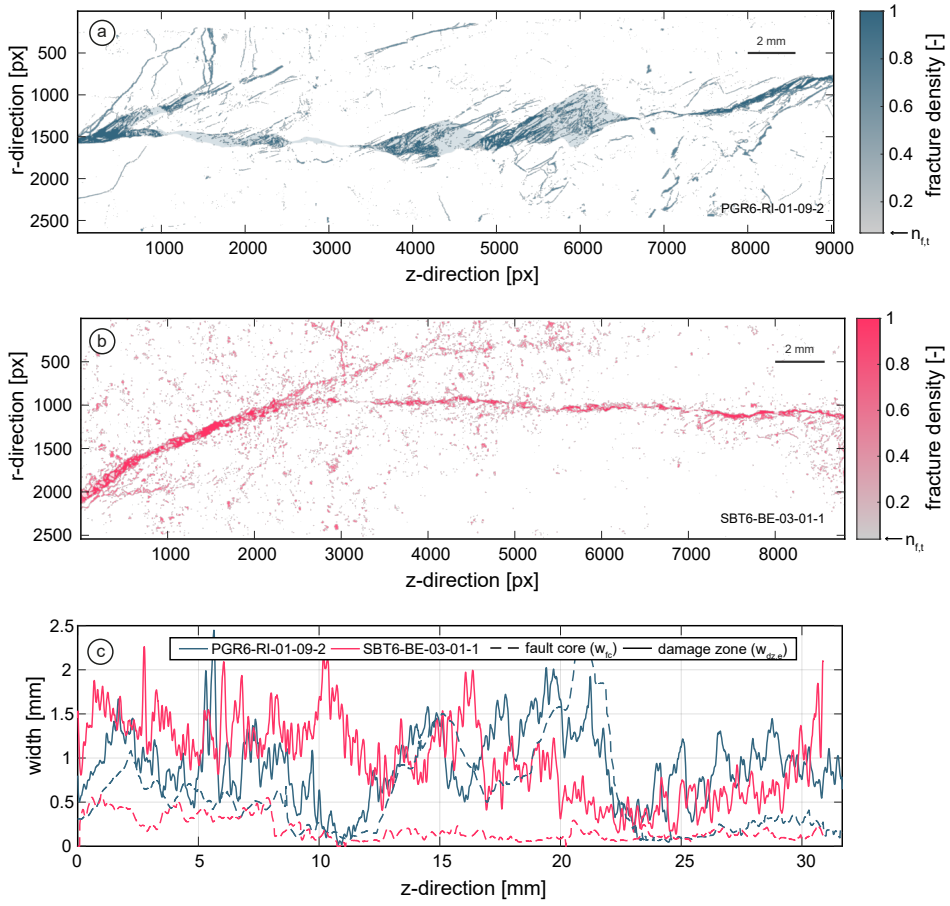

Figure 4.9: Fracture density of the original image (blue or red) and the extracted fault core (grey) in the Odenwald granite (PGR6-RI-01-09-2) (a) and Flechtingen sandstone (SBT6-BE-03-01-1) (b). The effective damage zone width, $w_{dz,e}$, and fault core width, w_{fc}, of both rocks (c).

a fracture density distribution along the fracture, we used two different approaches: (1) we shifted the maximum fracture density towards the center in the direction perpendicular to flow or (2) we sorted the fracture densities in ascending order to then calculate the distribution with the maximum in the center (see appendix). Shifting the fracture density, led to a distribution where the damage zone (low fracture density) was visible to the left and right of the normal distribution. The sorted distribution was smoother with the noise being included in the normal distribution. To separate the actual shear zone from the surrounding rock matrix, we used a threshold for the minimum fracture density to be considered as part of the shear zone. As fracture density threshold value, $n_{f,t}$, we used the intersection point of the shifted and sorted distribution assuming that at this point the fractures in the damage zone

(noise) become dominant (see appendix). This value must be higher than the background noise, which was the mean fracture density in the damage zone surrounding the fault core.

We then calculated the shear zone width by summing up all windows with a fracture density higher then the fracture density threshold, $n_{f,t}$:

$$w = l_{px} \sum_{1}^{N_{px}} n_f|_{n_f > n_{f,t}} \tag{4.6}$$

where w is the width, l_{px} is the length of a pixel (3.5 μm), N_{px} is the number of pixels of a profile, n_f is the fracture density in a single window reduced to a single pixel and $n_{f,t}$ is the fracture density threshold. The fracture density distribution for the granite and sandstone with their shear zone thicknesses are shown in figure 4.9c. The fracture density already shows, that this calculation included high fracture densities outside the main fracture, especially for the sandstone sample. This possibly led to an overestimation of the fault zone width. Therefore, we considered this width as the effective damage zone width, $w_{dz,e}$. The mean damage zone width, $\bar{w}_{dz,e}$, was defined as the mean of the damage zone width of all profiles along the z-direction. The calculated values were 0.93 mm (± 0.42 mm) for the granite and 0.99 mm (± 0.46 mm) for the sandstone (table 4.4). However, this width was similar for both rocks in the transtensional areas close to the lower notch. In the simple shear and transpressional regimes, the sandstone fault was thinner.

In a second approach, we extracted the fault core based on our structural interpretation of the thin sections (figures 4.5 and 4.7). We then applied the same procedure as for the original image (figures 4.9a, b). Computing the width of the extracted fault core with the same threshold, $n_{f,t}$, we found that the fault core width, w_{fc}, was much smaller for the extracted fault core in the sandstone samples compared the effective damage zone width, $w_{dz,e}$ (figure 4.9c). The fracture density threshold, $n_{f,t}$, must be about 0.5, to obtain a similar value of the mean effective damage zone width, $w_{dz,e}$, compared to the mean fault core thickness, $\bar{w}_{fc}$. For the sandstone, $\bar{w}_{fc}$ was about 0.2 mm. The mean fault core width of granite was 0.60 mm (± 0.51 mm) and 0.19 mm (± 0.13 mm) for the sandstone (table 4.4). In the granite sample, the thickness of the extracted fault core was little reduced compared to that of the original image.

We assume that analyzing the original image by extracting the entire void space of the image, we obtained the effective damage zone width, $w_{dz,e}$, or the cumulative area of flow. Contrary, the analysis of the extracted fault core allows to calculate its width, w_{fc}, based on the structural deformation. Comparing the width of the sandstone and granite samples (table 4.4), we see a narrower fault core for the sandstone sample.

4.4.4. VARIATIONS IN SHEAR ZONE WIDTH

Additionally, we calculated the spatial correlations of the width fluctuations along the fracture (in z-direction) using a self-affine geometrical model with a roughness exponent, H (Candela et al., 2009, 2012, Schmittbuhl et al., 1995a). Here we assume that the 2D profile width follows (Meakin, 1998):

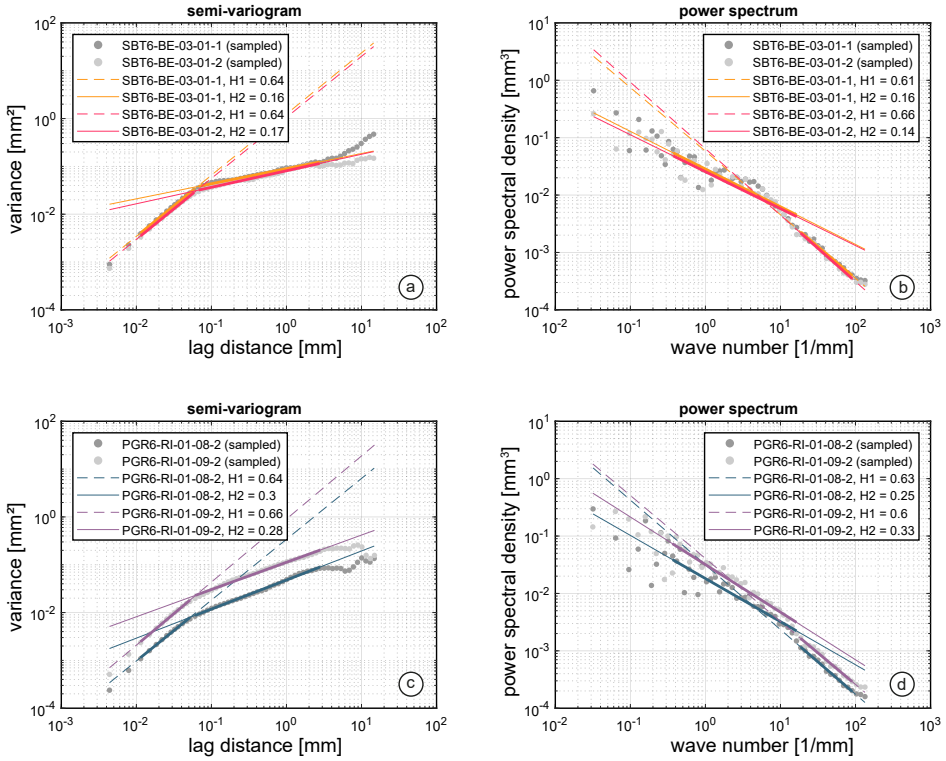

Figure 4.10: Semi-variogram (a,b) and power spectrum (c,d) of the width profiles of the Flechtingen sandstone and Odenwald granite resulting from the image analysis of the thin sections.

$$\delta x \rightarrow \lambda \delta x, \delta z \rightarrow \lambda^H \delta z \tag{4.7}$$

where δx is the coordinate along the 2D profile and δz the amplitude. Therefore, we calculated the power spectrum and the semi-variogram of the width fluctuations (Schmittbuhl et al., 1995a). The width profiles have a resolution of 3.5 μm in z-direction and were linearly detrended (Schmittbuhl et al., 1995b). The data comprised 9000 data points for each profile. Due to the logarithmic scale of the variogram and power spectrum, the data density of the frequencies and lag distances varied. To consider for equal weights of each data point for the fitting procedure, we re-sampled the data points with equidistance in log-space representing the raw data. As a result, we generated 100 data points as a mean from the raw data for further analysis. The Hurst exponent of the variogram, H_{var} was calculated from the slope of the variance, σ^2 in mm^2 vs. the lag distance, h in mm :

$$\sigma^2 = h^{2H_{var}} \tag{4.8}$$

where σ^2 is the variance, h the lag distance and H_{var} is the Hurst exponent from the variogram. The Hurst exponent of the power spectrum, H_{ps}, was calculated from the slope of the frequency spectrum of the fracture width profile in log space using the single-sided spectrum using (Candela et al., 2012):

$$P(k) = Ck^{-1-2H_{ps}} \tag{4.9}$$

where $P(k)$ is the Fourier power spectrum, k is the wave number, C is a pre-factor and H_{ps} is the Hurst exponent from the power spectrum.

The ranges for the fits were equal for the variogram (lag distance in mm) and the power-spectrum (wave number equals the inverse of the lag distance in 1/mm), as well as for the granite and sandstone samples. The results of the roughness calculations are shown in figure 4.10. We found a two power-law behaviour for both the granite and the sandstone samples with a cross-over at about 0.06 mm. The slopes were different for smaller distances between 0.01 to 0.06 mm and larger distances between 0.06 to 3 mm. The roughness exponent for small distances, H_{sd}, was 0.6 and was similar for the granite and sandstone samples. For larger distances the roughness exponent, H_{ld}, was about 0.3 for the granite and 0.15 for the sandstone. A significantly lower roughness exponent at large scales showed that there are low spatial correlations at large scale than at small scales. The close to zero value for the sandstone is an indication that width fluctuations are close to uncorrelated random fluctuations. For the granite, the width fluctuations were more spatially correlated at large scales. This evidences strong similarities of the scaling properties of the shear band width for both materials. However, there was a significative difference for the large scale roughness exponent which make a difference in width variation for both rock types. Variogram and power spectrum gave similar results validating the self-affine measurement. Using various fracture density thresholds, $n_{f,t}$, to calculate the roughness of the width profiles, we obtained similar roughness exponents up to a deviation of $\pm$ 0.1. Only for the power spectrum at smaller distances, H_{ps} reached a value of above 0.9 for a threshold, $n_{f,t}$, of 0.5, while the H_{ps} approached zero at larger scales for the sandstone (figure 4.11). The summarized data are given in table 4.4, where the mean Hurst exponent from the variogram and power spectrum for each sample and the respective ranges are given.

Table 4.4: Properties of fault architecture from the image analysis of the thin sections.

thin section ID	$n_{f,t}$	$\bar{w}_{dz,e}$ (σ)	$\bar{w}_{fc}$ (σ)	H_{sd}	H_{ld}
PGR6-RI-08-01-2	0.07	0.63 (0.35) mm	0.41 (0.19) mm	0.65	0.28
PGR6-RI-09-01-2	0.07	0.93 (0.42) mm	0.60 (0.51) mm	0.63	0.31
SBT6-BE-03-01-1	0.04	0.99 (0.46) mm	0.19 (0.13) mm	0.63	0.16
SBT6-BE-03-01-2	0.04	0.82 (0.45) mm	0.27 (0.15) mm	0.65	0.16

$n_{frac,t}$: fracture density threshold, $\bar{w}_{dz}$: mean damage zone width,
$\bar{w}_{fc}$: mean fault core width, H_{sd}: Hurst exponent for small distances,
H_{ld}: Hurst exponent for large distances, σ: standard deviation

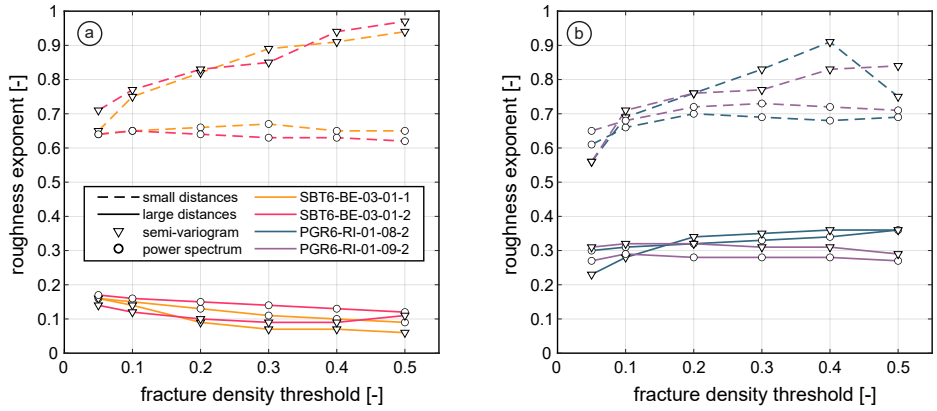

Figure 4.11: Roughness exponent, H, for different fracture density thresholds, $n_{f,t}$ for the Flechtingen sandstone (a) and Odenwald granite (b) at the respective small and large distances.

4.5. DISCUSSION

4.5.1. MICROFAULT PROPAGATION & MICROFAULT ARCHITECTURE

The aim of this paper is to relate macroscopically determined hydraulic and mechanical data to microstructural observations. Therefore, we first discuss the fault propagation mechanisms and structural features. We assume that our observations are related to the sample scale only and that the stress field is not known along the fracture. However, the damage zone microfractures provide a general trend for the largest principal stress (σ_1).

We presented a modified PTS test to generate a shear fracture from an initially intact rock sample with a general orientation that is parallel to the loading direction (Backers and Stephansson, 2012, Kluge et al., 2020). With this test, permeability changes in shear fractures were easy to obtain while shear fracture orientation in space can change with respect to the displacement direction (z-direction). Commonly, shear fractures are generated using tri-axial compression tests. In such tests, intact rock samples are loaded with a differential stress until failure, resulting in an inclined shear fracture at an angle to the loading direction (e.g. Kluge et al., 2017, Mitchell and Faulkner, 2008). This complicates any permeability measurement, because the fluid must flow through the matrix before reaching the fracture.

The fault zones in the sandstone and granite were found to change their orientation along the fracture plane leading to transpressional, simple shear and transtensional structures. Our structural observations include mode I and mode II fractures similar to Amitrano and Schmittbuhl (2002) in tri-axial experiments. We found microfractures oriented mainly 20° to 30° to the direction of the applied stress in both rock types. These open tensile fractures indicate the maximum principle stress direction (σ_1).

The mineral stiffness is important for the development of the microfractures in the damage zone. In the granite, compliant minerals seem to inhibit microfault-growth, which promotes

microcracking in adjacent stiff grains (Wibberley et al., 2000). This seems to enlarge the fault zones compared to the sandstone. Microfractures in granite were partly intergranular while being, both, intra- and partly inter-granular in the clastic sandstone. This is similar to reports by Cox and Scholz (1988). Stiff minerals, such as quartz or plagioclase fail mainly by tensile splitting of the entire mineral (figures 4.7, 4.8). Tensile splitting, previously defined as en echelon splitting (Wibberley et al., 2000), accommodates most of the displacement without generating cataclasis. More compliant minerals, such as mica, behave differently. They deform by either brittle failure, leading to a formation of broken fragments, or by plastic deformation, without fracturing (figure 4.8). This is caused by their anisotropy, such that their orientation within the stress field seems to impact the deformation process.

In low-porosity sandstone rocks, we suggest that the bonding strength between the grains controls the onset of macroscopic fracture propagation, especially in the presence of clay coating. We showed, that a narrow microfault favours to propagate along grain boundaries (intergranular) rather cutting through mineral grains, except when passing through an already split grain (Krishnan et al., 1998). Therefore, frictional sliding at the grain boundaries might be a more dominant process than a sudden rupture. This highlights the importance of soft clays. Additionally, no noticeable decrease or increase in damage zone porosity was found. This indicates, that the classification by Fossen et al. (2007) has limitations for smaller scale and low-displacement fault zones.

From the fault zones generated by the PTS test we can describe three stages of fracture generation for both rocks (figure 4.12): microfracture formation (stage I), principal shear-plane formation (stage II) and shearing (stage III).

During loading and after the samples start yielding, the previously described micro-fractures start to form (stage I, figure 4.12a). Yielding was observed at about 70 % of the peak load, which is slightly above the previously reported critical dilatancy stress of 50 % (Faulkner and Armitage, 2013, Vermilye and Scholz, 1999). The microfractures are assumed to form prior to the principal shear plane, since they surround the fault core (Dunn et al., 1973). In the sandstone they reveal the location and orientation of the fracture process zones.

During failure (stage II, figure 4.12b), a macroscopic fracture is assumed to connect these microfractures to form a principal shear plane (Cox and Scholz, 1988, Tenthorey and Cox, 2006, Vermilye and Scholz, 1999). Fracturing starts from the bottom notch of the sample due to the higher shear stress at this point (Backers and Stephansson, 2012, Kluge et al., 2020). The notch represents a pre-existing fracture where shear fractures commonly nucleate (Janssen et al., 2001, Reches and Lockner, 1994, Segall and Pollard, 1983).

With increasing shear displacement (stage III, figure 4.12c) different structures start to develop. Transtensional wedges are present in areas where the principle shear plane is oriented according to the micro-fractures (20 to 30 degrees). Simple shear structures form in areas where the principal shear plane is parallel to the direction of loading. Transpressional zones form where the principal shear plane is oriented opposite to the microfractures. These various structures are important for the fluid flow in shear zones, as we show in the next section. During progressive shearing, we did not observe a stress built up and release (stick-slip). We assume that the applied displacement of maximum 1.2 mm leaves the fault in an early

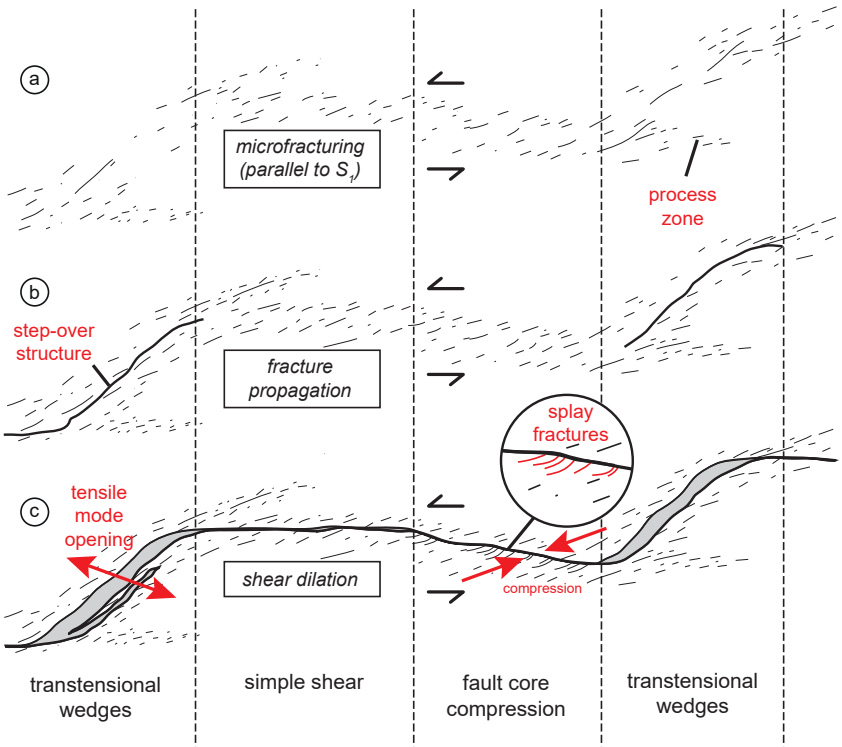

Figure 4.12: Interpretational model for the fracture propagation during shear fracture growth with (a) microfracturing, (b) fracture propagation and (c) shear dilation, as well as the resulting structural elements of the fault zone.

stage of fault propagation.

4.5.2. IMPACT OF FAULT ARCHITECTURE ON HYDRAULIC PROPERTIES

The permeability change caused by introducing a microfault into an intact rock sample under in-situ pressure conditions gave different results for granite and low-porosity sandstone. The granite showed an increase in permeability of 2 to 3 orders of magnitude, while the sandstone showed almost no increase in permeability. In the following, we discuss the experimental results with respect to microstructural features separately for Odenwald granite (PGR6-RI) and the Flechtingen sandstone (SBT6-BE).

For the granite, we assume the permeability increase is mainly related to the presence of the microfault connecting the lower and upper notches. This is because of the large permeability enhancement measured during microfault generation. The complex microfault architecture, consisting of a damage zone and fault core, mainly controls the fluid flow in the fractured sample.

When the fault zone is comprised of stiff minerals, fracturing due to brittle deformation and grain rotation is promoted. Consequently, in areas with a large quartz content the permeability is likely to be higher compared to areas with less quartz. Mica are critical to the fault permeability since they partially block the fracture porosity. This can be compensated by the existence of a damage zone surrounding impermeable zones. Here, opening mode fractures in the damage zone parallel or sub-parallel to maximum principal stress aid fluid flow.

Grain rotation is limited due to the relatively low applied displacement of 1.2 mm. The strength of the minerals therefore controls the frictional properties of the fault. At higher displacements the grain size of the cataclastic material controls the frictional strength and hydraulic properties (Bos and Spiers, 2001, Stünitz et al., 2010).

Very little permeability increase was measured during faulting and shearing for the Flechtingen sandstone samples, suggesting that the matrix permeability is higher than the fracture permeability. Fossen et al. (2007) argued that dilatant fractures are common for low porosity sandstone and compaction bands for high porosity sandstones. We could not proof such a phenomena. We assume, that the pore-throat fillings and possible grain coating minerals since the fault propagates along grain-boundaries. But although the fault might be dilatant in a low-porosity rock, permeability is not necessarily enhanced, especially in the presence of clay. Still, the microstructure indicates that there are still open sections (areas of transtension), enhancing fluid flow in flow directions perpendicular to the displacement direction.

We therefore suggest to classify the potential fault permeability including the presence of clay, similar to Fisher and Knipe (1998). They distinguished between clean and impure sandstones depending on the presence of more or less than 15% of clay. We already see an impact for the Flechtingen sandstone with 8% of clay. This especially affects low-displacement microfaults where the damage zone is not fully developed.

Granites potentially have a larger fracture width compared to sandstones, which is an additional explanation for the lower permeability measured in the sandstone samples. The measured fracture dilation, e_{mech}, was about 5 to 10 times lower for all samples compared to the fault core width, w_{fc}. This possibly resulted from the fact, that the fracture re-opened during unloading before preparing the thin sections. Additionally, the fault core width, w_{fc}, ignores particles within the fault core leading to an overestimation of fracture width. Still, it provides an understanding of the relative width distribution along the fracture. Furthermore, the fracture dilation, e_{mech}, was measured at a single point, at which the measured dilation can be higher or lower compared to the mean value along the fault (Marache et al., 2008). Lastly, the fracture zone width, w, and the fracture dilation, e_{mech}, were measured perpendicular to the flow direction. But because fractures were often inclined by 20° to 30° in areas of transtension, there is an additional aperture error of 6 to 14 %.

We suggest, that a self-affine scaling-relationship ($\delta x \rightarrow \lambda \delta x, \delta z \rightarrow \lambda^H \delta z$) exists not only for the fracture surface roughness (e.g. Candela et al., 2009), but also for the variations in fracture width in shear fractures. We found a two scale regime for roughness, similar to the analysis by Santucci et al. (2010). They related the crossover length scale to fluctuations in fracture toughness and the stress intensity factor which gave H = 0.6 to 0.7 for small

scales and $H = 0.3$ for large scales. However, at larger scales the sandstone gives a lower roughness exponent of about 0.15 compared to the granite with 0.3. This is similar to reports by Boffa et al. (1998). For the sandstone, the scaling relationship is lost at large scales using the power spectrum method, since H approaches zero. This indicates a constant rms-value independent of the scale, such that there is no spatial correlation.

The morphology of the fault controls the dilation potential and therefore the hydraulic properties. The scale-dependent dilation potential from our results can only be described qualitatively. The Odenwald granite showed a more pronounced morphology and a larger variety in structural features. This led to a larger fault zone width and possibly larger permeability compared to the Flechtingen sandstone. The sandstone has lower width fluctuations, a narrower fault core width, w_{fc}, shows clay in the pore-throats and has intergranular fractures in the damage zone. This reduces a potential permeability enhancement. But the much larger effective damage zone width, $w_{dz,e}$, and matrix porosity allows for fluid flow and deformation around the fracture.

In general, dilational jogs, step-over structures and transtensional wedges are favourable for fluid flow. They lead to larger apertures and almost no cataclasis or grain crushing (Janssen et al., 2001). This results in heterogeneous flow directions and increased local pore pressures built ups when fluid tries to flow from high aperture zones to low aperture zones (Passelègue et al., 2018). However, the impact of the magnitude of the external stress on fault permeability and structure needs to be investigated since several authors already suggested a dependence of fault permeability with confining stress (Wibberley et al., 2000, Zoback and Byerlee, 1975).

4.5.3. SUSTAINABILITY OF FAULT PERMEABILITY

In the following section, we discuss the fault permeability during variations in effective stress, or in other words, what controls the fracture closure and therefore the longevity of the generated permeability.

The largest permeability reduction in both rocks was caused by time-dependent processes after fault generation. Three possible mechanisms need to be considered responsible for fracture closure: (a) chemical rock-fluid interactions, i.e. dissolution or precipitation of minerals (Orywall et al., 2017), (b) fines migration leading to a blockage of fluid pathways within the fault (Blöcher et al., 2016), and (c) mechanical creep, i.e. compaction or rearrangement of fault gouge particles (Hofmann et al., 2016). Mechanical back-slip is not possible, since the axial displacement piston was hold in place when monitoring time-dependent permeability changes.

Rock-fluid interactions, re-crystallization or cementations are not influencing permeability in our short-term experiments. Such processes evolve over long time-scales of several weeks (Fisher and Knipe, 2001, Yasuhara and Elsworth, 2008) and require saline solution as pore fluid, while we used distilled water.

No fines migration or particle re-distribution was found in the microfaults we analysed. Fine particles or breccia in the fault core were not found to have migrated. Still, finer particles

might have been removed by the preparation process when blue epoxy was injected into the sample.

We assume that mechanical closure or power law compaction of the faults was the most contributing effect causing the permeability reduction. This is often frequently reported from laboratory experiments (Hofmann et al., 2016, Im et al., 2018). The permeability decrease of the granite samples follows a power law compaction, possibly by rearrangements of fault gouge material or asperities (Kluge et al., 2020). The permeability loss might be recovered by new slip events (Im et al., 2018), but this was not tested in our experiments. We attribute the permeability loss over time of the sandstone samples to compaction of the matrix and fracture, because of the larger dilation magnitudes, the higher porosity and the smaller fault core.

The reported reversible changes in permeability during effective pressure changes in both rocks are in contrast to existing studies. Other researchers found that any increase in effective pressure leads to a reduction in permeability with an increasing number of stress cycles (e.g. Chen et al., 2000, Hofmann et al., 2016, Pyrak-Nolte and Morris, 2000, Watanabe et al., 2009). The amount of permanent permeability changes might be controlled by: (a) the amount of plastic energy in the system, (b) the contact material of the fracture surfaces (c) the effective pressure coefficient.

We suggest that the lower amount of plastic energy in existing fault zones reduced the risk of a permanent fracture closure during changes in effective pressure. The amount of plastic energy depends on the conditions during fracture generation. Fracturing can occur when loading and fracturing under in-situ pressure or at ambient conditions. A high amount of plastic energy is to be expected when fractures are produced at ambient conditions, for example using manually displaced tensile or saw-cut fractures (Fang et al., 2017, Hofmann et al., 2016, Watanabe et al., 2009), as well as artificial fracture surfaces (Im et al., 2018, Ishibashi et al., 2020). Those experiments depict artificially generated fractures for example by hydraulic stimulation. They are potentially critical to larger magnitudes of permanent fracture closure. The experimental results obtained by the PTS test depict pre-existing shear fractures, possibly generated by tectonic movements. Since they are produced at in-situ stress conditions, they are less critical to permanent permeability changes.

We assume that cataclastic fault gouge and plastically deformed mica grains partly control the elastic and reversible behaviour of permeability. This is supported by the lack of any irreversible deformation, such as fractures oriented perpendicular to the displacement direction or grain crushing. Consequently, the contact points in areas of transpression or simple shearing should be used for modelling crustal strength, similar to what Bos and Spiers (2001) and Niemeijer and Spiers (2005) proposed.

Even larger changes in pore pressure in faults generated by tectonic movements are not necessarily critical to permeability. This is important for faulted low-porosity clastic geothermal reservoirs (Blöcher et al., 2016), as well as natural fault zones in granitic rocks (Genter et al., 2012). But more such evidence is needed on the field scale.

4.6. CONCLUSIONS

We measured the evolution of permeability and fracture dilation using an innovative experimental set-up, the Punch-Through Shear (PTS) test. We observed the following permeability evolution for Odenwald granite and Flechtingen sandstone: (I) fault generation and shearing leads to a permeability enhancement of more than 2 orders of magnitude in Odenwald granite, but an unchanged permeability in low-porosity Flechtingen sandstones. This might be caused by the presence of a larger fault core and a conductive damage zone in the Odenwald granite. The larger matrix permeability, a smaller fault core and the presence of clay leads to no noticeable increase for the low-porosity Flechtingen sandstone. Still, the presence of a variety of structural features might support a heterogenous flow field independent of the rock type. (II) The highest permeability loss was found during time-dependent processes during the first hours after fracture generation. This is likely caused by time-dependent compaction of the fracture and re-arrangements of fault particles, as well as the matrix compaction in the Flechtingen sandstone. (III) Pore pressure changes in a fault produced under in-situ pressure conditions cause an elastic permeability change. This is due to the low plastic energy contained in the fault zone because of the in-situ fracture generation. Therefore we assume that naturally faulted geothermal reservoirs might have a sufficient hydraulic sustainability considering only mechanical effects.

Thin section observations and image analysis revealed local width changes depending on the structural geometry of the fault: transtension, simple-shear or transpression. In transtensional regimes the permeability might even be increased in sandstone rocks. This would also lead to a bi-directional permeability, although this cannot be proven by the bulk permeability measurements. Furthermore, the width profiles indicated a self-affine scaling relationship similar to what is commonly observed for fracture surface roughness.

APPENDIX: DESCRIPTION OF IMAGE ANALYSIS PROCEDURES

To describe the procedure to calculate the width of the fault zone, $w_{dz,e}$ and w_{fc}, we will describe the methodology for one thin section images of the granite (PGR6-RI-01-09-2) and sandstone (SBT6-BE-03-01-1), respectively. The fracture density is given by amount of pixels identified as void space in a window of a certain size. Therefore, a squared sliding filter was applied to the binary image resulting from the extracting the blue epoxy (HSB range) from the thin section images (figures 4.13a and 4.14a). The fracture densities were re-arranged by either shifting or sorting the values for each profile along the fault (z-direction). Shifting was performed by finding the maximum fracture density in each profile and shifting the entire profile accordingly using the *circshift* function in MATLAB (figures 4.13b and 4.14b). Sorting was performed by sorting the fracture density of each profile in the ascending order (figures 4.13c and 4.14c). Both approaches result in a fracture density distribution of each profile (r-direction). These distributions were then stacked along the z-direction, such that the mean distribution could be calculated. This distribution is largely dependent on the window size used for the squared sliding filter. The window size was decided upon the largest peak in density distribution for the shifted fracture density. Therefore, several window sizes from 2 by 2 to 92 by 92 pixels were considered. Figures

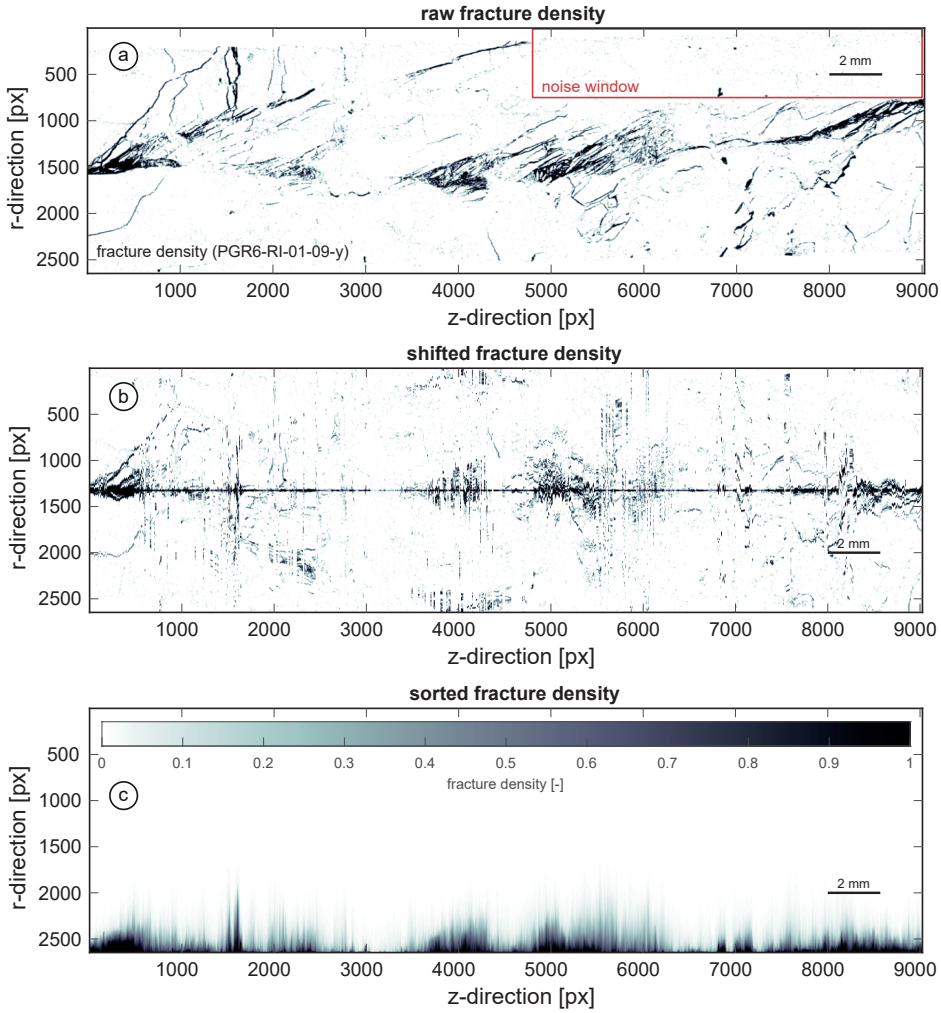

Figure 4.13: Fracture density of the original binary image (a), as well as the shifted (b) and sorted (c) fracture density of granite sample PGR6-RI-01-09-2.

4.15a and b show the fracture density distribution for the shifted fracture density for the granite and sandstone. For too small window sizes, the distribution is smeared out across each stacked profile without a clear peak. Too high window sizes lead to a large smoothing effect showing no clear peak. At a window size of 12 by 12 pixels we find a clear peak and an even distribution of fracture density across the profiles. Therefore we decided to use a window size of 12 by 12 for our calculations.

Three possible criteria for defining the fracture density threshold value, $n_{f,t}$, were considered: (1) the background noise, (2) the intersection of the sorted and shifted fracture density

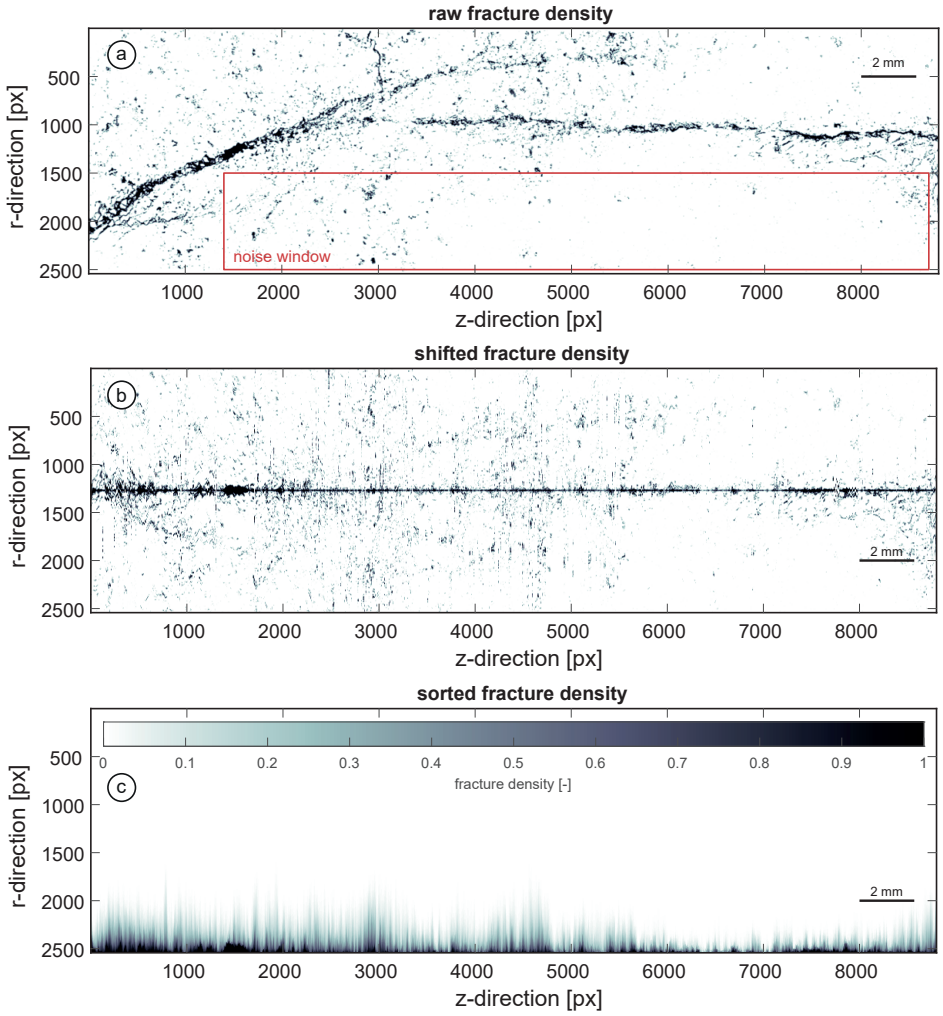

Figure 4.14: Fracture density of the original binary image (a), as well as the shifted (b) and sorted (c) fracture density of sandstone sample SBT6-BE-03-01-1.

distribution and (3) sample porosity. For the first criteria we assumed that background noise can be derived from the mean fracture density in an area outside the fault core. Therefore, we have applied the squared sliding filter in there areas of the sandstone and granite (figures 4.13a and 4.14a), assuming that this area is less affected by fracturing and calculated the mean fracture density. This analysis resulted in a mean fracture density of 0.003 for the background noise of the granite and 0.015 for the sandstone (figures 4.15c, d). These values, however, were too low when considering this for the shifted fracture density of entire image, since it is well below the limbs of the distribution. This results in an overestimation of the fracture width. A second approach was to consider the intersection of the shifted and

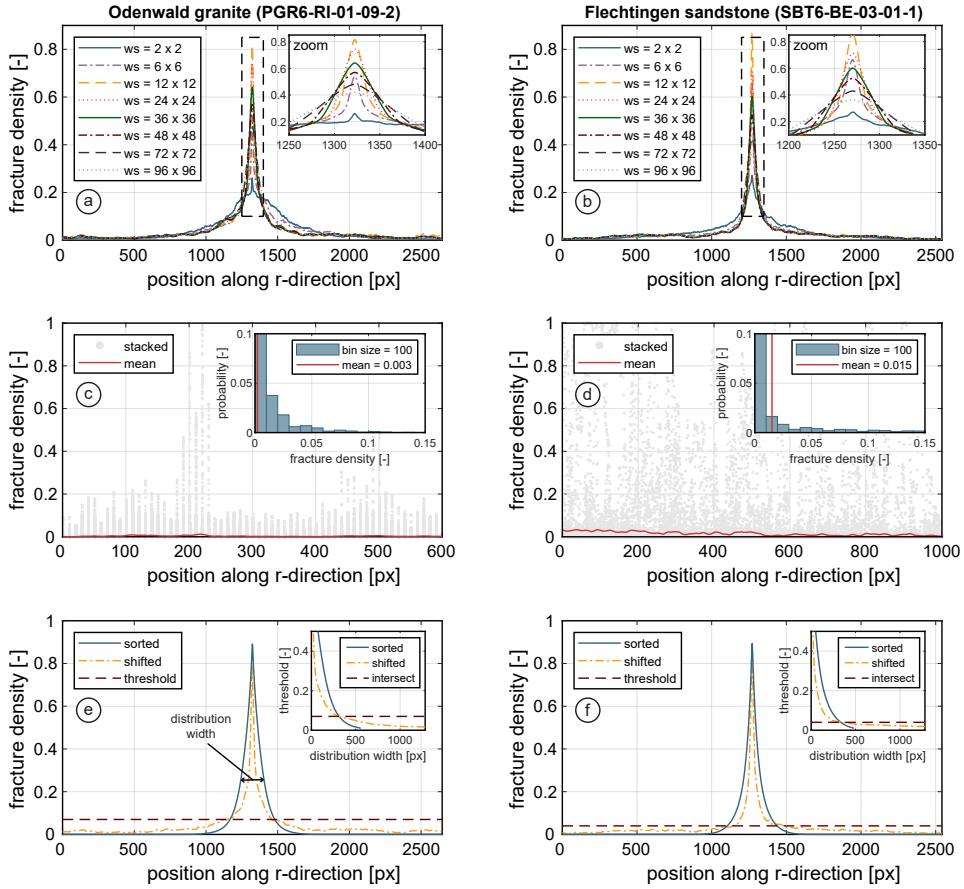

Figure 4.15: Fracture density distribution: effect of window size (a,b), measured fracture density noise (c,d) and intersection of the sorted and shifted fracture density distributions (e,f).

sorted fracture density distribution. The intersection of both distributions shows the onset at which the background noise or the fracture density of the damage zone becomes dominant in the shifted distribution. For the granite we found intersection point of the sorted and shifted distribution width at a fracture density of 0.07 and for the sandstone at 0.04 (figures 4.15e, f). Lastly, the sample porosity was considered as a threshold value, because the porosity of the sample should reflect the porosity in each profile, assuming that all porosity is filled with blue epoxy. However, the porosity for the granite is less than 1 % resulting in a fracture density threshold of 0.01, which is below the measured noise. Contrary, the porosity of the sandstone is about 7.5 % resulting in a fracture density threshold of 0.07, which is larger then the intersection point of the shifted and sorted distribution. Comparing all three methods and the resulting shear zone width (figure 4.12), we decided for the intersection point method to define the fracture density threshold.

REFERENCES

D. Amitrano and J. Schmittbuhl. Fracture roughness and gouge distribution of a granite shear band. *Journal of Geophysical Research: Solid Earth*, 107(B12):ESE 19–1–ESE 19–16, dec 2002. doi: 10.1029/2002JB001761.

T. Backers and O. Stephansson. ISRM suggested method for the determination of mode II fracture toughness. *Rock Mechanics and Rock Engineering*, 45(6):1011–1022, jul 2012. doi: 10.1007/s00603-012-0271-9.

A. Barnhoorn, S. F. Cox, D. J. Robinson, and T. Senden. Stress- and fluid-driven failure during fracture array growth: Implications for coupled deformation and fluid flow in the crust. *Geology*, 38(9):779–782, sep 2010. doi: 10.1130/G31010.1.

N. Barton, S. Bandis, and K. Bakhtar. Strength, deformation and conductivity coupling of rock joints. *International Journal of Rock Mechanics and Mining Sciences & Geomechanics Abstracts*, 22(3):121–140, jun 1985. doi: 10.1016/0148-9062(85)93227-9.

G. Blöcher, T. Reinsch, A. Hassanzadegan, H. Milsch, and G. Zimmermann. Direct and indirect laboratory measurements of poroelastic properties of two consolidated sandstones. *International Journal of Rock Mechanics and Mining Sciences*, 67:191–201, apr 2014. doi: 10.1016/j.ijrmms.2013.08.033.

G. Blöcher, T. Reinsch, J. Henninges, H. Milsch, S. Regenspurg, J. Kummerow, H. Francke, S. Kranz, A. Saadat, G. Zimmermann, and E. Huenges. Hydraulic history and current state of the deep geothermal reservoir groß schönebeck. *Geothermics*, 63:27–43, sep 2016. doi: 10.1016/j.geothermics.2015.07.008.

G. Blöcher, C. Kluge, T. Goense, L. Pei, R. R. Bakker, and D. F. Bruhn. Hydraulic-mechanical characterization of geothermal reservoir rocks. In *European Geothermal Congress 2019, Den Haag, The Netherlands, 11-14 June*, 2019.

J. M. Boffa, C. Allain, and J. P. Hulin. Experimental analysis of fracture rugosity in granular and compact rocks. *The European Physical Journal Applied Physics*, 2(3):281–289, jun 1998. doi: 10.1051/epjap:1998194.

B. Bos and C. J. Spiers. Experimental investigation into the microstructural and mechanical evolution of phyllosilicate-bearing fault rock under conditions favouring pressure solution. *Journal of Structural Geology*, 23(8):1187–1202, aug 2001. doi: 10.1016/S0191-8141(00)00184-X.

T. Candela, F. Renard, M. Bouchon, A. Brouste, D. Marsan, J. Schmittbuhl, and C. Voisin. Characterization of fault roughness at various scales: Implications of three-dimensional high resolution topography measurements. *Pure and Applied Geophysics*, 166(10-11): 1817–1851, jun 2009. doi: 10.1007/s00024-009-0521-2.

T. Candela, F. Renard, Y. Klinger, K. Mair, J. Schmittbuhl, and E. E. Brodsky. Roughness of fault surfaces over nine decades of length scales. *Journal of Geophysical Research: Solid Earth*, 117(B8):n/a–n/a, aug 2012. doi: 10.1029/2011JB009041.

G. Chambon, J. Schmittbuhl, A. Corfdir, N. Orellana, M. Diraison, and Y. Géraud. The thickness of faults: From laboratory experiments to field scale observations. *Tectonophysics*, 426(1-2):77–94, oct 2006. doi: 10.1016/j.tecto.2006.02.014.

L. Chen, J. F. Liu, C. Wang, J. Liu, R. Su, and J. Wang. Characterization of damage evolution in granite under compressive stress condition and its effect on permeability. *International Journal of Rock Mechanics and Mining Sciences*, 71:340–349, oct 2014. doi: 10.1016/j.ijrmms.2014.07.020.

Z. Chen, S. P. Narayan, Z. Yang, and S. S. Rahman. An experimental investigation of hydraulic behaviour of fractures and joints in granitic rock. *International Journal of Rock Mechanics and Mining Sciences*, 37(7):1061–1071, oct 2000. doi: 10.1016/S1365-1609(00)00039-3.

S. J. D. Cox and C. H. Scholz. On the formation and growth of faults: an experimental study. *Journal of Structural Geology*, 10(4):413–430, jan 1988. doi: 10.1016/0191-8141(88)90019-3.

H. P. G. Darcy. *Les Fontaines publiques de la ville de Dijon. Exposition et application des principes á suivre et des formules 'a employer dans les questions de distribution d'eau, etc.* V. Dalamont, 1856.

D. E. Dunn, L. J. LaFountain, and R. E. Jackson. Porosity dependence and mechanism of brittle fracture in sandstones. *Journal of Geophysical Research*, 78(14):2403–2417, may 1973. doi: 10.1029/JB078i014p02403.

J. E. Elkhoury, A. Niemeijer, E. E. Brodsky, and C. Marone. Laboratory observations of permeability enhancement by fluid pressure oscillation of in situ fractured rock. *Journal of Geophysical Research*, 116(B2), feb 2011. doi: 10.1029/2010JB007759.

J. P. Evans, C. B. Forster, and J. V. Goddard. Permeability of fault-related rocks, and implications for hydraulic structure of fault zones. *Journal of Structural Geology*, 19(11):1393–1404, nov 1997. doi: 10.1016/S0191-8141(97)00057-6.

Y. Fang, D. Elsworth, C. Wang, T. Ishibashi, and J. P. Fitts. Frictional stability-permeability relationships for fractures in shales. *Journal of Geophysical Research: Solid Earth*, 122(3):1760–1776, mar 2017. doi: 10.1002/2016JB013435.

Y. Fang, D. Elsworth, C. Wang, and Y. Jia. Mineralogical controls on frictional strength, stability, and shear permeability evolution of fractures. *Journal of Geophysical Research: Solid Earth*, 123(5):3549–3563, may 2018. doi: 10.1029/2017JB015338.

I. Faoro, A. Niemeijer, C. Marone, and D. Elsworth. Influence of shear and deviatoric stress on the evolution of permeability in fractured rock. *Journal of Geophysical Research: Solid Earth*, 114(B1), jan 2009. doi: 10.1029/2007JB005372.

D. Faulkner and P. Armitage. The effect of tectonic environment on permeability development around faults and in the brittle crust. *Earth and Planetary Science Letters*, 375:71–77, aug 2013. doi: 10.1016/j.epsl.2013.05.006.

D. Faulkner, C. Jackson, R. Lunn, R. Schlische, Z. Shipton, C. Wibberley, and M. Withjack. A review of recent developments concerning the structure, mechanics and fluid flow properties of fault zones. *Journal of Structural Geology*, 32(11):1557–1575, nov 2010. doi: 10.1016/j.jsg.2010.06.009.

Q. Fisher and R. Knipe. The permeability of faults within siliciclastic petroleum reservoirs of the north sea and norwegian continental shelf. *Marine and Petroleum Geology*, 18 (10):1063–1081, dec 2001. doi: 10.1016/S0264-8172(01)00042-3.

Q. J. Fisher and R. J. Knipe. Fault sealing processes in siliciclastic sediments. *Geological Society, London, Special Publications*, 147(1):117–134, 1998. doi: 10.1144/GSL.SP.1998.147.01.08.

H. Fossen, R. A. Schultz, Z. K. Shipton, and K. Mair. Deformation bands in sandstone: a review. *Journal of the Geological Society*, 164(4):755–769, jul 2007. doi: 10.1144/0016-76492006-036.

A. Genter, N. Cuenot, and X. G. and. Status of the soultz geothermal project during exploitation between 2010 and 2012. In *37th Workshop on Geothermal Reservoir Engineering, Stanford University, California, USA, Jan 2012, Stanford, United States. SGP-TR-194, 12 p. hal-00697602*, 2012.

A. Hansen and J. Schmittbuhl. Origin of the universal roughness exponent of brittle fracture surfaces:stress-weighted percolation in the damage zone. *Physical Review Letters*, 90(4), jan 2003. doi: 10.1103/PhysRevLett.90.045504.

A. Hassanzadegan, G. Blöcher, H. Milsch, L. Urpi, and G. Zimmermann. The effects of temperature and pressure on the porosity evolution of flechtinger sandstone. *Rock Mechanics and Rock Engineering*, 47(2):421–434, apr 2014. doi: 10.1007/s00603-013-0401-z.

H. Hofmann, G. Blöcher, H. Milsch, T. Babadagli, and G. Zimmermann. Transmissivity of aligned and displaced tensile fractures in granitic rocks during cyclic loading. *International Journal of Rock Mechanics and Mining Sciences*, 87:69–84, sep 2016. doi: 10.1016/j.ijrmms.2016.05.011.

K. Im, D. Elsworth, and Y. Fang. The influence of preslip sealing on the permeability evolution of fractures and faults. *Geophysical Research Letters*, 45(1):166–175, jan 2018. doi: 10.1002/2017GL076216.

T. Ishibashi, Y. Fang, D. Elsworth, N. Watanabe, and H. Asanuma. Hydromechanical properties of 3d printed fractures with controlled surface roughness: Insights into shear-permeability coupling processes. *International Journal of Rock Mechanics and Mining Sciences*, 128:104271, apr 2020. doi: 10.1016/j.ijrmms.2020.104271.

C. Janssen, F. Wagner, A. Zang, and G. Dresen. Fracture process zone in granite: a microstructural analysis. *International Journal of Earth Sciences*, 90(1):46–59, feb 2001. doi: 10.1007/s005310000157.

C. Kluge, H. Milsch, and G. Blöcher. Permeability of displaced fractures. *Energy Procedia*, 125:88–97, sep 2017. doi: 10.1016/j.egypro.2017.08.077.

C. Kluge, G. Blöcher, A. Barnhoorn, and D. Bruhn. Hydraulic-mechanical properties of microfaults in granitic rock using the punch-through shear test. *International Journal of Rock Mechanics and Mining Sciences*, 134:104393, oct 2020. doi: 10.1016/j.ijrmms.2020.104393.

G. Krishnan, X. Zhao, M. Zaman, and J.-C. Roegiers. Fracture toughness of a soft sandstone. *International Journal of Rock Mechanics and Mining Sciences*, 35(6):695–710, sep 1998. doi: 10.1016/S0148-9062(97)00324-0.

D. A. Lockner, J. D. Byerlee, V. Kuksenko, A. Ponomarev, and A. Sidorin. Quasi-static fault growth and shear fracture energy in granite. *Nature*, 350(6313):39–42, mar 1991. doi: 10.1038/350039a0.

A. Marache, J. Riss, and S. Gentier. Experimental and modelled mechanical behaviour of a rock fracture under normal stress. *Rock Mechanics and Rock Engineering*, 41(6): 869–892, apr 2008. doi: 10.1007/s00603-008-0166-y.

P. Meakin. *Fractals, scaling and growth far from equilibrium*. Cambridge university press, vol. 5 edition, 1998.

H. Milsch, H. Hofmann, and G. Blöcher. An experimental and numerical evaluation of continuous fracture permeability measurements during effective pressure cycles. *International Journal of Rock Mechanics and Mining Sciences*, 89:109–115, nov 2016. doi: 10.1016/j.ijrmms.2016.09.002.

T. M. Mitchell and D. R. Faulkner. Experimental measurements of permeability evolution during triaxial compression of initially intact crystalline rocks and implications for fluid flow in fault zones. *Journal of Geophysical Research*, 113(B11), nov 2008. doi: 10.1029/2008JB005588.

D. Moore and D. Lockner. The role of microcracking in shear-fracture propagation in granite. *Journal of Structural Geology*, 17(1):95–114, jan 1995. doi: 10.1016/0191-8141(94)E0018-T.

R. Myers and A. Aydin. The evolution of faults formed by shearing across joint zones in sandstone. *Journal of Structural Geology*, 26(5):947–966, may 2004. doi: 10.1016/j.jsg.2003.07.008.

A. Nicolas, G. Blöcher, C. Kluge, Z. Li, H. Hofmann, L. Pei, H. Milsch, J. Fortin, and Y. Guéguen. Pore pressure pulse migration in microcracked andesite recorded with fibre optic sensors. *Geomechanics for Energy and the Environment*, 24:100183, dec 2020. doi: 10.1016/j.gete.2020.100183.

A. R. Niemeijer and C. J. Spiers. Influence of phyllosilicates on fault strength in the brittle-ductile transition: insights from rock analogue experiments. *Geological Society, London, Special Publications*, 245(1):303–327, 2005. doi: 10.1144/GSL.SP.2005.245.01.15.

P. Orywall, K. Drüppel, D. Kuhn, T. Kohl, M. Zimmermann, and E. Eiche. Flow-through experiments on the interaction of sandstone with ba-rich fluids at geothermal conditions. *Geothermal Energy*, 5(1), oct 2017. doi: 10.1186/s40517-017-0079-7.

F. X. Passelègue, N. Brantut, and T. M. Mitchell. Fault reactivation by fluid injection: Controls from stress state and injection rate. *Geophysical Research Letters*, 45(23), dec 2018. doi: 10.1029/2018GL080470.

L. Pei, G. Blöcher, H. Milsch, F. Deon, G. Zimmermann, W. Rühaak, I. Sass, and E. Huenges. Thermal strain in a water-saturated limestone under hydrostatic and deviatoric stress states. *Tectonophysics*, 688:49–64, oct 2016. doi: 10.1016/j.tecto.2016.09.020.

D. D. Pollard. *Fundamentals of Structural Geology*. Cambridge University Press, 2005.

L. Pyrak-Nolte and J. Morris. Single fractures under normal stress: The relation between fracture specific stiffness and fluid flow. *International Journal of Rock Mechanics and Mining Sciences*, 37(1-2):245–262, jan 2000. doi: 10.1016/S1365-1609(99)00104-5.

Z. Reches and D. A. Lockner. Nucleation and growth of faults in brittle rocks. *Journal of Geophysical Research: Solid Earth*, 99(B9):18159–18173, sep 1994. doi: 10.1029/94JB00115.

S. Santucci, M. Grob, R. Toussaint, J. Schmittbuhl, A. Hansen, and K. J. Maløy. Fracture roughness scaling: A case study on planar cracks. *EPL (Europhysics Letters)*, 92(4):44001, nov 2010. doi: 10.1209/0295-5075/92/44001.

J. Schmittbuhl, F. Schmitt, and C. Scholz. Scaling invariance of crack surfaces. *Journal of Geophysical Research: Solid Earth*, 100(B4):5953–5973, apr 1995a. doi: 10.1029/94JB02885.

J. Schmittbuhl, J.-P. Vilotte, and S. Roux. Reliability of self-affine measurements. *Physical Review E*, 51(1):131–147, jan 1995b. doi: 10.1103/PhysRevE.51.131.

C. Schneider, W. Rasband, and K. Eliceiri. NIH image to ImageJ: 25 years of image analysis. *Nature Methods*, 9(7):671–675, jun 2012. doi: 10.1038/nmeth.2089.

P. Segall and D. D. Pollard. Nucleation and growth of strike slip faults in granite. *Journal of Geophysical Research*, 88(B1):555, 1983. doi: 10.1029/JB088iB01p00555.

H. Stünitz, N. Keulen, T. Hirose, and R. Heilbronner. Grain size distribution and microstructures of experimentally sheared granitoid gouge at coseismic slip rates – criteria to distinguish seismic and aseismic faults? *Journal of Structural Geology*, 32(1):59–69, jan 2010. doi: 10.1016/j.jsg.2009.08.002.

E. Tenthorey and S. F. Cox. Cohesive strengthening of fault zones during the interseismic period: An experimental study. *Journal of Geophysical Research*, 111(B9), 2006. doi: 10.1029/2005JB004122.

K. Terzaghi. *Erdbaumechanik Auf Bodenphysikalischer Grundlage*. Leipzig u. Wien, F. Deuticke, 1925.

L. W. Teufel. Permeability changes during shear deformation of fractured rock. In *28. U.S. Symposium on Rock Mechanics. Tucson, AZ, USA, 29 June*, 1987.

J. M. Vermilye and C. H. Scholz. Fault propagation and segmentation: insight from the microstructural examination of a small fault. *Journal of Structural Geology*, 21(11): 1623–1636, nov 1999. doi: 10.1016/S0191-8141(99)00093-0.

N. Watanabe, N. Hirano, and N. Tsuchiya. Diversity of channeling flow in heterogeneous aperture distribution inferred from integrated experimental-numerical analysis on flow through shear fracture in granite. *Journal of Geophysical Research*, 114(B4), apr 2009. doi: 10.1029/2008JB005959.

C. A. Wibberley, J.-P. Petit, and T. Rives. Micromechanics of shear rupture and the control of normal stress. *Journal of Structural Geology*, 22(4):411–427, apr 2000. doi: 10.1016/S0191-8141(99)00158-3.

T.-F. Wong. Micromechanics of faulting in westerly granite. *International Journal of Rock Mechanics and Mining Sciences & Geomechanics Abstracts*, 19(2):49–64, apr 1982. doi: 10.1016/0148-9062(82)91631-X.

H. Yasuhara and D. Elsworth. Compaction of a rock fracture moderated by competing roles of stress corrosion and pressure solution. *Pure and Applied Geophysics*, 165(7): 1289–1306, jul 2008. doi: 10.1007/s00024-008-0356-2.

Z. Ye and A. Ghassemi. Injection-induced propagation and coalescence of preexisting fractures in granite under triaxial stress. *Journal of Geophysical Research: Solid Earth*, 124(8):7806–7821, aug 2019. doi: 10.1029/2019JB017400.

A. Zang, F. C. Wagner, S. Stanchits, C. Janssen, and G. Dresen. Fracture process zone in granite. *Journal of Geophysical Research: Solid Earth*, 105(B10):23651–23661, oct 2000. doi: 10.1029/2000JB900239.

Q. Zhang, X. Li, B. Bai, L. Pei, L. Shi, and Y. Wang. Development of a direct-shear apparatus coupling with high pore pressure and elevated temperatures. *Rock Mechanics and Rock Engineering*, 52(9):3475–3484, feb 2019. doi: 10.1007/s00603-019-1735-y.

M. D. Zoback and J. D. Byerlee. The effect of microcrack dilatancy on the permeability of westerly granite. *Journal of Geophysical Research*, 80(5):752–755, feb 1975. doi: 10.1029/jb080i005p00752.

5

THE STRESS-MEMORY EFFECT OF FRACTURES

The hydraulic performance and mechanical stability of open fractures are crucial for several subsurface applications including fractured geothermal reservoirs or nuclear waste repositories. Their hydraulic and mechanical properties (fluid flow and fracture stiffness) are both strongly dependent on the fracture geometry. Any change in effective stress impacts aperture and thus the ability of fractures to promote flow. Here, we carried out flow experiments with shear displaced tensile fractures in pre-loaded, low-permeability sandstones with two different cyclic loading scenarios with up to 60 MPa hydrostatic confining pressure. During "constant cyclic loading" (CCL) experiments, the fracture was repeatedly loaded to the same peak stress (up to 60 MPa). During "progressive cyclic loading" (PCL) experiments, the confining pressure was progressively increased in each cycle (up to 15, 30, 45 and 60 MPa). The matrix and fracture deformation was monitored using axial and circumferential LVDT extensometers to obtain the fracture stiffness. The fracture geometry before and after the experiment was compared by calculating the aperture distribution from 3D surface scans. Initial loading with confining pressure of the fracture leads to a linear fracture specific stiffness evolution. For any subsequent stress cycles fracture stiffness shifts to a non-linear behaviour. The transition is shown to be related to a stress memory effect, similar to the "Kaiser Effect" for acoustic emissions. Lastly, progressive cyclic loading of fractures possibly leads to less permeability reduction compared to continuous cyclic loading.

This chapter is based on: C. Kluge, G. Blöcher, H. Hofmann, A. Barnhoorn, J. Schmittbuhl, D. Bruhn, *The stress-memory effect of fracture stiffness during cyclic loading in low-permeability sandstone*, Journal of Geophysical Research: Solid Earth, under review.

5.1. INTRODUCTION

The performance of geothermal and petroleum reservoirs, as well as the safety of underground constructions such as nuclear waste repositories, depend on the ability of fractures to either promote or inhibit fluid flow. In addition, the stability of faults and fractures during hydraulic stimulation requires information on how to minimize and mitigate the risks of induced seismicity (Hofmann et al., 2018) or the loss of the hydraulic integrity of the subsurface (Pyrak-Nolte and Nolte, 2016). Coupled hydro-mechanical processes during stress-related deformation of fractures remain notoriously difficult to predict especially in complex fractured rock masses (Rutqvist, 2015). Besides, the evolution of stress over time changes either short-term or at geological time scales and strongly governs the exploration strategies in geothermal reservoirs. Laboratory experiments can be used to develop tools and knowledge about how to characterize fractured rock mass to better predict hydraulic properties of rocks.

The memory of rocks is described as the capacity of rocks to retain "imprints" from their stress-history (Lavrov, 2005). Rocks therefore contain crucial information about the stress history during non-elastic deformation. Loading a rock to a large stress level generates damage or microcracks within the rock. This level of stress can be identified by reloading the rock above the previous stress level (Lockner, 1993), while monitoring acoustic emissions. Acoustic emissions will actually be present when exceeding the "ancient" stress level of the rock. This is known as the "Kaiser Effect" (Kaiser, 1953). Besides acoustic emissions, electromagnetic properties, infrared radiation, but also elastic wave velocity and electric resistivity can be used to monitor the Kaiser Effect on (Lavrov, 2005) on previously intact rocks being loaded in the non-elastic domain where damage is generated. The question we address here is to know, if only the generation of mircoscopic fractures in the rock matrix leads to a stress memory effect (Holcomb, 1993), or if other mechanisms are responsible for a "Kaiser effect"-like behaviour in rocks (Lavrov, 2003). In particular we aim at assessing if existing fractures could contain information about their stress history since they behave non-elastic over a larger range of stress owing to the damage of their asperities (Bandis et al., 1983).

Bandis et al. (1983) evaluated the mechanical behaviour of fractures during cyclic loading. Since then, a large number of data were published that study in detail the evolution of fracture closure and permeability during cyclic normal loading (e.g. Chen et al., 2000, Cook, 1992, Hofmann et al., 2016, Kluge et al., 2020, Milsch et al., 2016, Watanabe et al., 2009). The loading path in most of these experiments comprises multiple loading cycles to the same peak load. Such experiments allow for a qualitative description of the changes in physical properties by a repetition of the same loading path. This is important in understanding the performance of a reservoir during different injection and production scenarios (Kluge et al., 2020). Cyclic loading experiments contain more information when varying the stress path of each loading cycle. The pore fluid pressure oscillations technique can be used to analyse the frictional stability of the fault and to analyse the transition from stable to unstable slip by progressively increasing the magnitude of pore fluid pressure from one cycle to another (Noël et al., 2019). This technique can also be used by loading the sample with an increasing external confining pressure with the same differential stress through the

different cycles, instead of increasing pore fluid pressure at a constant confining stress.

The hydro-mechanical properties of fractures depend on fracture contact-area, fracture size, fracture roughness and loading stress history (Wang and Cardenas, 2016). These physical factors also control the stiffness of a fracture (Pyrak-Nolte and Morris, 2000). The normal stiffness describes how much a fracture closes when being subjected to an increasing normal load with respect to the normal plane. A general observation is that normal fracture stiffness evolves exponentially with load (Bandis et al., 1983). Two different models are usually applied to characterise fracture stiffness from laboratory experiments: (I) The fracture stiffness characteristic, χ, which is a parameter that is based on the semi-log closure model for a single loading cycle. It is a measure of the derivative of the stiffness with load which is a characteristic constant in an exponential formulation (Zangerl et al., 2008) and can be used to quantify changes of stiffness in a series of repetitive stress cycles (e.g. Bandis et al., 1983, Crawford et al., 2016, Kluge et al., 2020). In particular, it is useful to describe strain-hardening effects of fractures. However, this parameter is strongly based on a specific model, the semi-log model and can be poorly assessed if the model is not correctly describing the behavior of fractured rock. (II) The specific fracture stiffness, κ, is defined as the ratio of the increment of stress to the increment of displacement caused by a change of the void space in the fracture (Pyrak-Nolte and Morris, 2000). It was shown numerically and experimentally, that it depends on the elastic properties, the fracture geometry and stress history (e.g. Cook, 1992, Marache et al., 2008, Petrovitch et al., 2013, Pyrak-Nolte and Morris, 2000, Wang and Cardenas, 2016). This property enables to monitor dynamic changes of fracture stiffness for complex stress-paths.

Similar to the fracture stiffness, fracture permeability also depends on these parameters. Cyclic loading experiments on hydro-mechanical responses of fractured rocks have a long-history and have provided a large number of data (e.g. Chen et al., 2000, Hofmann et al., 2016, Milsch et al., 2016, Watanabe et al., 2009). Notably, these studies have focused on a repetition of periodic loading cycles with the same peak stress. Studies reporting results of aperture or permeability measurements during non-preiodic cyclic loading tests where the cycle's maximum stress is increased from cycle to cycle gained little attention in the past (Lavrov, 2005). Bandis et al. (1983) and Pyrak-Nolte and Morris (2000) showed, that larger apertures and therefore more permeable fractures were more compliant than fractures with initially lower aperture and permeability. The question is, whether mechanical (stiffness) and hydraulic properties (permeability) of fractured rocks are dependent on stress history and if stress cycling alters this relationship (Pyrak-Nolte and Morris, 2000, Pyrak-Nolte and Nolte, 2016). The fracture closure and stiffness is also expected to strongly depend on fracture surface roughness (Akarapu et al., 2011, Persson, 2007). This can only be shown by means of the specific fracture stiffness, κ, but not by the fracture stiffness characteristic, χ. The deformation of asperities at the fracture surface may lead to changes in the fracture topography and consequently the aperture. Previous studies showed the difficulties to quantify potential changes of fracture topography (e.g. Bandis et al., 1983, Vogler et al., 2016, Xia et al., 2003, Yoshioka, 1994, Zou et al., 2020). Further, it is not clear if potential topography changes affect the self-affine scaling properties, such as the power spectral density (Schmittbuhl et al., 1995a,b), of fracture surfaces. A combination of measuring the fracture stiffness and permeability during cyclic loading experiments with a progressively

increasing stress magnitude together with measurements of the fracture roughness evolution might enable to better understand the dependency of these properties and their relation to the stress history.

In this paper, we present results from a set of laboratory experiments on fractured rock samples with a single displaced tensile fracture, being cyclically loaded using two different loading scenarios: constant cyclic and progressive cyclic loading. We will first review the experimental results and analyze the fracture stiffness and fracture permeability evolution for two different loading scenarios. These will be discussed in respect of a possible memory effect of fracture stiffness, similar to that in intact rock during plastic deformation. We then elaborate how this impacts the relationship of the hydraulic-mechanical properties of a fracture under cyclic loading conditions and investigate possible fracture deformation mechanisms. Lastly, we discuss how the stress-paths possibly impacts the performance and sustainability of subsurface reservoirs in terms of productivity.

5.2. MATERIALS & METHODS

5.2.1. TESTING EQUIPMENT

The flow-through experiments were carried out in a conventional MTS tri-axial compression cell. The stiff, servo-controlled loading frame (MTS 815, Material Testing Systems Corporation) holds a loading capacity of up to 4600 kN (load cell calibrated to 2000 kN, calibration error <1 %) and a servo-controlled maximum hydrostatic confining pressure of 140 MPa applied via an oil-filled pressure vessel coupled to an external pressure intensifier. The pore fluid pressure was applied via four Quizix fluid pressure pumps (Model C6000-10K-HC-AT) with a maximum fluid pressure of 69.7 MPa. The differential fluid pressure, which is the difference between in- and outflow pressure, was measured using a differential pressure transducer (GP:50, Model 215; range: 1 MPa; line pressure max. 69.7 MPa; precision: ~ 1%). The circumferential strain was measured using a LVDT extensometer chain and the axial strain was measured with two axial LVDT extensometers (figure 5.1). All experiments have been performed at a temperature of 30 °C. Data were recorded at a frequency of 1 Hz. A detailed description of the machine can be found in Pei et al. (2016).

5.2.2. SAMPLE MATERIAL

The Flechtingen Sandstone (SBT6-BE) was taken from a quarry near Magdeburg in the North German Basin (Germany) and is a Permian, arkosic litharenite with quartz, feldspars, rock fragments of mainly volcanic origin, about 8 % of clay, predominantly illite and chlorite Hassanzadegan et al. (2014). This Rotliegend rock is used as an analogue to the sedimentary geothermal reservoirs in the Northern German Basin (Blöcher et al., 2014, 2016, Hassanzadegan et al., 2012). Grain size is between 0.05 and 0.2 mm for quartz and 0.05 to 0.1 mm for feldspar. All grains are partly rounded and well sorted. In contrast to Hassanzadegan et al. (2012), no microfractures were found in our samples. The porosity, ϕ, was measured using the Archimedes principal. The initial sample permeability, k_0, was measured using Darcy's law at 2 MPa confining pressure (table 5.1). The relatively low

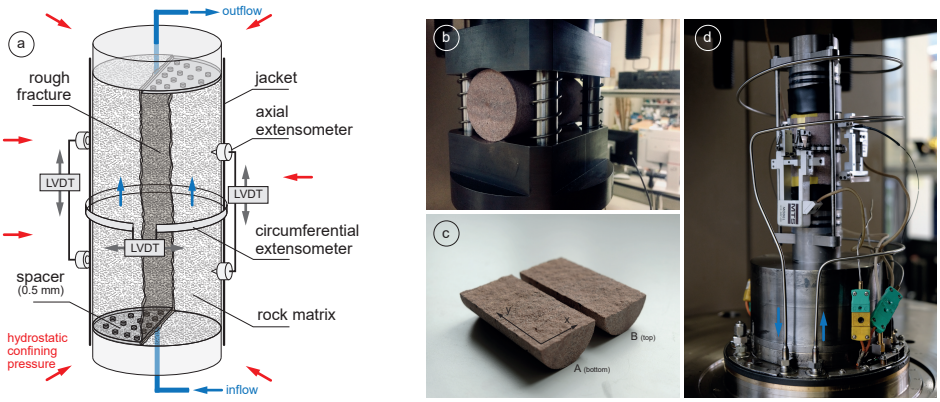

Figure 5.1: The experimental set-up of the flow-through experiments (a), the Brazilian test set-up for fracture generation (b), the resulting fracture surfaces (c) and the a photograph of the experimental set-up.

porosity and permeability results from a dense packing of grains, as well as illite partially blocking the pore space by coating the quartz grains. On some grain-contacts quartz dissolution occurred, which additionally reduced permeability. The sandstone samples were slightly layered characterised by grain size differences. All cores were therefore taken perpendicular to the bedding. A list of samples and their respective properties is given in table 5.1.

Table 5.1: List of samples, intact sample dimensions and test types.

sample ID	L, d [mm]	ϕ [%]	k_0 [m^2]	d [mm]	type
SBT6-BE-04-03	100.18, 49.93	5.86	$3.62 \cdot 10^{-15}$	0.5	CCL
SBT6-BE-04-09	100.12, 49.88	5.16	$2.75 \cdot 10^{-15}$	0.5	PCL
SBT6-BE-04-10	100.12, 49.90	5.31	$1.59 \cdot 10^{-15}$	0.5	PCL

L: sample length, d: sample diameter, ϕ: porosity, k_0: initial sample permeability
d: fracture offset, CCL: constant cyclic loading, PCL: progressive cyclic loading

5.2.3. EXPERIMENTAL PROCEDURE

The experimental procedure can be subdivided into four different stages: (1) pre-conditioning of samples under hydrostatic pressure conditions to remove the plastic strain in the sample, (2) tensile fracture generation using the Brazilian Disk test and surface scanning, (3) imposed rigid shear of the unloaded sample, (4) fracture flow experiment under constant cyclic loading conditions (CCL) and progressive cyclic loading conditions (PCL) using different kind of samples. The measured properties are the pressure dependent rock matrix permeability, the rock matrix porosity, the fracture surface geometry including aperture distribution and roughness, as well as the pressure dependent fracture closure and fracture permeability.

SAMPLE PRE-CONDITIONING

In order to remove the plastic strain of the intact rock samples, all cores were preloaded to a hydrostatic confining pressure of 65 MPa in seven loading cycles. This pressure is above the maximum hydrostatic pressure of 60 MPa applied in the actual fracture flow experiment. The intact samples were jacketed in a heat-shrink tube and placed into the MTS tri-axial cell. One circumferential and two axial LVDT extensometers recorded the lateral, axial and volumetric strain during the experiment. First, a hydrostatic confining pressure of 2 MPa was applied while the sample was saturated with distilled water under vacuum conditions of about 1 kPa for 24 h. The maximum pore fluid pressure was kept at 0.2 MPa during the entire pre-loading stage. At this point, the permeability of the unloaded sample was measured (table 5.1). Here we applied a continuous inflow rate, Q, and a constant fluid pressure at the sample outlet, p_{out} of 0.2 MPa. From the pressure difference, $\Delta p_p = p_{in} - p_{out}$, the inflow area, A, the temperature dependent fluid viscosity, μ, and the sample length, L, we calculated the sample permeability, k_s, using Darcy's law (Darcy, 1856):

$$k_s = \frac{Q}{A}\frac{\mu L}{\Delta p_p} \tag{5.1}$$

Once permeability was measured, the constant inflow rate was changed to a constant pressure mode. By applying a constant fluid pressure of 0.2 MPa at both sides of the sample using only one pump, we were able to measure the pore volume changes during loading. For pre-conditioning, a hydrostatic stress of 65 MPa was applied in a total of seven pressure cycles with a loading rate of 5 MPa/min (figure 5.2). The effective pressure resulting from the confining and pore pressure was calculated following Terzaghi's effective pressure law (Terzaghi, 1925), assuming a linear pressure gradient (Hofmann et al., 2016):

$$p_e = p_c - p_p \tag{5.2}$$

with

$$p_p = p_{p,out} + \frac{p_{p,in} - p_{p,out}}{2} \tag{5.3}$$

In six of the cycles the pore volume change was measured, while the sample permeability (equation 3.1) was measured at several hydrostatic pressure levels in a seventh cycle. The number of cycles has been chosen in a way that stress-strain curves were fully elastic at the last loading stage. After the samples were pre-conditioned they were retrieved from the tri-axial cell and dried in an oven at 50 C° for at least 24 hours.

The bulk volume change, V_{bulk} was calculated from the axial and circumferential strain, ϵ_a and ϵ_c, as well as the initial bulk volume, V_0:

$$\Delta V_{bulk} = (\epsilon_a + 2\epsilon_c) \cdot V_0 \tag{5.4}$$

TENSILE FRACTURE GENERATION

To generate a single tensile fracture cutting through the diametrical axis of the sample, a modified Brazilian Disk test was used. The core was split over its entire length of 10 cm (figure 5.1b). A low loading rate of 0.0003 mm/s was applied to avoid breakouts and to guarantee a smooth and relatively linear fracture. Once failure occurred, i.e. a drop in load was observed, the sample was loaded further until a fracture was visible. The tensile strength, σ_{ts}, was calculated from the maximum measured load, F_{max}:

$$\sigma_{ts} = \frac{2F_{max}}{\pi d L} \tag{5.5}$$

After unloading the two sample halves were taken apart carefully (figure 5.1c). Chipping of fragments from the surface could not be avoided completely.

SURFACE SCANNING, ROUGHNESS & APERTURE ANALYSIS

After tensile fracture generation, both surfaces of the sample were analyzed with a 3D profilometer using the fringe pattern projection. The Keyence VR-3200 was used to measure the surface topography of all fracture surfaces with a point distance of 47 μm and an accuracy of 3 μm and 2 μm in the vertical and horizontal direction, respectively. Each surface was analyzed for its roughness exponent. Here, we apply a power spectral density method to obtain the scale-independent roughness exponent, H (Candela et al., 2012, Schmittbuhl et al., 1995b), based on the scaling relationship of $\delta x \rightarrow \lambda \delta x, \delta z \rightarrow \lambda^H \delta z$ (Meakin, 1998). Assuming the self-affinity of rock fracture surface (Schmittbuhl et al., 1995a), the Fourier transform of all 1D profiles in x-y-direction across the surface provides the power spectral density for the given spatial frequency domain in log-space. The slope of the spectrum then provides the roughness exponent in x-y-direction for every surface (Candela et al., 2012):

$$P(K) = Ck^{-1-2H} \tag{5.6}$$

where $P(k)$ is the Fourier power spectrum, k is the wave number, C is a pre-factor and H is the roughness exponent. Since higher frequencies are over-represented in log-log-space, the mean spectra were re-sampled to 20 points (frequency) averaging the data in between for the linear fit. By doing so, all frequencies were evenly represented providing a better fit. The method was verified on a synthetic fault generated for two dimensional roughness exponents.

To obtain the aperture distribution of the top and bottom surface of one rock sample, the point cloud topography data of both surfaces were correlated. To calculate the aperture distribution of two independently scanned surfaces, both surfaces need to be matched. This was done by matching the best fitting principal planes of the bottom and top surface and applying a grid search algorithm. The surface data of both surfaces was interpolated on a grid with a point distance in x-y-direction of 0.05 mm. That way, the top and bottom surface have the same orientation and shared the same grid. The fracture surfaces were displaced to an offset of 0.5 mm, as in the experiment. At each point across the x-y grid, the aperture

(vertical distance) between the top and bottom surface was calculated to obtain the aperture distribution.

PROCEDURES FOR THE FRACTURE FLOW EXPERIMENTS

After generating and analysing the fracture and its geometry the samples were prepared to perform the actual fracture flow experiments, i.e. under the constant cyclic loading (CCL) and progressive cyclic loading (PCL). First, the two samples halves were placed together at a manual offset of 0.5 mm using perforated steel spacers at the opposite side of each sample half (figure 5.1a). Any rotation of the two fracture planes can be ruled out due to the parallelism of the end cap and the spacer. The rigid shear offset of 0.5 mm was chosen based on three criteria: (1) larger than the grain size, (2) a comparable initial mean aperture for all three samples and (3) not too large to be able to measure the sample permeability (equation 5.1) with our testing equipment (between $1 \cdot 10^{-18}$ m^2 and $1 \cdot 10^{-12}$ m^2). A brass stripe was used to cover the resulting holes caused by the spacers and the displaced fracture to avoid the heat-shrink tube to be punctuated (figure 5.1d).

After the sample was installed in the tri-axial cell, the confining pressure was again increased to 2 MPa with a loading rate of 0.5 MPa/min. The fractured sample was then saturated for 24 h under vacuum conditions with a constant pore fluid pressure of 0.2 MPa. When saturation was finished, a constant inflow rate of 2.5 to 10 ml/min was applied from one side of the sample, while the outflow pressure was kept constant at 0.2 MPa, resulting in an effective pressure according to equation 5.2.

The following parameters could be calculated from the experimental data: The sample permeability was measured over the entire duration of the experiment. Here we assumed that measured flow rate is the sum of the individual flow rates through the matrix and through the fracture ($A_s k_s = A_m k_m + A_f k_f$). The matrix permeability, k_m, is assumed negligible comparing it to the fracture permeability, k_f. With the approximation of a rectangular shape of the fracture inflow surface ($A_f = 2ar$), we calculated the hydraulic aperture, a_h (Hofmann et al., 2016):

$$a_h = \sqrt[3]{6\pi k_s r} \tag{5.7}$$

Here, a_h is the hydraulic fracture aperture, k_s is the measured sample permeability and r is the sample radius. From the hydraulic aperture we then calculated the fracture permeability, k_f, using the cubic law (Witherspoon et al., 1980):

$$k_f = \frac{a_h^2}{12} \tag{5.8}$$

Permeability errors were marginal and can hardly be quantified. The main errors sources were the frictional pressure losses within the capillary tubes connecting the fluid pumps and the sample, potentially leading to slight pressure changes. A second error source was the accuracy of the differential pressure transducer with an absolute error of 1 % of the pressure range (1 MPa), which corresponds to only 1 kPa.

The axial extensometers were placed at the center of each sample half to measure the strain of the elastic intact rock, ϵ_a, during loading (figure 5.1a). A circumferential LVDT extensometer chain was attached to the center of the sample to measure the bulk deformation of matrix and fracture. The intact elastic rock matrix was measured from the axial extensometers. The mechanical fracture closure was then corrected from the deformation of the rock sample, i.e. the measured axial strain, ϵ_a, was subtracted from the circumferential strain, ϵ_c (Hofmann et al., 2016):

$$\epsilon_{c,non-el} = \epsilon_c - \epsilon_a \tag{5.9}$$

The mechanical fracture aperture, a_m, was calculated from the circumferential extensometer deformation, u, and the non-elastic strain, $\epsilon_{c,non-el}$:

$$a_m = u \cdot \Delta\epsilon_{c,non-el} = 2\Delta a \rightarrow \Delta a = \frac{\Delta ext_{c,non-el}}{2} \tag{5.10}$$

In this equation, half of the change in non-elastic circumferential extension, $\Delta ext_{c,non-el}$, equals the change in fracture aperture, Δa. The fracture specific stiffness, κ, was defined as the ratio of the increment of stress to the increment of displacement caused by the deformation of the void space in the fracture. The fracture stiffness, κ, was calculated from the change in fracture closure, $\Delta a_m = a_m(n+1) - a_m(n)$, per increment effective pressure increase, $p_e(n)$ averaged over an interval of 720 sec (6 MPa):

$$\kappa = \frac{p_e(n+1) - p_e(n)}{a_m(n+1) - a_m(n)} \tag{5.11}$$

CONSTANT CYCLIC LOADING (CCL) EXPERIMENT

The constant cyclic loading (CCL) experiment at hydrostatic conditions was performed according to figure 5.2a, using sample SBT6-BE-04-03. The confining pressure was increased from 2 to 60 MPa at a constant loading rate of 0.5 MPa/min. At 60 MPa, the confining pressure was held for 20 min before unloading was started at the same rate as during loading. This process was repeated six times in order to obtain the fracture closure curves for a constant loading procedure with the same peak stress. After two cycles, the system was held at constant conditions for about 12 hours.

PROGRESSIVE CYCLIC LOADING (PCL) EXPERIMENTS

The progressive cyclic loading (PCL) at hydrostatic conditions was performed according to figure 5.2b, using samples SBT6-BE-04-09 and SBT6-BE-04-10. In this procedure, we distinguished between pressure cycles and pressure sub-cycles. The sub-cycles describe the stepwise increase of hydrostatic confining pressure from 2 to 15, 30, 45 and 60 MPa. One sub-cycle was therefore the increase from 2 to the respective stress level (15, 30, 45, 60 MPa) and the decrease or unloading from the respective stress-level to 2 MPa. The confining pressure was held for 20 min before unloading was started at the same rate as

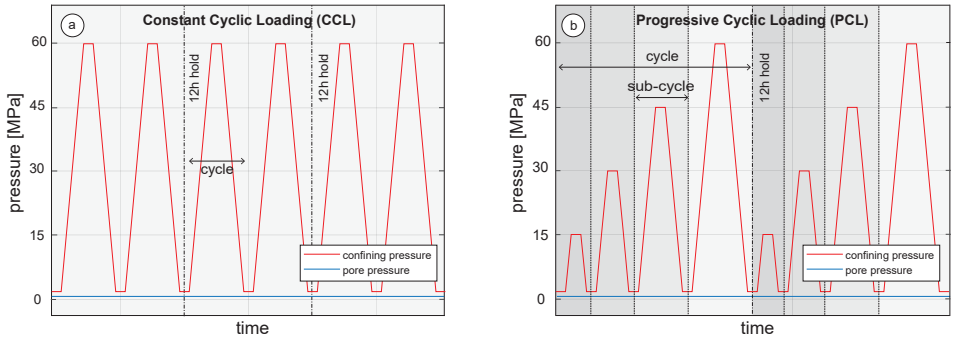

Figure 5.2: The experimental procedure for the constant cyclic loading, CCL, (a) and the progressive cyclic loading, PCL (b).

during loading. That way, the effective pressure was increased by additional 15 MPa over the previous pressure level to identify potential changes in the fracture closure or opening behavior when exceeding the previous stress level. This progressive cyclic loading was repeated two times, i.e. two complete cycles, with a hold phase of about 12 hours between the two. The loading rate for the confining pressure was 0.5 MPa/min for loading and unloading.

After the cyclic loading experiments were finished, the samples were removed from the cell and dried at 50 °C for at least 24 hours. The fracture surfaces were then scanned and analysed as described in section 5.2.3.

5.3. EXPERIMENTAL RESULTS

5.3.1. SAMPLE VOLUME & PERMEABILITY OF THE INTACT ROCK

Based on the bulk volume change (equation 5.4), the plastic and elastic sample deformation was monitored during six loading cycles up to 65 MPa (figures 5.3a,b,c). Most of the irreversible plastic deformation was found in the first loading cycle (figures 5.3a,b,c). After six pressure cycles, no more significant bulk strain changes suggested fully elastic sample deformation. The total volume loss was about 0.27 cm^3 measured by the volumetric strain and 0.39 cm^3 measured by the pore volume change. This corresponded to about 0.1 % of the initial porosity of 5 to 6 %. The 7th loading cycle is not shown here, because the fluid pressure in the sample was higher during the permeability measurements.

In the 7th loading cycle, the intact rock permeability (equation 5.1) was measured at four to five pressure levels during loading and unloading (figure 5.3d). The sample permeability, k_s at 2 MPa was reduced from about 1 to 3 $\cdot 10^{-15}$ m^2 before pre-conditioning down to 5 $\cdot 10^{-18}$ m^2 to 1 $\cdot 10^{-17}$ m^2 after pre-conditioning. This is equal to a difference of more than two orders of magnitude. The largest incremental change in permeability was found during the first 15 MPa of confining pressure, while the change becomes smaller after 40 MPa. At effective pressures larger than 40 MPa the permeability was about 1 $\cdot 10^{-19}$ m^2, which

was the lower limit of measurable permeability with our machine. The permeability of all measured samples showed a similar behaviour. During loading the permeability was overall higher compared to unloading. In general, the change in permeability was reversible after pre-conditioning.

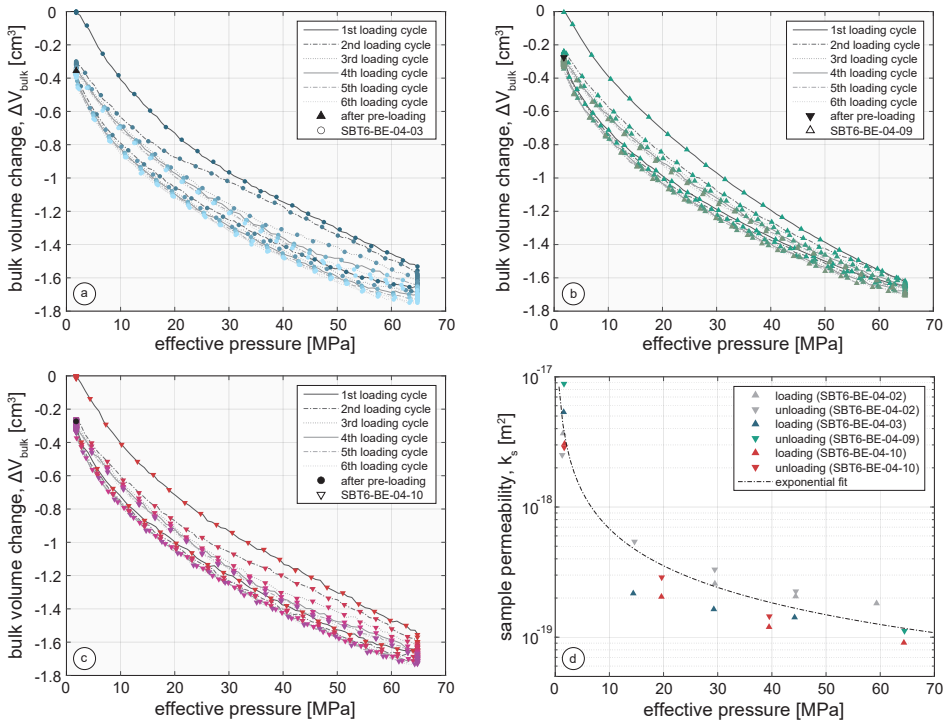

Figure 5.3: The bulk volume change during pre-conditioning (a,b,c) and the pressure-dependent permeability of the intact rock sample (d).

5.3.2. TENSILE FRACTURE GENERATION

To generate a flow-parallel tensile fracture, the modified Brazilian disk test was used. The tensile strength, TS, calculated from equation 5.5, for the three samples SBT6-BE-04-03, 09 and 10 was 5.4, 4.0 and 5.5 MPa, respectively. The mode I fracture toughness, K_{Ic}, was calculated after Guo et al. (1993) and was 0.78, 0.63 and 0.82 MPa·m$^{1/2}$, respectively. The sample halves were taken apart, loose fragments were carefully removed and possible breakouts at the corners were filled with an Araldite-sand mixture. This aimed to avoid inward bulging and rupture of the heat-shrink tube during loading. However, this did not lead to additional contact-area between the opposing fracture surface and had thus no impact on the strength or stiffness of the fracture.

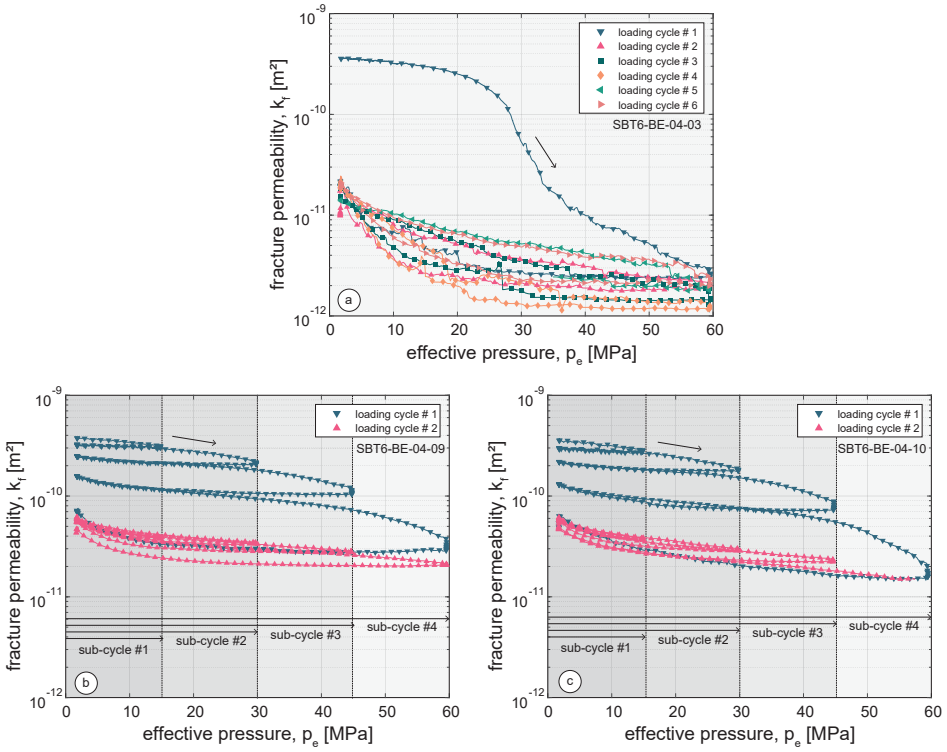

Figure 5.4: Fracture permeability of the constant cyclic loading (CCL) experiment (a) and the progressive cyclic loading (PCL) experiments (b,c).

5.3.3. FRACTURE PERMEABILITY & APERTURE DURING CCL

Comparing the initial sample permeability after pre-conditioning (figure 5.3b), to the initial sample permeability containing a fracture at 2 MPa effective pressure (equation 5.1), we found an increase from 5.4 $\cdot 10^{-18}$ m^2 to about 6.0 $\cdot 10^{-13}$ m^2. In the following we will refer permeability to the fracture permeability calculated following equation 5.8. During the first loading cycle from 2 to 60 MPa of confining pressure, the permeability reduced from 3.5 $\cdot 10^{-10}$ m^2 by more than 2 orders of magnitude to 2.9 $\cdot 10^{-12}$ m^2 (figure 5.4a). While the permeability changes were only minor during the first 20 MPa, the largest permeability decrease was observed above a confining pressure of 20 MPa. During the hold phase the permeability continued to drop but reached a constant level within 20 min. The permeability recovery when reducing the effective pressure was slower than the permeability loss during the effective pressure increase. When reaching 2 MPa, the irrecoverable permeability loss was more than 1 order of magnitude with a permeability of about 2$\cdot 10^{-11}$ m^2 at the end of the first cycle. During the second loading cycle the incremental permeability decrease was larger at lower stress, while only minor permeability losses were observed at an effective pressure above 30 MPa. The minimum permeability at 60 MPa in the second cycle was 1.9

$\cdot 10^{-12}$ m^2. In the following cycles the trend of the second loading cycle was maintained and a rather reversible fracture permeability was observed. Smaller and short-term peaks in permeability were related to changes in the flow rate during loading and unloading.

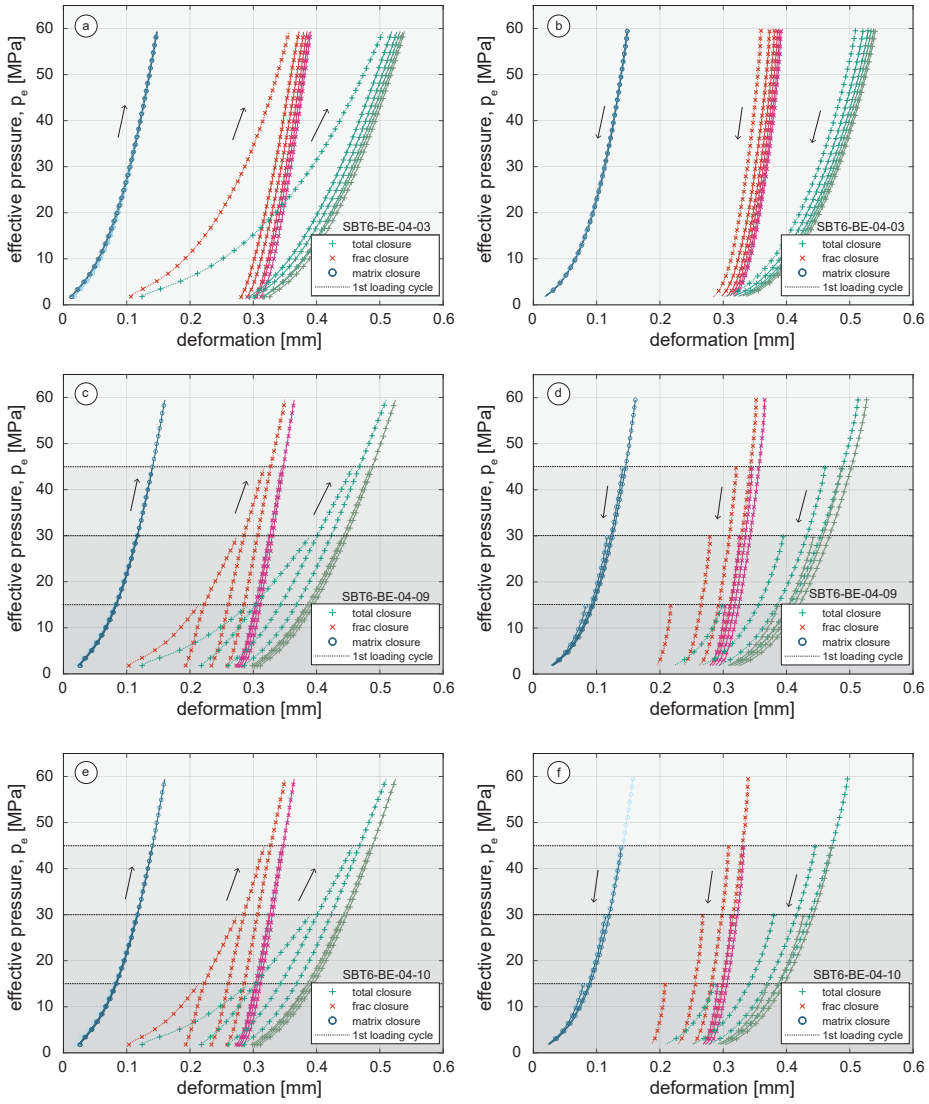

Figure 5.5: The total fracture closure during constant cyclic loading (CCL) and progressive cyclic loading (PCL) experiments during loading (a,c,e) and unloading (b,d,e).

The maximum elastic matrix deformation measured with the axial extensometers was no more than 0.14 mm at 60 MPa (figure 5.5a). Subtracting this from the total radial deformation of about 0.53 mm after the first loading cycle, the actual fracture closure was roughly

75 % of the total measured deformation resulting from six cycles. While the matrix compaction was fully elastic within the six loading cycles, the residual fracture closure was 0.28 mm after the first loading cycle at 2 MPa. The following cycles showed further fracture closure by up to 0.37 mm. The incremental fracture closure with increasing stress was rather linear at effective pressures larger than 20 MPa. During unloading, the fracture re-opened more slowly compared to the loading phase (figure 5.5b).

5.3.4. FRACTURE STIFFNESS EVOLUTION DURING CCL

The fracture stiffness was calculated following equation 5.11 at intervals of 720 sec. This was done to reduce the noise related to the sensors which impacted the signal quality of the fracture stiffness. The results were separated to first address the fracture stiffness during the respective loading cycles (figures 5.6a). In the first loading cycle, the fracture stiffness increased linearly from about 70 MPa/mm to about 550 MPa/mm at 60 MPa. The 2nd to 6th loading cycles showed a non-linear but reversible fracture stiffness evolution. Only minor increases with progressive loading cycles within an error of the measurements were found. This reversible fracture stiffness from the second loading cycle on was higher compared to the first loading cycle, with values between 300 MPa/mm at 2 MPa and up to 1000 MPa/mm at 60 MPa. The increase of fracture stiffness per cycle was only minor.

Interestingly, the fracture stiffness showed a different trend during unloading (figures 5.6b). The fracture was much stiffer compared to the loading cycles, with a maximum of about 5000 MPa/mm at 60 MPa. The measured fracture stiffness was not continuous when switching from the loading to unloading at constant effect pressure. The sudden increase of fracture stiffness at the onset of unloading can be explained by three superimposed processes: (1) a time-dependent creep resulting in a slower fracture opening with decreasing effective pressure, (2) the plastic and (3) the elastic deformation of asperities. The unloading curves merged with the loading curves for pressures below 20 MPa.

5.3.5. PERMEABILITY & APERTURE DURING PCL

When presenting the results for the respective loading scenarios, we refer to sub-cycles as the pressure change from 2 - 15 MPa, 2 - 30 MPa, 2 - 45 MPa and 2 - 60 MPa, as well as a full cycle, which is a complete set of the four sub-cycles (figure 5.2). We performed a total of two complete cycles for sample SBT6-BE-04-09 and 10.

The fracture permeability was first measured at 2 MPa confining pressure. At this low stress, the permeability was about 3.7 - 3.8 $\cdot 10^{-10}$ m^2 (figures 5.4b,c). This was close to the highest permeability that can be measured in our testing device. The flow rate was set to a maximum of 10 ml/min to avoid turbulent flow conditions. Permeability reduced after every loading cycle, with an increasing reduction with increasing pressure in the respective sub-cycle. The permeability reductions after each sub-cycle during the first loading cycle to 15, 30, 45 and 60 MPa were by a factor of 1.2, 1.3, 1.6 and 2.2 compared to the initial permeability. Interestingly, during re-loading the permeability follows the same permeability trend as during unloading up to 20 MPa. At stresses higher than 20 MPa, the permeability was lower during loading compared to unloading. Furthermore, permeability at stresses of 45

Table 5.2: Fracture stiffness results during the respective loading cycles.

stress-path per cycle [MPa]	cycle number[1)]	stiffness range [MPa/mm]	stiffness trend
	SBT6-BE-04-03 (CCL)		
(2-60)	1	75 to 550	linear
(2-60)	2 to 6	350 to 1000	non-linear
(60-2)	unloading	200 to >5000	non-linear
	SBT6-BE-04-09 (PCL)		
(2-15-2-30-2-45-2-60)	1	75 to 600	linear to non-linear[2)]
(2-15-2-30-2-45-2-60)	2	350 to 900	non-linear
(15-2-30-2-40-2-60-2)	unloading	300 to >5000	non-linear
	SBT6-BE-04-10 (PCL)		
(2-15-2-30-2-45-2-60)	1	75 to 600	linear to non-linear[2)]
(2-15-2-30-2-45-2-60)	2	350 to 900	non-linear
(15-2-30-2-40-2-60-2)	unloading	300 to >5000	non-linear

[1)] one cycle is one repetition of the stress-path per cycle.
[2)] transition when exceeding the previous stress level during each sub-cycle.

and 60 MPa showed a creep-like behaviour and reduced over time at constant stress. After the first loading cycle a permeability loss by a factor of 5.2 was measured for both samples. This corresponds to about 3.5 - 3.7 $\cdot 10^{-10}$ m^2 at the beginning and 0.5 - 0.7 $\cdot 10^{-10}$ m^2 at the end of the first cycle. In the second loading cycle, the permeability was rather reversible, following the same trend during loading and unloading.

The elastic matrix deformation was roughly 30 % of the bulk deformation measurement. Therefore, about 70 % of the total deformation was related to fracture closure (figures 5.5c,e). When re-loading the fracture, the aperture follows the unloading path until reaching the previous stress level. After that, the fracture closure was larger, meaning that the slope of the fracture closure vs. effective pressure curve was shallower. This trend was similar in all sub-cycles up to 60 MPa. The total closure in sample SBT6-BE-04-09 and 10 at the end of the second loading cycle was 0.37 and 0.35 mm. During unloading, the fracture re-opened more slowly compared to the loading phase (figures 5.5d,f).

5.3.6. FRACTURE STIFFNESS EVOLUTION DURING PCL

The fracture stiffness results during the respective sub-cycles are summarized in table 5.2. Both PCL experiments (SBT6-BE-04-09 and 10) showed the same trend and magnitudes of fracture stiffness. The effective stress was increased from 2 to 15 MPa during the first sub-cycle. This resulted in a linear increase in fracture stiffness with increasing effective pressure from around 80 to about 180 MPa/mm. (figures 5.6c,e). During the 2nd sub-cycle, the pressure was increased from 2 to 30 MPa. The fracture stiffness initially followed the non-linear fracture stiffness curve of the 2nd to the 6th of the CCL experiment (SBT6-BE-

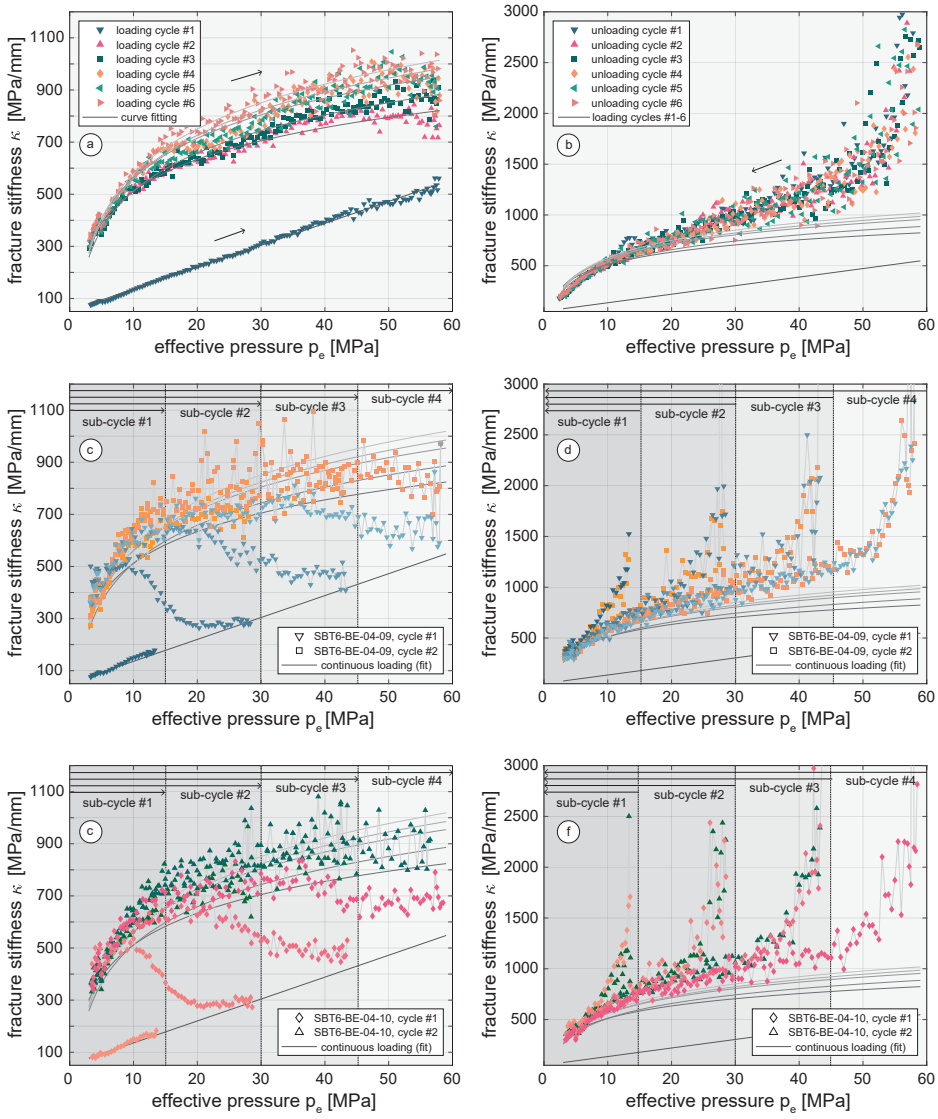

Figure 5.6: The fracture stiffness evolution during constant cyclic loading (CCL) and progressive cyclic loading (PCL) experiments during loading (a,c,e) and unloading (b,d,e).

04-03), starting from around 300 MPa/mm. The fracture stiffness then decreased shortly before reaching the effective stress of 15 MPa. The curve returned back to the linear fracture stiffness curve of the first loading cycle of the CCL experiment. This resulted in a fracture stiffness of around 300 MPa/mm at 30 MPa for all samples. During the 3rd sub-cycle, the stress was increased from 2 to 45 MPa. The fracture stiffness again followed the non-linear trend of the 2nd to 6th loading cycle of the CCL experiment, as well as the 2nd sub-cycle

recorded before that, starting from around 300 MPa/mm. Both samples kept following this trend exceeding a pressure of 15 MPa, but fracture stiffness started to decrease shortly before reaching the previous stress level of 30 MPa. Again, the fracture stiffness returned to the linear trend of the 1st loading cycle of the CCL experiment, reaching an end value of about 450 MPa/mm at 45 MPa. During the 4th and last sub-cycle, the pressure was increased from 2 to 60 MPa. The fracture stiffness was again similar to that of the 2nd to 6th loading cycle of the CCL experiment, as well as the 1st and 2nd sub-cycle of the PCL experiment, starting from about 300 MPa/mm. As before, the fracture stiffness then deviated from the non-linear fracture stiffness shortly before reaching 45 MPa, but the reduction was less compared to the clear drop of the 2nd sub-cycle before 15 MPa. However, the fracture stiffness almost reached the end value of about 550 MPa/mm of the first loading cycle of the CCL experiment at 60 MPa. At stresses larger then 50 MPa we found less changes in fracture stiffness with increasing stress. The smaller reduction in stiffness when reaching the previous stress level of 45 MPa indicated less fracture closure with increasing stress. The four sub-cycles were repeated in a second cycle of the PCL experiments, increasing pressure from 2 to 15, 30, 45 and 60 MPa, respectively. During all subsequent loading sub-cycles, the fracture stiffness followed the same non-linear trend as during the 2nd to 6th loading cycle of the CCL experiment.

Additionally, the fracture stiffness was calculated for all unloading paths during the progressive sub-cycles. When unloading from 15 to 2 MPa, the fracture stiffness was reduced from about 1600 MPa/mm to 300 MPa/mm (figures 5.6d, f). This higher stiffness during unloading agrees with the observation of a slower fracture opening during unloading compared to the fracture closure during loading (figure 5.5). They remaining unloading sub-cycles from 30, 45 and 60 MPa to 2 MPa showed a similar behaviour. Fracture stiffness decreased from 2400, 3000 and above 5000 MPa/mm to 300 MPa/mm, respectively. During the last unloading sub-cycle from 60 to 2 MPa, the fracture stiffness followed the same trend as all unloading curves during the CCL experiment.

5.3.7. FRACTURE ROUGHNESS EXPONENT BEFORE & AFTER TESTING

The roughness exponent was determined using the power spectral density approach as explained in section 5.2.3. Assuming that the tensile fracturing in sandstones was exclusively intergranular, the higher frequencies reflect the surface roughness of the grains (Boffa et al., 1998). Those frequencies led to deviations in the power spectrum. They were suppressed by a frequency cut-off for length-scales that are double the grain size, i.e. two times 0.2 mm. The resulting cut-off frequency additionally marks a break in the slope and a deviation from a linear trend in log-space. Figure 5.7 and 5.8 show the power spectrum for the surfaces before and after the flow-through experiments in x-y-directions. The slope of the fitted trend eventually leads to the roughness exponent (equation 5.6).

The power spectra indicate a similar roughness exponent for all surfaces independent of the direction (table 5.3). We found a mean of 0.58 (± 0.02) in x-direction and 0.57 (± 0.02) in y-direction (shear direction) before the experiment. These values are in agreement with roughness exponents of around 0.5 to 0.6 for sandstones that are commonly slightly lower than the 0.8 found for most other rock types (Boffa et al., 1998). After the cyclic loading

Table 5.3: Fracture roughness exponents.

surface ID	x-direction before	x-direction after	y-direction before	y-direction after
SBT6-BE-04-03-A (CCL)	0.55	0.55	0.58	0.58
SBT6-BE-04-03-B (CCL)	0.60	0.56	0.57	0.60
SBT6-BE-04-09-A (PCL)	0.57	0.57	0.58	0.54
SBT6-BE-04-09-B (PCL)	0.58	0.57	0.59	0.56
SBT6-BE-04-10-A (PCL)	0.58	0.58	0.60	0.61
SBT6-BE-04-10-B (PCL)	0.59	0.59	0.61	0.61

experiment, the surface topography was obtained a second time in the same orientation as before. The post-experimental mean values for the roughness exponent in the x-y-direction were 0.57 (± 0.01) and 0.58 (± 0.03), respectively. This indicated no distinct change in the scaling properties of the surface roughness due to the cyclic loading.

5

FRACTURE APERTURE DISTRIBUTION & CONTACT-AREA RATIO

From the surface topography from each fracture surface, we calculated the aperture distribution by matching the top and bottom surface as explained in chapter 5.2.3 (figures 5.9a, c, e; left). The aperture, a, was taken as the distance between each point across a x-y-grid (point distance 0.05 mm). This was done to calculate the initial aperture distribution of every sample. We considered this aperture distribution as the initial aperture, a_{ini}, at zero stress. With the assumption of two interpenetrating surfaces under normal load, i.e. geometrically overlapping regions are assumed to be in contact without deformation, (the 'overlap' model (Pei et al., 2005)), we calculated the resulting evolution of contact-area ratio, R_c. It is commonly defined as the ratio of the surface area in contact, A_c and the total surface area, A_t:

$$R_c = \frac{A_c}{A_t} \tag{5.12}$$

Considering only one contact point at zero stress would lead to an overestimation of the mean aperture when small fragments protrude from the fracture surface. Similar to Wang and Cardenas (2016), we therefore defined a threshold to shift the normal distribution to the left and reduced the aperture. The two fracture surfaces were brought into contact at an initial contact-area ratio, R_c, of 0.1 %. Furthermore, we consider the contact-area (zero aperture) as a discontinuity (delta function) in the aperture distribution (Pyrak-Nolte and Morris, 2000) and excluded these values when calculating the mean aperture.

The initial aperture distribution of all samples showed a similar normal distribution of aperture (figures 5.9b ,d, e), with mean apertures of 0.46, 0.43 and 0.42 mm (table 5.4). The larger local apertures of sample SBT6-BE-04-03 were caused by small fragments removed during the tensile fracturing process. The maximum fracture normal closure during loading was obtained from the LVDT extensometer and calculated according to equation 5.10. The

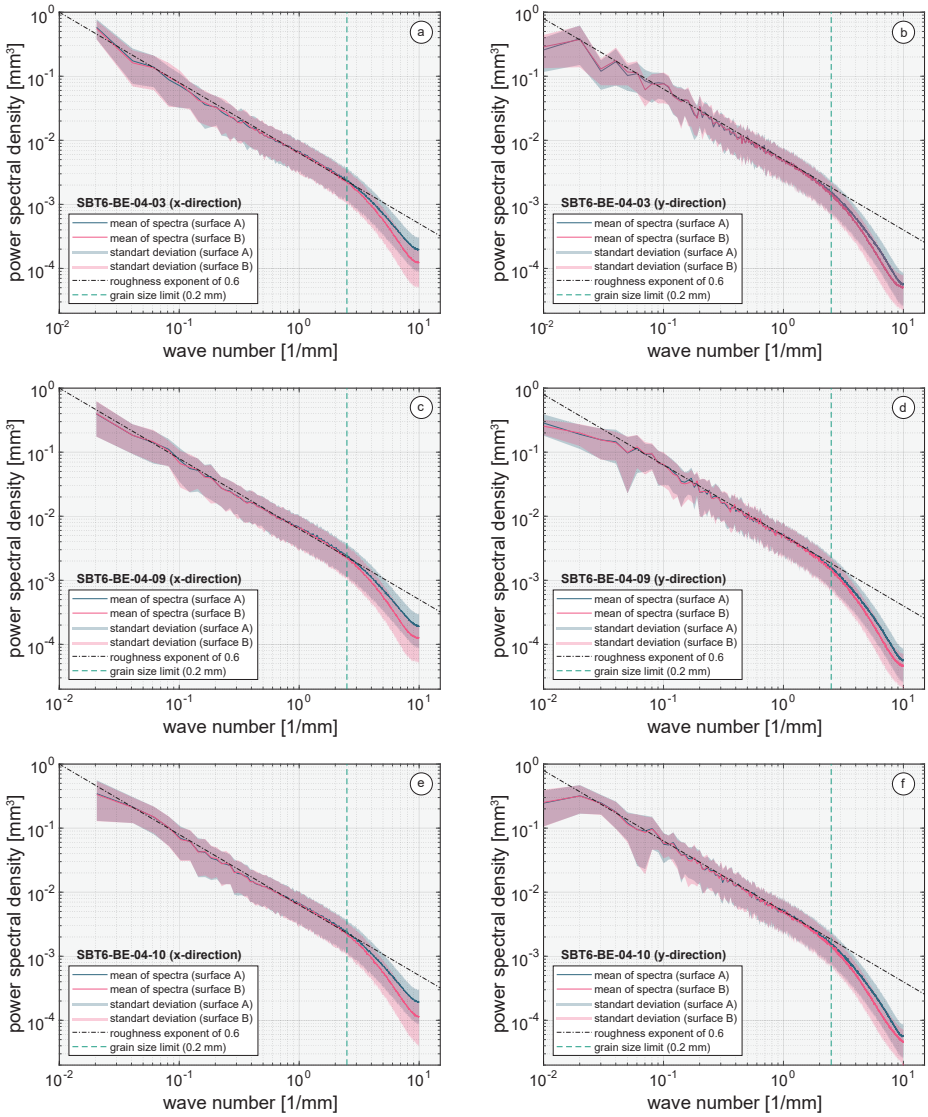

Figure 5.7: The direction-dependent roughness exponent of all fracture surfaces A and B before cyclic loading.

maximum measured fracture closure at about 60 MPa in the 2nd cycle, Δa_{max}, was subtracted from the initial aperture distribution, a_{ini}. Although this simplifies the process of two surfaces coming into contact, it allowed for an estimation of the mean fracture aperture at the largest stress. The maximum fracture closure, Δa_{max}, for sample SBT6-BE-04-03, 09 and 10 were -0.372, -0.365 and -0.350 mm. The resulting minimum mean apertures at highest effective stress in the 2nd loading cycle, $\bar{a}_{min}$, were 0.09, 0.07 and 0.07 mm, respectively (table 5.4). There was a slight trend in the data that the higher the initial mean

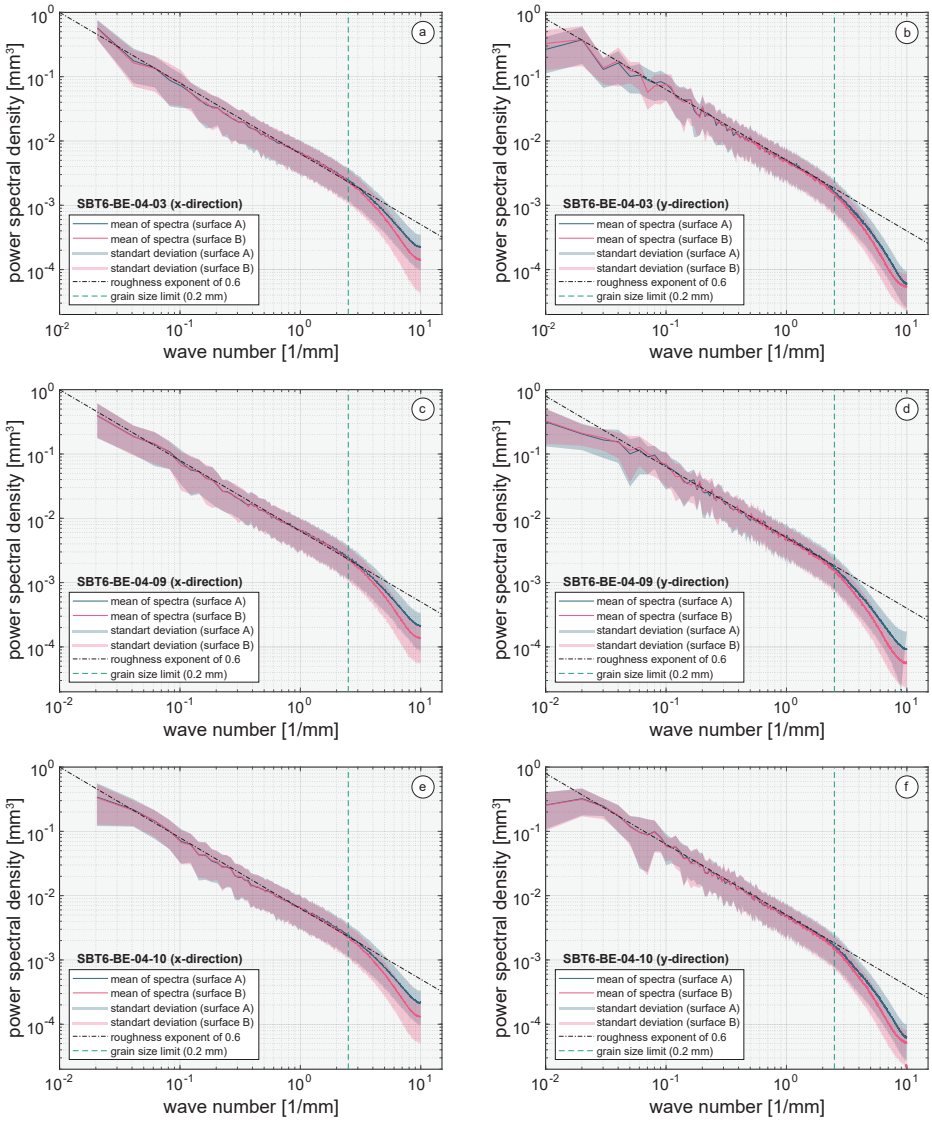

Figure 5.8: The direction-dependent roughness exponent of all fracture surfaces A and B after cyclic loading.

aperture, the higher the fracture closure at the end of the 2nd complete loading cycle. The maximum contact-area ratio, $R_{c,max}$, at the maximum effective stress at the end of the 2nd loading cycle was between 30 and 32 % for all samples (table 5.4). The contact-area, i.e. zero apertures, were marked in red in figures 5.9a, c, e (center). Here, we observed that the layering of the sample (perpendicular to the y-direction), was visible in the contact-area distribution leading to "contact bands" along the bedding. This possibly resulted in smaller

necks for fluid flow at large stress. The contact points were predominantly distributed along the edges of the sample indicating a generally concave shape of the fracture surface. This might result from a combination of the tensile fracture generation during diametrical loading conditions deforming the fracture surface and the finite size effect of the samples. After the experiment, the mean aperture at no confining pressure was between 0.31 and 0.34 mm for all samples, which corresponds to a total permanent aperture reduction of about 0.09 to 0.12 mm (figures 5.9a, c, e; right). A kink at the peak of the normal distribution in the post-experimental aperture distribution shows indicates changes in the fracture topography (figures 5.9b, d, f).

Table 5.4: Mean fracture aperture and contact-area ratio.

sample ID	$\bar{a}_{ini}$ [mm]	Δa_{max} [mm]	$\bar{a}_{min}$ [mm]	$R_{c,max}$ [-]	$\bar{a}_{post}$ [mm]
SBT6-BE-04-03 (CCL)	0.46	-0.372	0.09	0.30 ± 0.05	0.34
SBT6-BE-04-09 (PCL)	0.43	-0.365	0.07	0.32 ± 0.05	0.31
SBT6-BE-04-10 (PCL)	0.42	-0.350	0.07	0.31 ± 0.05	0.33

$\bar{a}_{ini}$: initial mean aperture, Δa_{max}: maximum measured fracture closure, $\bar{a}_{min}$: minimum mean aperture, $R_{c,max}$: maximum contact-area ratio, $\bar{a}_{post}$: post mean aperture

The mean aperture with increasing shear offset before and after the experiment was compared and is shown in figure 5.10b. Here we found a mechanical imprint after cyclic loading, meaning that the mean aperture at zero offset was higher and reduced towards the given shear offset applied during the experiment (0.5 mm). The lowest mean aperture, however, was found at a shear offset of 0.35 mm. At a shear offset above 1 mm, the mean apertures after the experiment are similar to those before the experiment. Although no change in roughness above grain scale was found, a change in fracture topography was visual when comparing the mean aperture with increasing shear displacement.

5.4. DISCUSSION

5.4.1. FRACTURE STIFFNESS & THE STRESS MEMORY EFFECT

In this section we discuss the evolution of fracture stiffness with increasing stress. We address the debate about the linearity of fracture stiffness with increasing effective pressure, as well as the hysteresis effect during loading and unloading. We then relate our findings to a possible "memory effect" of fracture stiffness during the progressive cyclic loading.

The loading and unloading path of fracture closure during loading shows a hysteresis effect (figure 5.5). This is well known and was documented numerously (Bandis et al., 1983, Brown and Scholz, 1986, Cook, 1992, Pyrak-Nolte, 1987, Skurtveit et al., 2020, Thörn et al., 2015, Yoshioka, 1994, Zou et al., 2020). During cyclic loading, hysteresis decreases and consequently the displacement between cycles decreases (Bandis et al., 1983, Brown and Scholz, 1986, Pyrak-Nolte, 1987). We see the same behaviour in our constant cyclic loading experiments (CCL). During unloading, the fracture opened slower compared to

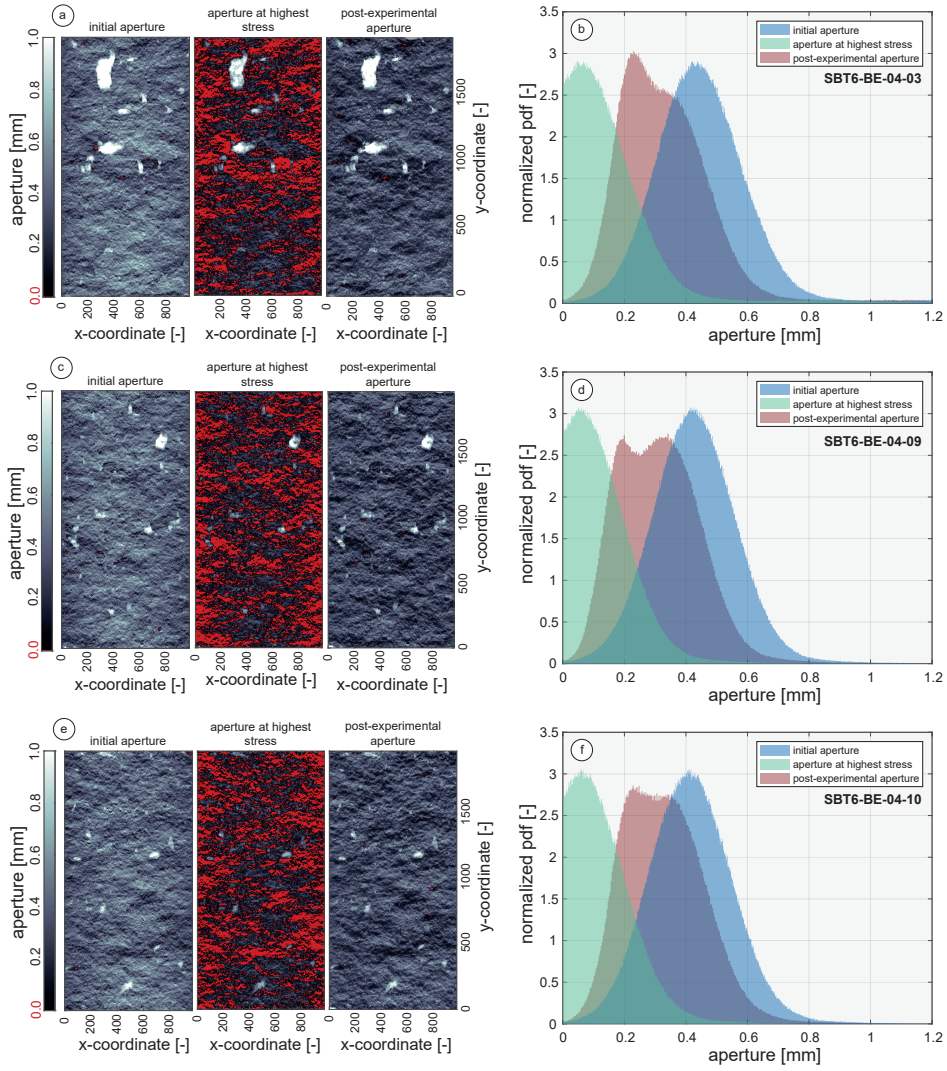

Figure 5.9: Fracture aperture before and after cyclic loading, as well as the aperture distribution before the experiments, at the highest stress, and after the experiment.

during loading while applying the same pressure rate of 0.5 MPa/min. This leads to larger and permanent fracture closure magnitudes, especially during and after the first loading cycle. This effect reduces in all subsequent loading cycles. We assume, that this difference comes from the boundary conditions of the experiment. The relaxation of the fracture is possibly slower because no active load is applied to open the fracture compared to when closing the fracture.

The fracture stiffness magnitudes were similar for all three experiments (figure 5.6). We assume that the data of all three experiments are repeatable and that the experimental workflow and boundary conditions led to consistent data. However, small deviations in fracture geometry between the samples can cause large deviations in fracture stiffness (Pyrak-Nolte and Morris, 2000). It is still important to note, that the measured fracture normal closure was largely dependent on the position along the sample. Furthermore, the measured values are strongly dependent on local variations caused by local aperture and contact-area variations (Cook, 1992, Marache et al., 2008). Overall, our calculated stiffness values were in the range of 100 to 800 MPa/mm for a sample scale of 10 cm, similar to experiments at the same effective pressure ranges with sandstone reported by Chen et al. (2017) and Skurtveit et al. (2020).

From the constant cyclic loading (CCL) experiments, we found a stress-path dependent fracture stiffness with a linear trend during the initial loading phase and a non-linear but reversible trend for all subsequent loading cycles (figure 5.6a). Previous studies reported contrasting results: while most authors describe a linear relationship of stiffness and stress with different slopes for different stress magnitudes (Akarapu et al., 2011, Bandis et al., 1983, Cook, 1992, Persson, 2007, Pyrak-Nolte, 1996, Wang and Cardenas, 2016, Zou et al., 2020), some reported a partly non-linear increase of fracture stiffness (Cook, 1992, Pyrak-Nolte and Morris, 2000, Pyrak-Nolte, 1987, Raven and Gale, 1985). From our data we see that linearity or non-linearity of fracture stiffness is not trivial, but depends on the stress history of a fracture. During initial loading, the stiffness trend with increasing stress is linear up to at least 60 MPa. The linear behaviour can be caused by multiple rheologies, such as elastic, plastic and elasto-plastic (Greenwood and Williamson, 1966, Kling et al., 2018, Pei et al., 2005, Persson, 2006, Zou et al., 2020). At higher stresses and depending on the rock type, roughness and host rock properties, a change in slope at a certain stress level during initial loading might be possible (Wang and Cardenas, 2016). This linear behaviour is not reversible when re-loading the sample within the same range of stress. During these subsequent loading cycles, the system becomes non-linear. The non-reversible behaviour clearly indicates plastic effects. The non-linear fracture stiffness trend is characterized by an initially steep increase at effective pressures up to 10 MPa and an almost horizontal trend at effective pressures higher than 30 MPa for sandstones. Several repeated loading cycles lead to a slight increase in the non-linear stiffness trend indicated by the grey curves in figure 5.6a. Therefore, a certain plastic component during repeated loading cannot be excluded. The much higher fracture stiffness value during initial unloading (figures 5.6b) can be explained by the slower opening of the fracture compared to during loading as explained in the previous paragraph (hysteresis effect). It might be that a longer or shorter hold phase than the 20 min in our experiments might impact the stiffness evolution during unloading.

When exceeding the previous stress level during re-loading, however, the non-linear fracture stiffness trend returns to a linear trend (figures 5.6c, e). This behaviour could be demonstrated in our progressive cyclic loading (PCL) experiments. During unloading, this effect is erased and shows again a non-linear trend. Every-time exceeding the previous stress, however, the change from non-linear to linear fracture stiffness behaviour can be repeated. We conclude, this effect is similar to the "Kaiser Effect" (e.g Kaiser, 1953) and reveals a stress-memory effect of fracture stiffness during progressive cyclic loading. Figure 5.10a

summarises the fracture stiffness evolution during constant cyclic loading (CCL) and progressive cyclic loading (PCL) for stresses of up to 60 MPa. It seems that at higher stresses fracture stiffness approaches a limiting value independent of the number of cycles. The turning point from non-linear to linear was visible shortly before the previous peak load is reached. This is similar to the classic "Kaiser Effect" in uniaxially loading tests with intact rock while monitoring acoustic emissions (Lavrov, 2005). Additionally, the fracture stiffness seems to reach its initial path with some delay.

Lavrov (2005) argued that the stress-memory effect may decay in the course of time, i.e. when the time interval between successive loading cycles is increased. Whether the stress-memory effect of fracture stiffness decays over time is not yet clear from our data. This is simply because the time frame of the experiments was too short. Still, we could show that the stress-memory effect is measurable using saturated samples. Experiments by Lavrov (2003) showed that a change in moisture is critical using acoustic emission when trying to detect the "Kaiser Effect".

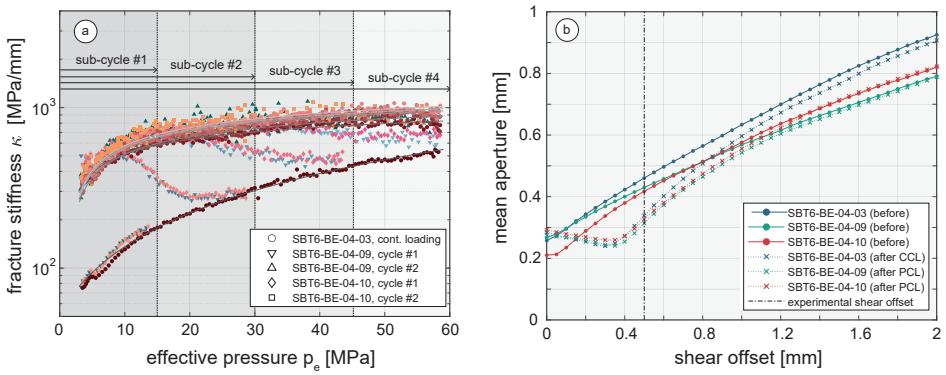

Figure 5.10: Summary of fracture stiffness evolution during constant cyclic loading (CCL) and progressive cyclic loading (PCL) (a) and the fracture mean aperture vs. the shear offset (b).

5.4.2. RELATIONSHIP OF MECHANICAL & HYDRAULIC PROPERTIES

The fracture stiffness describes the amount of closure of fracture with increasing normal stress and therefore directly affects the hydraulic properties of fractures. In this section we will shortly revise and then discuss how permeability and stiffness are related using our data. We will then discuss the role of the fracture geometry and how the previously described stress-memory of fracture stiffness impacts the evolution of permeability during progressive cyclic loading (PCL).

Pyrak-Nolte and Morris (2000) described that fluid flow and fracture specific stiffness are implicitly related since both depend on the size and spatial distribution of aperture and contact-area, or more general, the fracture geometry. Additionally, stiffness is not only dependent on stress magnitude, since all of the fractures they tested appeared to behave very differently, such that any interrelationship among the fracture properties was obscured.

They related this to the formation of new contact area as a direct function of the aperture distribution affecting the fracture normal closure. Albeit no relation to the stress magnitude was found, it was then concluded that stiffness is dependent on the stress path. Our data supports this assumption, while we also observed similar stiffness values at similar stress states. This is possibly due to the accurate sample selection from one block and the resulting compatibility of the three experiments. Contrary, the variety of trends shown by Pyrak-Nolte and Morris (2000) can be caused by a larger variety in fracture geometries of natural fractures. Attempts to normalize the relation of fracture stiffness and permeability were made by Pyrak-Nolte and Nolte (2016) based on numerical simulations. Unfortunately, the required scale-dependent fractures stiffness and permeability cannot be derived from the bulk measurements we obtained in the laboratory.

Progressive and constant cyclic loading leads to hysteresis effects in permeability, especially between the first and second loading cycle. We could show that after the first complete loading cycle up to 60 MPa, permeability was permanently reduced. In all following loading cycles, permeability also showed hysteresis effects. Permeability was always reduced to about the same value at the lowest applied normal load. Such a behaviour was shown numerous times already (e.g. Chen et al., 2000, Hofmann et al., 2016, Kluge et al., 2017a, Milsch et al., 2016, Pyrak-Nolte and Morris, 2000, Watanabe et al., 2009). Applying a progressive cyclic loading (PCL) procedure, however, shows a surprising behaviour. When reloading the fracture, permeability reduces less than during initial loading and permeability starts to decrease more when the previous peak load is exceeded, as expected. When directly comparing the total permeability reduction after the second cycle, however, we found that progressive loading obviously leads to less permeability reduction compared to constant loading conditions. This behaviour was only observed for the permeability. The measured mechanical aperture showed no distinct differences for PCL and CCL experiments.

The stiffening effect by progressive loading might be explained by three factors: (I) The overall longer duration when a fracture is loaded in progressive cycles. Since simply more time passes during the loading and unloading procedure, the fracture has more time for compaction. Asperity deformation might be reduced and fracture consolidation is more effective. (II) Other factors might be particle transportation causing partial blockage of fluid pathways. Unfortunately, we could not analyze the effluent on any changes in fluid composition or fines migration. (III) The observed stiffening effect could simply be sample dependent. All samples showed the same initial fracture permeability and similar fracture stiffness evolution suggesting a good experimental comparability and reproducibility. In fact, it cannot be ruled out that the permeability deviations during CCL and PCL scenarios can be caused by any variations of the sample by either variations in fracture geometry, asperity strength, clay content, etc.

The roughness, aperture distribution and contact-area control the plastic and elastic deformation of asperities, as well as the fluid flow in fractures (e.g. Cook, 1992, Kluge et al., 2017b, Pyrak-Nolte and Morris, 2000, Zou et al., 2020). We did not find a change in roughness by cyclic loading experiments, similar to Yoshioka (1994). The roughness exponent was found to be similar before and after the experiment at frequencies above the length of the grain size. Most changes in surface topography are related to changes at the grain

surface scale and/or even an elastic rearrangement of grains near contact-areas. However, calculating the mean aperture at various shear offsets using the post-experimental fracture surface scans (figure 5.10b) and the aperture histograms (figure 5.9) revealed a mechanical imprint. Therefore it is likely that fractures stiffness is not controlled by the bulk properties of rock, but the grain properties. Still, the self-affine roughness exponent is not affected by a complex mechanical loading history, proving its universality. The amount of aperture reduction did not exceed 0.12 mm comparing the mean aperture before and after the experiment. While plastic deformation of asperities seems to dominate the initial loading cycle with permanent fracture closure and permeability reduction, the following loading cycles lead to reversible fracture closure. The deformation process is strongly dependent on the distribution of asperities (Zou et al., 2020). Hence, fracture stiffness depends on the shear offset and the resulting evolution of the fracture aperture. It might be, that larger or smaller offsets than the 0.5 mm from our experiments, lead to a different evolution of stiffness. Especially when considering a percolation threshold that leads to large permeability reductions. The contact-area and is dominated by the elastic properties of rock (Cook, 1992, Pyrak-Nolte and Morris, 2000) after the first loading cycle when most plastic deformation was done.

What we cannot address in this study are the mechanics behind each released pressure step and the dependency of a variety of geometries on the stress-paths dependent permeability. These are some potential aspects that should be considered in future studies.

5.4.3. LIMITATIONS OF THE EXPERIMENTAL DATA

In the following we review the assumptions made for our calculations and the limitations that emerged.

The fracture stiffness was calculated from the corrected fracture closure (equation 5.11) by using the axial and circumferential extensometer data (equation 5.9) according to Bandis et al. (1983). Due to the cylindrical geometry with a diametrical fracture, the measured strain is a length phenomenon depending on the size of the fracture and the matrix surrounding it. Strain is therefore not homogeneous within the sample and correcting a change in circumference by a change in length is also not trivial. Additionally, the measured change in aperture (equation 5.10) depends on the local position of the extensometer along the sample and is controlled by local closure magnitudes. The roughness measurements (section 5.3.7), showed, that plastic asperity deformation takes place on the grain scale, although we consider bulk measurements of fracture closure and stiffness. Consequently, the aperture measurement must be considered as an indirect measurement.

Similar to the strain distribution, the hydrostatic confining pressure applied to the sample is not distributed equally throughout the sample. Depending on the fracture topography and sample geometry, the stress acting across sample and fracture varies. In the following we tried to estimate the stress acting across the contact-area. From the aperture distribution (figure 5.9) and the measured fracture closure, Δa, we calculated the evolution of the contact-area, R_c, as described in section 5.3.7 (figures 5.11a, c). Dividing the applied confining pressure by the computed contact-area, we obtained the stress acting on the fracture contacts at the respective applied effective pressure level (figures 5.11b, d). During initial

loading, the contact stress during the constant cyclic loading (CCL) reached its peak of around 500 MPa at about 4 MPa applied effective pressure and a decrease to about 240 MPa at 60 MPa (figure 5.11b). The 240 MPa contact stress exceed the uniaxial compressive strength of about 57 MPa for the Flechtingen sandstone as measured by Hassanzadegan et al. (2012). In all subsequent loading cycles, the contact stress was rather reversible without a peak. This shows, that most asperity damage is done during initial loading at low applied effective pressures. Applying the same procedure to the progressive cyclic loading (PCL) data, the contact stress increased until reaching the previous stress level (figure 5.11d). The contact stress then approached a limiting value of about 240 MPa at 60 MPa applied pressure. This suggests, that there is an universal contact stress level, in our case of about 240 MPa, which controls the fracture stiffness at larger applied stresses. What this value represents, e.g. the uniaxial compressive strength of a quartz grain, is not clear.

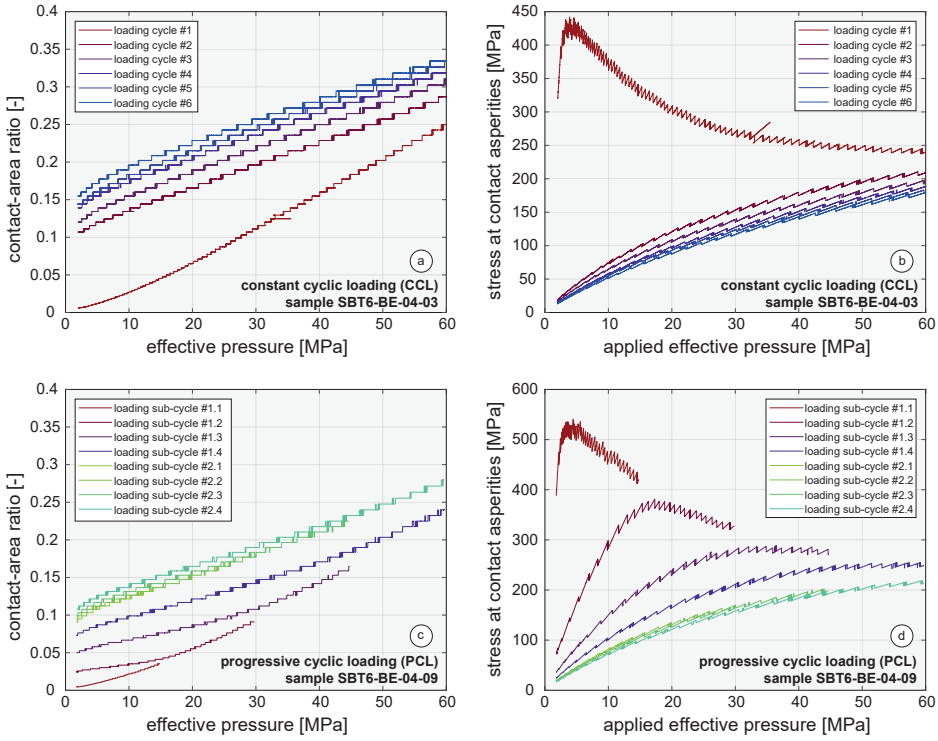

Figure 5.11: The fracture contact-area ratio (a,c) and the fracture contact-stress (b,d) at the respective applied effective pressure.

Although this shows the complex stress distribution within the sample, we assumed a homogeneous strain and stress distribution. We also consider fracture stiffness as a bulk property, albeit it is not controlled by the bulk properties of rock. Therefore, the uniaxial compressive strength of the bulk rock is not controlling the asperity strength as described by Milsch et al. (2016). These calculations and considerations reveal that we need to define clearly, what is

actually measured and what is assumed in such laboratory experiments.

5.4.4. SUSTAINABILITY OF PERMEABILITY & IMPLICATIONS

In this section, we discuss how the loading cycle pattern or stress history of a fractured rock impacts the permeability. We then discuss implications for fractured reservoirs and suggest an alternative pressure drawdown function.

As shown in the last section, the initial large decrease in permeability can be explained by a change of flow regime from sheet-like to channelized flow. In this "percolation regime", the contact-area ratio is sufficiently large, such that the rock matrix stiffness controls the fracture closure. In this regime, contact-area remains rather unchanged (Cook, 1992, Pyrak-Nolte, 1987, Zimmerman, 2008) and permeability will not fall below a certain level. This is known as the residual fracture permeability (Milsch et al., 2016) where permeability becomes increasingly independent of stress (Petrovitch et al., 2013, Pyrak-Nolte, 1987). Additionally, we found that a step-wise and cyclic increase of effective pressure seems to cause less permeability reduction, compared to when directly loading a fracture to the peak stress without interrupting. This stiffening effect must be considered to preserve the permeability of a fracture and highlights that permeability is also a stress-path dependent property. Progressive cyclic loading (PCL) might be a strategy to retain a higher permeability level.

Experimental data showed, that newly generated tensile fractures are initially more compliant with a potentially larger permanent reduction of permeability during the initial increase of effective stress (e.g. Bandis et al., 1983, Chen et al., 2000, Hofmann et al., 2016, Kluge et al., 2017a, Milsch et al., 2016, Watanabe et al., 2009). Contrary, testing of pre-existing or natural fractures shows less or no permanent reduction in permeability when repeatedly being subjected to a normal load as shown by Kluge et al. (2020) and Pyrak-Nolte (1987). From our results we deduce, that the change from a linear to a non-linear fracture stiffness indicates that a previous stress level is exceeded and is followed by a permanent reduction of permeability. This possibly explains the different permeability evolutions documented in cyclic loading experiments using different fracture types.

Although we understand that up-scaling laboratory results remains a challenge (Rutqvist, 2015), such information is crucial when developing an exploitation strategy and when assessing sustainability and safety of engineered subsurface projects. Blöcher et al. (2016) summarized the productivity evolution of the geothermal reservoir of Groß Schönbeck in the North German Basin. The Flechtingen sandstone tested in our experiments is considered as an analogue rock to the sandstones of the North German Basin (Blöcher et al., 2014, Hassanzadegan et al., 2012). The production well at Groß Schönbeck was stimulated twice in 2007 and production tests were performed between 2011 and 2013 (Blöcher et al., 2016). During that period, a continuous decline in productivity of the reservoir was found from more than 8 to less than 2 m^3/h/MPa. This was related to several potential processes, such as wellbore fill, wellbore skin, two-phase flow and hydraulic barriers or the closure of newly generated fractures. Pressure drawdowns were performed with a continuous pressure decrease. In case fractures are the main cause for the observed decrease, it would be interesting to investigate if a non-continuous pressure drawdown would cause less reductions.

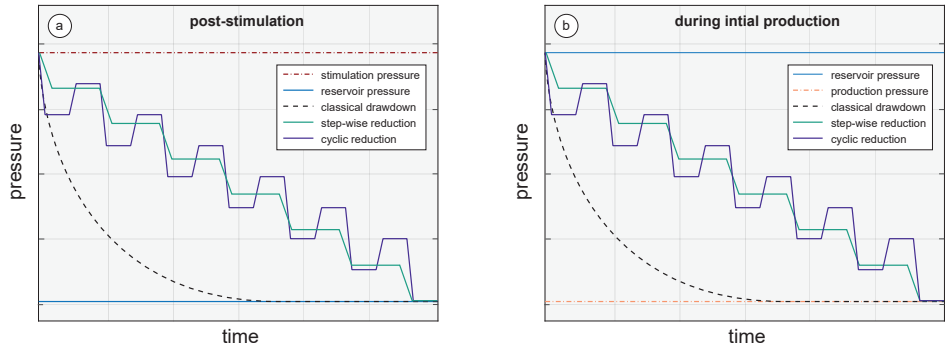

Figure 5.12: Classical pressure drawdown after stimulation (a) and during production (b), as well as the suggested step-wise and cyclic step-wise pressure functions.

We therefore recommend to apply a step-wise cyclic pressure function when lowering the fluid pressure after stimulation (figure 5.12a). Commonly, pore pressure is reduced continuously to the reservoir pressure after stimulation. A step-wise cyclic function might lead to a more effective compaction and consolidation of asperities. The same procedure could be applied when initially producing from a reservoir (figure 5.12b). During the initial pressure reduction by production, for example with a casing-lift test, it might be suggested to also do this in a step-wise cyclic procedure. After the initial pressure reduction in the reservoir, the fractures might behave elastic and no more cycling would be necessary. Whether a step-wise function without increasing the fluid pressure after each step would be sufficient, needs to be investigated in the future. Such a field test would show whether this procedure holds true in large-scale applications and whether it leads to a more sustainable fracture permeability due to a stiffening effect.

Furthermore, any resulting reduction in flow performance cannot be recovered by an increase in pore pressure at a stage later than stimulation and initial production. After initial loading of a fracture, any further reduction in flow performance might be caused by processes other than fracture closure, such as chemical processes, fines migration, etc. Lastly, the onset of linear fracture stiffness can help to identify the ancient or previously reached stress state in a fractured reservoir. This would be a similar approach as the "Kaiser Effect". It is unclear, however, how a single fracture behaves in a reservoir with a distinct fracture network of multiple fractures in various orientations at larger scale, as well as whether this is actually measurable in the field.

5.5. CONCLUSIONS

In this work, we were able to demonstrate a novel experimental procedure to depict the fracture stiffness evolution during two different loading scenarios: constant cyclic loading (CCL) and progressive cyclic loading (PCL). Due to the high resolution of the deformation and pressure data, we were able to reveal a stress-memory effect of fracture stiffness during

cyclic hydrostatic loading. Measuring the evolution of the hydraulic properties suggested that the permeability is dependent on the stress-history.

Overall, we suggest the following conclusion to be made from our experimental results: (I) Initial loading of a fracture leads to a linear stiffness evolution. The linear trend is non-reversible when re-loading the fracture within the same stress range. The second and all subsequent cycles show a non-linear and almost reversible behaviour. The responsible micro-mechanical deformation modes (elastic, plastic, elasto-plastic) in each phase remain to be evaluated. (II) When exceeding the previous stress level, the stiffness evolution turns from a non-linear to a linear behaviour. This suggests a stress-memory effect in fractures similar to the "Kaiser Effect" in intact rocks. (III) The permeability of a fracture is stress-path dependent. Progressive cyclic loading potentially leads to a stiffening of the fracture. Therefore, the reduction caused by effective stress changes in fractured rocks could potentially be mitigated by a cyclic, step-wise pressure function. (IV) The stiffening effect might also hold for larger scale reservoirs where a reduction in productivity can be related to a decrease in pore pressure after stimulation and during production. We therefore suggest to verify cyclic or step-wise pressure reductions in field tests. (V) The fracture surface roughness above grain scale remains unchanged although applying stress of up to 60 MPa. This supports the universality of the self-affine roughness exponent, since it is not affected by a complex mechanical loading history. Still, topography changes were indicated by a change in aperture distribution and a mechanical imprint, which reduces the self-propping effect at the given displacement.

Experimental studies need to emphasize the limitations of the laboratory measurements. When measuring bulk properties, the underlying physics and scale controlling the measured property need to be understood.

REFERENCES

S. Akarapu, T. Sharp, and M. O. Robbins. Stiffness of contacts between rough surfaces. *Physical Review Letters*, 106(20), may 2011. doi: 10.1103/Physrevlett.106.204301.

S. Bandis, A. Lumsden, and N. Barton. Fundamentals of rock joint deformation. *International Journal of Rock Mechanics and Mining Sciences & Geomechanics Abstracts*, 20 (6):249–268, dec 1983. doi: 10.1016/0148-9062(83)90595-8.

G. Blöcher, T. Reinsch, A. Hassanzadegan, H. Milsch, and G. Zimmermann. Direct and indirect laboratory measurements of poroelastic properties of two consolidated sandstones. *International Journal of Rock Mechanics and Mining Sciences*, 67:191–201, apr 2014. doi: 10.1016/j.ijrmms.2013.08.033.

G. Blöcher, T. Reinsch, J. Henninges, H. Milsch, S. Regenspurg, J. Kummerow, H. Francke, S. Kranz, A. Saadat, G. Zimmermann, and E. Huenges. Hydraulic history and current state of the deep geothermal reservoir groß schönebeck. *Geothermics*, 63:27–43, sep 2016. doi: 10.1016/j.geothermics.2015.07.008.

J. M. Boffa, C. Allain, and J. P. Hulin. Experimental analysis of fracture rugosity in granular and compact rocks. *The European Physical Journal Applied Physics*, 2(3):281–289, jun 1998. doi: 10.1051/epjap:1998194.

S. R. Brown and C. H. Scholz. closure of rock joints. *Journal of Geophysical Research*, 91 (B5):4939, 1986. doi: 10.1029/JB091iB05p04939.

T. Candela, F. Renard, Y. Klinger, K. Mair, J. Schmittbuhl, and E. E. Brodsky. Roughness of fault surfaces over nine decades of length scales. *Journal of Geophysical Research: Solid Earth*, 117(B8):n/a–n/a, aug 2012. doi: 10.1029/2011JB009041.

Y. Chen, W. Liang, H. Lian, J. Yang, and V. P. Nguyen. Experimental study on the effect of fracture geometric characteristics on the permeability in deformable rough-walled fractures. *International Journal of Rock Mechanics and Mining Sciences*, 98:121–140, oct 2017. doi: 10.1016/j.ijrmms.2017.07.003.

Z. Chen, S. P. Narayan, Z. Yang, and S. S. Rahman. An experimental investigation of hydraulic behaviour of fractures and joints in granitic rock. *International Journal of Rock Mechanics and Mining Sciences*, 37(7):1061–1071, oct 2000. doi: 10.1016/S1365-1609(00)00039-3.

N. Cook. Natural joints in rock: Mechanical, hydraulic and seismic behaviour and properties under normal stress. *International Journal of Rock Mechanics and Mining Sciences & Geomechanics Abstracts*, 29(3):198–223, may 1992. doi: 10.1016/0148-9062(92)93656-5.

B. R. Crawford, M. C. Tsenn, J. M. Homburg, J. A. Freysteinson, and W. C. Reese. Incorporating universal scaling of fracture stiffness and surface roughness effects for improved productivity prediction in naturally fractured reservoirs. In *50th U.S. Rock Mechanics/Geomechanics Symposium, 26-29 June, Houston, Texas, ARMA-2016-285*, 2016.

H. P. G. Darcy. *Les Fontaines publiques de la ville de Dijon. Exposition et application des principes á suivre et des formules 'a employer dans les questions de distribution d'eau, etc.* V. Dalamont, 1856.

J. A. Greenwood and J. B. P. Williamson. Contact of nominally flat surfaces. *Proceedings of the Royal Society of London. Series A. Mathematical and Physical Sciences*, 295(1442):300–319, dec 1966. doi: 10.1098/rspa.1966.0242.

H. Guo, N. Aziz, and L. Schmidt. Rock fracture-toughness determination by the brazilian test. *Engineering Geology*, 33(3):177–188, feb 1993. doi: 10.1016/0013-7952(93)90056-I.

A. Hassanzadegan, G. Blöcher, G. Zimmermann, and H. Milsch. Thermoporoelastic properties of flechtinger sandstone. *International Journal of Rock Mechanics and Mining Sciences*, 49:94–104, jan 2012. doi: 10.1016/j.ijrmms.2011.11.002.

A. Hassanzadegan, G. Blöcher, H. Milsch, L. Urpi, and G. Zimmermann. The effects of temperature and pressure on the porosity evolution of flechtinger sandstone.

Rock Mechanics and Rock Engineering, 47(2):421–434, apr 2014. doi: 10.1007/s00603-013-0401-z.

H. Hofmann, G. Blöcher, H. Milsch, T. Babadagli, and G. Zimmermann. Transmissivity of aligned and displaced tensile fractures in granitic rocks during cyclic loading. *International Journal of Rock Mechanics and Mining Sciences*, 87:69–84, sep 2016. doi: 10.1016/j.ijrmms.2016.05.011.

H. Hofmann, G. Zimmermann, A. Zang, and K.-B. Min. Cyclic soft stimulation (CSS): a new fluid injection protocol and traffic light system to mitigate seismic risks of hydraulic stimulation treatments. *Geothermal Energy*, 6(1), dec 2018. doi: 10.1186/s40517-018-0114-3.

D. Holcomb. General theory of the kaiser effect. *International Journal of Rock Mechanics and Mining Sciences & Geomechanics Abstracts*, 30(7):929–935, dec 1993. doi: 10.1016/0148-9062(93)90047-H.

J. Kaiser. Erkenntnisse und folgerungen aus der messung von geräuschen bei zugbeanspruchung von metallischen werkstoffen. *Archiv für das Eisenhüttenwesen*, 24(1-2):43–45, jan 1953. doi: 10.1002/srin.195301381.

T. Kling, D. Vogler, L. Pastewka, F. Amann, and P. Blum. Numerical simulations and validation of contact mechanics in a granodiorite fracture. *Rock Mechanics and Rock Engineering*, 51(9):2805–2824, may 2018. doi: 10.1007/s00603-018-1498-x.

C. Kluge, G. Blöcher, H. Milsch, H. Hofmann, A. Nicolas, Z. Li, and J. Fortin. Sustainability of fractured rock permeability under varying pressure. jul 2017a. doi: 10.1061/9780784480779.148.

C. Kluge, H. Milsch, and G. Blöcher. Permeability of displaced fractures. *Energy Procedia*, 125:88–97, sep 2017b. doi: 10.1016/j.egypro.2017.08.077.

C. Kluge, G. Blöcher, A. Barnhoorn, and D. Bruhn. Hydraulic-mechanical properties of microfaults in granitic rock using the punch-through shear test. *International Journal of Rock Mechanics and Mining Sciences*, 134:104393, oct 2020. doi: 10.1016/j.ijrmms.2020.104393.

A. Lavrov. The kaiser effect in rocks: principles and stress estimation techniques. *International Journal of Rock Mechanics and Mining Sciences*, 40(2):151–171, feb 2003. doi: 10.1016/S1365-1609(02)00138-7.

A. Lavrov. Fracture-induced physical phenomena and memory effects in rocks: A review. *Strain*, 41(4):135–149, nov 2005. doi: 10.1111/j.1475-1305.2005.00233.x.

D. Lockner. The role of acoustic emission in the study of rock fracture. *International Journal of Rock Mechanics and Mining Sciences & Geomechanics Abstracts*, 30(7):883–899, dec 1993. doi: 10.1016/0148-9062(93)90041-B.

A. Marache, J. Riss, and S. Gentier. Experimental and modelled mechanical behaviour of a rock fracture under normal stress. *Rock Mechanics and Rock Engineering*, 41(6): 869–892, apr 2008. doi: 10.1007/s00603-008-0166-y.

P. Meakin. *Fractals, scaling and growth far from equilibrium*. Cambridge university press, vol. 5 edition, 1998.

H. Milsch, H. Hofmann, and G. Blöcher. An experimental and numerical evaluation of continuous fracture permeability measurements during effective pressure cycles. *International Journal of Rock Mechanics and Mining Sciences*, 89:109–115, nov 2016. doi: 10.1016/j.ijrmms.2016.09.002.

C. Noël, F. X. Passelègue, C. Giorgetti, and M. Violay. Fault reactivation during fluid pressure oscillations: Transition from stable to unstable slip. *Journal of Geophysical Research: Solid Earth*, 124(11):10940–10953, nov 2019. doi: 10.1029/2019JB018517.

L. Pei, S. Hyun, J. Molinari, and M. Robbins. Finite element modeling of elasto-plastic contact between rough surfaces. *Journal of the Mechanics and Physics of Solids*, 53(11): 2385–2409, nov 2005. doi: 10.1016/j.jmps.2005.06.008.

L. Pei, G. Blöcher, H. Milsch, F. Deon, G. Zimmermann, W. Rühaak, I. Sass, and E. Huenges. Thermal strain in a water-saturated limestone under hydrostatic and deviatoric stress states. *Tectonophysics*, 688:49–64, oct 2016. doi: 10.1016/j.tecto.2016.09.020.

B. Persson. Contact mechanics for randomly rough surfaces. *Surface Science Reports*, 61 (4):201–227, jun 2006. doi: 10.1016/j.surfrep.2006.04.001.

B. N. J. Persson. Relation between interfacial separation and load: A general theory of contact mechanics. *Physical Review Letters*, 99(12), sep 2007. doi: 10.1103/PhysRevLett.99.125502.

C. L. Petrovitch, D. D. Nolte, and L. J. Pyrak-Nolte. Scaling of fluid flow versus fracture stiffness. *Geophysical Research Letters*, 40(10):2076–2080, may 2013. doi: 10.1002/grl.50479.

L. Pyrak-Nolte. The seismic response of fractures and the interrelations among fracture properties. *International Journal of Rock Mechanics and Mining Sciences & Geomechanics Abstracts*, 33(8):787–802, dec 1996. doi: 10.1016/S0148-9062(96)00022-8.

L. Pyrak-Nolte and J. Morris. Single fractures under normal stress: The relation between fracture specific stiffness and fluid flow. *International Journal of Rock Mechanics and Mining Sciences*, 37(1-2):245–262, jan 2000. doi: 10.1016/S1365-1609(99)00104-5.

L. J. Pyrak-Nolte. Hydraulic and mechanical properties of natural fractures in low-permeability rock. *Lawrence Berkeley National Laboratory. LBNL Report LBL-22718*, 1987.

L. J. Pyrak-Nolte and D. D. Nolte. Approaching a universal scaling relationship between fracture stiffness and fluid flow. *Nature Communications*, 7(1), feb 2016. doi: 10.1038/ncomms10663.

K. Raven and J. Gale. Water flow in a natural rock fracture as a function of stress and sample size. *International Journal of Rock Mechanics and Mining Sciences & Geomechanics Abstracts*, 22(4):251–261, aug 1985. doi: 10.1016/0148-9062(85)92952-3.

J. Rutqvist. Fractured rock stress-permeability relationships from in situ data and effects of temperature and chemical-mechanical couplings. *Geofluids*, 15(1-2):48–66, sep 2015. doi: 10.1111/gfl.12089.

J. Schmittbuhl, F. Schmitt, and C. Scholz. Scaling invariance of crack surfaces. *Journal of Geophysical Research: Solid Earth*, 100(B4):5953–5973, apr 1995a. doi: 10.1029/94JB02885.

J. Schmittbuhl, J.-P. Vilotte, and S. Roux. Reliability of self-affine measurements. *Physical Review E*, 51(1):131–147, jan 1995b. doi: 10.1103/PhysRevE.51.131.

E. Skurtveit, A. Sundal, T. I. Bjørnarå, M. Soldal, G. Sauvin, V. Zuchuat, I. Midtkandal, and A. Braathen. Experimental investigation of natural fracture stiffness and flow properties in a faulted CO 2 bypass system (utah, USA). *Journal of Geophysical Research: Solid Earth*, 125(7), jul 2020. doi: 10.1029/2019JB018917.

K. Terzaghi. *Erdbaumechanik Auf Bodenphysikalischer Grundlage*. Leipzig u. Wien, F. Deuticke, 1925.

J. Thörn, L. O. Ericsson, and Å. Fransson. Hydraulic and hydromechanical laboratory testing of large crystalline rock cores. *Rock Mechanics and Rock Engineering*, 48(1):61–73, jan 2015. doi: 10.1007/s00603-013-0538-9.

D. Vogler, F. Amann, P. Bayer, and D. Elsworth. Permeability evolution in natural fractures subject to cyclic loading and gouge formation. *Rock Mechanics and Rock Engineering*, 49(9):3463–3479, jun 2016. doi: 10.1007/s00603-016-1022-0.

L. Wang and M. B. Cardenas. Development of an empirical model relating permeability and specific stiffness for rough fractures from numerical deformation experiments. *Journal of Geophysical Research: Solid Earth*, 121(7):4977–4989, jul 2016. doi: 10.1002/2016JB013004.

N. Watanabe, N. Hirano, and N. Tsuchiya. Diversity of channeling flow in heterogeneous aperture distribution inferred from integrated experimental-numerical analysis on flow through shear fracture in granite. *Journal of Geophysical Research*, 114(B4), apr 2009. doi: 10.1029/2008JB005959.

P. A. Witherspoon, J. S. Y. Wang, K. Iwai, and J. E. Gale. Validity of cubic law for fluid flow in a deformable rock fracture. *Water Resources Research*, 16(6):1016–1024, dec 1980. doi: 10.1029/WR016i006p01016.

C. Xia, Z. Yue, L. Tham, C. Lee, and Z. Sun. Quantifying topography and closure deformation of rock joints. *International Journal of Rock Mechanics and Mining Sciences*, 40 (2):197–220, feb 2003. doi: 10.1016/S1365-1609(02)00134-X.

N. Yoshioka. The role of plastic deformation in normal loading and unloading cycles. *Journal of Geophysical Research*, 99(B8):15561, 1994. doi: 10.1029/94JB00931.

C. Zangerl, K. Evans, E. Eberhardt, and S. Loew. Normal stiffness of fractures in granitic rock: A compilation of laboratory and in-situ experiments. *International Journal of Rock Mechanics and Mining Sciences*, 45(8):1500–1507, dec 2008. doi: 10.1016/j.ijrmms.2008.02.001.

R. W. Zimmerman. A simple model for coupling between the normal stiffness and the-hydraulic transmissivity of a fracture. *42nd US Rock Mechanics Symposium and 2nd U.S.-Canada Rock Mechanics Symposium, San Francisco, June 29-July 2, 2008, ARMA 08-314*, 2008.

L. Zou, B. Li, Y. Mo, and V. Cvetkovic. A high-resolution contact analysis of rough-walled crystalline rock fractures subject to normal stress. *Rock Mechanics and Rock Engineering*, 53(5):2141–2155, dec 2020. doi: 10.1007/s00603-019-02034-w.

6

Discussion & Conclusion

In this thesis, the capacity of rock fractures to conduct fluid was investigated for a range of physical boundary conditions. The cubic law approximation was investigated depending on fracture surface roughness and shear displacement in 3D numerical simulations. The potential enhancement of permeability by faulting and the resulting sustainability under varying effective pressure was determined experimentally for crystalline and clastic rocks. Lastly, the importance of the stress-history on permeability and stiffness was explored in cyclic loading experiments with displaced tensile fractures. From the previous chapters, the scientific and technical implications are discussed with a focus on: (I) the complexity of fractured rock systems and the resulting importance of innovative inter-scalar experiments, (II) processes controlling the permeability evolution in shear and tensile fractures during fracture generation and effective pressure changes and (III) the possible consequences for operational strategies in fractured reservoirs.

6.1. Integrated Discussion

The Complexity Of Fractured Systems

Fractures are some of the most heterogeneous media that can be studied. In the majority of studies, their structure and behaviour were therefore simplified. Laboratory methods allow for the constraint of the physical boundary conditions in an experiment, such as using distilled water instead of a saline solution, keeping the temperature constant, or using simplified sample geometries, etc. This is a reasonable approach to determine and isolate specific processes that are aimed to be studied or that one needs to implement in a numerical code for further research. Analysing complex data from laboratory experiments in which a variety of processes, for example temperature changes, chemical reactions and stress changes influence each other, is almost impossible. With certain simplifications in experimental rock testing for fundamental research, the interplay between the physical processes involved might be ignored. Consequently, field-scale experiments in fractured reser-

voirs often lead to results that cannot be explained with controlled laboratory experiments. Certain simplifications or approximations can therefore be applied, but require a critical assessment of their potential to reproduce the complexity the physical processes that are inherent to the system. For the hydro-mechanical characterisation of fractures, two methods are often applied: "simplifying" (I) fracture geometries and (II) physical processes involved.

The simplification of the fracture geometry is a popular technique in laboratory rock testing. It involves using planar geometries which are considered as rough fracture surfaces. Therefore, displaced tensile fractures or planar saw-cut fractures are often used to determine the evolution of permeability, aperture or frictional properties in shear fractures (e.g. Im et al., 2018, Ishibashi et al., 2020, Noël et al., 2019). Studies on structural features in natural fault zones indicate that such simplifications are critical (e.g. Bense et al., 2013, Caine et al., 1996, Faulkner et al., 2010, Kim et al., 2004). The PTS experiments (chapter 3 and 4) show, that the range of possible outcomes is much larger than previously anticipated. That is, that shearing does not necessarily enhance permeability depending on the specific type of rock being tested (Kluge et al., 2021a). Further, whether there is a permeability reduction during cyclic loading depends on the conditions at which a fracture formed (Kluge et al., 2020). In-situ pressure conditions lead to a dissipation of plastic energy during fracture propagation and consequently a reversible permeability during effective pressure changes. Contrarily, displaced tensile fractures with a rigid shear offset (displacement at zero stress) lead to a high amount of plastic asperity deformation and consequently permanent permeability reduction in each pressure cycle (Hofmann et al., 2016, Kluge et al., 2017a). These results demonstrate how simplifications of the fracture geometry in laboratory experiments may tend to neglect important physical processes.

The simplification of physical processes during fracture flow is popular in numerical simulations. Fluid flow through fractures is often approximated by the flow through two planar surfaces separated by a fixed distance, known as the cubic law (Witherspoon et al., 1980). The presented results demonstrate, that this assumption overestimates permeability in rough and displaced fractures, especially at lower apertures (chapter 2). This is due to the complexity of flow evolving when the percolation regime, characterised by channeling and larger pressure disturbances, governs flow (Kluge et al., 2017b). It can further be assumed, that this approximation generally fails when trying to describe the flow in complex fault zones. In this study (chapter 2), another simplification is made that greatly impacts the flow in rough fractures: the interaction of fluid flow and fluid pressure between the rock matrix and the fracture itself is neglected. This is often done for several reasons, including reducing the required calculation capacity and the absence of numerical tools to couple Stokes and Darcy flow. In a collaborating work, Blöcher et al. (2019) showed that the interaction of flow between matrix and fracture can be captured in 3D numerical simulations.

Consequently, there will always be a need for innovative experiments that combine a certain amount complexity without overly simplifying the geometries and processes. The development of new technologies especially, such as fibre optic sensing during rock fracturing tested in a collaborating work (Nicolas et al., 2020), holds a high potential to extend possibilities to measure complex physical processes. Further, numerical simulations need to anticipate the complexity of fractured systems to better predict the hydro-mechanical behaviours of rocks and fractures.

(SUSTAIN)ABILITY OF FRACTURE PERMEABILITY

The ability of fractures to conduct fluids is crucial for geothermal energy exploitation. Two different reservoir types are commonly targeted: (I) faulted reservoirs that contain pre-existing and displaced faults cutting through several geological units, (II) tight reservoirs that require stimulation to generate artificial (engineered) fractures in the target horizon. In this chapter, an attempt is made to provide general recommendations to maintain a sufficient permeability in fractured rocks based on our laboratory findings in chapter 3, 4 and 5. These recommendations apply to the experimental scale of a few millimeters to centimeters and are related to hydro-mechanical processes only. First, the potential of fractures to act as a main fluid pathways in previously intact rocks is described. After that, it is shown how effective pressure changes affect the permeability evolution (sustainability) and what processes control their behaviour. Generally, we distinguish between shear fractures and tensile fractures.

Shear fractures are characterized by the presence of a fault core containing one or more principal shear planes and a surrounding damage zone. On the large scale, such faults are highly complex such that it is difficult to reproduce such fractures on the laboratory scale (Bense et al., 2013, Kim et al., 2004). Still, laboratory testing can provide insights about the behaviour of the variety of structures present in faults. The difficulty is, however, to cover the variety structures depending on host rock, stress history and stress regime (Caine et al., 1996, Faulkner et al., 2010). In chapter 3 and 4, the evolution of permeability while introducing a small fault into previously intact crystalline and clastic rocks is described. The permeability enhancement in crystalline rocks, such as granite, can be at least two to three orders of magnitude (Kluge et al., 2020). Permeability measurements in the laboratory over many orders of magnitude are difficult. The enhancement potential might even be greater considering studies where permeability was measured during the onset of fracturing (Mitchell and Faulkner, 2008). This potential, however, is likely to be affected by host rock properties, such as grain size and mineral composition, as well as the degree of weathering. The presence of phyllosilicates is important since they can block potential fluid pathways in the event that they are smeared out and because they are most prone to weathering (Kluge et al., 2021a). For clastic rocks, such as sandstones, almost no enhancement by faulting was found (Kluge et al., 2017a, 2021a). Clastic rocks containing clay or minerals other then quartz are, compared to crystalline rocks, more difficult to understand. The deformation process is not limited to a fault core and damage zone. Due to the larger initial porosity and the reduced grain bonding strength depending on their deposition history, deformation takes place by deforming the nearby pore space and by the rearrangement of grains. Pore filling minerals or clays and porosity itself have therefore a large impact on the formation of the fault zone and consequently the permeability evolution (Fossen et al., 2007). The diffuse strain accommodation in small faults may lead to an absence of a damage zone (Kluge et al., 2021a), which is commonly considered as most conductive (Bense et al., 2013).

Tensile fractures are characterized as a discrete feature, separating the rock by generating two almost identical fracture surfaces. When being displaced, these tensile fractures remain open due to the "self-propping" effect. Without any displacement, they instantly close when applying a normal stress, or require proppants to remain "open". The introduction of a tensile fracture in a previously intact rock can lead to bulk permeability enhancements of

up to five orders of magnitude, even in sandstone rocks (Kluge et al., 2021a). Similar results were obtained for crystalline rocks (Hofmann et al., 2016). This permeability potential is much higher compared to shear fractures, as described before. The main controlling factor to achieve a high permeability in tensile fractures, are the aperture distribution and the shear displacement, as well as the resulting contact-area ratio. These are controlled by the fracture surface roughness. The higher the roughness and the larger the displacement, the higher the aperture (Kluge et al., 2017b). However, a high aperture leads to more compliant fractures (Pyrak-Nolte and Morris, 2000), which consequently jeopardize the sustainability of fracture permeabiltiy.

The ability of fractures to serve as a fluid conduit can be altered by several factors. From a hydro-mechanical perspective, one of the main causes for permeability changes are effective pressure changes. Therefore, it is important to investigate the sustainability of tensile and shear fractures, or in other words, the ability to resist fracture closure due to external load or internal pressure reductions.

Form the presented experiments, it was found that the permeability of a microfault in crystalline rock is almost reversible when subjected to effective pressure changes of up to 10 MPa (Kluge et al., 2020). This in contrast to other experiments with cyclically loaded tensile fractures in crystalline rocks. Hofmann et al. (2016) found a permanent decrease in permeability in each loading cycle using granitic rock samples. However, they tested displaced tensile fractures that are substantially different in their deformation behaviour. Shear fractures, generated and displaced under in-situ pressure conditions, are affected by pre-dominantly elastic fracture deformation during effective pressure changes, since their plastic energy dissipated during the propagation processes (Kluge et al., 2020). Contrarily, displaced tensile fractures contain a large amount of plastic energy when taken apart and displaced at zero confining pressure. Therefore, they are affected by plastic fracture deformation during initial loading (Kluge et al., 2021b). Cyclic loading experiments with sandstones containing a single displaced tensile fracture also showed that, not only the stress magnitude, but also the loading history controls the fracture closure and thus fracture permeability. They showed that plastic deformation can be identified by a linear fracture stiffness evolution. A non-linear fracture stiffness evolution indicates a predominantly elastic deformation of asperities (Kluge et al., 2021b). This "stress-memory" effect of fracture stiffness can help in the identification of previous stress levels and can help in the understanding of the range of stresses at which no permanent permeability decrease can be expected. Lastly, progressive cyclic loading, at which the peak stress is increased in every cycle, can lead to a stiffening effect. This potentially causes the permeability to reduce less compared to a continuous loading path. This might be crucial for any reservoir application where the pore pressure is reduced. Whether this "stress-memory" effect and the stiffening effect holds true for crystalline rocks, remains to be tested in the future.

Of course, these results cannot be extrapolated to large scale faults and fracture systems directly. Furthermore, every rock is different and in itself highly heterogeneous. Not all aspects and possible outcomes can be covered by this experimental study. Nonetheless, these results can provide important information about how shear and tensile fractures within a complex fracture system might behave depending on the host rock (crystalline and clastic rocks). This is crucial to understand fluid barriers and conduits in such fractured reservoirs,

as well as to assess the sustainability of fracture permeability. Besides hydro-mechanical properties, thermal properties and rock-fluid interactions are considered to be a main cause for permeability changes in fractured rocks (Cheng and Milsch, 2020). The influence of temperature changes or chemical related alterations were not considered in this work. Coupling all four processes (THMC) in laboratory experiments remains a challenge and further work is needed to quantify their respective impact on the flow properties of fractured rocks.

IMPLICATIONS FOR FRACTURED RESERVOIRS

The main motivation for this experimental study was to identify the controlling properties on fracture permeability to be able to derive implications for fractured geothermal reservoirs. In this chapter, we will focus on faulted crystalline reservoirs and engineered tight reservoirs. Relating the previously described experimental observations to large scale field experiments is of course difficult (Rutqvist, 2015). The reasons for that are the complexity of natural systems compared to laboratory experiments, as well as the difference in scale of the physical processes controlling the fracture properties. However, it is attempted to directly relate the experimental observations to observations on the field scale. This is to provide implications and recommend new techniques to improve the sustainability of engineered geothermal reservoirs.

Based on our experimental evidences, faulted crystalline reservoirs hold a high potential for sufficient production. The reversibility of permeability during effective pressure changes can additionally lead to sustainable fluid production (Kluge et al., 2020). A highly representative geothermal site for crystalline rocks is Soultz-sous-Forêts in the Upper Rhine Graben in France. This reservoir is characterized by hydrothermally altered joints and faults in the crystalline basement that were utilized to circulate fluids (Baria et al., 1999b). The hydraulic data over many years suggests similar results compared to our experimental observations: fault permeability and hydraulic connectivity via faults can be maintained long-term for sufficient production although the effective pressure might be changed for operational reasons (Schill et al., 2015). Therefore, a high productivity index (PI) could be maintained at a level of about 36 $m^3h^{-1}MPa^{-1}$ for several years.

Other potential geothermal reservoirs are tight sandstone formations that require engineered fractures to achieve sufficient production. Such reservoirs can be considered appropriate, when introducing large tensile fractures with a shear offset. Without a shear offset, and therefore no "self-propping" effect, proppants are required to keep fractures "open". The latter is not part of this study. The experiments performed in this study were performed with a Rotliegend sandstone, which can be used as an analogue rock for geothermal sites in the Northern German Basin, for example the "GeneSys" geothermal sites Horstberg and Buchholz near Hannover (Tischner et al., 2013) and the Groß Schönebeck site north of Berlin (Blöcher et al., 2016). The stimulation and production history of Groß Schönebeck is well documented. The Rotliegend sandstone formations were stimulated twice in 2007, which led to an initial enhancement of the reservoir with a productivity index (PI) of about 10 $m^3h^{-1}MPa^{-1}$. During a series of production tests between 2011 and 1013 the productivity was found to decline from about 8 to less than 2 $m^3h^{-1}MPa^{-1}$ (Blöcher et al., 2016). This was related to several mechanisms, such as the reservoir geology, rock-fluid interactions or

the hydro-mechanical properties of fractures. Only the latter is addressed here. Assuming that after the fracture generation the fracturing pressure was continuously decreased to the reservoir pressure during shut in, the newly generated fractures were subjected to an effective pressure increase. Such an initial increase in effective stress potentially leads to plastic deformation of the fracture asperities (Kluge et al., 2021b). The same applies to the initial production, where pore pressure is further reduced leading to a further increase of effective stress that the fractures experience for the first time. With a cyclic pressure function and potentially resulting stiffening effect, fracture closure might be reduced such that the productivity could be maintained at higher levels. Such an approach has never been applied in large scale reservoirs. It is highly recommended to test cyclic pressure functions on all scales. Further, experimental evidence for the stress-memory effect in granitic fractured rocks is required.

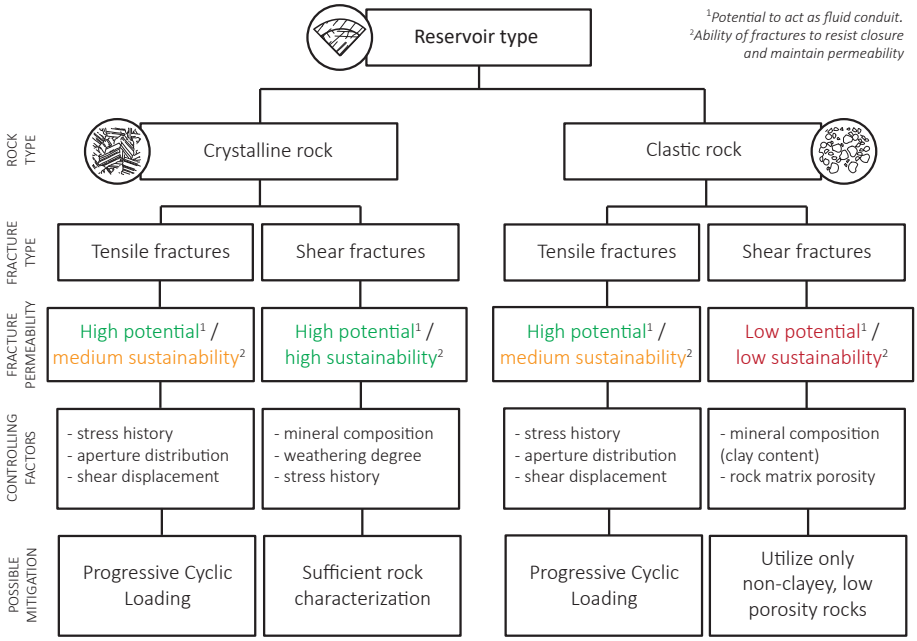

Figure 6.1: Recommendations for successful reservoir utilization based on rock and fracture type, the main controlling factors and possible mitigation strategies. The potential of fracture permeability describes the ability of fractures to act as fluid conduits in general. The sustainability of fracture permeability describes the ability of fractures to resist fracture closure and consequent permeability reductions during effective pressure changes.

6.2. CONCLUSIONS

In this thesis, a comprehensive set of experiments and numerical simulations to determine the controlling properties on the sustainability of fracture permeability is presented. The requirement of a high permeability potential and sustainability depends on the subsurface

application. While some engineered fractured systems require impermeable structures (for example nuclear waste repositories), others require a high fracture permeability (for example geothermal reservoirs). In this work, the main focus was to study the impact on geothermal reservoirs. The results demonstrate the complex dependency on a variety of parameters and highlights the different physical processes depending on mainly rock type and fracture type. An attempt was made to assess the potential of fractures to act as fluid conduits in reservoirs, as well their hydraulic sustainability during effective pressure changes. An overview for different rock (crystalline and clastic) and fracture types (tensile and shear), their permeability potential and sustainability, the main controlling properties and possible mitigation strategies to better maintain fracture permeability, is shown in figure 6.1.

The following conclusions can be drawn from the presented work: (a) the complexity of fractured systems and their underlying physical processes remain a challenge. Experimental testing or numerical simulations require a critical assessment of their potential to reproduce the processes of a "real" system. (b) The permeability of faults depends mainly on the host rock type (crystalline or clastic) and contains less plastic energy when generated under in-situ pressure conditions. This leads to a reversible permeability during effective pressure variations which is favourable for geothermal reservoir rocks. Shear fractures in clastic rocks seem to have a very limited potential. (c) The permeability evolution of displaced tensile fractures during effective pressure changes is more complex and depends on the loading history. Any applied stress that exceeds the previous stress level leads to a predominantly plastic and permanent permeability reduction. This can be understood as a stress-memory effect of fracture stiffness (closure) that directly controls permeability.

To be able to evaluate the sustainability or long-term performance of fractured of faulted geothermal reservoirs in general, the scientific focus needs to be adjusted. Enhancement strategies, such as hydraulic stimulation, are the most debated topic in the geomechanics society at the moment. This is of course important for reservoir performance (sufficient flow rates) and social acceptance (induced seismicity). However, little attention has been given to whether or not the achieved permeability enhancement can be sustained. Only reservoir enhancement strategies resulting in a sustainable productivity increase can guarantee the scientific and political breakthrough of geothermal energy supply.

REFERENCES

R. Baria, J. Baumgärtner, A. Gérard, R. Jung, and J. Garnish. European HDR research programme at soultz-sous-forêts (France) 1987-1996. *Geothermics*, 28(4-5):655–669, aug 1999b. doi: 10.1016/S0375-6505(99)00036-X.

V. Bense, T. Gleeson, S. Loveless, O. Bour, and J. Scibek. Fault zone hydrogeology. *Earth-Science Reviews*, 127:171–192, dec 2013. doi: 10.1016/j.earscirev.2013.09.008.

G. Blöcher, T. Reinsch, J. Henninges, H. Milsch, S. Regenspurg, J. Kummerow, H. Francke, S. Kranz, A. Saadat, G. Zimmermann, and E. Huenges. Hydraulic history and current state of the deep geothermal reservoir groß schönebeck. *Geothermics*, 63:27–43, sep 2016. doi: 10.1016/j.geothermics.2015.07.008.

G. Blöcher, C. Kluge, H. Milsch, M. Cacace, A. B. Jacquey, and J. Schmittbuhl. Permeability of matrix-fracture systems under mechanical loading – constraints from laboratory experiments and 3-d numerical modelling. *Advances in Geosciences*, 49:95–104, sep 2019. doi: 10.5194/adgeo-49-95-2019.

J. S. Caine, J. P. Evans, and C. B. Forster. Fault zone architecture and permeability structure. *Geology*, 24(11):1025, 1996. doi: 10.1130/0091-7613(1996)024<1025:FZAAPS>2.3.CO;2.

C. Cheng and H. Milsch. Permeability variations in illite-bearing sandstone: Effects of temperature and NaCl fluid salinity. *Journal of Geophysical Research: Solid Earth*, 125 (9), sep 2020. doi: 10.1029/2020JB020122.

D. Faulkner, C. Jackson, R. Lunn, R. Schlische, Z. Shipton, C. Wibberley, and M. Withjack. A review of recent developments concerning the structure, mechanics and fluid flow properties of fault zones. *Journal of Structural Geology*, 32(11):1557–1575, nov 2010. doi: 10.1016/j.jsg.2010.06.009.

H. Fossen, R. A. Schultz, Z. K. Shipton, and K. Mair. Deformation bands in sandstone: a review. *Journal of the Geological Society*, 164(4):755–769, jul 2007. doi: 10.1144/0016-76492006-036.

H. Hofmann, G. Blöcher, H. Milsch, T. Babadagli, and G. Zimmermann. Transmissivity of aligned and displaced tensile fractures in granitic rocks during cyclic loading. *International Journal of Rock Mechanics and Mining Sciences*, 87:69–84, sep 2016. doi: 10.1016/j.ijrmms.2016.05.011.

K. Im, D. Elsworth, and Y. Fang. The influence of preslip sealing on the permeability evolution of fractures and faults. *Geophysical Research Letters*, 45(1):166–175, jan 2018. doi: 10.1002/2017GL076216.

T. Ishibashi, Y. Fang, D. Elsworth, N. Watanabe, and H. Asanuma. Hydromechanical properties of 3d printed fractures with controlled surface roughness: Insights into shear-permeability coupling processes. *International Journal of Rock Mechanics and Mining Sciences*, 128:104271, apr 2020. doi: 10.1016/j.ijrmms.2020.104271.

Y.-S. Kim, D. C. Peacock, and D. J. Sanderson. Fault damage zones. *Journal of Structural Geology*, 26(3):503–517, mar 2004. doi: 10.1016/j.jsg.2003.08.002.

C. Kluge, G. Blöcher, H. Milsch, H. Hofmann, A. Nicolas, Z. Li, and J. Fortin. Sustainability of fractured rock permeability under varying pressure. jul 2017a. doi: 10.1061/9780784480779.148.

C. Kluge, H. Milsch, and G. Blöcher. Permeability of displaced fractures. *Energy Procedia*, 125:88–97, sep 2017b. doi: 10.1016/j.egypro.2017.08.077.

C. Kluge, G. Blöcher, A. Barnhoorn, and D. Bruhn. Hydraulic-mechanical properties of microfaults in granitic rock using the punch-through shear test. *International Journal of Rock Mechanics and Mining Sciences*, 134:104393, oct 2020. doi: 10.1016/j.ijrmms.2020.104393.

C. Kluge, G. Blöcher, A. Barnhoorn, J. Schmittbuhl, and D. Bruhn. Permeability evolution during shear zone initiation in low-porosity rocks. *Rock Mechanics and Rock Engineering*, feb 2021a. doi: 10.1007/s00603-020-02356-0.

C. Kluge, G. Blöcher, H. Hofmann, A. Barnhoorn, J. Schmittbuhl, and D. Bruhn. The stress-memory effect of fracture stiffness during cyclic loading in low-permeability sandstone. *Journal of Geophysical Research*, submitted, 2021b.

T. M. Mitchell and D. R. Faulkner. Experimental measurements of permeability evolution during triaxial compression of initially intact crystalline rocks and implications for fluid flow in fault zones. *Journal of Geophysical Research*, 113(B11), nov 2008. doi: 10.1029/2008JB005588.

A. Nicolas, G. Blöcher, C. Kluge, Z. Li, H. Hofmann, L. Pei, H. Milsch, J. Fortin, and Y. Guéguen. Pore pressure pulse migration in microcracked andesite recorded with fibre optic sensors. *Geomechanics for Energy and the Environment*, 24:100183, dec 2020. doi: 10.1016/j.gete.2020.100183.

C. Noël, F. X. Passelègue, C. Giorgetti, and M. Violay. Fault reactivation during fluid pressure oscillations: Transition from stable to unstable slip. *Journal of Geophysical Research: Solid Earth*, 124(11):10940–10953, nov 2019. doi: 10.1029/2019JB018517.

L. J. Pyrak-Nolte and J. P. Morris. Single fractures under normal stress: The relation between fracture specific stiffness and fluid flow. *International Journal of Rock Mechanics and Mining Sciences*, 37(1-2):245–262, jan 2000. doi: 10.1016/S1365-1609(99)00104-5.

J. Rutqvist. Fractured rock stress-permeability relationships from in situ data and effects of temperature and chemical-mechanical couplings. *Geofluids*, 15(1-2):48–66, sep 2015. doi: 10.1111/gfl.12089.

E. Schill, N. Cuenot, A. Genter, and T. Kohl. Review of the hydraulic development in the multi-reservoir / multi-well egs project of soultz-sous-forêts. In *Proceedings World Geothermal Congress 2015 Melbourne, Australia, 19-25 April*, 2015.

T. Tischner, S. Krug, E. Pechan, A. Hesshaus, R. Jatho, M. Bischoff, and T. Wonik. Massive hydraulic fracturing in low permeable sedimentary rock in the genesys project. In *Proceedings Thirty-Eighth Workshop on Geothermal Reservoir Engineering, Stanford University, Stanford, California*, 2013.

P. A. Witherspoon, J. S. Y. Wang, K. Iwai, and J. E. Gale. Validity of cubic law for fluid flow in a deformable rock fracture. *Water Resources Research*, 16(6):1016–1024, dec 1980. doi: 10.1029/WR016i006p01016.

ACKNOWLEDGEMENTS

First of all I would like to thank the European Union's Horizon 2020 research and innovation programme under grant agreement No. 654662 and the ReSalt project funded by the Federal Ministry for Economic Affairs and Energy (BMWi) under grant agreement No. 0324244C for supporting this work.

Special thanks goes to my daily supervisor Guido Blöcher for sharing his encompassing knowledge with me and who supported me in every aspect. I would like to thank my promoter David Bruhn for giving me the opportunity to realize this thesis and his guidance within the scientific community. My promoter Auke Barnhoorn deserves special thanks for his support and guidance regarding my project structure, the personal motivation and the advises and comments regarding the publications. I would also like to thank the committee members for their fruitful comments and corrections on the thesis. Thank also goes to Jean Schmittbuhl and Hannes Hofmann, for their cooperations and for their fruitful discussions that highly improved the quality of the publications. Thanks goes also to Barnaby Fryer for the language corrections and for accepting my humor since our studies in Delft. Furthermore, I am thankful to collaborating scientists and colleagues who supported me on a variety of topics including technical, scientific and thesis related issues. That is Anne Pluymakers, Richard Bakker, Rémi Charton, Baptiste Lepellier, Aurelien Nicholas, Morgan Tranter and Harald Milsch. For the translation of the summary into Dutch I would like to thank Willemijn van Rooijen.

I would also like to thank Ronny Giese for designing and realizing the experimental testing set-ups and his technical advices, as well as Tanja Ballerstedt and Florian Jasper Zimmermann for the technical support at the MTS. Furthermore, I would like to thank Stefan Gehrmann for preparing the high quality thin sections. In general, I would like to thank the section GeoEnergy at GFZ Potsdam for the excellent working conditions and the positive social atmosphere. The moral and social support of my PhD colleagues helped a lot to get through the tough times. I wish all PhD good luck and a strong mind to finish their projects.

Lastly and most importantly, I would like to thank my family for giving me the support and motivation to realize my dissertation. Thank you, Mi, for giving me the time to work on my thesis, the moral and psychological motivation and for accepting the struggles that this project brought along. Ed, thanks for being the sweetest and most relaxed child. Thank you, mom and dad, for supporting me all the way up, from an unhopeful pupil to a doctoral degree.

CURRICULUM VITÆ

Christian Kluge

BORN: Lutherstadt Wittenberg, Germany | 28 January 1989
EMAIL: christian.kluge@gfz-potsdam.de

EDUCATION

2016 - 2021 | PHD CANDIDATE, Delft Technical University and GFZ German Research Centre for Geosciences
Geothermal Engineering
"Sustainability of engineered fractured systems - An experimental study on the hydro-mechanical properties", promoter: Prof. Dr. David Bruhn (TU Delft / GFZ Potsdam), Dr. Auke Barnhoorn (TU Delft), supervisor: Dr. Guido Blöcher (GFZ Potsdam).

2014 - 2016 | MASTER OF SCIENCE, Delft Technical University, The Netherlands
Petroleum Engineering and Geosciences (Reservoir Geology)
Thesis: "A Structural Modeling Approach on Timing & Evolution of Mesozoic Anticlines in the Western High Atlas, Morocco", Mentor: Prof. Dr. Giovanni Bertotti (TU Delft), Dr. R. Charton (TU Delft). | Master thesis

2010 - 2014 | BACHELOR OF SCIENCE, University of Potsdam, Germany
Earth- and Environmental Sciences
Thesis: "Monitoring of the Kaiser Effect for saturated and unsaturated Brazilian Disk experiments with granite", Supervisors: Prof. Dr. Georg Dresen (GFZ Potsdam) and Dr. Tobias Backers (geomecon GmbH).

2013 | EXCHANGE SEMESTER, University of Bergen, Norway
Applied Earth Sciences
Participation in the Erasmus program.

2009 | ABITUR, Luth. Wittenberg, Germany
European High-School for Economics.

List of Publications

Journal Publications

10. **C. Kluge**, G. Blöcher, H. Hofmann, A. Barnhoorn, J. Schmittbuhl, D. Bruhn, *The stress-memory effect of fracture stiffness during cyclic loading in low-permeability sandstone*, Journal of Geophysical Research: Solid Earth, under review.

9. M. Jarrahi, G. Blöcher **C. Kluge**, H. M. Holländer, *Elastic-plastic fracture propagation modeling in rock fracturing via punch through shear test*, Rock Mechanics and Rock Engineering, under review.

8. R. Charton, **C. Kluge**, D. Fernández-Blanco, A. Duval-Arnould, G. Bertotti, *Syn-depositional Mesozoic siliciclastic pathways on the Moroccan Atlantic margin linked to evaporite mobilisation*, Marine and Petroleum Geology, in press.

7. **C. Kluge**, G. Blöcher, A. Barnhoorn, J. Schmittbuhl, D. Bruhn, *Permeability evolution during shear zone initiation in low-porosity rocks*, Rock Mechanics and Rock Engineering, (2021).

6. A. Nicholas, G. Blöcher, **C. Kluge**, H. Hofmann, L. Pei, H. Milsch, J. Fortin, Y. Guéguen, *Pore pressure pulse migration in microcracked andesite recorded with fibre optic sensors*, Geomechanics for Energy and the Environment **24**, (2020).

5. **C. Kluge**, G. Blöcher, A. Barnhoorn, D. Bruhn, *Hydraulic-mechanical properties of microfaults in granitic rock using the Punch-Through Shear test*, International Journal of Rock Mechanics and Mining Sciences **134**, (2020).

4. D. Fernández-Blanco, M. Gouiza, R. Charton, **C. Kluge**, J. Klaver, K. Brautigam, G. Bertotti, *Anticline growth by shortening during crustal exhumation of the Moroccan Atlantic margin*, Journal of Structural Geology **140**, (2020).

3. G. Blöcher, **C. Kluge**, H. Milsch, M. Cacace, A. B. Jacquey, J. Schmittbuhl, *Permeability of matrix-fracture systems under mechanical loading – constraints from laboratory experiments and 3-D numerical modelling*, Advances in Geosciences **49**, 95-104 (2019).

2. G. Blöcher, M. Cacace, A.B. Jacquey, A. Zang, O. Heidbach, H. Hofmann, **C. Kluge**, G. Zimmerman, *Evaluating Micro-Seismic Events Triggered by Reservoir Operations at the Geothermal Site of Groß Schönebeck (Germany)*, Rock Mechanics and Rock Engineering **51**, 3265-3279 (2018).

1. **C. Kluge**, H. Milsch, G. Blöcher, *Permeability of displaced fractures*, Energy Procedia **125**, 88-97 (2017).

CONFERENCE PROCEEDINGS

15. **C. Kluge**, G. Blöcher, A. Barnhoorn, J. Schmittbuhl, D. Bruhn, *The evolution of fracture stiffness during constant and progressive cyclic loading*, 8th European Geothermal Workshop, Strasbourg (2020).

14. G. Blöcher, **C. Kluge**, M. Cacace, J. Schmittbuhl, *Fracture-matrix system under normal stress: The evolution of specific stiffness and permeability*, 8th European Geothermal Workshop, Strasbourg (2020).

13. G. Blöcher, **C. Kluge**, M. Cacace, H. Milsch, J. Schmittbuhl, *Impact of a partly sealed fault on hydro-mechanical properties of a granite reservoir*, EGU General Assembly Conference, Vienna (2020).

12. **C. Kluge**, Blöcher, A. Barnhoorn, D. Bruhn, *Hydraulic-mechanical characterisation of microfaults in low porosity rocks – an experimental study*, Abstracts, 13th EURO-Conference on Rock Physics and Geomechanics, Potsdam (2019).

11. M. Cacace, G. Blöcher, A. Jacquey, A. Zang, O. Heidbach, H. Hofmann, **C. Kluge**, G. Zimmermann, *Evaluating the potential of induced seismicity during reservoir operations – case study of Groß Schönebeck (Germany)*, 7th International Conference on Coupled THMC Processes in Geosystems, Utrecht, The Netherlands, (2019).

10. G. Blöcher, **C. Kluge**, T. Goense, L. Pei, R.R. Bakker, D. Bruhn, *Hydraulic-mechanical characterisation of geothermal reservoir rocks*, European Geothermal Congress, Den Haag, The Netherlands, 11-14 June (2019).

9. G. Blöcher, **C. Kluge**, H. Milsch, M. Cacace, A. Jacquey, *Permeability of matrix-fracture system under mechanical loading - constraints from laboratory experiments and 3D numerical modelling*, EGU General Assembly Conference, Vienna (2019).

8. **C. Kluge**, G. Blöcher, A. Barnhoorn, D. Bruhn, *Laboratory Investigation of Microfault Permeability: the Punch-Through Shear (PTS) Test*, 10th European Geothermal PhD Day, Potsdam, Germany (2019).

7. C. Cheng, H. Milsch, **C. Kluge**, *Permeability sensitivity of fractured sandstone on account of scale-dependent aperture evolution*, International Conference on Coupled Processes in Fractured Geological Media: Observation, Modeling, and Application – CouFrac, Wuhan, China (2018).

6. **C. Kluge**, G. Blöcher, H. Milsch, D. Bruhn, *Permeability evolution of induced shear fractures at varying effective pressures using the saturated Punch-Through Shear test*, EGU General Assembly Conference, Vienna (2018).

5. M. Cacace, G. Blöcher, A. Jacquey, A. Zang, O. Heidbach, H. Hofmann, **C. Kluge**, M. Brehme, T. Reinsch, G. Zimmermann, *Evaluating the potential of induced seismicity during reservoir operations in EGS* , EGU General Assembly Conference, Vienna, p. 8887 (2018).

4. **C. Kluge**, G. Blöcher, D. Bruhn, *Hydraulic-Mechanical Characterization of Shear Fracture Permeability*, 9th European Geothermal PhD Day, Zurich, Switzerland (2018).

3. **C. Kluge**, G. Blöcher, H. Milsch, H. Hofmann, A. Nicholas, Z. Li, J. Fortin, *Sustainability of Fractured Rock Permeability under Varying Pressure*, In Poromechanics VI, 1192-1199 (2017).

2. A. Nicholas, G. Blöcher, Z. Li, **C. Kluge**, L. Pei, H. Hofmann, H. Milsch, Y. Guéguen, *Microseismicity and permeability enhancement in sandstone and andesite ruptured by fluid injection under triaxial conditions* , EGU General Assembly Conference, p.7799, Vienna (2017).

1. **C. Kluge**, G. Blöcher, *Experimental & Numerical Investigation of Fracture Permeability*, 8th European Geothermal PhD Day, Bochum, Germany (2017).

Faults and fractures control the structural integrity of the subsurface and the ability of rock to conduct fluids. They are crucial for the majority of subsurface engineering applications, including geothermal energy. When the properties for subsurface flow are insufficient they often require stimulation ("Enhanced Geothermal Systems"). While the effectiveness of the stimulation was often demonstrated, less attention was paid to the longevity of the enhancement (sustainability). This thesis aims to experimentally understand and interrelate hydraulic-mechanical properties of fractures and examines how they control the sustainability of an enhanced system.

TU Delft Delft University of Technology

GFZ Helmholtz Centre Potsdam

ISBN: 978-94-6366-392-2